Title
Formation of Reactive Oxygen Species by Ambient Particulate Matter: Probing causative agents and the underlying mechanism

Author
KUANG, XIAOBI Michelle

Publication Date
2017

Peer reviewed|Thesis/dissertation

UNIVERSITY OF CALIFORNIA

Los Angeles

Formation of Reactive Oxygen Species by Ambient Particulate Matter: Probing causative agents and the underlying mechanism

A dissertation submitted in partial satisfaction of the requirements of the degree Doctor of Philosophy in Atmospheric and Oceanic Sciences

by

Xiaobi Kuang

2017

ABSTRACT OF THE DISSERTATION

Formation of Reactive Oxygen Species by Ambient Particulate Matter: Probing causative agents and the underlying mechanism

by

Xiaobi Kuang

Doctor of Philosophy in Atmospheric and Oceanic Sciences

University of California, Los Angeles 2017

Professor Suzanne E. Paulson, Chair

Aerosol aging plays an important role in modifying aerosol chemical composition, hygroscopicity, cloud condensation nuclei activity and optical properties. Aqueous phase aerosol aging often involves reactive oxygen species (ROS), which include hydroxyl radicals (OH), hydrogen peroxide (H_2O_2), superoxide anion ($O_2^{\cdot -}$) and organic peroxides. Similar oxidation processes in cloud water may provide a pathway for secondary organic aerosol (SOA) formation through cloud processing during nighttime. Very limited studies have reported the direct quantification of OH and H_2O_2 production by ambient particles; and the contribution from different redox-active species to formation of ROS is not well understood. To address these questions, we combine field studies with laboratory experiments. Two field campaigns were carried out at Claremont, CA in summer and Fresno, CA in the winter. Samples collected on

Teflon filters were extracted in an atmospherically relevant solution (water at pH3.5) and physiologically relevant solutions (surrogate lung fluid, pH 7.4). Marine samples of engine emissions from a research vessel when operating on Ultra Low Sulfur Diesel (ULSD) and Hydrogenation-Derived Renewable Diesel (HDRD) were collected during dedicated cruises in 2014 and 2015, including aged samples collected by re-intercepting the ship plume. These samples were analyzed for particle mass, H_2O_2 and OH generation, soluble transition metals and speciated soluble iron (iron speciation and H_2O_2 was not quantified in the marine samples).

Our results show that soluble iron was about 50% Fe(II) and 50% Fe(III) in the Claremont samples but that the balance was slightly in favor of Fe(II) in the Fresno samples (65%) in pH3.5. The mass concentration was somewhat higher in Fresno, and on a per-mass basis, the Fresno PM generated a similar amount of H_2O_2 but far more OH than the Claremont PM. This high OH production was driven by the nighttime and morning samples, which were about 2.5 times more active than the Claremont samples; afternoon samples in Fresno were less active than Claremont. Nighttime and morning samples in Fresno had a strong signature from biomass burning HUmic LIke Substances (BBHULIS), and this material was very strongly correlated with OH formation, r^2=0.89. Because of fluorescence interference in the OH assay from BBHULIS, a method was developed to separate the BBHULIS from the OH probe (4-hydroxyterephthalic acid) using Hydrophilic Lipophilic Balance (HLB) cartridges.

Particles generated from HDRD combustion had slightly to significantly (5-50%) higher OH generation activity when extracted under surrogate lung fluid (SLF) than those from ULSD and freshly emitted particles exhibited lower activity than aged plumes. To better understand the mechanism of ROS formation by ambient samples, the ability of synthetic mixtures containing quinones, metals and Humic/Fulvic acids (surrogates for BBHULIS) to produce ROS was

investigated. When added alone, most of the redox active species tested did not produce ROS at atmospherically relevant concentrations. Addition of quinones did not show or only showed slight enhancement of ROS formation from Fe. In the contrast, the synergism of Cu and 1,4-Naphthoquinone produced more ROS than Cu alone.

The dissertation of Xiaobi Kuang is approved.

Jochen Stutz

Qinbin Li

Yifang Zhu

Suzanne E. Paulson, committee chair

University of California, Los Angeles 2017

Table of Contents

List of Figures

List of Tables

Acknowledgement

First and foremost, I would like to thank my advisor, Suzanne Paulson, for all of her support during my PhD life here. She has offered tremendous guidance and insight, making my PhD life much easier and fulfilled. She is the best advisor any student could ask for; I would not have come this far without her advice and encouragement. She's not only supportive in my academic life but also my personal life. She cried with me during my difficult times and laughed with me for all the excitements in my life. In these years, she has not only taught me how to be a good researcher and writer but also a good person.

I would like to also thank my committee members, Jochen Stutz, Qinbin Li and Yifang Zhu for their advice and suggestions. Thank you all for always be so accommodating and supportive when choosing proposal and dissertation defense date and time and their valuable ideas to my research work.

My work would not have been successful without our collaborators and colleagues. I would like to thank the Hasson group in California State University, Fresno and Cort Anastasio at University of California, Davis and Prof. Gisele Olimpio da Rocha form U. de Bahia for their useful discussion and suggestions. Thanks to Dr. Tiffany Charbouillot, Kennedy Vu and Catalina for their assistance in sample collections during the field campaigns in Claremont and Fresno and UCLA undergraduate students, Christopher Cala, Yu Zhong, Zane Karl and Kevin Huynh for their assistance in the lab. I particularly thank Prof. Leila Hawkins at Harvey Mudd College in Claremont for all the assistance she has provided during the Claremont Field Campaign. Many thanks to Lynn Russell at University of California, San Diego for the fun experience in participating in a fun project on a research vessel and Dr. Derek Price and Dr. Ragu Betha for useful discussion.

My PhD life would have been dull without my charming lab mates, David Gonzalez, Dilhara Ranasinghe and John Scott. We went from strangers to now more like family members over the years. Thank you guys for always there to support me, witnessing the important moments in my life. Thank you for easing my frustrations when the instruments don't work. Thank you all for the helpful discussion on my project, especially David. Thank you for sharing all those fun stories in your lives with me. Thank you for all the silly jokes. I would like to also thank other friends at AOS, Cenlin He, Mei Gao, Xuan Ji, and Chao Yue for their support and all those fun, random and sometime silly conversations. You are all wonderful and brilliant people I had great pleasure to work and hang out with.

Finally, I would like to thank my family for putting up with me, supporting me and loving me all these years. Thank you mom and Alice for always loving me unconditionally, I wouldn't have gone through all the difficulties without you guys. I especially would like to thank my husband, Charles, for always being there for me. Thanks for solving my technical problems, cook for me and do all the chores when I am busy, comforting me when I was stressed and encouraging me to becoming a better person; you are truly the best husband.

Vita

XIAOBI Michelle Kuang

SUMMARY

PhD candidate with research interest in atmospheric chemistry. Currently investigating the intrinsic ability of ambient particulate matter to produce reactive oxygen species, with the focus on the causative agents and the underlying mechanism.

EDUCATION

M.S. Atmospheric and Oceanic Sciences - University of California, Los Angeles 06/2013

B.S. Chemistry - University of California, San Diego
06/2010

SKILLS

Technical

- MS Office, MATLAB

Research

- Analytical techniques (High Performance Liquid Chromatography (HPLC), fluorescence spectrometer, gas chromatography, Inductive Coupled Plasma Atomic Emission Spectroscopy, LWCC)
- Aerosol characterization (Scanning Mobility Particle Sizer, Condensation Particle Counter, Polar Naphelometer)

Language

- Fluent in Mandarin and Cantonese

EXPERIENCE

Laboratory experience UCLA
06/2011 – Present

- Quantified Reactive Oxygen Species formation (ROS) by ambient fine particles under atmospherically and physiologically relevant conditions
- Developed a method to solve the optical interference with the fluorescence technique used to quantify hydroxyl radicals
- Analyzed iron speciation using Liquid Waveguide Capillary Cell with UV-Vis detection
- Analyzed soluble transition metals present in aerosol samples using ICP-AES
- Assisted with secondary organic aerosol chamber experiments, including photochemistry experiments and ozonolysis of VOC
- Performed model calculation of aqueous chemistry from CAPRAM using FACSIMLE
- Routinely checked instruments to ensure optimal performance
- Able to identify and troubleshoot problems associated with instruments
- Coordinated with undergrad students, guided them on basic laboratory techniques and sample analysis
- Managed laboratory supplies and hazardous waste management

Field Experience

- Conducted two field campaigns, one in summer 2012 and one in winter 2013, each for about 21 days
- Extensively participated in preparation for the field campaigns,

including experiment planning, chemical reagents, laboratory supplies, and filter preparation
- Collected samples three times a day to account for diurnal variations and performed on site chemical analysis during the field campaigns
- Able to solve any unforeseen problems occurred during the field campaigns
- Participated in a five-day scientific cruise around the Channel Islands on a research vessel to study the effects of diesel and biodiesel aerosols on marine environments and collected samples from the ship's exhaust, diluted plumes and aged plumes.

Teaching Assistant, Atmospheric and Oceanic Sciences, UCLA
09/2010 – 03/2012

- Conducted discussion sections and office hours for more than 100 students
- Assisted with exam grading and maintaining student records
- Provided support for individual student inside and outside the classroom
- Instructed in courses including air and water pollution

Publication:

Kuang, X. M., J. A. Scott, G. O. da Rocha, R. Betha, D. J. Price, L. M. Russell, D. R. Cocker, S. E. Paulson (2017). Hydroxyl radical formation and soluble trace metal content in particulate matter from renewable diesel and ultra-low sulfur diesel in at-sea operations of a research vessel. Aerosol Sci. Tech.:1-12.

Price, D. J., C.-L. Chen, L. M. Russell, M. A. Lamjiri, R. Betha, K. Sanchez, J. Liu, A. K. Lee, D. R. Cocker (2017). More unsaturated, cooking-type hydrocarbon-like organic aerosol particle emissions from renewable diesel compared to ultra low sulfur diesel in at-sea operations of a research vessel. Aerosol Science And Technology 51:135-146.

Betha, R., L. M. Russell, K. J. Sanchez, J. Liu, D. J. Price, M. A. Lamjiri, C.-L. Chen, X. M. Kuang, G. O. da Rocha, S. E. Paulson (2017). Lower NO x but higher particle and black carbon emissions from renewable diesel compared to ultra low sulfur diesel in at-sea operations of a research vessel. Aerosol Science And Technology 51:123-134.

1. Introduction

1.1 Background

Aerosols are of central importance for atmospheric chemistry, physics and climate change. Particularly, aerosol aging, i.e. oxidation of aerosols after their initial release, plays an important role in the modifying the chemical composition (Lim et al., 2010; Sato et al., 2011; Shrivastava et al., 2008), cloud condensation nuclei activity (Shilling et al., 2007), hygroscopic properties, (Suda et al., 2014), as well as optical properties of aerosols (Kim and Paulson 2013). Furthermore, inhalation of fine particulate matter has shown correlation with adverse health impacts, including asthma, cardiovascular diseases, pulmonary inflammation, lung cancer and mortality (Beelen et al., 2014; Brook et al., 2010; Dockery et al., 1993; McConnell et al., 2010; Pope et al., 2006; Thorne 2000). The mechanism of the health impacts caused by ambient particles are not yet completely understood, but a leading hypothesis under active investigation is that the adverse health impacts may derive from oxidative stress, which is initiated by formation of reactive oxygen species (ROS) within affected cells (Apel and Hirt 2004; Tao et al., 2003). ROS include hydroxyl radicals (OH), superoxide anion ($O_2^{\cdot -}$), hydrogen peroxide (H_2O_2), organic peroxides and organic peroxides. Aerosol aging processes are often mediated by reactive oxygen species, especially in the presence of OH.

1.2 Atmospheric Chemistry of ROS

Reactions in fog and cloud drops can have significant impact on the composition and chemistry of the troposphere. The fate of organic and inorganic compounds in the aqueous phase in the atmosphere is controlled by reactive oxygen species such as hydroxyl radicals, hydrogen peroxide, and superoxide anion.

1.2.1 Atmospheric chemistry of Hydrogen peroxide

Hydrogen peroxide serves as an important link between gas and aqueous phase chemistry due to its ability to partition into the aqueous phase. Hydrogen peroxide is highly soluble in water; with Henry's constant of $1x10^5$ M atm^{-1} (Sander 1999). Hydrogen peroxide is known to be the major oxidant that converts SO_2 to sulfuric acid, contributes to local or regional acid deposition and acidification of fog, cloud and rain. Gas-phase H_2O_2 is formed in the atmosphere by the bimolecular self-reaction of HO_2 radicals, and water reacting with Criegee radicals produced by alkene ozonolysis (Hasson et al., 2001a). Measurements of gas phase hydrogen peroxide have shown that its concentration can range up to 10 ppb (Jackson and Hewitt 1999; Lee et al., 2000), although it is more typically around 1ppb (Arellanes et al., 2006). Hydrogen peroxide can also be formed from photo-oxidation of formaldehyde (Bufalini et al., 1979) and organic carbon (Zuo and Deng 1997).

In addition to correlations with transition metals and quinones (as shown in the following sections), H_2O_2 is also correlated with several environmental factors and other metrics. Khurshid et al., (2014) showed that ROS formation by ambient $PM_{2.5}$ samples measured by dichlorofluorescein diacetate ($DCFH_2$) assay was correlated significantly with ozone concentration, ambient temperature and incident solar radiation; furthermore, hydrogen peroxide equivalent concentrations were about a factor of 4 higher in the summer than that in the winter, supporting that photochemistry is an important source of hydrogen peroxide. Hung and Wang (2001) also showed a correlation between ROS generation by ambient PM with various size fractions collected in Taiwan and the ozone concentration, especially for the smaller particles. Wang et al., (2011) on the other hand showed the formation of hydrogen peroxide by fine particles was independent on aerosol mass concentration but dependent on the presence of a

subset of transition metals.

1.2.2 Aqueous Atmospheric chemistry of hydroxyl radicals

OH is the most important oxidant in the atmosphere, including in atmospheric waters. In the aqueous phase it contributes significant to S(IV) oxidation in atmospheric waters (Pandis and Seinfeld 1989), as well as the oxidation of organics, generally at diffusion-controlled rates (Buxton et al., 1988). OH can initiate free radical chain reactions that can further enhance the oxidizing capacity of atmospheric water drops (Faust and Allen 1993), such as OH oxidation of organics which generates organic peroxyl radicals ($RO_2^{\cdot}$), which in turn react with NO, NO_3 or other $RO_2^{\cdot}$ radicals to form alkoxy radicals ($RO^{\cdot}$).

Several sources of OH formation in the presence of strong sunlight have been well documented. Faust and Allen (1993) suggested 4 sources of photoformed OH: 1) gas-drop partitioning of gas phase OH; 2) gas-drop partitioning of gas phase O_3 followed by reaction with $O_2^{-\cdot}$; 3) photolysis of H_2O_2, NO_3^-, NO_2^- and $Fe(OH)^{2+}$ and 4) photo-Fenton reaction : Fe(II) + H_2O_2 → Fe(III) + OH^- +OH. Faust and Hoigné (1990) showed the photolysis of $Fe(OH)^{2+}$ is a significant source to OH Formed in cloud, fog and raindrops. Arakaki and Faust (1998) showed that photo-Fenton reaction is a dominant source of OH for stored cloud water samples collected at Whiteface Mountain, Vermont. The lifetime of OH was found to be 2.4-10.6 μs, decreasing with increasing dissolved organic carbon concentration. Anastasio and McGregor (2001) measured photoformation of OH from photolysis of NO_2^-, HNO_2 and NO_3^- and found that nitrite was a significant source to photochemically formed $OH^{\cdot}$ in fog water, accounting for 47-100% of OH production. The lifetime of OH measured by Anastasio and McGregor (2001) was shorter than that reported by Arakaki and Faust (1998), which may suggest the presence of organic compounds in the fog droplets that were reacted with $OH^{\cdot}$. Using a modeling approach, Graedel

et al., (1986) showed that Fenton reaction was an important OH source at night but not in the daytime, this further indicates chemical reactions take place in the dark are important pathways to produce OH.

Hydroxyl radicals also play a role in modifying the composition of the aqueous phase in the atmosphere by oxidizing aldehydes to their corresponding carboxylic acids as well as involving in the loss of polycyclic aromatic hydrocarbons (PAHs). Studies have shown that hydroxyl radicals are also responsible for the oxidation of hydroxymethansulfonate to sulfuric acid, which is unreactive toward hydrogen peroxide and ozone. These oxidation processes are not only taking place in cloud and fog droplets, but can definitely occur in aerosol, rain and dew.

1.3 Health impacts of particulate matter and Endogenous production of ROS

1.3.1 Health impacts of fine particulate matter

Epidemiological studies have shown many associations between adverse health effects and particulate air pollution. These associations were first highlighted in a cross-sectional cohort study of six metropolitan cities conducted between 1975 and 1991 with a sample size of 8111 adults with age range from 25 to 74 years old at the time of enrollment. This study showed that long-term exposure to fine particulate air pollution was strongly correlated with cardiopulmonary diseases, lung cancer and mortality (Dockery et al., 1993). Since then substantial progress has made in the assessment of toxicity of fine particulate pollution. Fine PM is of particular importance due to its size and ability to penetrate deeper into the lungs than coarse particles. An increase of 10 $\mu g/m^3$ $PM_{2.5}$ long term exposure can lead to up to 17% increase in relative risk of mortality due to all cause and up to ~27% increase with mortality associated with cardiopulmonary disease and lung cancer (Pope and Dockery 2006). Traffic-related air pollution has shown to contribute to the development of asthma (Heinrich and Wichmann 2004;

McConnell et al., 2010; Oftedal et al., 2009). McConnell et al., (2010) conducted a cohort study of 5,349 children from kindergarten and first grade at time of enrollment in communities with significant traffic influence and found that the hazard ratio for traffic-related onset of asthma is 1.51 from roadways near home and 1.45 near schools. The mechanism of adverse health impacts by PM is not well understood, a leading hypothesis under active investigation is oxidative stress induced by PM, followed by inflammation and other health impacts.

1.3.2 Endogenous formation of ROS

Cellular formation of ROS is initiated by the reduction of oxygen by biological reducing agents such as NADPH (Jiang et al., 2011) to form superoxide as a defense mechanisms in neutrophils and macrophage cells. This process is catalyzed in the presence of electron transfer enzymes and redox active chemical species. Excess ROS in cells may alter cellular redox homeostasis, leading to a series of events associated with inflammation in lungs, characterized by increased cytokine/chemokine production (Li et al., 2008), mitochondrial and DNA damage (Li et al., 2015; Risom et al., 2005) and apoptosis (cell death) (Guo et al., 2013).

The epithelial lining fluid serves as an interface between the atmosphere and the human body, it contains a range of surfactants and antioxidants such as ascorbate (Asc), uric acid (UA) and glutathione (Van Der Vliet et al., 1999). Exogenous sources of ROS can be environmental oxidants, including cigarette smoke and ozone. ROS can also be produced by particulate matter upon inhalation. A number of studies have shown that redox active components such as transition metals (Charrier and Anastasio 2011; Valavanidis et al., 2005; Wang et al., 2010), quinones (Chen and Pignatello 1997; Chung et al., 2006; Duesteberg and Waite 2007; Shang et al., 2012; Xia et al., 2004), and can lead to ROS formation. Transition metals, either as free ions or as metal-ligand complexes, are capable of generating ROS through redox reactions (R1.1-R1.4).

The presence of electron donors can catalyze the redox cycling of iron (R1.4) and thus enhance ROS production. Several studies have also confirmed the role transition metals play in the formation of ROS by adding metal chelators such as chelex and desferroxamine, and these have been shown to remove of majority of the ROS activity (>90%) (Shafer et al., 2010; Vidrio et al., 2009).

$$Fe(II) + O_2 \rightarrow Fe(III) + O_2^{\cdot -} \quad (R1.1)$$
$$Fe(II) + O_2^{\cdot -} + 2H^+ \rightarrow H_2O_2 + Fe(III) \quad (R1.2)$$
$$Fe(II) + H_2O_2 \rightarrow Fe(III) + OH + HO^- \quad (R1.3)$$
$$Fe(III) + Asc\ (red) \rightarrow Fe(II) + Asc\ (ox) \quad (R1.4)$$

Endogenous formation of ROS through multiple redox reaction cycles in the epithelial lining fluid is depicted in Fig. 1.1. This process begins with the transfer of electron from antioxidant, in this case ascorbate, to transition metals (Fe or Cu) and/or quinones to form reduced metals and semiquinone radicals ($Q_2^{\cdot}$). The reduced metals and $Q_2^{\cdot}$ will then react with oxygen to form superoxide anion as well as regenerating the oxidized form of metals and quinones. Superoxide will react with superoxide dismutase (SOD) to form hydrogen peroxide, which in the presence of metals, can be broken down to OH via Fenton/Fenton-like reactions (R3). ROS levels in healthy human health is about 100 nM (Lakey et al., 2016), however, ROS generated by particulate matter can be in the micro molar ranges (Paulson et al., 2016; Shen and Anastasio 2012).

As antioxidants act as electron donors, they can play an important role in ROS formation by particulate matter under physiological conditions. Ascorabte has been found to increase ROS formation from transition metals (Charrier and Anastasio 2011; DiStefano et al., 2009; Jung et al., 2006; Shen and Anastasio 2011). Ascorbate can be an effective reducing agent for Fe. Its ability to reduce Fe is comparable to hydroxylamine, a well known reducing agent for Fe

(Elmagirbi et al., 2012). The resulting reduced form of transition metals can reduce dissolved oxygen and subsequently form $O_2^{\cdot -}$, H_2O_2 and $OH^{\cdot}$, and ascorbate can catalyze the redox cycling of transition metals, thus increasing ROS formation (R1.1-R1.4). Ascorbate appears to act as pro-oxidant at low concentrations (below 0.5 mM) and anti-oxidant at high concentrations. The rationale is that in the presence of ascorbate, catalytic metals will initiate radical chain oxidation. At high concentrations (15mM), the oxidation chain length is low due to the antioxidant chemistry of ascorbate; and it maybe at high enough concentration that it scavenges or consumes OH, since the reaction between ascorbate and $OH^{\cdot}$ is very rapid (R1.7) (Buettner and Jurkiewicz 1996). While at low concentrations, the rate of antioxidant processes of ascorbate are lowered (reaction R7), and ascorbate can catalyze the redox cycle of iron (R1.5 and R1.6).

$$Fe(III) + O_2^{\cdot -}/AscH^- \rightarrow Fe(II) + O_2/Asc^{\cdot -} \quad \text{(R1.5)}$$

$$Fe(II) + H_2O_2 \rightarrow Fe(III) + OH^{\cdot} + OH^- \quad \text{(R1.6)}$$

$$AscH^- + OH \rightarrow Asc^{\cdot -} + H_2O \quad \text{(R1.7)}$$

This lengthens the oxidation chain, and enhances oxidant formation (Buettner and Jurkiewicz 1996). Since the ascorbate concentrations used by Anastasio and co-workers were low (50-200μM), it would be expected to increase oxidant production.

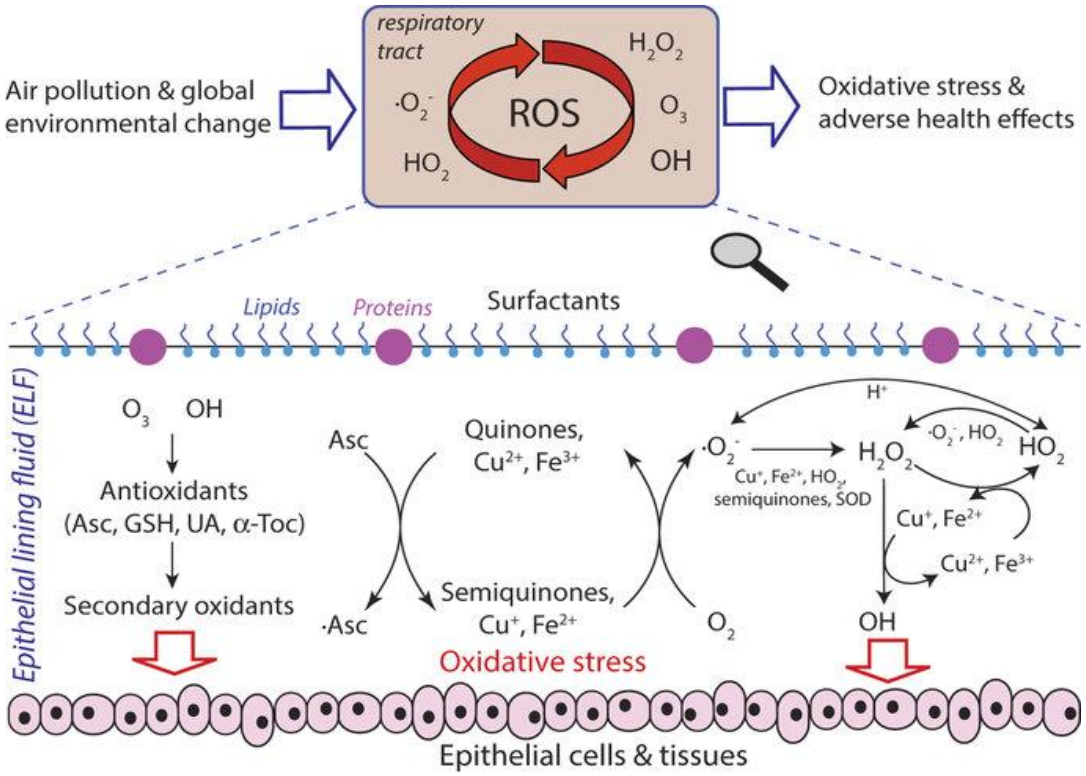

Fig. 1.1 Formation of ROS in the epithelial lining fluid in the human respiratory tract (Figure adapted from Lakey et al., (2016)

1.4 Role of transition metals in ROS formation

Transition metals, either as free ions or as metal-ligand complexes, are capable of generating ROS through redox reactions. These reactions can be catalyzed by electron donors such as ascorbate (R1.1-R1.4). The soluble fractions of transition metals have received attention for their role in generating ROS (Knaapen et al., 2002; Roberts et al., 2004; Wang et al., 2011). Zhang et al., (2008) measured ROS activity with a bioassay and apportioned different particulate sources using positive matrix factorization (PMF) and showed that ROS activity was related to an iron source, soil source and a water-soluble source factor, and a linear combination of the 3 sources accounted for 70% of ROS activity, in which the iron source accounted for the greatest fraction of ROS activity. Other studies have also confirmed the role transition metals play in the formation of ROS by adding metal chelators such as chelex and desferroxamine, resulting in the

removal of majority of the ROS reactivity (>90%). (Shafer et al., 2010; Vidrio et al., 2009) Wang et al., (2010) showed that hydrogen peroxide (1 nmol/m^3) generated by the coarse particles collected in Riverside, CA was strongly correlated with Fe, Cu and Zn. However, See et al., (2007) showed a different set of transition metals, Cd, Co, Cu, Fe, Mn, and Ni, were correlated with ROS (5.71 nmol H_2O_2/m^3) generated by wood smoke, gas cooking and other aerosol sources. The water-soluble transition metals content in these particles in both studies were in good agreement; Cu and Fe were the most abundant metals. Furthermore, Shafer et al., (2010) found a similar subset as See et al., (2007): the redox-active metals, Mn, Co, Fe, and Ni, showed strong correlations with ROS activity while the non-redox active metals, Zn, Pb and Cd, showed very weak correlations. This project seeks to expand on the small existing data set that had begun to unravel the transition metal activity in ambient particles, including the speciation of the redox active metals. Recently, Gonzalez et al (2017) have shown that the rate of both superoxide and OH formation by iron is enhanced by Humic Like Substances (HULIS); HULIS can enhance the rates of these reactions by more than two orders of magnitude.

1.5 Role of quinones in ROS formation

Quinones have received increasing attention due to their potential contribution to oxidative stress and redox activity in the ambient aqueous phase. Quinone redox cycling is shown in Fig. 1.2. In the presence of an electron donor, quinones are converted to semiquinone radical anions with concomitant production of superoxide radicals and hydrogen peroxide. Superoxide then facilitates reformation of quinone, accompanied by production of production of additional H_2O_2 (Fig. 1.2). Several studies have shown association of quinones with ROS production. Xia et al., (2004) fractionated diesel exhaust particles into aliphatic, aromatic and polar organic compounds and found that the quinone-enriched polar organic fraction is more

potent in superoxide radical formation. Chung et al., (2006) measured H_2O_2 formation by ambient fine particles collected in Fresno, CA and measured several quinone concentrations in the samples. Of the speciated quinones, 1,4-naphthoquinone (0.15 ng/m^3), 1,2-naphthoquinone (1.1 ng/m^3) and phenanthaquinone (1.1 ng/m^3) were the most reactive quinones in generating ROS. Shang et al., (2012) showed that the concentration of quinones had an effect on hydroxyl radicals formation: at low concentrations, 1,4-naphthoquinone consumed superoxide anion and suppressed OH formation; however, at high concentrations, OH formation was correlated with 1,4-naphthoquinone. Additionally, hydroquinones and semi-quinone radicals are able to reduce Fe^{3+} to Fe^{2+} and can act as an electron transfer catalyst (Chen and Pignatello 1997; Duesterberg and Waite 2007) and thus play an important role in OH· formation.

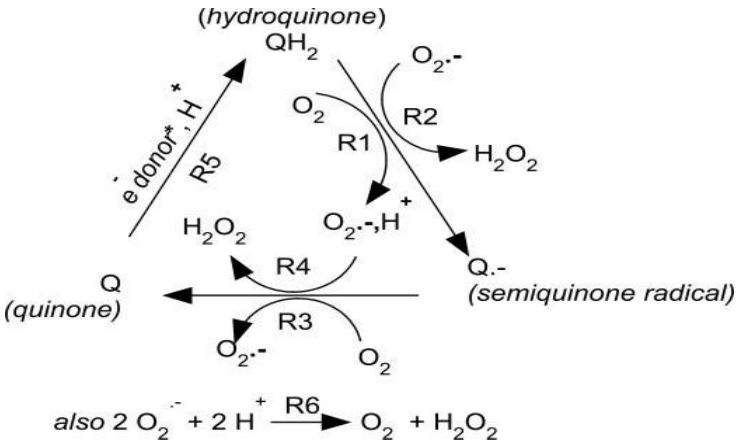

Fig. 1.2 Quinone redox chemistry.

1.6 Role of humic like substances (HULIS)

HULIS has gained more attention in their potential role in ROS generation. The term HULIS was first used by Havers et al., (1998) to describe these macromolecular organic compounds that resemble terrestrial and aquatic humic and fulvic acid. HULIS contributes a major fraction to water soluble organic carbon in aerosols, ranging from 38-72% for samples collected in rural site (Kiss et al., 2002), up to 62% in urban sites. (Duarte et al., 2004; Krivácsy

et al., 2008; Lin et al., 2010) HULIS accounted for 30% of the fresh biomass (Crop residue) burning in China (Lin et al., 2010) and 50% of the water-soluble organic carbon of biomass burning aerosols over Amazonia. (Mayol- Bracero et al., 2002) The origin of HULIS is not well understood. However, several studies suggested that HULIS is potentially originated from biomass burning (Hoffer et al., 2006; Mukai and Ambe 1986; Zappoli et al., 1999) and formed via secondary reactions (Decesari et al., 2001; Limbeck et al., 2005), soot oxidation and aerosol-phase polymerization of organic compounds from soil and other natural sources. (Graber and Rudich 2006)

Because of the multifunctionality nature of HULIS, it is believed that HULIS plays an important role in the production of ROS. To date, several studies have reported the ability of HULIS to produce ROS. An earlier study by Moonshine et al., (2008) showed that atmospheric HULIS extracted from wood burning PM samples enhanced the degradation of pyrene and phenol by promoting the Fenton reaction in the absence of light. Although this study did not measure ROS directly, but the degradation of these organic contaminates by oxidation were largely mediated by OH radicals. Using a dithiothreitol assay, Lin and Yu (2011) suggested that HULIS isolated from ambient PM samples is the major redox active species in the water-soluble fraction in PM. The redox activity of HULIS in the DTT assay was higher than the two standard fulvic acid tested and the rate of DTT consumption was dependent on the concentration of HULIS.

1.7 Other complex organic compounds

Several studies have suggested contributions from transition metals and quinones alone cannot account for all of the ROS observed, suggesting additional compounds that are responsible for the remaining ROS generation. Chen et al., (2011) found that secondary organic

aerosol (SOA) from limonene ozonolysis produced 5.2-14.5 nmol/m^3 equivalent of H_2O_2, activity that decreased by 3-17% upon aging. Rattanavaraha et al., (2011) showed that SOA from α-pinene + toluene had a high ROS response. These results are consistent with those from our group, in which photochemical and ozonolysis SOA from α-pinene, β-pinene and toluene were all observed to produce H_2O_2; the biogenics were more active (Wang et al., 2011).

1.8 ROS Measurement Methods

Numerous different methods, including cellular bioassays and *in vitro* chemical assays have been applied to quantify ROS formation by ambient particles. Bioassays provide a direct cellular response by quantifying PM-induced ROS within cells. Different cells types have been studied. Landreman et al., (2008) and Heo et al., (2015) quantified ROS formation by PM in rat alveolar macrophage cells while Schafer et al. (2003) used endothelial cells from porcine aorta; both methods used dichlorofluorescein diacetate as a fluorescent probe (Heo et al., 2015; Landreman et al., 2008; Schafer et al., 2003).

On the other hand, dithiothreitol (DTT) and dichlorofluorescein diacetate ($DCFH_2$-DA) are widely used as chemical assays to quantify ROS generation by PM. In the DTT assay, redox active compounds in particulate matter can catalyze the reduction of O_2 to superoxide by DTT (R5-R8), where Q represents quinone in the reaction schemes. The superoxide formed can further produce H_2O_2 and OH. The redox active species in PM oxidize DTT to its disulfide form and the rate of consumption of DTT is directly proportional to the concentration of redox active material present in PM (Charrier and Anastasio 2012; Cho et al., 2005). $DCFH_2$-DA is a non-fluorescent compound that responds to a wide variety of ROS, including, but not limit to hydrogen peroxide, hydroxyl radicals, organic peroxides and peroxynitrite anions ($ONOO^-$)

(Rota et al., 1999); thus quantification of ROS using this assay will most likely overestimate the actual concentration of ROS.

$$Q + DTT \rightarrow \text{semi-Q} + \text{DTT-thiyl} \quad \text{(R8)}$$

$$\text{semi-Q} + \text{DTT-thiyl} \rightarrow \text{semi-Q} + \text{DTT disulfide} \quad \text{(R9)}$$

$$2\ \text{semi-Q} + 2O_2 \rightarrow 2Q + 2O_2^{\cdot -} \quad \text{(R10)}$$

$$DTT + 2O_2 \rightarrow \text{DTT-disulfide} + 2O_2^{\cdot -} \quad \text{(R11)}$$

Since both DTT and $DCFH_2$-DA assay do not directly measure ROS, we employ a much more direct and selective method to quantify OH formation by ambient PM. A direct measurement of hydroxyl radical in aqueous extraction solutions is challenging due to its short lifetime and high reactivity, as well as its similarity to the aqueous solvent. Chemical probes such as benzene (Anastasio and McGregor 2001; Faust and Allen 1993), nitrobenzene (Zepp et al., 1992), benzoic acid (Charrier and Anastasio 2011; Jung et al., 2006; Vidrio et al., 2009), and terephthalate (Charbouillot et al., 2011; Saran and Summer 1999; Šnyrychová and Hideg 2008) have been used to detect OH radicals. For each of these analyses, the probe is added in excess, and the hydroxylated probe reaction products are detected. Of available probes, terephthalate (TA) has the potential to be the most sensitive, and yields only one fluorescent product, 2-hydroxyterephthalic acid (hTA), upon reaction with OH.

ROS formation in atmospheric aqueous system is important for degradation of organics and transformation of aerosols and is proposed to be the initial step in the oxidative stress induction in cell, thus it is important to understand the underlying mechanism of its formation. The ability of PM to produce ROS depends on aerosol sources, chemical composition, and

temporal/spatial characteristics. The direct measurement of OH and hydrogen peroxide in this study can serve as a fast and effective screening tool to identify redox active components in PM that are responsible for ROS formation. There are four main objectives in this work: 1) to develop a method to improve quantification of OH using TA as a probe (Chapter 2); 2) to quantify ROS formation by ambient PM samples collected in Claremont and Fresno, CA, to examine the effect of chemical composition on ROS formation (Chapters 3-4); 3) to quantify OH formation by marine aerosols under physiologically relevant solutions (Chapter 5) and 4) to determine reactivity of different redox active species (quinones, hydroquinones, metals and FA) to produce ROS, including concentration effect, as well as how the mixtures of these redox active species affect ROS formation (Chapter 6).

References

Anastasio, C. and K. G. McGregor (2001). Chemistry of fog waters in California's Central Valley: 1. In situ photoformation of hydroxyl radical and singlet molecular oxygen. Atmospheric Environment 35:1079-1089.

Apel, K. and H. Hirt (2004). Reactive oxygen species: metabolism, oxidative stress, and signal transduction. Annu. Rev. Plant Biol. 55:373-399.

Arakaki, T. and B. C. Faust (1998). Sources, sinks, and mechanisms of hydroxyl radical (• OH) photoproduction and consumption in authentic acidic continental cloud waters from Whiteface Mountain, New York: The role of the Fe (r)(r= II, III) photochemical cycle. Journal of Geophysical Research: Atmospheres 103:3487-3504.

Arellanes, C., S. E. Paulson, P. M. Fine, C. Sioutas (2006). Exceeding of Henry's law by hydrogen peroxide associated with urban aerosols. Env. Sci. Tech. 40:4859-4866.

Beelen, R., O. Raaschou-Nielsen, M. Stafoggia, Z. J. Andersen, G. Weinmayr, B. Hoffmann, K. Wolf, E. Samoli, P. Fischer, M. Nieuwenhuijsen (2014). Effects of long-term exposure to air pollution on natural-cause mortality: an analysis of 22 European cohorts within the multicentre ESCAPE project. Lancet 383:785-795.

Brook, R. D., S. Rajagopalan, C. A. Pope, J. R. Brook, A. Bhatnagar, A. V. Diez-Roux, F. Holguin, Y. L. Hong, R. V. Luepker, M. A. Mittleman, A. Peters, D. Siscovick, S. C. Smith, L. Whitsel, J. D. Kaufman (2010). Amer Heart Assoc Council Epidemiol,Council Kidney CardiovascDis,CouncilNutrPhys Activity Metab:Particulate Matter Air Pollutionand Cardiovascular Disease AnUpdate to the ScientificStatement From the AmericanHeart Association. Circulation 121

Buettner, G. R. and B. A. Jurkiewicz (1996). Catalytic metals, ascorbate and free radicals: combinations to avoid. Radiation Res. 145:532-541.

Bufalini, J., H. Lancaster, G. Namie, B. Gay Jr (1979). Hydrogen peroxide formation from the photooxidation of formaldehyde and its presence in rainwater. J. Environ. Sci. Health Part A 14:135-141.

Buxton, G. V., C. L. Greenstock, W. P. Helman, A. B. Ross (1988). Critical review of rate constants for reactions of hydrated electrons, hydrogen atoms and hydroxyl radicals (· OH/· O− in aqueous solution. Journal of Physical and Chemical Reference Data 17:513-886.

Charbouillot, T., M. Brigante, G. Mailhot, P. R. Maddigapu, C. Minero, D. Vione (2011). Performance and selectivity of the terephthalic acid probe for OH as a function of temperature, pH and composition of atmospherically relevant aqueous media. Journal of Photochemistry and Photobiology A: Chemistry 222:70-76.

Charrier, J. G. and C. Anastasio (2011). Impacts of antioxidants on hydroxyl radical production from individual and mixed transition metals in a surrogate lung fluid. Atmos. Environ. 45:7555-7562.

Charrier, J. G. and C. Anastasio (2011). Impacts of antioxidants on hydroxyl radical production from individual and mixed transition metals in a surrogate lung fluid. Atmospheric Environment 45:7555-7562.

Charrier, J. G. and C. Anastasio (2012). On dithiothreitol (DTT) as a measure of oxidative potential for ambient particles: evidence for the importance of soluble transition metals. Atmospheric chemistry and physics (Print) 12:11317.

Chen, R. and J. J. Pignatello (1997). Role of quinone intermediates as electron shuttles in Fenton and photoassisted Fenton oxidations of aromatic compounds. Env. Sci. Tech. 31:2399-2406.

Chen, R. Z. and J. J. Pignatello (1997). Role of quinone intermediates as electron shuttles in Fenton and photoassisted Fenton oxidations of aromatic compounds. Environmental science & technology 31:2399-2406.

Chen, X., P. K. Hopke, W. P. L. Carter (2011). Secondary Organic Aerosol from Ozonolysis of Biogenic Volatile Organic Compounds: Chamber Studies of Particle and Reactive Oxygen Species Formation. Env. Sci. Tech. 45:276-282.

Cho, A. K., C. Sioutas, A. H. Miguel, Y. Kumagai, D. A. Schmitz, M. Singh, A. Eiguren-Fernandez, J. R. Froines (2005). Redox activity of airborne particulate matter at different sites in the Los Angeles Basin. Environmental Research 99:40-47.

Chung, M. Y., R. A. Lazaro, D. Lim, J. Jackson, J. Lyon, D. Rendulic, A. S. Hasson (2006). Aerosol-borne quinones and reactive oxygen species generation by particulate matter extracts. Env. Sci. Tech. 40:4880-4886.

Decesari, S., M. C. Facchini, E. Matta, F. Lettini, M. Mircea, S. Fuzzi, E. Tagliavini, J. P. Putaud (2001). Chemical features and seasonal variation of fine aerosol water-soluble organic compounds in the Po Valley, Italy. Atmos. Environ. 35:3691-3699.

DiStefano, E., A. Eiguren-Fernandez, R. J. Delfino, C. Sioutas, J. R. Froines, A. K. Cho (2009). Determination of metal-based hydroxyl radical generating capacity of ambient and diesel exhaust particles. Inhalation Toxicology 21:731-738.

Dockery, D. W., C. A. Pope, X. P. Xu, J. D. Spengler, J. H. Ware, M. E. Fay (1993). An association between air-pollution and mortality in 6 United-States cities N Engl J Med 329 (24): 1753–1759.

Duarte, R., C. A. Pio, A. C. Duarte (2004). Synchronous scan and excitation-emission matrix fluorescence spectroscopy of water-soluble organic compounds in atmospheric aerosols. J. Atmos. Chem. 48:157-171.

Duesteberg, C. K. and T. D. Waite (2007). Kinetic modeling of the oxidation of p-hydroxybenzoic acid by Fenton's reagent: Implications of the role of quinones in the redox cycling of iron. Environmental science & technology 41:4103-4110.

Duesterberg, C. K. and T. D. Waite (2007). Kinetic modeling of the oxidation of p-hydroxybenzoic acid by Fenton's reagent: implications of the role of quinones in the redox cycling of iron. Env. Sci. Tech. 41:4103-4110.

Elmagirbi, A., H. Sulistyarti, A. Atikah (2012). Study of ascorbic acid as iron (III) reducing agent for spectrophotometric iron speciation. J. Pure. Appl. Chem. Res. 1:11-17.

Faust, B. C. and J. Hoigné (1990). Photolysis of Fe (III)-hydroxy complexes as sources of OH radicals in clouds, fog and rain. Atmos. Environ.A. General Topics 24:79-89.

Faust, B. C. and J. M. Allen (1993). AQUEOUS-PHASE PHOTOCHEMICAL FORMATION OF HYDROXYL RADICAL IN AUTHENTIC CLOUDWATERS AND FOGWATERS. Environmental science & technology 27:1221-1224.

Graber, E. R. and Y. Rudich (2006). Atmospheric HULIS: How humic-like are they? A comprehensive and critical review. Atmos. Chem. Phys. 6:729-753.

Graedel, T., M. Mandich, C. Weschler (1986). Kinetic model studies of atmospheric droplet chemistry: 2. Homogeneous transition metal chemistry in raindrops. Journal of Geophysical Research: Atmospheres 91:5205-5221.

Guo, Y., W. Zhang, Y.-y. Yan, C.-g. Ma, X. Wang, C. Wang, J.-l. Zhao (2013). Triterpenoid pristimerin induced HepG2 cells apoptosis through ROS-mediated mitochondrial dysfunction. Journal of Buon 18:477-485.

Hasson, A. S., G. E. Orzechowska, S. E. Paulson (2001a). Production of stabilized Criegee intermediates and peroxides in the gas phase ozonolysis of alkenes: 1. Ethene, trans-2-butene, and 2,3-dimethyl-2-butene. J. Geophys. Res. 106:34,131-134,142.

Havers, N., P. Burba, J. Lambert, D. Klockow (1998). Spectroscopic characterization of humic-like substances in airborne particulate matter. J. Atmos. Chem. 29:45-54.

Heinrich, J. and H.-E. Wichmann (2004). Traffic related pollutants in Europe and their effect on allergic disease. Curr. Opin. Allergy Clin. Immunol. 4:341-348.

Heo, J., D. S. Antkiewicz, M. M. Shafer, D. A. Perkins, C. Sioutas, J. J. Schauer (2015). Assessing the role of chemical components in cellular responses to atmospheric particle matter (PM) through chemical fractionation of PM extracts. Anal. Bioanal. Chem. 407:5953-5963.

Heo, J., D. S. Antkiewicz, M. M. Shafer, D. A. K. Perkins, C. Sioutas, J. J. Schauer (2015). Assessing the role of chemical components in cellular responses to atmospheric particle matter

(PM) through chemical fractionation of PM extracts. Analytical and Bioanalytical Chemistry 407:5953-5963.

Hoffer, A., A. Gelencsér, P. Guyon, G. Kiss, O. Schmid, G. Frank, P. Artaxo, M. Andreae (2006). Optical properties of humic-like substances (HULIS) in biomass-burning aerosols. Atmosph. Chem. Phys. 6:3563-3570.

Hung, H. F. and C. S. Wang (2001). Experimental determination of reactive oxygen species in Taipei aerosols. J. Aerosol Sci. 32:1201-1211.

Jackson, A. V. and C. N. Hewitt (1999). Atmospheric hydrogen peroxide and organic hydroperoxides: a review. Crit. Rev. Env. Sci. Tech. 29:175-228.

Jiang, F., Y. Zhang, G. J. Dusting (2011). NADPH Oxidase-Mediated Redox Signaling: Roles in Cellular Stress Response, Stress Tolerance, and Tissue Repair. Pharmacological Reviews 63:218-242.

Jung, H., B. Guo, C. Anastasio, I. M. Kennedy (2006). Quantitative measurements of the generation of hydroxyl radicals by soot particles in a surrogate lung fluid. Atmos. Environ. 40:1043-1052.

Jung, H., B. Guo, C. Anastasio, I. M. Kennedy (2006). Quantitative measurements of the generation of hydroxyl radicals by soot particles in a surrogate lung fluid. Atmospheric Environment 40:1043-1052.

Khurshid, S. S., J. A. Siegel, K. A. Kinney (2014). Technical Note: Particulate reactive oxygen species concentrations and their association with environmental conditions in an urban, subtropical climate. Atmos. Chem. Phys. 14:6777-6784.

Kim, H. and S. E. Paulson (2013). Real refractive indices and volatility of secondary organic aerosol generated from photooxidation and ozonolysis of limonene, alpha-pinene and toluene. Atmos. Chem. Phys. 13:7711-7723.

Kiss, G., B. Varga, I. Galambos, I. Ganszky (2002). Characterization of water‐soluble organic matter isolated from atmospheric fine aerosol. J. Geophys. Res.: Atmospheres 107

Knaapen, A. M., T. Shi, P. J. Borm, R. P. Schins (2002). Soluble metals as well as the insoluble particle fraction are involved in cellular DNA damage induced by particulate matter. Mol. Cell. Biochem. 234:317-326.

Krivácsy, Z., G. Kiss, D. Ceburnis, G. Jennings, W. Maenhaut, I. Salma, D. Shooter (2008). Study of water-soluble atmospheric humic matter in urban and marine environments. Atmos. Res. 87:1-12.

Lakey, P. S. J., T. Berkemeier, H. Tong, A. M. Arangio, K. Lucas, U. Pöschl, M. Shiraiwa (2016). Chemical exposure-response relationship between air pollutants and reactive oxygen species in the human respiratory tract. Sci. Report 6:32916.

Landreman, A. P., M. M. Shafer, J. C. Hemming, M. P. Hannigan, J. J. Schauer (2008). A macrophage-based method for the assessment of the reactive oxygen species (ROS) activity of atmospheric particulate matter (PM) and application to routine (daily-24 h) aerosol monitoring studies. Aerosol Science and Technology 42:946-957.

Lee, M., B. G. Heikes, D. W. O'Sullivan (2000). Hydrogen peroxide and organic hydroperoxide in the troposphere: A review. Atmos. Environ. 34:3475-3494.

Li, N., T. Xia, A. E. Nel (2008). The role of oxidative stress in ambient particulate matter-induced lung diseases and its implications in the toxicity of engineered nanoparticles. Free Radical Biology and Medicine 44:1689-1699.

Li, R., X. Kou, H. Geng, J. Xie, Z. Yang, Y. Zhang, Z. Cai, C. Dong (2015). Effect of Ambient PM2.5 on Lung Mitochondrial Damage and Fusion/Fission Gene Expression in Rats. Chemical research in toxicology 28:408-418.

Lim, Y., Y. Tan, M. Perri, S. Seitzinger, B. J. Turpin (2010). Aqueous chemistry and its role in secondary organic aerosol (SOA) formation. Atmos. Chem. Phys. 10:10521-10539.

Limbeck, A., M. Handler, B. Neuberger, B. Klatzer, H. Puxbaum (2005). Carbon-specific analysis of humic-like substances in atmospheric aerosol and precipitation samples. Anal. Chem. 77:7288-7293.

Lin, P., X.-F. Huang, L.-Y. He, J. Z. Yu (2010). Abundance and size distribution of HULIS in ambient aerosols at a rural site in South China. J. Aerosol Sci. 41:74-87.

Lin, P. and J. Z. Yu (2011). Generation of reactive oxygen species mediated by humic-like substances in atmospheric aerosols. Env. Sci. Tech. 45:10362-10368.

Mayol‐Bracero, O. L., P. Guyon, B. Graham, G. Roberts, M. O. Andreae, S. Decesari, M. C. Facchini, S. Fuzzi, P. Artaxo (2002). Water‐soluble organic compounds in biomass burning aerosols over Amazonia 2. Apportionment of the chemical composition and importance of the polyacidic fraction. Journal of Geophysical Research: Atmospheres (1984‐2012) 107:LBA 59-51-LBA 59-15.

McConnell, R., T. Islam, K. Shankardass, M. Jerrett, F. Lurmann, F. Gilliland, J. Gauderman, E. Avol, N. Künzli, L. Yao (2010). Childhood incident asthma and traffic-related air pollution at home and school. Environ. Health Perspect.:1021-1026.

Moonshine, M., Y. Rudich, S. Katsman, E. Graber (2008). Atmospheric HULIS enhance pollutant degradation by promoting the dark Fenton reaction. Geophys. Res. Lett. 35

Mukai, H. and Y. Ambe (1986). Characterization of a humic acid-like brown substance in airborne particulate matter and tentative identification of its origin. Atmos. Environ. 20:813-819.

Oftedal, B., W. Nystad, B. Brunekreef, P. Nafstad (2009). Long-term traffic-related exposures and asthma onset in schoolchildren in Oslo, Norway. Environ. Health Perspect. 117:839.

Pandis, S. N. and J. H. Seinfeld (1989). Sensitivity analysis of a chemical mechanism for aqueous ‐ phase atmospheric chemistry. Journal of Geophysical Research: Atmospheres 94:1105-1126.

Paulson, S. E., A. Hasson, C. Anastasio, Xiaobi M. Kuang, J. Adlin Scott, David H. Gonzalez-Martinez, Tiffany Charbouillot , Kennedy K-T Vu, James Baroi, Catalina Olea, Annabelle Lolinco and Kylie Markarian, Jessica G. Charrier, Alexander S. McFall, N. K. Richards-Henderson (2016). Probing the Intrinsic Ability of Particles to Generate Reactive Oxygen Species and the Effect of Physiologically Relevant Solutes. Calif. Air Resources Board Annu. Report

Pope, C. A. and D. W. Dockery (2006). Health effects of fine particulate air pollution: Lines that connect. J Air Waste Manage 56

Pope, C. A., J. B. Muhlestein, H. T. May, D. G. Renlund, J. L. Anderson, B. D. Horne (2006). Ischemic heart disease events triggered by short-term exposure to fine particulate air pollution. Circulation 114:2443-2448.

Rattanavaraha, W., E. Rosen, H. Zhang, Q. Li, K. Pantong, R. M. Kamens (2011). The reactive oxidant potential of different types of aged atmospheric particles: An outdoor chamber study. Atmos. Environ. 45:3848-3855.

Risom, L., P. Moller, S. Loft (2005). Oxidative stress-induced DNA damage by particulate air pollution. Mutation Research-Fundamental and Molecular Mechanisms of Mutagenesis 592:119-137.

Roberts, J. R., M. D. Taylor, V. Castranova, R. W. Clarke, J. M. Antonini (2004). Soluble Metals Associated with Residual Oil Fly Ash Increase Morbidity and Lung Injury After Bacterial Infection in Rats. J. Toxicol. Environ. Health, Part A 67:251-263.

Rota, C., C. F. Chignell, R. P. Mason (1999). Evidence for free radical formation during the oxidation of 2'-7'-dichlorofluorescin to the fluorescent dye 2'-7'-dichlorofluorescein by horseradish peroxidase: possible implications for oxidative stress measurements. Free Radical Bio. Med. 27

Sander, R. (1999). Compilation of Henry's Law Constants for Inorganic and Organic Species of Potential Importance in Environmental Chemistry (Version 3). http://www.mpch-mainz.mpg.de/~sander/res/henry.html.

Saran, M. and K. H. Summer (1999). Assaying for hydroxyl radicals: hydroxylated terephthalate is a superior fluorescence marker than hydroxylated benzoate. Free radical research 31:429-436.

Sato, K., S. Nakao, C. H. Clark, L. Qi, D. R. Cocker iii (2011). Secondary organic aerosol formation from the photooxidation of isoprene, 1, 3-butadiene, and 2, 3-dimethyl-1, 3-butadiene under high NO x conditions. Atmos. Chem. Phys. 11:7301-7317.

Schafer, M., C. Schafer, N. Ewald, H. M. Piper, T. Noll (2003). Role of redox signaling in the autonomous proliferative response of endothelial cells to hypoxia. Circulation Research 92:1010-1015.

See, S. W., Y. H. Wang, R. Balasubramanian (2007). Contrasting reactive oxygen species and transition metal concentrations in combustion aerosols. Environ. Res, 103:317-324.

Shafer, M. M., D. A. Perkins, D. S. Antkiewicz, E. A. Stone, T. A. Quraishi, J. J. Schauer (2010). Reactive oxygen species activity and chemical speciation of size-fractionated atmospheric particulate matter from Lahore, Pakistan: an important role for transition metals. J. Environ. Monit. 12:704-715.

Shafer, M. M., D. A. Perkins, D. S. Antkiewicz, E. A. Stone, T. A. Quraishi, J. J. Schauer (2010). Reactive oxygen species activity and chemical speciation of size-fractionated atmospheric particulate matter from Lahore, Pakistan: an important role for transition metals. Journal of Environmental Monitoring 12:704-715.

Shang, Y., C. Chen, Y. Li, J. Zhao, T. Zhu (2012). Hydroxyl Radical Generation Mechanism During the Redox Cycling Process of 1,4-Naphthoquinone. Environmental science & technology 46:2935-2942.

Shang, Y., C. Chen, Y. Li, J. Zhao, T. Zhu (2012). Hydroxyl radical generation mechanism during the redox cycling process of 1, 4-naphthoquinone. Env. Sci. Tech. 46:2935-2942.

Shen, H. and C. Anastasio (2011). Formation of hydroxyl radical from San Joaquin Valley particles extracted in a cell-free surrogate lung fluid. Atmospheric Chemistry and Physics 11:9671-9682.

Shen, H. and C. Anastasio (2012). A comparison of hydroxyl radical and hydrogen peroxide generation in ambient particle extracts and laboratory metal solutions. Atmos. Environ. 46:665-668.

Shilling, J. E., S. M. King, M. Mochida, S. T. Martin (2007). Mass spectral evidence that small changes in composition caused by oxidative aging processes alter aerosol CCN properties. J. Phys. Chem. A 111:3358-3368.

Shrivastava, M. K., T. E. Lane, N. M. Donahue, S. N. Pandis, A. L. Robinson (2008). Effects of gas particle partitioning and aging of primary emissions on urban and regional organic aerosol concentrations. J. Geophys. Res., [Atmos.] 113

Šnyrychová, I. and É. Hideg (2008). First Application of Terephthalate as a Fluorescent Probe for Hydroxyl Radicals in Thylakoid Membranes, in Photosynthesis. Energy from the Sun, Springer, 1553-1556.

Suda, S. R., M. D. Petters, G. K. Yeh, C. Strollo, A. Matsunaga, A. Faulhaber, P. J. Ziemann, A. J. Prenni, C. M. Carrico, R. C. Sullivan, S. M. Kreidenweis (2014). Influence of Functional Groups on Organic Aerosol Cloud Condensation Nucleus Activity. Env. Sci. Tech. 48:10182-10190.

Tao, F., B. Gonzalez-Flecha, L. Kobzik (2003). Reactive oxygen species in pulmonary inflammation by ambient particulates. Free Radical Biology and Medicine 35:327-340.

Thorne, P. S. (2000). Inhalation toxicology models of endotoxin-and bioaerosol-induced inflammation. Toxicology 152:13-23.

Valavanidis, A., K. Fiotakis, E. Bakeas, T. Vlahogianni (2005). Electron paramagnetic resonance study of the generation of reactive oxygen species catalysed by transition metals and quinoid redox cycling by inhalable ambient particulate matter. Redox Report 10:37-51.

Van Der Vliet, A., C. A. O'Neill, C. E. Cross, J. M. Koostra, W. G. Volz, B. Halliwell, S. Louie (1999). Determination of low-molecular-mass antioxidant concentrations in human respiratory tract lining fluids. Am. J.Physiol Lung Cell. Molec. Physiol. 276:L289-L296.

Vidrio, E., C. H. Phuah, A. M. Dillner, C. Anastasio (2009). Generation of Hydroxyl Radicals from Ambient Fine Particles in a Surrogate Lung Fluid Solution. Environmental science & technology 43:922-927.

Wang, Y., C. Arellanes, D. B. Curtis, S. E. Paulson (2010). Probing the Source of Hydrogen Peroxide Associated with Coarse Mode Aerosol Particles in Southern California. Environmental science & technology 44:4070-4075.

Wang, Y., A. Chung, S. E. Paulson (2010). The effect of metal salts on quantification of elemental and organic carbon in diesel exhaust particles using thermal-optical evolved gas analysis. Atmos. Chem. Phys. 10:11447-11457.

Wang, Y., C. Arellanes, S. E. Paulson (2011). Hydrogen Peroxide Associated with Ambient Fine Mode, Diesel and Biodiesel Aerosol Particles in Southern California. Submitted to: Atmos. Environ.

Wang, Y., H. Kim, S. E. Paulson (2011). Hydrogen Peroxide Generation from a- and b-Pinene and Toluene Secondary Organic Aerosols. . Atmos. Environ.

Xia, T., P. Korge, J. N. Weiss, N. Li, M. I. Venkatesan, C. Sioutas, A. Nel (2004). Quinones and aromatic chemical compounds in particulate matter induce mitochondrial dysfunction: Implications for ultrafine particle toxicity. Environmental health perspectives 112:1347-1358.

Xia, T., P. Korge, J. N. Weiss, N. Li, M. I. Venkatesen, C. Sioutas, A. Nel (2004). Quinones and aromatic chemical compounds in particulate matter induce mitochondrial dysfunction: implications for ultrafine particle toxicity. Environ. Health Perspect.:1347-1358.

Yan, M., M. Li, D. Wang, F. Xiao (2013). Optical property of iron binding to Suwannee River fulvic acid. Chemosphere 91:1042-1048.

Zappoli, S., A. Andracchio, S. Fuzzi, M. Facchini, A. Gelencser, G. Kiss, Z. Krivacsy, A. Molnar, E. Meszaros, H.-C. Hansson (1999). Inorganic, organic and macromolecular components of fine aerosol in different areas of Europe in relation to their water solubility. Atmospheric Environment 33:2733-2743.

Zepp, R. G., B. C. Faust, J. Hoigne (1992). Hydroxyl radical formation in aqueous reactions (pH 3-8) of iron (II) with hydrogen peroxide: the photo-Fenton reaction. Environmental science & technology 26:313-319.

Zhang, Y., J. J. Schauer, M. M. Shafer, M. P. Hannigan, S. J. Dutton (2008). Source apportionment of in vitro reactive oxygen species bioassay activity from atmospheric particulate matter. Env. Sci. Tech. 42:7502-7509.

Zuo, Y. G. and Y. W. Deng (1997). Iron(II)-catalyzed photochemical decomposition of oxalic acid and generation of H2O2 in atmospheric liquid phases. Chemosphere 35:2051-2058.

2. The Terephthalate Probe for Hydroxyl Radicals: Yield of 2-Hydroxy Terephthalic acid, Transition Metal Interference and Separation from Complex Organics in Environmental Samples

2.1 Introduction

OH plays an important role in various atmospheric and surface water processes. Aerosol aging by OH can modify chemical composition (Lim et al., 2010; Sato et al., 2011; Shrivastava et al., 2008), cloud condensation nuclei (CCN) activity (Shilling et al., 2007), hygroscopic properties (Suda et al., 2014), and optical properties of aerosols (Kim and Paulson 2013). Hydroxyl radical also plays an important role in the chemistry of surface waters (Goldstone et al., 2002; Lindsey and Tarr 2000), degradation of drugs after release into the environment (Rosenfeldt and Linden 2004), in oxidative stress in marine organisms (Lesser 2006) and in waste water treatment (Fernandez-Castro et al., 2015).

Inhalation of fine particulate matter has shown correlation with adverse health impacts, including asthma, cardiovascular diseases, pulmonary inflammation, lung cancer and mortality (Brook et al., 2002; Pope et al., 2004; Pope et al., 2006; Thorne 2000). While the mechanism(s) by which ambient particles impact health is not yet completely understood, a hypothesized cause under active investigation is oxidative stress, mediated by reactive oxygen species (ROS).

A direct measurement of hydroxyl radical in aqueous solutions is difficult due to its low concentrations, short lifetime and chemical and physical similarity to the aqueous solvent. Chemical probes such as benzene (Faust and Allen 1993), nitrobenzene (Zepp et al., 1992), benzoate (Jung et al., 2006) and terephthalate (TA) (Charbouillot et al., 2011; Li et al., 2007; Matthews 1980; Saran and Summer 1999) have been used to quantify OH. These methods

depend on fluorescence (2-hydroxyterephthalic acid) or UV absorption (Benzene derivatives) of oxidation products. A major advantage of the terephthalate are its low detection limits; as low as ~2 nM (Tab. 2.1), compared to 30 nM for benzoate (Shen and Anastasio 2012).

Tab. 2.1 Excitation/emission wavelengths and detection limits for OH detection using terephthalic acid

Excitation (nm)	Emission (nm)	hTA Detection Limit	OH generation System	Reference
320	420	1.4 nM	Ambient particles	This study
315	435	$5x10^{-7}$ M	Microdialysis	Freinbichler et al., (2008)
309	412	5nM	Fenton reaction	Linxiang et al., (2004)
320	420	*	Photolysis of Nitrate/H_2O_2	(Charbouillot et al., 2011)
323	435	50nM	radiolysis	Saran and Summer (1999)
240/310	435	‡	Photolysis of Nitrate	Page et al., (2010)

‡Detection limit of formation of hTA. These authors state hTA can be detected at "sub-nM levels, but do not provide a number or limit of detection determination methodology.

*****These authors reported detection limits as rates ($5x10^{-12}$ M/s) but did not report the integration times, so detection limits in absolute terms are not known.

Of the hydroxyl radical probes, terephthalate has several advantages. Due to its symmetric configuration, the OH reaction with terephthalate results in only one ring- preserving product, 2-hydroxyterephthalic acid (hTA, Fig. 2.1). Furthermore, 2-hydroxyterephthalic acid is strongly fluorescent (Armstrong et al., 1963), facilitating low detection limits. As fluorescence is a specific assay, this offers the possibility that under many circumstances, the terephthalate assay may be used without separation. Avoiding a separation step facilitates the use of stand-alone fluorescence spectrometers, which can have lower detection limits than High Performance Liquid Chromatography (HPLC) – based analyses. In addition, TA is more soluble, has a more

stable fluorescent product and is less susceptible to pH changes compared to several other OH probes (Son et al., 2015).

Accurate quantification of OH with the terephthalate probe requires knowledge of the yield of the fluorescent product, hTA, per molecule of OH reacted. Two studies have quantified the OH formation yield: Matthews (1980) using radiolysis and Charbouillot et al., (2011) using photolysis of nitrate or H_2O_2 (Fig. 2.2). The yield was found to depend on O_2 concentration in the sample (Matthews 1980; Saran and Summer 1999), and have a weak dependence on pH (Fig. 2.2)(Charbouillot et al., 2011; Matthews 1980). Charbouillot et al., (2011) found that the yield is not influenced by ionic strength, ammonium or sulfate ions within the 0.25 – 2 mM range studied, and that it has a fairly strong temperature dependence; the yield increases by about a factor of 2 between 278 and 303 K at pH 5.4. However, the yields reported by Matthews (1980) of 30.5% at pH 2, increasing to 35% for pHs > 9, are much higher than those reported by Charbouillot et al., (2011): 14 to 23% over the pH range 4 – 7.5 (Fig. 2.2). A possible reason for the discrepancy is discussed below. Here, we report a new measurement of the hTA yield. Because little data is available for the yield of hTA under acidic conditions relevant to atmospheric (Falconer and Falconer 1980) and aerosols (Bougiatioti et al., 2016), we measure Y_{hTA} at pH 3.5 using a dark ferrous Fenton system to generate OH.

The TA method may be susceptible to interference from complexation of TA or hTA with transition metals; several studies have reported the ability of terephthalate to complex metals, including Cu(II), Co(II), Fe(II), Mn(II) and Ni(II) at high concentrations (Acheson and Galwey 1967; Carson et al., 2009; Rabu et al., 2001; Sherif 1970). Due to its abundance in the atmospheric samples, here we examine the ability of Cu(II) to interfere with the hTA assay.

The TA method may also be subject to interference from other species with native fluorescence in the same wavelength range as hTA, and to compounds that absorb at either its absorption or fluorescence wavelengths. Most compounds common in atmospheric and surface waters, including inorganic salts and acids, water, and most organics do not fluoresce or absorb strongly at the wavelengths of interest here. However, strong fluorescence of both atmospheric and surface water organic carbon (HUmic Like substances, HULIS) such as fulvic and humic acids (FA and HA) and biomass burning aerosol has been reported by several groups (Duarte et al., 2004; Krivacsy et al., 2000; Nakajima et al., 2008) and includes wavelengths that overlap the hTA assay. Pullin and co-workers (Mobed et al., 1996; Pullin and Cabaniss 1995) found the fluorescence spectra of six standard humic substances are strongly pH dependent; their fluorescence intensity increased by a factor of three or more as the pH is increased from 3 to 11. Similar but weaker trends have been observed for fresh water dissolved organic matter from various locations in UK (Spencer et al., 2007). As a result, samples with moderate to high concentrations of complex organics may require additional steps to quantify OH, especially if the samples are at higher pH. Simply lowering the pH can cause precipitation of HULIS (below), which may not be desirable.

Varga et al., (2001) developed a method to isolate HULIS from environmental samples using a hydrophilic lipophilic balance (HLB) sorbent material. HLB has been used successfully in several studies to isolate HULIS from ambient samples (Kuang et al., 2015; Lin et al., 2010; Lin and Yu 2011; Varga et al., 2001; Verma et al., 2012). HLB is a reverse phase sorbent for acidic, basic and neutral compounds, consisting two monomers: hydrophilic N-vinylpyrrolidone and lipophilic divinylbenzene. Here we use the Varga et al., (2001) method as a starting point for a high efficiency method to separate hTA from FA and HA and complex water-soluble organic

material in biomass burning aerosol. While hTA is a much smaller species than those comprising HULIS, they share shares many chemical characteristics, including an aromatic ring, and hydroxyl and carboxylic acid functional groups, presenting challenges for its separation.

2.2 Materials and Methods

2.2.1 Materials

Disodium terephthalate (TA) was purchased from TCI. 2-hydroxy terephthalic acid (hTA) and fulvic acid (FA) were purchased from Apollo Sci., and the International Humic Substance Society (IHSS), respectively. Methanol (HPLC grade) and sulfuric acid (reagent grade), Chelex® 100 sodium form (50-100 dry mesh), humic acid (HA), uric acid (>99%), sodium Citrate tribasic dihydrate (>99%), L-ascorbic acid (BioXtra, >99%), L-glutathione reduced (>98%), ethylenediaminetetraacetic acid (EDTA), horseradish peroxidase type II, para-hydroxyphenyl acetic acid, potassium hydrogen phthalate, H_2O_2 (30%) and $FeSO_4$ (>98%) were purchased from Sigma Aldrich. Sodium phosphate dibasic and potassium phosphate monobasic were purchased from Acros Organics. Ferrozine (4,4'-[3-(2-pyridinyl)-1,2,4-triazine-5,6-diyl] dibenzenesulfonate) was purchased from Fluka Analytic. Hydrophilic Lipophilic Balance cartridges were purchased from Waters (Oasis, 10mg). All materials were used as received.

A rigorous cleaning process was followed for all glass and Teflon containers. After each use, the glass/plastic ware was washed with warm water and soap, then rinsed deionized (18 MΩ DI) water (3×), ethanol (3×), and finally DI water (3×). The vessels were then soaked in a 1 M nitric acid bath overnight, rinsed with DI water (3x) and air-dried. Nitric acid baths were replaced after being used twice.

Stock solutions were prepared with chelexed 18 MΩ DI water. pH was measured with a bench top pH meter (HANNA instruments, HI 3220), calibrated daily. Stock solutions of hTA (10^{-3} M) and Fe(II) (5.1 mM) were wrapped in foil; hTA was kept refrigerated for a few months and Fe(II) was prepared daily and refrigerated.

2.2.2 Fluorescence Spectroscopy and quantification of hTA

The Excitation-Emission Matrix (EEM) scan mode was used to elucidate the fluorescence features for hTA, HA/FA and water-soluble biomass burning HULIS from ambient samples. EEM scans were performed with 10 nm excitation and emission slit widths, 5 nm intervals scanning at 60 nm/s with 10 ms integration time. Analyte recovery/breakthrough analyses of FA, HA and soluble biomass burning HULIS were quantified using fluorescence at the respective maximum excitation and emission wavelengths.

hTA fluorescence intensity was measured in single wavelength mode at excitation/emission wavelengths of 320/420 nm with a Lumina Fluorescence Spectrometer (Thermo Scientific). hTA calibration curves were prepared in pH 3.5 or 7.4 solutions at hTA concentrations of 50, 100, 500 and 800 nM. A 10^{-3} M Stock solution of hTA in milli-Q water (18MΩ.cm) was prepared using an acid cleaned Teflon bottle which was wrapped in aluminum, and stored in the refrigerator. A 5-point calibration was performed prior to each experiment. The 1mg/mL HA/FA stock solution was prepared weekly.

2.2.3 Quantification of Fe(II)

Fe(II) was quantified with the ferrozine method (Stookey 1970) using a liquid waveguide capillary cell (LWCC-3100, World Precision Instruments Inc.), a UV-Vis light source (AvaLight-DHS, Avantes) and UV-Vis spectrometer (AvaSpec 2048L, Avantes). The Fe(II)-ferrozine complex has a maximum absorbance at 562 nm (A_{562}). To account for instrument drift

and solution turbidity, the absorbance at 700 nm (A_{700}) was subtracted from A_{562}. Aliquots were analyzed by adding 10 µL of 5.1 mM ferrozine to 2.0 mL aliquots. The initial Fe(II) concentration was determined by adding 10 µL of 10 mg/mL hydroxyl amine to the first 2.0 mL aliquot and allowing the mixture to incubate at room temperature for 20 minutes before injection. This ensures that any Fe(III) formed is reduced to Fe(II). Fe(II) calibration curves are made by preparing a stock solution of 2 mM Iron Sulfate (Sigma-Aldrich) at pH 3.5 and diluting to between 0.012 and 0.75 µM Fe(II).

2.2.4 Quantification of H_2O_2

Quantification of aqueous H_2O_2 was performed using a High Performance Liquid Chromatograph equipped with a fluorescence detector (Shimadzu RF-10AXL detector).(Arellanes et al., 2006) The eluent, water with 0.1 mM EDTA adjusted to pH 3.5 with 0.1 N sulfuric acid, was delivered at 0.6 mL/min to a C18 guard column. H_2O_2 elutes at 0.5 min, after which it is mixed with a fluorescent reagent containing horseradish peroxidase and para-hydroxyphenyl acetic acid (POHPAA). The peroxidase enzyme catalyzes a reaction between H_2O_2 and POHPAA to form a fluorescent dimer, which is detected at the $\lambda_{ex}/\lambda_{em}$ of 320/400nm. The solution is mixed with ammonium hydroxide (30%) to increase its fluorescence intensity prior to detection. The HPLC was calibrated at least weekly with 10^{-8} to 10^{-6} M standards prepared from a 0.3% stock solution, titrated with sodium thiosulfate to determine the concentration.

2.2.5 Oxidation of TA via a Ferrous Fenton System

Experiments to derive hTA yields were carried out as follows. Triplicate samples of 4.44-4.77 µM $FeSO_4$ and 5.38-6.00 µM H_2O_2 (Tab. 2.2) were mixed with excess terephthalate (~500 µM, 100-fold excess) in 60 mL Teflon bottles and allowed to react in the dark with gentle

shaking (25rpm, Heidolph Rotamax) at 20° C. $FeSO_4$ was added last as to initiate the Fenton reaction. The resulting solution was monitored in triplicate for H_2O_2, Fe(II) and hTA every 20 minutes for 2 h. Initial concentrations of H_2O_2 and Fe(II) are shown in Tab. 2-2. Blanks consisted of TA in pH 3.5. Aliquots were diluted by 5 - 10x to fall within the ranges of detection for Fe(II) and H_2O_2. At µM concentrations, the system is sensitive to trace contaminants, including metals and organics, which can change OH formation chemistry and/or the ability of terephthalate to scavenge all available OH, thus rigorous cleaning, dust exclusion and high purity reagents were critical for these experiments.

A 54-reaction chemical kinetics model (Tab. 2.3) including reactions describing Fenton chemistry, acid-base equilibria, iron sulfate chemistry and odd oxygen free radical chemistry was developed to derive hTA yields. Concentrations as a function of time were calculated from initial concentrations using FACSIMILIE (MCPA Software).

Tab. 2.2 Initial conditions for hydroxy terephthalic acid (hTA) yield experiments

Trial	$[Fe(II)]_o$ µM	$[H_2O_2]_o$ µM
1	4.44 ± 0.16	6.00 ± 0.34
2	4.55 ± 0.22	5.38 ± 0.06
3	4.77 ± 0.06	5.48 ± 0.25

Tab. 2.3 Kinetic Model used to fit to experimental data.

#	Reaction	k_f	k_r	K_{eq}	Ref

	General Equilibria				
1	$H_2O \rightleftharpoons H^+ + OH^-$	1.3×10^{-3}	1.3×10^{11}	10^{-14}	[6]
2	$Fe^{3+} + H_2O \rightleftharpoons FeOH^{2+} + H^+$	6.46×10^{7}	10^{10}	6.46×10^{-3}	[7]
3	$Fe^{3+} + 2\ H_2O \rightleftharpoons Fe(OH)_2^{+} + 2H^+$	2.14×10^{3}	10^{10}	2.14×10^{-6}	[7]
4	$2\ Fe^{3+} + 2\ H_2O \rightleftharpoons Fe_2(OH)_2^{4+} + 2H^+$	1.12×10^{7}	10^{10}	1.12×10^{-3}	[7]
5	$Fe^{2+} + H_2O \rightleftharpoons FeOH^{+} + H^+$	3.16	10^{10}	3.16×10^{-10}	[7]
6	$H_2O_2 \rightleftharpoons HO_2^- + H^+$	1.26×10^{-2}	10^{10}	1.26×10^{-12}	[7]
7	$HO_2 \rightleftharpoons O_2^- + H^+$	1.58×10^{5}	10^{10}	1.58×10^{-5}	[7]
8	$Fe^{3+} + H_2O_2 \rightleftharpoons FeHO_2^{2+} + H^+$	5×10^{-3}	1.36	3.65×10^{-3}	[8]
9	$FeOH^{2+} + H_2O_2 \rightleftharpoons Fe(OH)(HO_2)^{+} + H^+$	2×10^{6}	10^{10}	2×10^{-4}	[7]
	Terephthalate Probe				
10	$TA + OH \rightarrow (Y)\ hTA + (1\text{-}Y)X$	4.4×10^{9}			[5]
11	$X + OH \rightarrow Z$	10^{9}			[9]
12	$hTA + OH \rightarrow hTA_{ox}$	6.3×10^{9}			[5]
	Fe(II)/Fe(III) Reactions				
13	$Fe^{2+} + O_2 \rightarrow Fe^{3+} + O_2^-$	0.111 ± 0.007			[10]
14	$Fe^{2+} + O_2^- + 2H^+ \rightarrow Fe^{3+} + H_2O_2$	10^{7}			[10]
15	$Fe^{2+} + H_2O_2 \rightarrow Fe^{3+} + OH + OH^-$	76			[11]
16	$FeOH^{+} + H_2O_2 \rightarrow Fe^{3+} + OH + 2\ OH^-$	5.9×10^{6}			[7]
17	$FeHO_2^{2+} \rightarrow HO_2 + Fe^{2+}$	2.3×10^{-3}			[8]
18	$Fe(OH)(HO_2)^{+} \rightarrow Fe^{2+} + HO_2 + OH^-$	2.3×10^{-3}			[7]
19	$Fe^{2+} + OH \rightarrow Fe^{3+} + OH^-$	2.7×10^{8}			[7]

20	$FeOH^+ + OH \rightarrow Fe^{3+} + 2\ OH^-$	2.7×10^8			[12]
21	$Fe^{2+} + HO_2 \rightarrow Fe^{3+} + HO_2^-$	1.2×10^6			[7]
22	$FeOH^+ + HO_2 \rightarrow FeOH^{2+} + HO_2^-$	1.2×10^6			[7]
23	$Fe^{2+} + O_2^- \rightarrow Fe^{3+} + O_2^{2-}$	10^7			[7]
24	$FeOH^+ + O_2^- \rightarrow FeOH^{2+} + O_2^-$	10^7			[7]
25	$Fe^{3+} + HO_2 \rightarrow Fe^{2+} + O_2 + H^+$	3.1×10^3			[12]
26	$FeOH^{2+} + HO_2 \rightarrow FeOH^+ + O_2 + H^+$	2×10^4			[7]
27	$Fe(OH)_2^+ + HO_2 \rightarrow Fe(OH)_2 + O_2 + H^+$	2×10^4			[7]
28	$Fe^{3+} + O_2^- \rightarrow Fe^{2+} + O_2$	5×10^7			[7]
29	$FeOH^{2+} + O_2^- \rightarrow FeOH^+ + O_2$	5×10^7			[7]
30	$Fe(OH)_2^+ + O_2^- \rightarrow Fe(OH)_2 + O_2$	5×10^7			[7]
	ROS Reactions				
31	$H_2O_2 + OH \rightarrow HO_2 + H_2O$	3.3×10^7			[7]
32	$HO_2 + OH \rightarrow O_2 + H_2O$	7.1×10^9			[12]
33	$O_2^- + OH \rightarrow O_2 + OH^-$	10^{10}			[12]
34	$OH + OH \rightarrow H_2O_2$	5.2×10^9			[7]
35	$H_2O_2 + HO_2 \rightarrow OH + O_2 + H_2O$	0.5			[12]
36	$HO_2 + HO_2 \rightarrow H_2O_2 + O_2$	8.3×10^5			[7]
37	$HO_2 + O_2^- \rightarrow HO_2^- + O_2$	9.7×10^7			[7]
38	$O_2^{2-} + H^+ \rightarrow HO_2^-$	10^{10}			[7]
39	$O_2^- + H_2O_2 \rightarrow OH^- + OH + O_2$	10^{-4}			[12]
	Sulfate Equilibria				
40	$H^+ + SO_4^{2-} \rightleftharpoons HSO_4^-$	9.77×10^{11}	10^{10}	97.7	[7]

41	$Fe^{2+} + SO_4^{2-} \rightleftharpoons FeSO_4$	1.78×10^{12}	10^{10}	178	[7]
42	$Fe^{3+} + SO_4^{2-} \rightleftharpoons FeSO_4^{+}$	8.31×10^{13}	10^{10}	8.31×10^{3}	[7]
43	$Fe^{3+} + 2\ SO_4^{2-} \rightleftharpoons Fe(SO_4)_2^{-}$	2.63×10^{15}	10^{10}	2.63×10^{5}	[7]
	Sulfate Reactions				
44	$FeSO_4 + H_2O_2 \rightarrow Fe^{3+} + SO_4^{2-} + OH + OH^{-}$	78			[7]
45	$FeSO_4 + OH \rightarrow Fe^{3+} + SO_4^{2-} + OH^{-}$	2.7×10^{8}			[7]
46	$FeSO_4 + HO_2 \rightarrow Fe^{3+} + SO_4^{2-} + HO_2^{-}$	1.2×10^{6}			[7]
47	$FeSO_4 + O_2^{-} \rightarrow Fe^{3+}\ SO_4^{2-} + O_2^{2-}$	5×10^{8}			[7]
48	$Fe^{2+} + SO_4^{-} \rightarrow Fe^{3+} + SO_4^{2-}$	3×10^{8}			[7]
49	$FeOH^{+} + SO_4^{-} \rightarrow Fe^{3+} + SO_4^{2-}$	3×10^{8}			[7]
50	$FeSO_4 + SO_4^{-} \rightarrow Fe^{3+} + 2\ SO_4^{2-}$	3×10^{8}			[7]
51	$FeSO_4^{+} + O_2^{-} \rightarrow Fe^{2+} + SO_4^{2-} + O_2$	10^{3}			[7]
52	$FeSO_4^{+} + HO_2 \rightarrow Fe^{2+} + SO_4^{2-} + O_2 + H^{+}$	10^{3}			[7]
53	$Fe(SO_4)_2^{-} + HO_2 \rightarrow Fe^{2+} + 2\ SO_4^{2-} + O_2 + H^{+}$	10^{3}			[7]
54	$Fe(SO_4)_2^{-} + O_2^{-} \rightarrow Fe^{2+} + SO_4^{2-} + O_2$	10^{3}			[7]

Page et al., (2010); Miller et al., (2012); De Laat and Le (2005); Walling and Goosen (1973); Klöpffer and Kohl (1991): the rate constants of between OH and most organics in aqueous solution are on the order of $10^9\ M^{-1}S^{-1}$, the rate constant of products from the OH reaction with TA other than hTA was estimated based on this. Pham and Waite (2008); Zuo and Hoigne (1992); Bielski et al., (1985)

2.2.6 Biomass Burning HULIS Collection and Extraction

Biomass burning aerosol samples were collected in January-February 2013 in Fresno, CA, on Teflon coated glass filters (8" x 10", 0.45μm, Tisch Environmental), using a Hi-Volume $PM_{2.5}$ sampler (TE-6070 Tisch Environmental) operating at 1.13 $m^3\ min^{-1}$. Biomass burning

aerosol has been widely observed in Fresno during winter, especially at night, and is attributed primarily to residential wood burning (Gorin et al., 2006).

Aerosol mass concentration for the Fresno samples was determined using a microbalance (Sartorius). One square inch of the filter was cut using a ceramic blade (to avoid metal contamination) and was extracted with gentle agitation for 2 hours in phosphate buffer (pH7.4) containing 4 antioxidants at physiologically relevant concentrations: 100 μM uric acid, 100 μM L-Glutathione, 200 μM ascorbic acid and 300 μM citrate and 10 mM terephthalate. 125μL aliquots of the extraction solution were used in separations. The HLB columns were first conditioned with 250μL of methanol and then equilibrated with 250μL of Milli-Q water. Additional conditioning necessary for separation and final elution steps are described below.

2.2.7 Interference of Cu(II) with the hTA assay

EEM scans were performed to probe fluorescence of terephthalate and Cu(II) complex, if any. The potential reduction of hTA fluorescence intensity by Cu(II) was done by adding 1μM to 250 μM of Cu(II) to 800nM hTA, and measuring fluorescence using the single-wavelength scan mode after 2 hours. Additionally, H_2O_2 formation from 20 μm Cu(II) with different concentrations of TA (0.5 to 10mM) was measured every 30 minutes for 2 hours. 20 μM of Cu(II) was chosen because this concentration produces significant amounts of H_2O_2 in the dark (this work, Fig. 2.3).

2.3 Results

2.3.1 hTA Yield

Fig. 2.1 shows experimental data (symbols) and model best fit (lines) for the average of three experiments; error bars show the standard deviation of nine measurements at each time point (three replicates from each of three experiments). The model is most sensitive to the rate

constant for Fe(II) reacting with H_2O_2 to make OH and co-products (the Fenton reaction, k_{15} in Tab. 2.3). Most published rates for this reaction fall within the range 55 -76 $M^{-1}s^{-1}$. (De Laat and Le 2005; Zuo and Hoigne 1992) We obtained the best fit to measured H_2O_2 and Fe(II) with 76 $M^{-1}s^{-1}$; this results in mean square errors (MSEs) of 4.3 and 3.1 % for Fe(II) and H_2O_2, respectively (Fig. 2.1). We then adjusted the yield of hTA (Y_{hTA}) to minimize the MSE between the model and the average concentration of hTA, and found a best-fit Y_{hTA} = 31.5 ± 7%, with and MSE of 0.24%. Altering Y_{hTA} does not affect the modeled Fe(II) and H_2O_2 concentrations. The error bars for the yield was derived by finding the best fit Y_{hTA} for ± 1 σ of the measured hTA concentrations (Fig. 2.1).

At pHs above 4, formation of iron hydroxide and iron sulfate precipitates increase,(De Laat and Le 2005) compromising the utility of the Fe(II)/H_2O_2 system as an OH source, so we were not able to measure Y_{hTA} at higher pHs. Fig 2.2 summarizes reported measurements of hTA yields as a function of pH. Our results are in good agreement with the results of Matthews (1980) and about double those of Charbouillot et al., (2011). Extrapolating from the temperature dependence reported by Charbouillot et al., (2011) differences in the temperature of this work (293 K) and Charbouillot et al., (2011) would suggest the values should differ by only about 20%. To generate OH radicals, Matthews (1980) used radiolysis, while Charbouillot et al., (2011) photolyzed either nitrate or H_2O_2 using a 1000 W xenon lamp (λ > 300 nm). Page et al., (2010) reported a UV absorption spectrum for hTA. It contains a weak absorption between 275 - 365 nm, and a stronger band at shorter wavelengths (<250 nm), with a slight pH dependence. They further showed that wavelengths below 365 nm cause decomposition of hTA, and concluded that nitrate photolysis could not be used to probe hTA formation.(Page et al., 2010) Charbouillot et al., (2011) had good agreement between results using nitrate or H_2O_2 as the OH

source, but since they used the same lamp, similar degradation of hTA likely occurred. We conclude that the Matthews (1980) yields are correct and recommend a yield of 35% for pHs above 7 and slightly lower yields at lower pHs.

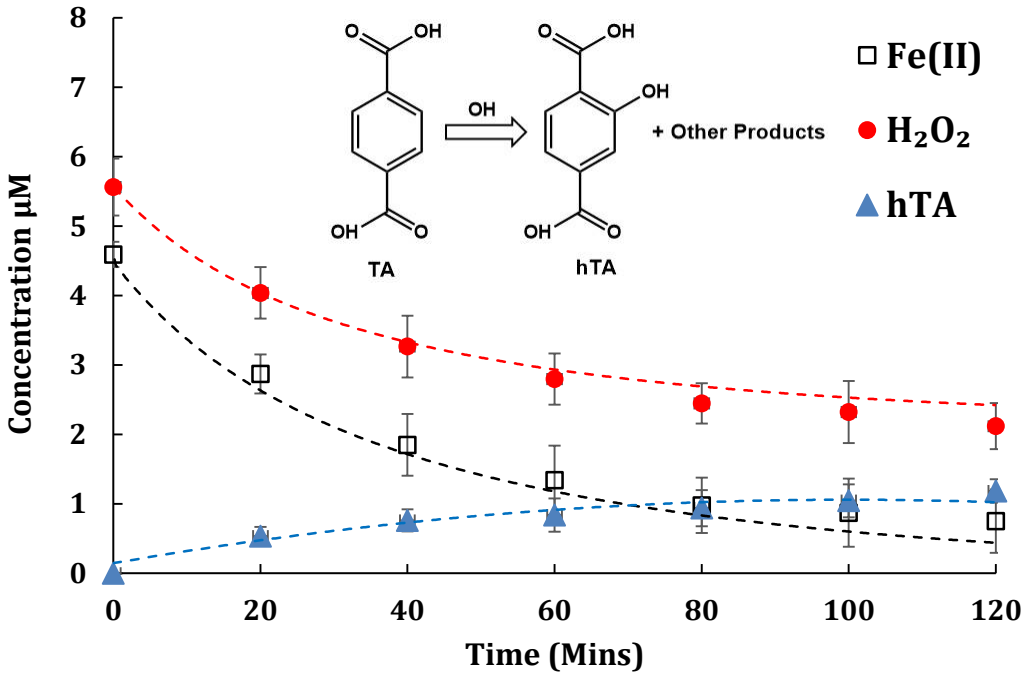

Fig. 2.1 Concentration profiles of Fe(II), H_2O_2 and hTA averaged from triplicate measurements of three experimental trials. Error bars represent ± one standard deviation of 9 samples. Dashed lines indicate model fit to experimental data. Average initial concentrations of Fe(II) and H_2O_2 were 4.59 and 5.56 µM, respectively. The yield of hTA is estimated to be 31.5 ±7%.

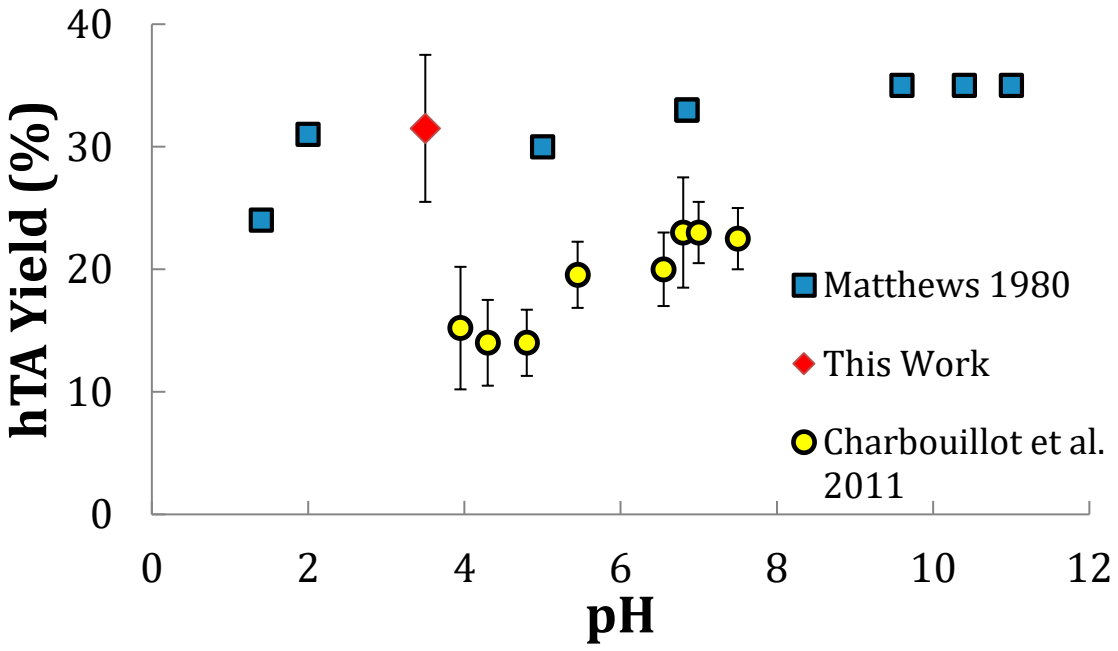

Fig. 2.2 hTA yields as a function of pH. Matthews (1980) did not indicate error bars or the experimental temperature; Charbouillot et al., (2011) measurements were performed at 288 K; this work was performed at 293 K.

2.3.2 Potential interference of Cu(II) with hTA assay

We performed several experiments to explore the potential for Cu(II) to interfere with TA of hTA, and vis-versa. At high concentrations, terephthalate and Cu(II) in water at pH3.5 rapidly form a blue precipitate (Carson et al., 2009). However, mixtures of 1 – 250 µM Cu(II) and 10 mM TA did not produce an observable precipitate (this study), and did not exhibit fluorescence in EEM scans. Next, we examined the effect of TA concentration on the formation of H_2O_2 from 200 µM Cu(II) and the results showed that H_2O_2 formation was independent of TA concentration over the range of 0.5 to 10 mM (Fig. 2.3). Figure 2.4 shows the reduction in the fluorescence intensity of 800 nM hTA with added Cu(II) in both pH3.5 and phosphate buffer. The result showed that significant reduction (>10%) of hTA intensity occurs only at concentration above about 50 µM of Cu(II) (Fig. 2. 4), a high concentration relative to copper concentrations in many

environmental extracts (e.g., (Paulson et al., 2016)). We conclude that under most conditions, Cu(II) does not interfere with the TA assay.

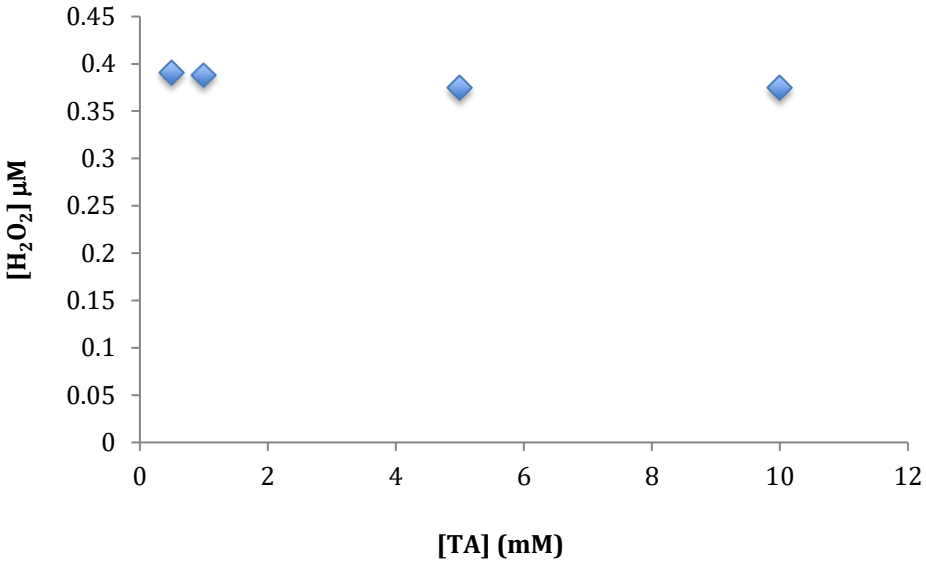

Fig. 2.3 H_2O_2 formation at 2 hours from 20µM Cu with different [TA] in pH3.5 solution.

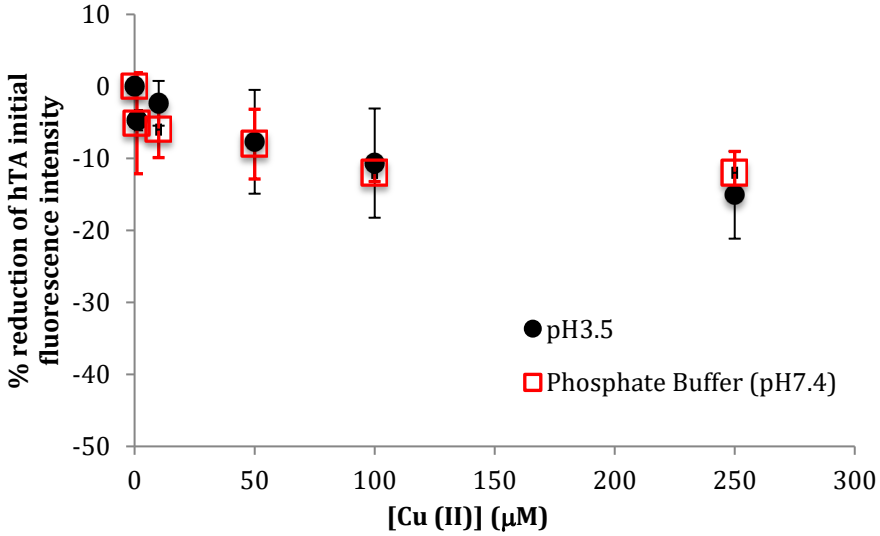

Fig. 2.4 Reduction of hTA fluorescence intensity (at 418 nm) by Cu(II).

2.3.3 Separation of hTA from fulvic acid (FA), humic acid (HA), and soluble biomass burning humic like substances (HULIS).

2.3.3.1 Fluorescence characteristics of hTA, HA, FA and soluble biomass burning HULIS

A sample scanning excitation-emission fluorescence spectrum of soluble biomass burning HULIS in Fresno $PM_{2.5}$ nighttime samples is shown in Fig. 2.5; spectra for HA, FA can be found in the literature (Duarte et al., 2004)(Mobed et al., 1996; Page et al., 2010) and are shown in Fig. 2.6. Summarizing, the EEM spectrum of hTA is very confined and symmetrical, with a maximum intensity at $\lambda_{ex}/\lambda_{em}$ of 320nm and 418nm, consistent with a single fluorophore (Fig. 2.6). pH 7.4 EEM spectra of fulvic Acid has one dominant fluorescence region at $\lambda_{ex}/\lambda_{em}$ of 340-370 nm and 460-470nm, respectively. Humic acid exhibits a broader spectrum, with two peaks at $\lambda_{ex}/\lambda_{em}$ of 360-420nm and 450-460nm and $\lambda_{ex}/\lambda_{em}$ 460nm and 500-540nm respectively. As such, neither FA and HA absorb incoming 320 nm photons, however they absorb emitted photons from hTA at ~418 nm. Soluble biomass burning HULIS directly overlaps hTA, thus all three can reduce the hTA fluorescence signal and it is desirable to develop a method to separate soluble biomass burning HULIS, FA and HA from hTA.

The relatively broad spectra of HA and FA are both consistent with the presence of multiple fluorophores. EEM spectra of soluble biomass burning HULIS (Fig. 2.5) vary somewhat from sample to sample, but they generally resemble fulvic acid more than HA. Increasing pH has been shown to increase fluorescence of humic substances, a property attributed to changes in fluorescent characteristics of phenols and phenolate functional groups (Lakowicz 2013; Mobed et al., 1996). Furthermore, pH-induced conformational changes in humic molecules have been attributed to changes in fluorescence (Miano et al., 1988; Mobed et al., 1996).

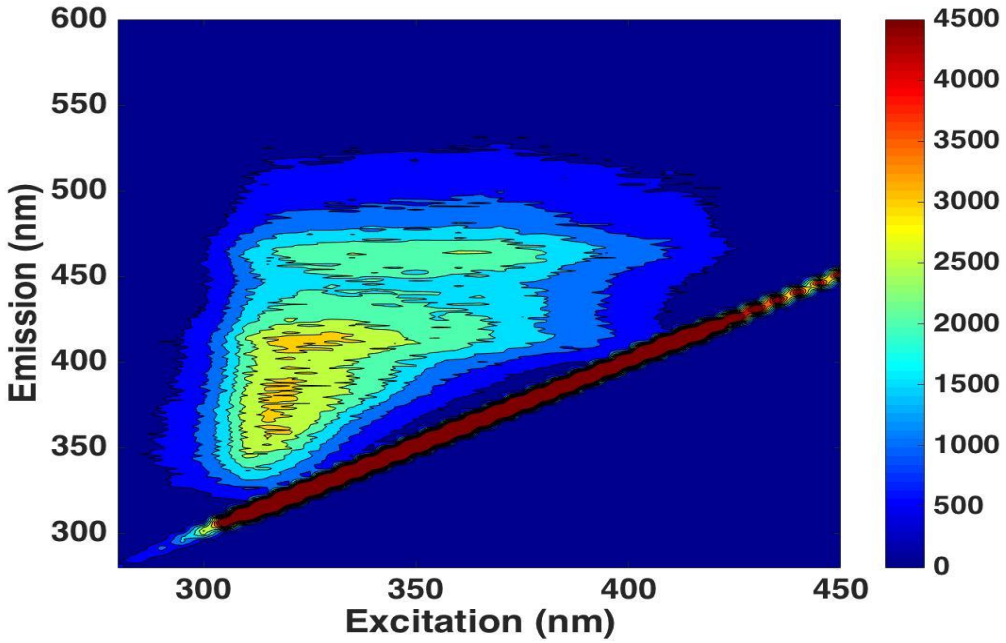

Fig. 2.5 EEM of water-soluble soluble biomass burning HULIS extracted from a nighttime sample (Jan. 19) collected in winter in Fresno, in SLF, with a mass concentration of 45 μg/m^3.

a **b**

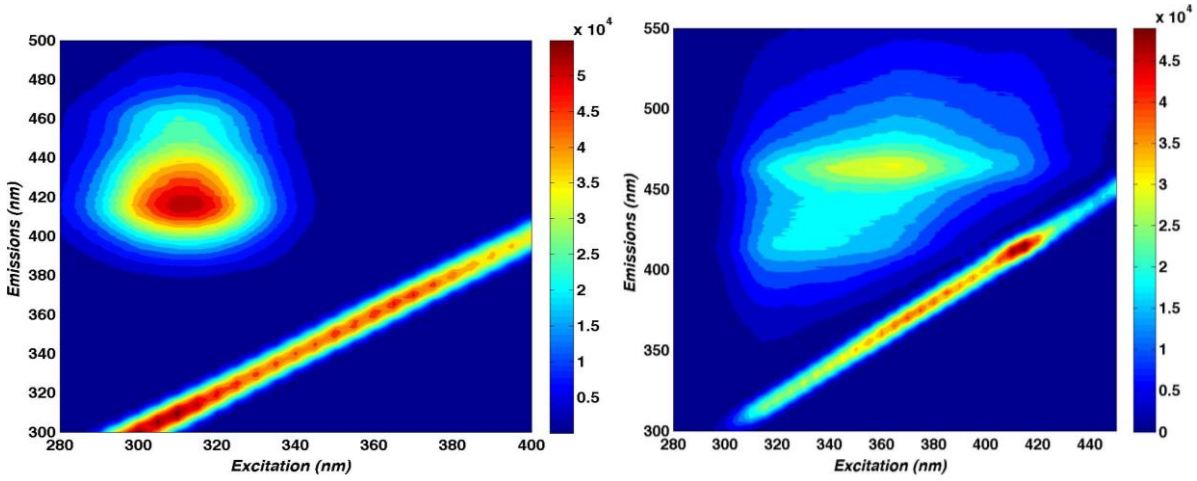

c

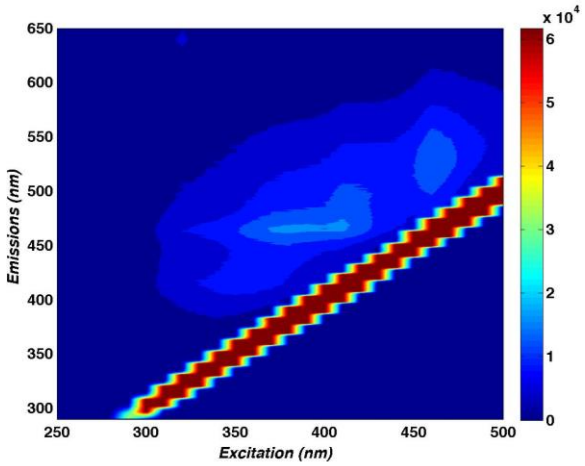

Fig. 2.6 EEM spectrum of 800nM of hTA (a), 50 μg/mL of FA (b) and 100 μg/mL HA.

2.3.3.2 Inference with hTA measurement by HA/FA

To quantify HA/FA interference with hTA, 5 to 50 μg/mL of FA/HA were added to 800nM of hTA, and the fluorescence of the mixtures were measured by EEM mode. Fig. 2.7 shows calibration curves of hTA by itself (50-800nM) and with added FA (5-50 μg/mL) using a single $\lambda_{ex}/\lambda_{em}$. Background fluorescence increases as FA is added, resulting in high intercepts and lower slopes, and concentrations of hTA at lower concentrations (50 – 100 nM) are somewhat affected at 5 μg/mL and strongly affected at higher concentrations (Fig. 2.8). In contrast, 800 nM hTA is only significantly affected above 20 μg/mL FA or HA (Figs. 2.9 and 2.10).

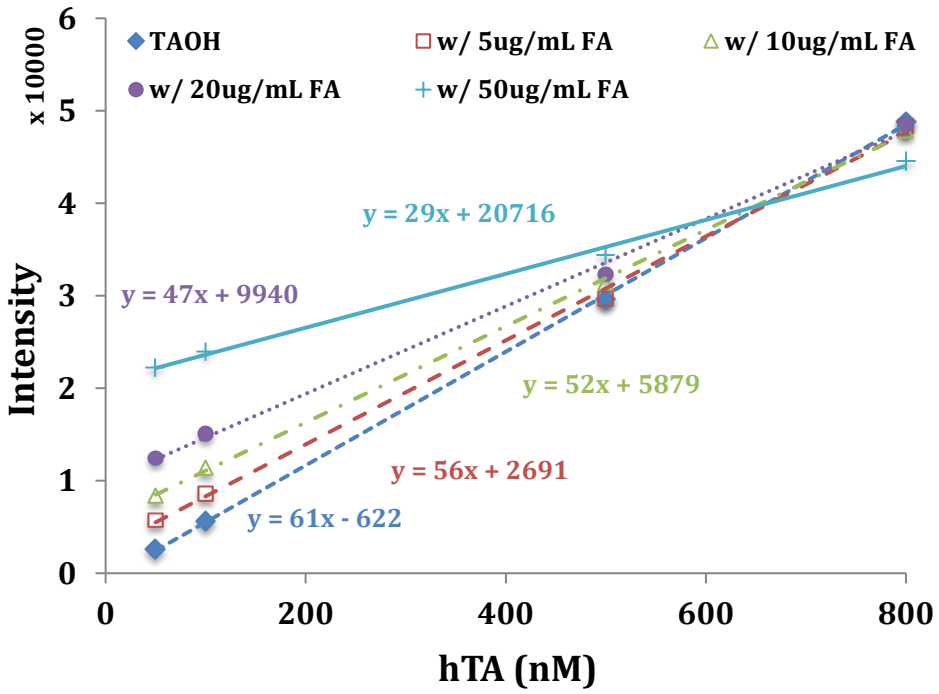

Fig. 2.7 Fluorescence intensity as a function of hTA concentration for different FA concentrations added.

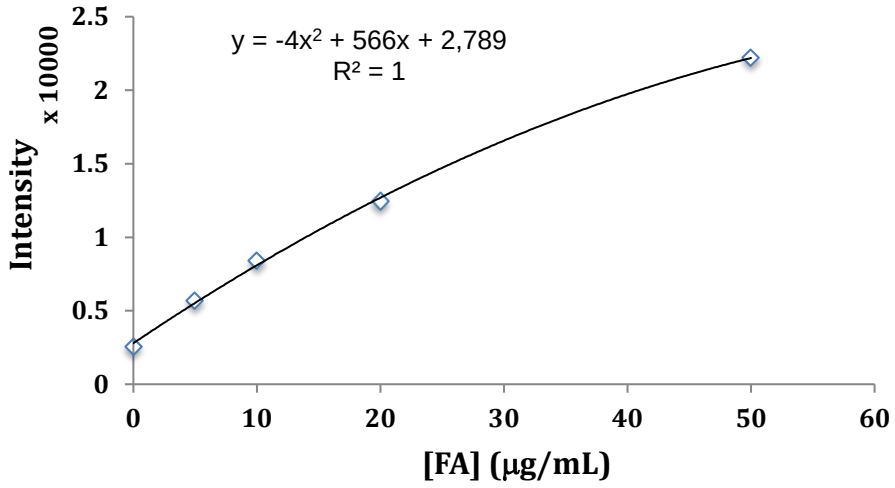

Fig. 2.8 Effect of concentration of FA on fluorescent intensity of hTA at 50nM.

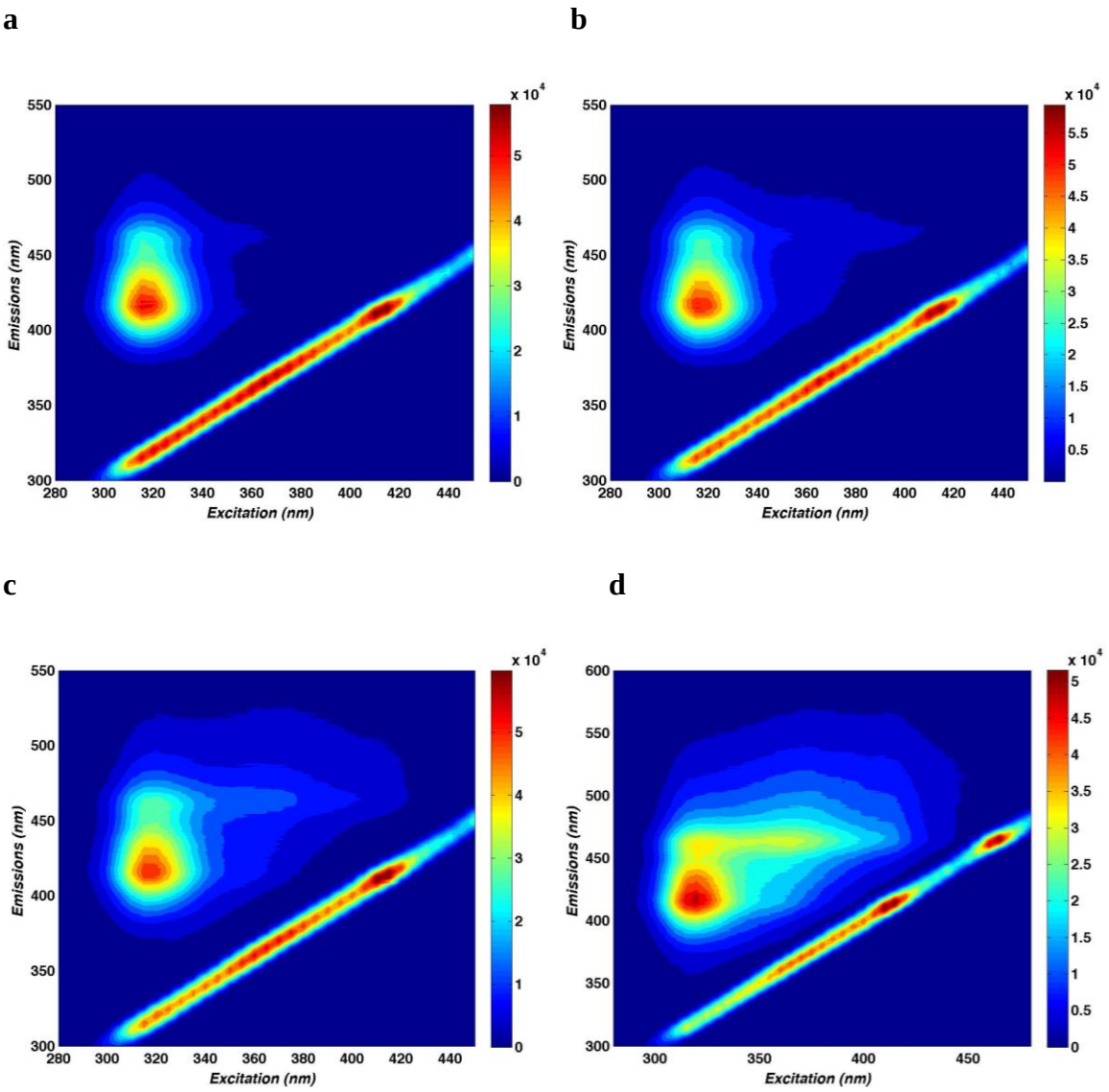

Fig. 2.9 EEM of 800nM hTA with 5 (a), 10 (b), 20 (c) and 50 (d) μg/mL FA in SLF.

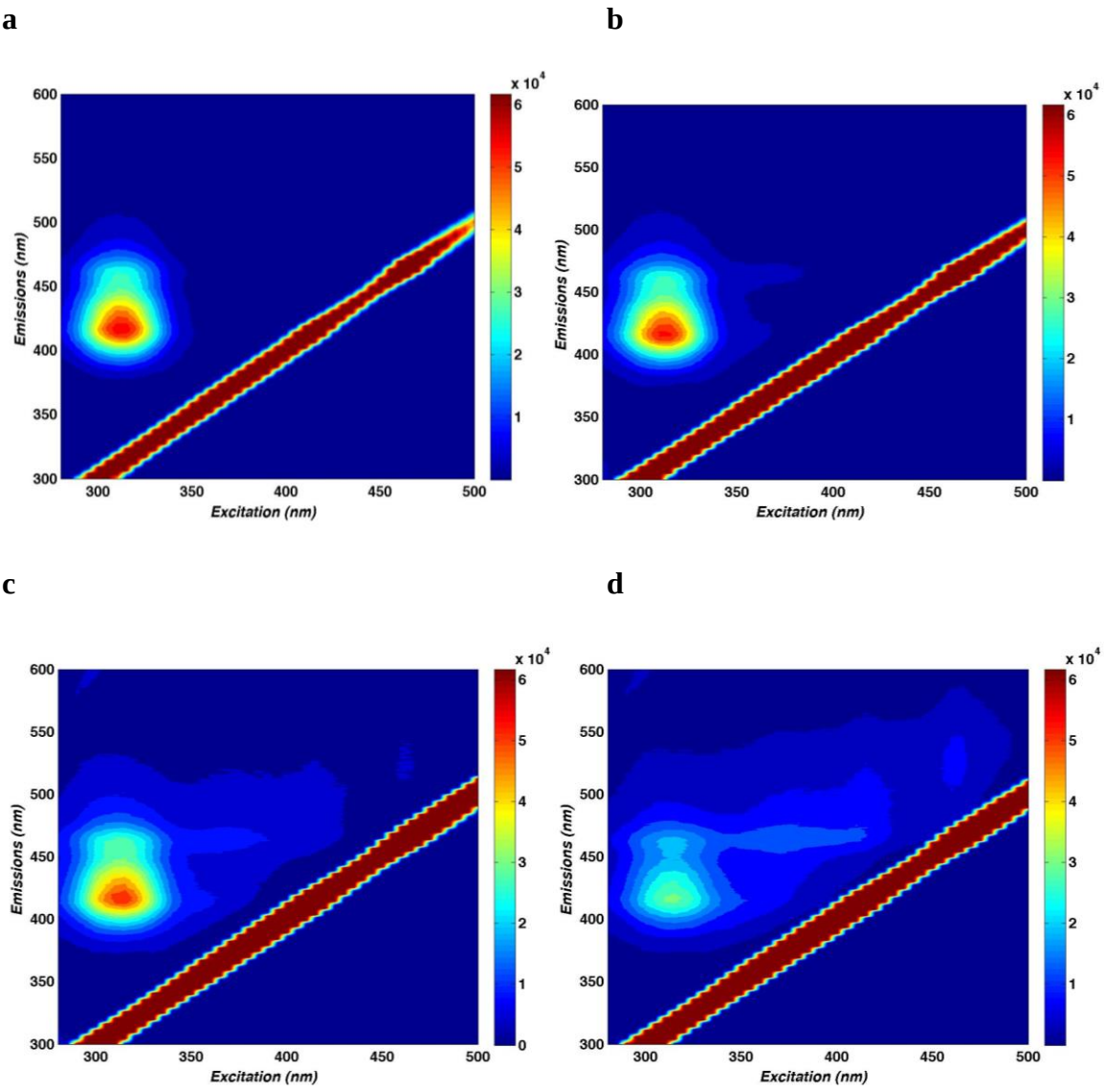

Fig. 2.10 EEM of 800nM hTA with 5 (a), 10 (b), 20 (c) and 50 (d) μg/mL HA in SLF.

3.3.3 Separation method development

In this study, HLB was chosen to separate hTA from HULIS for several reasons. It is available in small sizes (here we used 10mg sorbent size), suitable for small samples (up to 2mL); it is reasonably inexpensive (< $2/cartridge in 2014); and it is stable over the pH range 0 – 14, facilitating the use of pH as a tool to develop effective separation methods. Furthermore, it has been used to successfully isolate atmospheric HULIS (Fan et al., 2012; Krivácsy et al., 2008;

Lin et al., 2010); for example, Varga et al., (2001) showed that about 60% of the water soluble organic compounds extracted from aerosol samples collected in a forest could be retained on the HLB Cartridge, and this material contained more than 90% of the fluorescence and 70% of UV absorbance of the total water-soluble organic carbon. Hydrophilic compounds that typically make up a large fraction of ambient aerosols such as inorganic ions and acids, and small organic acids are expected to largely pass through the cartridge, while larger polar, aromatic ring-bearing compounds are more strongly retained (Varga et al., 2001).

Analytes with acid groups are retained on HLB columns when they are fully protonated, and can then be eluted with methanol (Varga et al., 2001). Practically, compounds have higher retention on the HLB cartridge when they are about 2 pH units below their lowest pK_a (Corporation 2014). Several studies (Krivácsy et al., 2008; Lin et al., 2010; Varga et al., 2001) successfully isolated HULIS from atmospheric samples using HLB columns by pre-acidifying to pH 2, followed by elution with methanol to recover the HULIS. The pK_as of Humic acid are ~4 and 9 (Choppin and Kullberg 1978). hTA has pK_as of 3.62, 6.47 and 9.86 (Page et al., 2010).

If the same acidification/methanol elution is applied to hTA/HULIS mixtures, due to the chemical similarities of hTA and HULIS, hTA elutes with the HULIS. Analytes are most strongly adsorbed to the HLB cartridge when protonated, and most easily eluted when deprotonated. By adjusting pH of the solutions that were loaded onto the columns and using a mixture of water and methanol in the elution step, we were able to recover 100% of the hTA, and leave most FA/HA on the column. Initial trials acidifying the hTA/FA and hTA/HA mixtures to pH ~1.67 (2 pH units below the first pK_a of hTA, 3.62) showed incomplete retention on the columns, a problem that was solved by lowering the pH to 1.34. Following this, the samples were washed with 250 μL of water, followed by a 10:90% methanol: water solution to remove

compounds other than hTA and HULIS. Eluting hTA + HA/FA mixture with 90% methanol yielded the highest recovery of hTA and greatest retention of HA or FA, resulting in good but not perfect separation. The eluted samples were evaporated and reconstituted in the original solution for subsequent fluorescence measurements (Fig. 2.11).

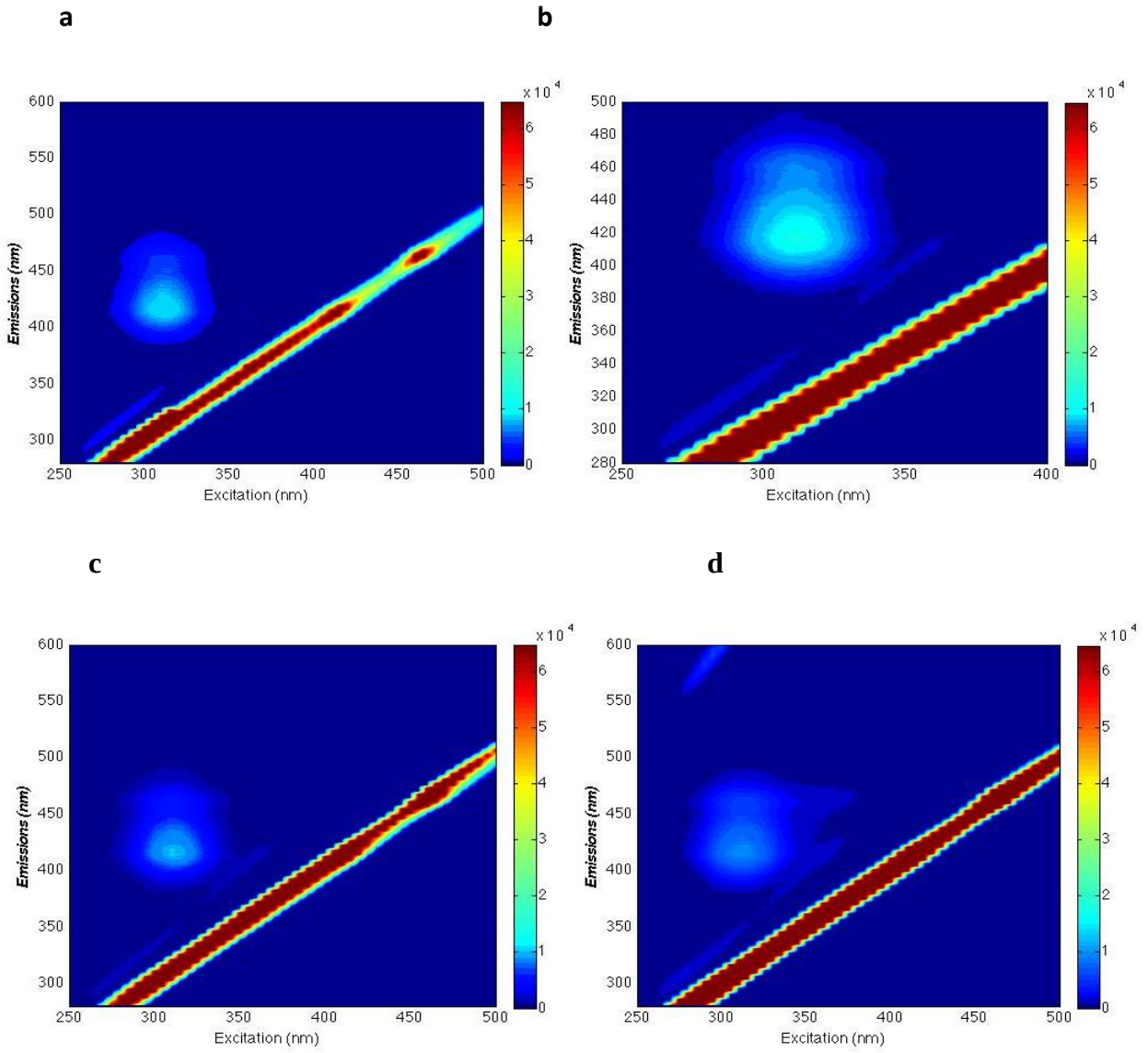

Fig. 2.11 Fluorescence EEM of hTA (800nM) and HA/FA (20μg/mL) mixture under different pH values and methanol to water ratio: upper panels show the mixture of hTA/FA were acidified to pH2 (a) and pH1.67 (b) and eluted with 90% methanol. The lower panels show the mixture of hTA and FA (c) and HA (d) were acidified to pH1.34 and eluted with 90% methanol. Note: the eluent was evaporated and reconstitute in the original solution.

Application of this procedure to soluble biomass burning HULIS was less successful than it was for FA and HA, thus we developed another eluent system to improve the separation. As above, samples were first acidified to pH 1.34 and then loaded on the columns, followed by the same wash steps. The elution step used for HA/FA, 90% methanol, elutes hTA but also some soluble biomass burning HULIS. Using the different retention of protonated/unprotonated compounds, but recognizing hTA and soluble biomass burning HULIS have several similar pKas, finding a successful pH for the final elution step was challenging. We chose pH 4 as it is higher than the lowest pK_a of hTA but does not exceed the lowest pK_a of humic substances (~4). To maintain the pH of the eluent at ~4, we used a phosphate buffer. Combination of phosphate buffer with 0, 10 and 20% methanol resulted in lower recovery of hTA, but 70:30 pH4 phosphate buffer: methanol resulted in 100% hTA recovery, with no observable soluble biomass burning HULIS fluorescence in the eluent (Fig. 2.12).

a **b**

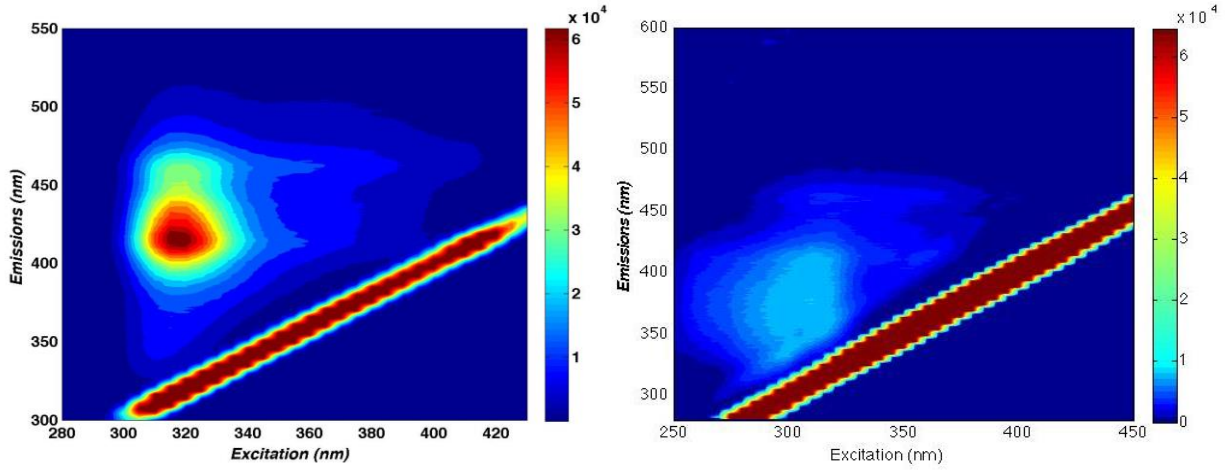

c

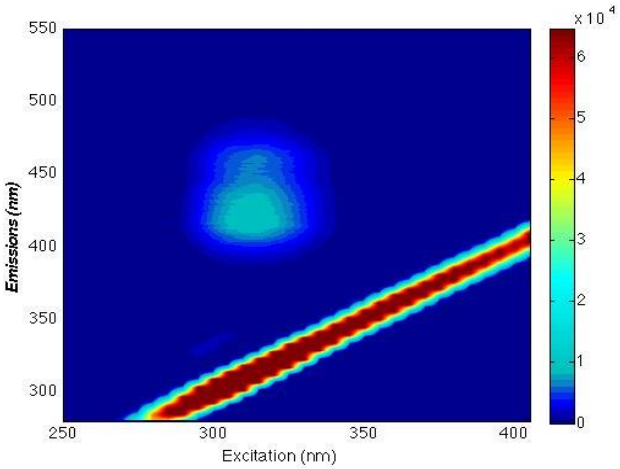

Fig. 2.12 Original aqueous extract of biomass burning aerosol sample without separation (a); separation of hTA from HULIS using 90% methanol as eluent system, 1:3.3 dilution (b) and separation of hTA from HULIS using 70% phosphate buffer and 30% methanol as eluent system, 1:6 dilution (c).

Applying the 70:30 phosphate buffer:methanol eluent to hTA/FA/HA results in better separations than the water system (compare Figs. 2-11 and 2-13). For this eluent system, the limitation on the maximum HULIS load at which separations are successful was explored. Fig. 2.13 shows that when the concentration of HA (which is more difficult to separate than FA) was higher than 20 μg/mL, hTA was completely separated from HA. This suggests that the techniques presented here will not work at higher concentrations of HA/HULIS, thus dilution of the sample extract will be needed before applying the separation method.

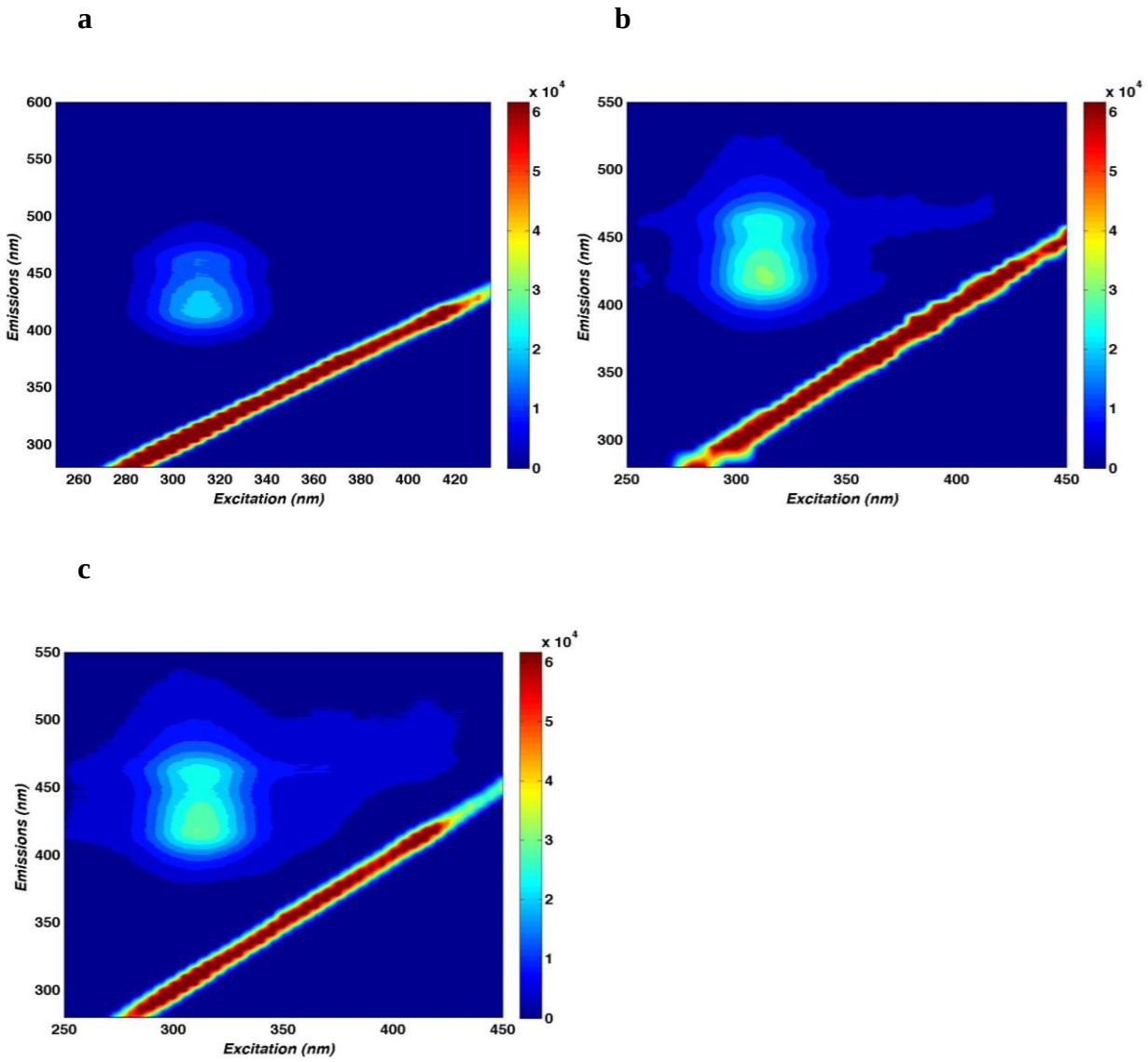

Fig. 2.13 Separation of hTA (800nM) from 20µg/mL (a), 40µg/mL (b) and 60µg/mL of HA (c) using 70% phosphate buffer at pH4 and 30% methanol as eluent.

2.4 Conclusions

The terephthalate method for quantification of hydroxyl radical is a robust, straightforward method under most conditions. Care should be taken if target samples contain

high concentrations of metals such as Cu(II), or species that absorb or fluoresce in the region of the excitation and emission wavelengths of 2-hydroxyterephthalic acid.

References

Acheson, R. and A. Galwey (1967). The thermal decomposition of nickel terephthalate and nickel salts of other carboxylic acids. J. Chem. Soc. A: Inorg. Phys. Theor.:1174-1178.

Arellanes, C., S. E. Paulson, P. M. Fine, C. Sioutas (2006). Exceeding of Henry's Law by Hydrogen Peroxide Associated with Urban Aerosols. . Envir. Sci. Tech.:DOI: 10.1021/es0513786.

Armstrong, W. A., R. A. Facey, D. W. Grant, W. G. Humphreys (1963). A tissue-equivalent chemical dosimeter sensitive to 1 rad. Can. J. Chem. 41:1575-1577.

Bielski, B. H., D. E. Cabelli, R. L. Arudi, A. B. Ross (1985). Reactivity of HO2/O− 2 radicals in aqueous solution. Journal of Physical and Chemical Reference Data 14:1041-1100.

Bougiatioti, A., P. Nikolaou, I. Stavroulas, G. Kouvarakis, R. Weber, A. Nenes, M. Kanakidou, N. Mihalopoulos (2016). Particle water and pH in the eastern Mediterranean: source variability and implications for nutrient availability. Atmos. Chem. Phys. 16:4579-4591.

Brook, R. D., J. R. Brook, B. Urch, R. Vincent, S. Rajagopalan, F. Silverman (2002). Inhalation of fine particulate air pollution and ozone causes acute arterial vasoconstriction in healthy adults. Circulation 105:1534-1536.

Carson, C. G., K. Hardcastle, J. Schwartz, X. Liu, C. Hoffmann, R. A. Gerhardt, R. Tannenbaum (2009). Synthesis and structure characterization of copper terephthalate metal–organic frameworks. Eur. J. Inorg. Chem. 2009:2338-2343.

Charbouillot, T., M. Brigante, G. Mailhot, P. R. Maddigapu, C. Minero, D. Vione (2011). Performance and selectivity of the terephthalic acid probe for (OH)-O-center dot as a function of temperature, pH and composition of atmospherically relevant aqueous media. Journal of Photochemistry and Photobiology a-Chemistry 222:70-76.

Choppin, G. R. and L. Kullberg (1978). Protonation thermodynamics of humic acid. J. Inorg. Nucl. Chem. 40:651-654.

Corporation, W. (2014). Oasis HLB cartridge and 96-well plates care and user manual

.

De Laat, J. and T. G. Le (2005). Kinetics and modeling of the Fe (III)/H2O2 system in the presence of sulfate in acidic aqueous solutions. Env. Sci. Tech. 39:1811-1818.

Duarte, R., C. A. Pio, A. C. Duarte (2004). Synchronous scan and excitation-emission matrix fluorescence spectroscopy of water-soluble organic compounds in atmospheric aerosols. Journal Of Atmospheric Chemistry 48:157-171.

Duarte, R., C. A. Pio, A. C. Duarte (2004). Synchronous scan and excitation-emission matrix fluorescence spectroscopy of water-soluble organic compounds in atmospheric aerosols. J. Atmos. Chem. 48:157-171.

Falconer, R. and P. Falconer (1980). Determination of cloud water acidity at a mountain observatory in the Adirondack Mountains of New York State. Journal of Geophysical Research: Oceans 85:7465-7470.

Fan, X., J. Song, P. a. Peng (2012). Comparison of isolation and quantification methods to measure humic-like substances (HULIS) in atmospheric particles. Atmos. Environ. 60:366-374.

Faust, B. C. and J. M. Allen (1993). Aqueous-phase photochemical formation of hydroxyl radical in authentic cloudwaters and fogwaters. Env. Sci. Tech. 27:1221-1224.

Fernandez-Castro, P., M. Vallejo, M. F. San Roman, I. Ortiz (2015). Insight on the fundamentals of advanced oxidation processes. Role and review of the determination methods of reactive oxygen species. J. Chem. Tech. Biotech. 90:796-820.

Freinbichler, W., M. A. Colivicchi, M. Fattori, C. Ballini, K. F. Tipton, W. Linert, L. Della Corte (2008). Validation of a robust and sensitive method for detecting hydroxyl radical formation together with evoked neurotransmitter release in brain microdialysis. Journal of neurochemistry 105:738-749.

Goldstone, J. V., M. J. Pullin, S. Bertilsson, B. M. Voelker (2002). Reactions of hydroxyl radical with humic substances: Bleaching, mineralization, and production of bioavailable carbon substrates. Env. Sci. Tech. 36:364-372.

Gorin, C. A., J. L. Collett Jr, P. Herckes (2006). Wood smoke contribution to winter aerosol in Fresno, CA. Journal of the Air & Waste Management Association 56:1584-1590.

Jung, H., B. Guo, C. Anastasio, I. M. Kennedy (2006). Quantitative measurements of the generation of hydroxyl radicals by soot particles in a surrogate lung fluid. Atmos. Environ. 40:1043-1052.

Kim, H. and S. E. Paulson (2013). Real refractive indices and volatility of secondary organic aerosol generated from photooxidation and ozonolysis of limonene, alpha-pinene and toluene. Atmospheric Chemistry And Physics 13:7711-7723.

Klöpffer, W. and E.-G. Kohl (1991). Bimolecular OH rate constants of organic compounds in solution: 1. Measurements in water using hydrogen peroxide as an OH source. Ecotoxicology and environmental safety 22:67-78.

Krivacsy, Z., G. Kiss, B. Varga, I. Galambos, Z. Sarvari, A. Gelencser, A. Molnar, S. Fuzzi, M. C. Facchini, S. Zappoli, A. Andracchio, T. Alsberg, H. C. Hansson, L. Persson (2000). Study of humic-like substances in fog and interstitial aerosol by size-exclusion chromatography and capillary electrophoresis. Atmospheric Environment 34:4273-4281.

Krivácsy, Z., G. Kiss, D. Ceburnis, G. Jennings, W. Maenhaut, I. Salma, D. Shooter (2008). Study of water-soluble atmospheric humic matter in urban and marine environments. Atmospheric Research 87:1-12.

Kuang, B. Y., P. Lin, X. H. H. Huang, J. Z. Yu (2015). Sources of humic-like substances in the Pearl River Delta, China: positive matrix factorization analysis of PM 2.5 major components and source markers. Atmos. Chem. Phys. 15:1995-2008.

Lakowicz, J. R. (2013). Principles of fluorescence spectroscopy. Springer Science & Business Media.

Lesser, M. P. (2006). Oxidative stress in marine environments: Biochemistry and physiological ecology, in Annu. Rev. Physiol., Annual Reviews, Palo Alto, 253-278.

Li, L. X., Y. Abe, K. Kanagawa, T. Shoji, T. Mashino, M. Mochizuki, M. T. Aka, N. Miyata (2007). Iron-chelating agents never suppress Fenton reaction but participate in quenching spin-trapped radicals. Analytica Chimica Acta 599:315-319.

Lim, Y., Y. Tan, M. Perri, S. Seitzinger, B. J. Turpin (2010). Aqueous chemistry and its role in secondary organic aerosol (SOA) formation. Atmos. Chem. Phys. 10:10521-10539.

Lin, P., X.-F. Huang, L.-Y. He, J. Z. Yu (2010). Abundance and size distribution of HULIS in ambient aerosols at a rural site in South China. J. Aerosol Sci. 41:74-87.

Lin, P. and J. Z. Yu (2011). Generation of reactive oxygen species mediated by humic-like substances in atmospheric aerosols. Env. Sci. Tech. 45:10362-10368.

Lindsey, M. E. and M. A. Tarr (2000). Inhibition of hydroxyl radical reaction with aromatics by dissolved natural organic matter. Env. Sci. Tech. 34:444-449.

Linxiang, L., Y. Abe, Y. Nagasawa, R. Kudo, N. Usui, K. Imai, T. Mashino, M. Mochizuki, N. Miyata (2004). An HPLC assay of hydroxyl radicals by the hydroxylation reaction of terephthalic acid. Biomedical Chromatography 18:470-474.

Matthews, R. W. (1980). THE RADIATION-CHEMISTRY OF THE TEREPHTHALATE DOSIMETER. Radiation Research 83:27-41.

Matthews, R. W. (1980). THE radiation-chemistry of the terephthalate dosimeter. Radiation Research 83:27-41.

Matthews, R. W. (1980). The Radiation Chemistry Of The Terephthalate Dosimeter. Radiation Research 83:27-41.

Miano, T., J. Martin, G. Sposito (1988). Flourescence Spectroscopy of Humic Substances. Soil Sci. Soc. Am. J. 52:1016-1019.

Miller, C. J., A. L. Rose, T. D. Waite (2012). Hydroxyl radical production by H2O2-mediated oxidation of Fe (II) complexed by Suwannee River fulvic acid under circumneutral freshwater conditions. Env. Sci. Tech. 47:829-835.

Mobed, J. J., S. L. Hemmingsen, J. L. Autry, L. B. McGown (1996). Fluorescence characterization of IHSS humic substances: Total luminescence spectra with absorbance correction. Environmental Science & Technology 30:3061-3065.

Mobed, J. J., S. L. Hemmingsen, J. L. Autry, L. B. McGown (1996). Fluorescence characterization of IHSS humic substances: Total luminescence spectra with absorbance correction. Env. Sci. Tech. 30:3061-3065.

Nakajima, H., K. Okada, Y. Kuroki, Y. Nakama, D. Handa, T. Arakaki, A. Tanahara (2008). Photochemical formation of peroxides and fluorescence characteristics of the water-soluble fraction of bulk aerosols collected in Okinawa, Japan. Atmospheric Environment 42:3046-3058.

Page, S. E., W. A. Arnold, K. McNeill (2010). Terephthalate as a probe for photochemically generated hydroxyl radical. J. Environ. Monit. 12:1658-1665.

Page, S. E., W. A. Arnold, K. McNeill (2010). Terephthalate as a probe for photochemically generated hydroxyl radical. Journal of Environmental Monitoring 12:1658-1665.

Paulson, S. E., A. Hasson, C. Anastasio, Xiaobi M. Kuang, J. Adlin Scott, David H. Gonzalez-Martinez, Tiffany Charbouillot , Kennedy K-T Vu, James Baroi, Catalina Olea, Annabelle Lolinco and Kylie Markarian, Jessica G. Charrier, Alexander S. McFall, N. K. Richards-Henderson (2016). Probing the Intrinsic Ability of Particles to Generate Reactive Oxygen Species and the Effect of Physiologically Relevant Solutes. Calif. Air Resources Board Annu. Report

Pham, A. N. and T. D. Waite (2008). Oxygenation of Fe (II) in natural waters revisited: Kinetic modeling approaches, rate constant estimation and the importance of various reaction pathways. Geochimica et Cosmochimica Acta 72:3616-3630.

Pope, C. A., R. T. Burnett, G. D. Thurston, M. J. Thun, E. E. Calle, D. Krewski, J. J. Godleski (2004). Cardiovascular mortality and long-term exposure to particulate air pollution epidemiological evidence of general pathophysiological pathways of disease. Circulation 109:71-77.

Pope, C. A., J. B. Muhlestein, H. T. May, D. G. Renlund, J. L. Anderson, B. D. Horne (2006). Ischemic heart disease events triggered by short-term exposure to fine particulate air pollution. Circulation 114:2443-2448.

Pullin, M. J. and S. E. Cabaniss (1995). RANK ANALYSIS OF THE PH-DEPENDENT SYNCHRONOUS FLUORESCENCE-SPECTRA OF SIX STANDARD HUMIC SUBSTANCES. Environmental Science & Technology 29:1460-1467.

Rabu, P., J. Rueff, Z. Huang, S. Angelov, J. Souletie, M. Drillon (2001). Copper (II) and cobalt (II) dicarboxylate-based layered magnets: influence of π electron ligands on the long range magnetic ordering. Polyhedron 20:1677-1685.

Rosenfeldt, E. J. and K. G. Linden (2004). Degradation of endocrine disrupting chemicals bisphenol A, ethinyl estradiol, and estradiol during UV photolysis and advanced oxidation processes. Env. Sci. Tech. 38:5476-5483.

Saran, M. and K. H. Summer (1999). Assaying for hydroxyl radicals: Hydroxylated terephthalate is a superior fluorescence marker than hydroxylated benzoate. Free Radical Res. 31:429-436.

Saran, M. and K. H. Summer (1999). Assaying for hydroxyl radicals: hydroxylated terephthalate is a superior fluorescence marker than hydroxylated benzoate. Free radical research 31:429-436.

Sato, K., S. Nakao, C. H. Clark, L. Qi, D. R. Cocker iii (2011). Secondary organic aerosol formation from the photooxidation of isoprene, 1, 3-butadiene, and 2, 3-dimethyl-1, 3-butadiene under high NO x conditions. Atmos. Chem. Phys. 11:7301-7317.

Shen, H. and C. Anastasio (2012). A comparison of hydroxyl radical and hydrogen peroxide generation in ambient particle extracts and laboratory metal solutions. Atmos. Environ. 46:665-668.

Sherif, F. G. (1970). Heavy metal terephthalates. Indust. Eng. Chem. Prod. Res. Dev. 9:408-412.

Shilling, J. E., S. M. King, M. Mochida, S. T. Martin (2007). Mass spectral evidence that small changes in composition caused by oxidative aging processes alter aerosol CCN properties. J. Phys. Chem. A 111:3358-3368.

Shrivastava, M. K., T. E. Lane, N. M. Donahue, S. N. Pandis, A. L. Robinson (2008). Effects of gas particle partitioning and aging of primary emissions on urban and regional organic aerosol concentrations. J. Geophys. Res., [Atmos.] 113

Son, Y., V. Mishin, W. Welsh, S.-E. Lu, J. D. Laskin, H. Kipen, Q. Meng (2015). A Novel High-Throughput Approach to Measure Hydroxyl Radicals Induced by Airborne Particulate Matter. Int. J. Environ. Res. Pub. Health 12:13678-13695.

Spencer, R. G. M., L. Bolton, A. Baker (2007). Freeze/thaw and pH effects on freshwater dissolved organic matter fluorescence and absorbance properties from a number of UK locations. Water Research 41:2941-2950.

Stookey, L. L. (1970). FERROZINE - A NEW SPECTROPHOTOMETRIC REAGENT FOR IRON. Analytical Chemistry 42:779-&.

Suda, S. R., M. D. Petters, G. K. Yeh, C. Strollo, A. Matsunaga, A. Faulhaber, P. J. Ziemann, A. J. Prenni, C. M. Carrico, R. C. Sullivan, S. M. Kreidenweis (2014). Influence of Functional Groups on Organic Aerosol Cloud Condensation Nucleus Activity. Env. Sci. Tech. 48:10182-10190.

Thorne, P. S. (2000). Inhalation toxicology models of endotoxin-and bioaerosol-induced inflammation. Toxicol. 152:13-23.

Varga, B., G. Kiss, I. Ganszky, A. Gelencser, Z. Krivacsy (2001). Isolation of water-soluble organic matter from atmospheric aerosol. Talanta 55:561-572.

Verma, V., R. Rico-Martinez, N. Kotra, L. King, J. M. Liu, T. W. Snell, R. J. Weber (2012). Contribution of Water-Soluble and Insoluble Components and Their Hydrophobic/Hydrophilic Subfractions to the Reactive Oxygen Species-Generating Potential of Fine Ambient Aerosols. Env. Sci. Tech. 46:11384-11392.

Walling, C. and A. Goosen (1973). Mechanism of the ferric ion catalyzed decomposition of hydrogen peroxide. Effect of organic substrates. Journal Of The American Chemical Society 95:2987-2991.

Zepp, R. G., B. C. Faust, J. Hoigne (1992). Hydroxyl radical formation in aqueous reactions (pH 3-8) of iron (II) with hydrogen peroxide: the photo-Fenton reaction. Env. Sci. Tech. 26:313-319.

Zuo, Y. and J. Hoigne (1992). Formation of hydrogen peroxide and depletion of oxalic acid in atmospheric water by photolysis of iron (III)-oxalato complexes. Env. Sci. Tech. 26:1014-1022.

3. Formation of hydroxyl radical and hydrogen peroxide by aerosols: relationships with chemical composition

3.1 Introduction

Aerosols are of central importance for atmospheric chemistry, physics and climate change. Aerosol aging via oxidation modifies particulate chemical composition (Donahue et al., 2012; Sato et al., 2011; Shrivastava et al., 2008), cloud condensation nuclei (CCN) activity (Engelhart et al., 2008; Shilling et al., 2007), hygroscopic properties (Asa-Awuku et al., 2011; Suda et al., 2014), and optical properties of aerosols (Kim 2014). The relative contributions of gas- and condensed phase oxidative reactions are not well understood.

Aqueous phase oxidation reactions involve a group of species referred to as reactive oxygen species (ROS). ROS includes hydrogen peroxide (H_2O_2), and OH, HO_2, superoxide ($O_2^{\cdot-}$) radicals and other species. Here we focus on the intrinsic ability of aerosols to produce hydroxyl radical and H_2O_2.

H_2O_2 and OH are tightly linked, primarily by Fenton-like reactions such as:

$$H_2O_2 + Fe(II) \rightarrow Fe(III) + OH^- + OH \qquad (R3.1a)$$

$$H_2O_2 + Cu(I) \rightarrow Cu(II) + OH^- + OH \qquad (R3.1b)$$

H_2O_2 concentrations are determined by the balance of production and destruction, with the primary metal-mediated ROS production reaction being:

$$Fe(II) + O_2 \rightarrow Fe(III) + O_2^{\cdot-} \qquad (R3.2)$$

Which can then be converted to H_2O_2, especially at neutral and acidic pH:

$$Fe(II) + O_2^{\cdot-} + 2H^+ \rightarrow Fe(III) + H_2O_2 \qquad (R3.3)$$

While H_2O_2 and OH can partition from the gas phase, Arellanes et al., (2006) showed that aerosols generate much more H_2O_2 than levels predicted by Henry's Law, underscoring the intrinsic ability of particles to continuously produce ROS.

To date, several studies have investigated formation of H_2O_2 and related species by ambient aerosols. Studies conducted by the UCLA group showed that H_2O_2 formation by fine mode particles from several sites in the Los Angeles area in atmospheric relevant solution ranged from 5 ± 5 to 12 ± 9 ng/m^3 (Arellanes et al., 2006; Hasson and Paulson 2003; Shang et al., 2012; Wang et al., 2010). H_2O_2 formation by fine particulate matter at an urban site in central California measured in a physiologically relevant solution showed similar amount of H_2O_2 produced 15 ± 8 ng/m^3 (Shen et al., 2011).

OH is the most important oxidant in the atmosphere, including in atmospheric waters. It contributes significantly to S(IV) oxidation in atmospheric waters (Pandis and Seinfeld 1989), as well as the oxidation of organics, generally at diffusion-controlled rates (Buxton et al., 1988). The four sources of OH in condensed phase (Faust and Allen 1993) include: 1) gas-drop partitioning of gas phase OH; 2) gas-drop partitioning of gas phase O_3 followed by reaction with $O_2^{-\cdot}$; 3) photolysis of H_2O_2, NO_3^-, NO_2^- and $Fe(OH)^{2+}$ and 4) the Fenton and Fenton-like reactions (R1) mediated by iron and other transition metals such as copper. Using a modeling approach, Graedel et al., (1986) suggested that the Fenton reaction was an important OH source at night but not during daytime.

A small handful of studies have investigated the formation of OH by ambient aerosols, especially in the absence of light. Many of these have performed analysis in extraction solutions designed to mimic some characteristics of lung fluid, such as pH, ionic strength, and in some cases presence of antioxidants, such as ascorbate. As species such as ascorbate act as electron

donors, overwhelming the intrinsic ability to generate OH, these studies are not comparable to pH3.5 on an absolute basis. On a relative basis, these studies have shown site-to-site variability and much higher activity from PM2.5 than flame soot particles (Jung et al., 2006; Shen and Anastasio 2012). Kuang et al., (2017) measured OH generation by particles in ship emissions, and showed that particles generated from Hydrogenation-Derived Renewable Diesel (HDRD) produced more OH than Ultra Low Sulfur Diesel (ULSD) extracted in in concentrated aqueous solution at pH3.5. More oxidized ship emissions also showed higher OH generation activity than freshly emitted particles.

A number of studies have shown that transition metals (Valavanidis et al., 2005; Wang et al., 2010), quinones (Chen and Pignatello 1997; Chung et al., 2006; Duesterberg and Waite 2007; Shang et al., 2012; Xia et al., 2004) as well as other unknown organics in particles, may contribute to ROS formation. Since hydroxyl radicals are formed primarily from hydrogen peroxide (R1), they are expected to share similar sources.

Transition metals, either as free ions or as metal-ligand complexes, are capable of generating ROS through redox reactions if present in the particles (R3.1-R3.3). Several studies have also confirmed the role transition metals play in the formation of ROS by adding metal chelators such as chelex and desferoxamine, which has removed of majority of the ROS reactivity (>90%) (Shafer et al., 2010; Vidrio et al., 2008). Several studies have shown correlations between H_2O_2 and redox active transition metals; consistently Fe and Cu. Corrlations have also been observed for non-redox active transition metals, but there is less agreement among them. Wang et al. (2010a) observed that hydrogen peroxide (1 nmol/m^3) generated by coarse particles collected in Riverside, CA was strongly correlated with Fe, Cu and Zn. See et al., (2007) also observed correlations with Fe and copper, as well as Cd, Co, Ni, and

Mn, for samples originated from wood smoke, gas cooking and other aerosol sources. The water-soluble transition metal content in the particles in both Wang et al. (2010a) and See et al. (2007) were in good agreement, and Cu and Fe were the most abundant. Similar observation was found in samples collected in Lahore, Pakistan that redox-active metals, Mn, Co, Fe, and Ni, showed strong correlations with ROS activity while the non-redox active metals, Zn, Pb and Cd, showed very weak correlations (Shafer et al., 2010).

To better understand the mechanism of formation of hydrogen peroxide and OH by ambient particles, we conducted a field campaigns in Claremont, CA during summer to 1) quantify transition metals in the PM and iron speciation; 2) measure simultaneous formation of H_2O_2 and OH in two different locations and seasons under atmospherically relevant conditions; and 3) determine the contribution from different redox-active species to formation of ROS. $PM_{2.5}$ mass in the Los Angeles region is fairly constant throughout the year, and are predominantly anthropogenic in origin. In summer, particularly at receptor sites such as Claremont, there is a larger component of photochemical secondary organic (Hasheminassab et al., 2014).

3.2 Methods

3.2.1 Field campaigns

Samples were collected at rooftop sites about 30m above ground level at Harvey Mudd College, Claremont, CA from July 26 – Aug. 13, 2012. Sets of ambient samples (PM_4) were collected three times a day, from 7 am to 1 pm, 1 to 6 pm, and 6 pm to 7 am. Samples were collected on acid washed, pre-weighed Teflon filters (PALL, 47mm, 2μm pore size) using 5 URG cyclone inlets; flow rates were controlled at 50 LPM by rotameters (Kings Instruments 7530). A total of 300 filters were collected. The cut point was intended to be 2.5 μm, however due to a misunderstanding on the rotometer operation used resulting in a 4 μm cutpoint. Mass on

the filters was estimated to be 22% higher (Paulson et al., 2016). Matched full field blanks were created using the same handling procedures as samples, but with the pump turned on for only 30 s. These filters were analyzed for mass, hydrogen peroxide and hydroxyl radical, trace metals and speciated iron. Mass, hydroxyl radical quantification and iron speciation were performed on site, while the filters for other analyses were stored in the freezer until later use.

3.2.2 Materials

Disodium terephthalate was purchased from TCI. Methanol (HPLC grade) and sulfuric acid (reagent grade), Trifluoroethanol (≥ 99%), Hydroxylamine hydrochloride, ethylenediaminetetraacetic acid (EDTA), horseradish peroxidase type II, para-hydroxyphenyl acetic acid (POHPAA), potassium hydrogen phthalate (KHP) were purchased from Sigma Aldrich. Ferrozine (4,4'-[3-(2-pyridinyl)-1,2,4-triazine-5,6-diyl]dibenzenesulfonate), sulfuric acid (reagent grade) and sodium thiosulfate (1M) were purchased from Fluka Analytic. Nitric acid (70% trace metal grade) and ammonium hydroxide (30% ACS reagent grade) were purchased from Fisher. All materials were used as received.

3.2.3 Trace metal cleaning and Particle extraction

A rigorous cleaning process was followed for all glass and Teflon containers, as detailed in Kuang et al., (2017), Chapter 2. All analytical solutions were prepared with 18 MΩ DI water that had been passed through a chelex column to remove trace metals. pH was measured with a bench top pH meter (HANNA instruments, HI 3220), calibrated daily.

Filters were cut in half using a cleaned ceramic blade. Half filters were first wetted with 50 μL of trifluroethanol then extracted in 4 mL (and 10 mL for iron speciation) aqueous pH3.5 solution (adjusted using 0.1 N sulfuric acid) in Teflon petri dishes with gentle agitation at 20 rpm on a shaker (Heidolph, Rotamax 120) .

3.2.4 Soluble speciated iron

The ferrozine assay (Stookey 1970) was used to determine concentrations of soluble $Fe(II)_{fzn}$ and $Fe(tot)_{fzn}$. Rapid complexation of divalent iron with ferrozine (3-(2-pyridyl)-5,6-bis(4-phenylsulfonic acid)-1,2,4-triazine) forms a stable magenta complex that can be probed with UV/Vis spectroscopy at λ_{max} = 562 nm. The assay was performed with a Liquid Waveguide Capillary Cell (LWCC) (World Precision Instruments), equipped with an UV-Vis detector, consisting of a 1-meter-long fiber optic (200µm ID) flow cell (LPC-FS-1000,), halogen source light (AvaLight-DH-S-DUV) and spectrometer (AvaSpec-ULS2048L-USB2). Using a 1 meter LPC allows the quantification of very low concentrations of iron (with detection limit of a few nM). To account for instrument drift and solution turbidity, absorbance at the non-absorbing wavelength of 700 nm (A_{700}) was subtracted from A_{562}. To quantify $Fe(tot)_{fzn}$, a strong reducing agent, 10 µL/mL of solution of 20mg/mL of hydroxylamine hydrochloride was added to convert all $Fe(III)_{fzn}$ to $Fe(II)_{fzn}$. Calibration of $Fe(II)_{fzn}$ was performed daily and the LWCC was rigorously cleaned between each use. The $Fe(II)_{fzn}$ stock solution (2 mM Iron Sulfate (Sigma-Aldrich) at pH 3.5) was freshly prepared for each measurement. $Fe(II)_{fzn}$ calibration curves were made by diluting the stock solution to concentrations between 0.012 and 0.75 µM $Fe(II)_{fzn}$. Stock solutions of ferrozine and hydroxylamine hydrochloride are stable for a month when stored at 4°C in the dark. To avoid interference with photochemical processes, all solutions were prepared in a dark room equipped with a sodium lamp.

3.2.5 Hydrogen Peroxide

100µL aliquots were analyzed for H_2O_2 every 30 minutes for the first 2 hours, and again at 24 hours using a High Performance Liquid Chromatography (HPLC), (Shimadzu RF-10AXL) (Arellanes et al., 2006). The eluent system, consisting of pH3.5 solution adjusted with 0.1 N

sulfuric acid and with 0.1 mM EDTA, was delivered by an isocratic pump (Shimadzu LC-10-Ai) at 0.6 mL/min. A C18 guard column was installed to remove any impurities. H_2O_2 was eluted at 0.5 min, after which it was mixed with a fluorescent reagent containing Horseradish peroxidase and para-hydroxyphenyl acetic acid (POHPAA). The peroxidase enzyme catalyzes the reaction between H_2O_2 and POHPAA, forming a fluorescent dimer, which is detected with a fluorescence detector at the excitation/emission wavelengths of 300/420 nm. Calibrations were performed weekly or when the HPLC conditions were changed. 10^{-8} to 10^{-6} M standards were prepared from 0.3% Stock solution, which was titrated with sodium thiosulfate to determine the stock solution concentration (about 0.1 M). The detection limit for this method is 10 nM.

3.2.6 Hydroxyl Radical (OH)

Terephthalate (TA) was used to probe OH production (kuang et al.) Excess terephthalate (10mM) scavenges OH and forms a fluorescent product, 2-hydroxyterephthalic acid (hTA), which is detected at $\lambda_{ex}/\lambda_{em}$ of 320/420 nm using a sensitive fluorometer (Lumina, Thermo Scientific). An aliquot of 150µL of sample was analyzed for OH formation at 20, 40, 60, 90 and 120 minutes; and again at 24 h. A calibration was performed daily for 5 x 10^{-8} to 8 x 10^{-7} M of hTA.

3.2.7 Particle mass and trace metal analysis

Particle masses were determined using a microbalance (1 µg precision, ME 5, Sartorius) in a temperature (22-24 °C) and humidity (42-44%) controlled room. Filters were allowed to equilibrate in the weighing room for one hour before weighing. Charge on the Teflon filters was removed using a charge neutralizer (NRG) for about 10 seconds. During the field campaign, the filters were weighed using a microbalance with similar precision, within an hour of sampling.

10 transition metals (Fe, Cu, Mn, V, Ni, Zn, Cr, Co, Pb, and Cd) will be measured by inductively coupled plasma mass spectrometry, ICP-MS (Shimadzu). These analyses will be performed using the aliquots from solutions used for hydrogen peroxide, which had been stored in a freezer.

3.2.8 Back Trajectory analysis

A Hybrid Single Particle Lagrangian Integrated Trajectory (HYSPLIT) model developed by NOAA was used to analyze the origin of air masses prior arriving the sampling site. A 6-hour back trajectory was retrieved for every sample collected. Air masses descending from an elevation above 200m before arriving at the collection site during the sampling periods are classified as aloft samples, representing more aged aerosols.

3.2.9 Quantification of Quinones

Quinone measurements were done by our collaborator and the assay is detailed in Paulson et al., (2016). Briefly, samples collected on a teflon coated glass fiber filter using a Hi-Vol sampler was extracted in a phosphate buffer containing antioxidants at pH 7.2. Residue left on the filter after initial extraction was further extracted using dichloromethane. These solutions were combined to analyze for quinones using GC-MS.

3.3 Results and discussion

3.3.1 General features: mass, ROS, speciated iron, trace metal and quinone concentrations in PM extracts

Average mass concentrations, mass normalized OH, steady-state concentrations of H_2O_2, ferrozine iron and the ratio of $Fe(II)_{fzn}$ to $Fe\ (tot)_{fzn}$, at 2 and 24 hours are shown in Fig. 3.1. Mass concentrations for each sample are shown in Fig. 3.2. Several general features are

observed. The average mass concentration in Claremont was 23 ± 5 μg/m^3, and average mass was nearly identical in morning and afternoon samples and slightly lower for the nighttime samples (Fig. 3.1a). Ferrozine iron and H_2O_2 concentrations were highest in the morning for both 2 and 24 hr samples (Figs. 3.1a and b). OH was more similar. Iron exists as approximately 50/50 $Fe(II)_{fzn}$ and Fe in the afternoon and overnight samples but slightly dominated by $Fe(II)_{fzn}$ in the morning samples, for both 2 and 24 hr samples (Fig. 3.1c). Fig. 3-1d shows the mass-normalized quinone concentrations in PM extracts; the value parentheses indicates the percent of samples with concentrations above the detection limit. For instance, phenanthraquinone was only found in 27% of the samples collected while 1,4-Naphthoquinone was more ubiquitous in the samples. All of the quinones had higher concentrations in the daytime samples compared to nighttime. In this small data set, quinones did not correlate with either ROS or metals, and mass of aerosols measured in this study.

In complex aerosols and their extraction solutions, there is the possibility of saturation effects; an effect that would result in a dependence on the mass of aerosol in the extraction solution. Figs. 3.9 c-f show mass-normalized ROS and speciated iron concentrations were not correlated with aerosol mass, thus solution saturation effects were not of concern.

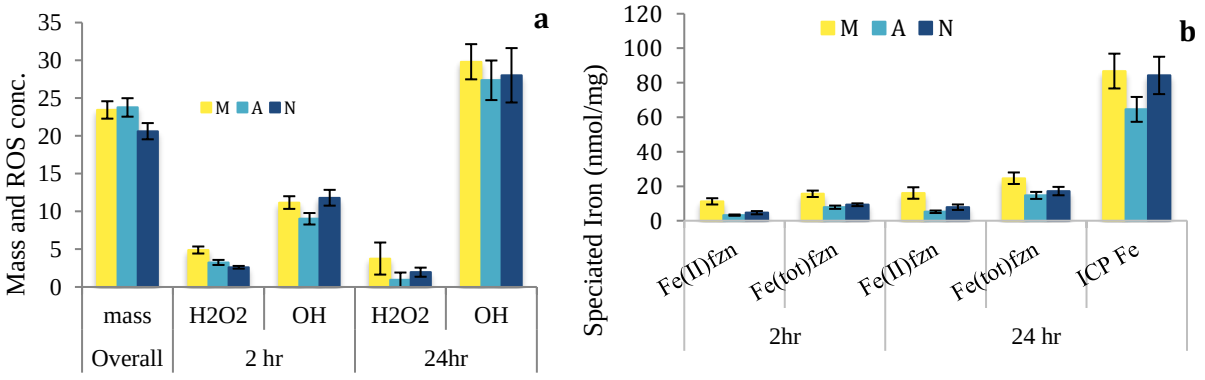

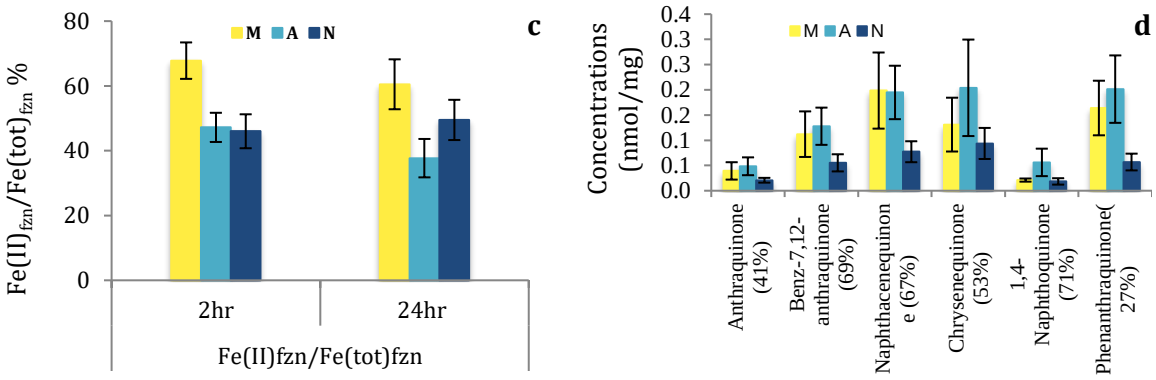

Fig. 3.1. Mass concentration (μ g/m^3), mass normalized oncentrations of ROS, speciated iron and quinones (nmol/mg) and Fe(II)$_{fzn}$ to Fe(tot)$_{fzn}$ ratios at 2 and 24 hours in Claremont. Yellow, light blue and dark blue bars represent morning(M), afternoon (A) and overnight (N) samples, respectively. Error bars indicate standard errors.

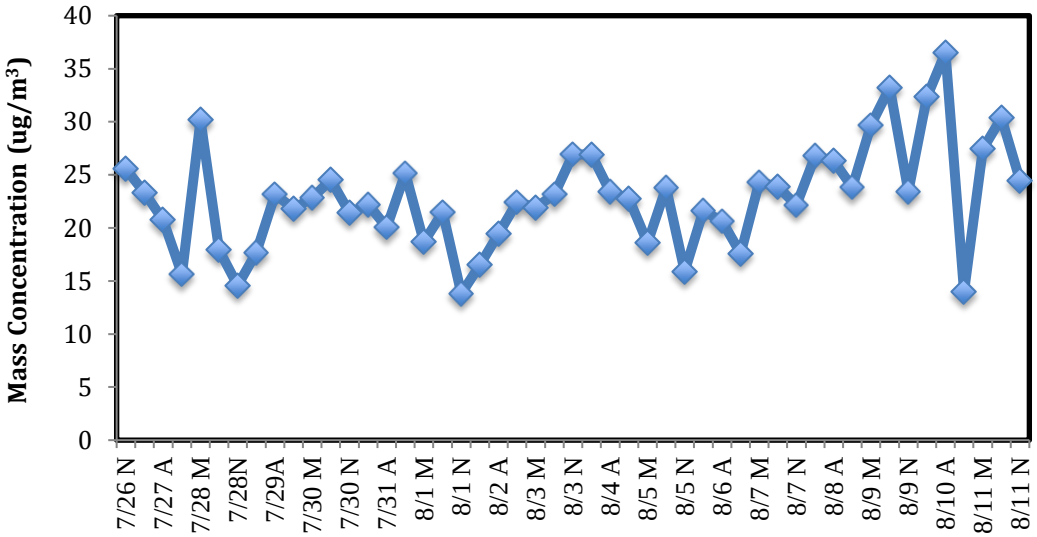

Fig. 3.2. Mass concentration over the collection period in Claremont, CA, 2012.

3.3.2 Ferrozine Iron.

Here, we report both speciated Fe(II)$_{fzn}$ and Fe(tot)$_{fzn}$ (measured with the ferrozine assay) and soluble iron measured with ICP. Ferrozine, has a high binding constant, K = 3.65 x 10^{15} (Gibbs 1976), which is believed to detect only free iron (Rose and Waite 2005), detects only 28, 23 and 20% of the Fe measured by ICP for M, A and N samples, respectively (Fig 3.1b). Fe(II)$_{fzn}$

was highest in the morning samples, and similar for afternoon and night, averaging 11 ± 2, 3.2 ± 0.4 and 5 ± 1 nmol/mg for M, A and N, respectively, at 2 hr extraction. At 24 hr, these values increased by 43-68% to 16 ± 3, 5 ± 1 and 8 ± 2 nmol/mg. $Fe(tot)_{fzn}$ followed the similar diurnal trend as $Fe(II)_{fzn}$, the increase in $Fe(tot)_{fzn}$ concentration was greater than $Fe(II)_{fzn}$, by 58 to 87%, the greatest increase was observed for the afternoon samples. $Fe(II)_{fzn}/Fe(tot)_{fzn}$ ratios decreased or remained about the same at 24 hours.

Studies reporting Fe(II)/ Fe(III) measured with the ferrozine method are summarized in Tab. 3.1. particles were extracted either in water or acetate; acetate is added to mimic the organics taken up by cloud drops or rain over time in the atmosphere. Upadhyay et al., (2011) reported that acetate greatly enhanced Fe solubility, although all of the measurements fall in the range 3-50 ng/m^3. Generally, the water extractions have lower values, and Arizona samples aside, urban samples are higher than rural samples, most falling in the range 1-10 ng/m^3.this is in excellent agreement with our values for total soluble Fe measured with the ferrozine method.

This is consistent with the notions that 1. iron present in the aerosol is more or less oxidized depending on the level of oxidation/photochemical processes of the aerosols and 2. The soluble iron is mostly chelated, rather than as free iron in solution and therefore maintains its oxidation state for at least several hours. The differences in $Fe(II)_{fzn}/Fe(tot)_{fzn}$ ratios between 2 and 24 hr were not significant for any 2/24 hr pairs ($p>0.05$). However, the interpretation of this behavior is unclear as two processes are taking place simultaneously: aqueous oxidation of $Fe(II)_{fzn}$ to $Fe(III)_{fzn}$ and dissolution of $Fe(II)_{fzn}$ and $Fe(III)_{fzn}$ which may take places at different rates.

The Ferrozine iron only accounts for 30, 22 and 18% of ICP Fe (figure 3-3) from M, A and N samples, respectively. This suggests that most of iron were complexed by organic material

present in the samples, as the Ferrozine method can only measure free iron (Yamamoto et al., 2010).

Tab. 3.1 Comparison of soluble iron concentrations measured by the ferrozine method in ambient $PM_{2.5.}$

Location	Season	Extraction solution	Fe(tot)	Fe(II) (ng/m^3)	Fe(II)/Fe(tot)	References
Claremont, CA	Summer	pH3.5	13.6±1.4	8.0±1.3	0.53±0.22	This study
Fresno, CA	Winter	pH3.5	14.8±1.2	9.6±1.0	0.63±0.22	This study
$PM_{2.5,}$ Rural Winder GA,	Summer	DI water	4.3±0.17	2.0±0.08	0.47±0.06	Oakes et al., (2012)
	Winter		5.8±0.23	4.9±0.2	0.84±0.10*	
Urban Atlanta, GA (Fire station 8)	Summer		13.6±0.18	4.6±0.06	0.34±0.03*	
	Winter		49.9±1.64	30.0±1.0	0.60±0.05*	
Urban Atlanta, GA (Ft. McPherson)	Summer		12.9±0.14	4.0±0.04	0.31±0.01*	
	Winter		12.2±0.16	6.9±0.09	0.57±0.05*	
Urban Atlanta, GA (S. Dekalb)	Summer		10.8±022	5.8±0.01	0.54±0.003	
	Winter		3.4±0.07	3.0±0.06	0.88±0.03*	
E. St Louis, IL	Winter	Acetate buffer, pH4.3	7.5±3	6.2±2	0.85±0.09*	Majestic et al., (2007)
Los Angeles, CA	Winter		14±5	12±5	0.81±0.04*	
Waukesha, WI	summer		10.5±4	5.0±3	0.47±0.06*	
Parking garage[a] ASU, AZ		Acetate buffer, (pH4.3)	42.9±5.2	41.6±4.7	0.97±0.16*	Upadhyay et al., (2011)
School of life Science, ASU,ZA[a]			46.7±8.5	46±8.2	0.99±0.25*	
Post office at US-Mexico border, AZ			31.0±10.7	31.2±11.1	1±0.5*	
CSUF, CA[b]			18±10	16.8±9.2	0.93±0.73*	
Atlanta, GA	Spring	PILS[c]		14.8±13.7		Oakes et al., (2010)
	Summer			13.4±28.3		
Dearborn, MI				17.7±26.3		

* Ratio of Fe(II)/Fe(tot) is calculated from the available data.

a. Parking garage/rooftop of a building at School of Life Science at Tempe campus of Arizona State University (ASU)

b. California State University, Fresno

c. PILS: Particle into liquid Sampler, transferred particles to purified water, was coupled to a portable UV-VIS spectrometer with Liquid Waveguide Capillary Cell (LWCC) for iron measurement.

3.3.3 Soluble Trace Metals

Fig. 3.3 shows the mass normalized concentrations of soluble trace metals at 24 hours. Among the metals measured, Fe is the most abundant (80 ± 6nmol/mg), followed by Zn and Cu (38 ± 3 and 25 ± 2 nmol/mg, respectively), the rest of the trace metals were generally lower than 4 nmol/mg. Most metals were least abundant in the afternoon samples with the exception of Zn, V, Ni, and Pb . Different diurnal variations were observed for different metals, but generally Cu, V and Se showed the highest concentration at night while Zn, Cr, Mn, Ni and Pb showed higher concentrations during daytime. Fe has fairly similar amounts in the morning and the overnight samples. Trace metals measured in this study generally showed higher concentrations compared to those reported in the literature (Tab. 3-2), except for those measured by See et al., (2007).

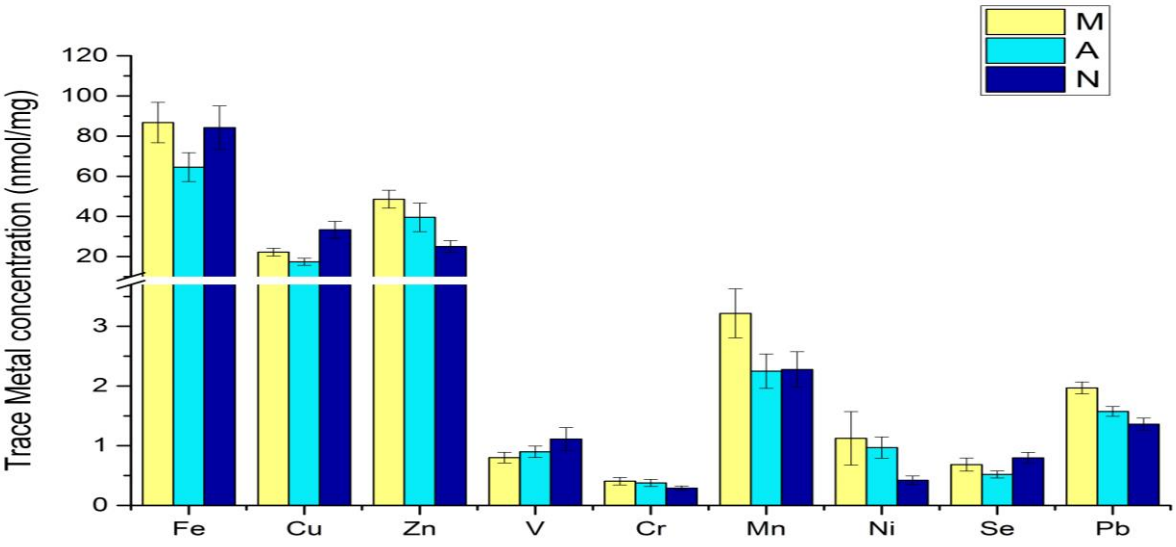

Fig. 3.3. Concentration of metals analyzed by ICP-MS at 24 hours in Claremont; yellow, light blue and dark blue bars represent morning (M), afternoon (A) and overnight (N) samples, respectively for all figures unless otherwise noted.

Tab. 3.2 Comparison of several transition metal concentrations in ambient particulate matter

PM Size	Location	Season	Extraction Solution	V	Cr	Mn	Fe (ng/m^3)	Ni	Cu	Zn	Se	Pb	Ref
PM_4	Claremont	Summer	pH3.5	1.0± 0.5	0.4± 0.3	3.2± 2	96± 48	1.0± .1.5	32± 12	55± 36	1.1± 0.6	3.3± 1.4	This study
PM_4	Fresno	Winter	pH3.5	0.2± 0.2	0.5± 0.3	3.4± 1.6	123± 67	1.8± 1.7	31± 21	69± 64	0.8± 0.7	6.9± 3.8	
$PM_{2.5}$	Riverside, CA	Summer	pH3.5				118± 99		92± 83	55± 28		12± 8	Wang et al., (2010)
Fine	Los Angeles-Long Beach Harbor	March - May	water	0.8-1.7	0.02-0.04	0.4-1.3	3.1-11.8	0.4-0.5	0.9-3.0	3.9-6.9			Hu et al., (2008)
$PM_{2.5}$	Singapore	December 2005	Water			6.0± 0.4	74.5± 0.4		361± 295	102± 6			See et al., (2007)
$PM_{2.5}$	Megalopolis Greece (Industrial)	Yearlong	Ultra pure water	0.25	0.79	1.28	8.51	2.06	0.94	51.7		2.90	Manousakas et al., (2014)
	Patras, Greece (Coastal)			1.33	1.25	1.25	11.9	4.92	2.67	163		3.16	
$PM_{2.5}$	Steubenville Ohio	yearlong	DI water w/ 2% isopropanol	1.04		7.8	19.6	0.7	3.2	55.6	4.7	8.9	Connel et al. 2005
$PM_{2.5}$	Thessaloniki, Greece	Winter (2012, 2013)	Milli-Q Water	0.44± 0.05	0.07± 0.01	1.7±0 .2	5±1	0.3±0.1	0.6±0 .1	16.5± 2.5		1.6± 0.25	Saffari et al., (2013)
$PM_{2.5}$	Lahore, Pakistan	Yearlong	Water	1.0±0. 4	1.1±0. 4	63±1 2	19±7	3.5±0.2	5.5±1 .3	291± 189		53± 19	Shafer et al., (2010)
$PM_{2.5}$	Denver, CO	Yearlong	MQ Water	0.07±0 .01	0.05± 0.01	1.0±0 .1	6.0±0.7	0.5±0.1	1.3±0 .2	7.4±1 .3		0	Zhang et al., (2008)

3.3.4 Wind directions.

Wind directions were retrieved from a representative Air Resources Board monitoring site (ARB Claremont site, Station ID: CMOC1; Latitude: 34.137, Longitude: -117.71). This monitoring site is fairly close to the sampling site (Latitude: 34.106, Longitude: -117.71), both are located on the eastern San Gabriel Valley, on the foothills of the San Gabriel Mountains, with little residential influence. Typical of the Los Angeles area, there was a distinctive diurnal land-sea breeze pattern observed over the entire campaign collection (Fig. 3.4). Daytime samples were dominated by air masses coming from the southwest (morning) and west-southwest (afternoon), most recently travelling from areas such as the port of Long Beach and the extensively urbanized area of greater Los Angeles, consisting of ~60 km of urbanized/residential areas and broadened by ~50 km of undeveloped areas. Overnight samples were dominated by air masses from the north. Results from mass normalized ROS formation and soluble trace metals as a function of wind direction are shown in Fig. 3.5. Wind directions were placed in 22.5˚ bins. Typical standard deviation of wind directions is within 13˚. Size of the wedges indicates the number of samples in that bin (Fig. 3.5a) and the color represents the ROS and metal concentrations. Average H_2O_2 and $Fe(tot)_{fzn}$ were higher in the samples associated with the air masses originating from the southwest (Figs. 2a and c) while OH, ICP Fe and Cu were higher average concentrations in the samples arriving from the north (Figs. 3.5b, d and e). The peak concentrations of H_2O_2, $Fe(tot)_{fzn}$ and ICP Fe were associated with the same morning sample (Aug. 6) and the highest OH and ICP Cu concentrations correspond to an overnight sample (Aug. 10). This is consistent with the observation that ferrozine iron were the best predictor for H_2O_2 formation, and OH was most strongly correlated with Fe and Cu, (discussed below Figs. 3-8 and 10).

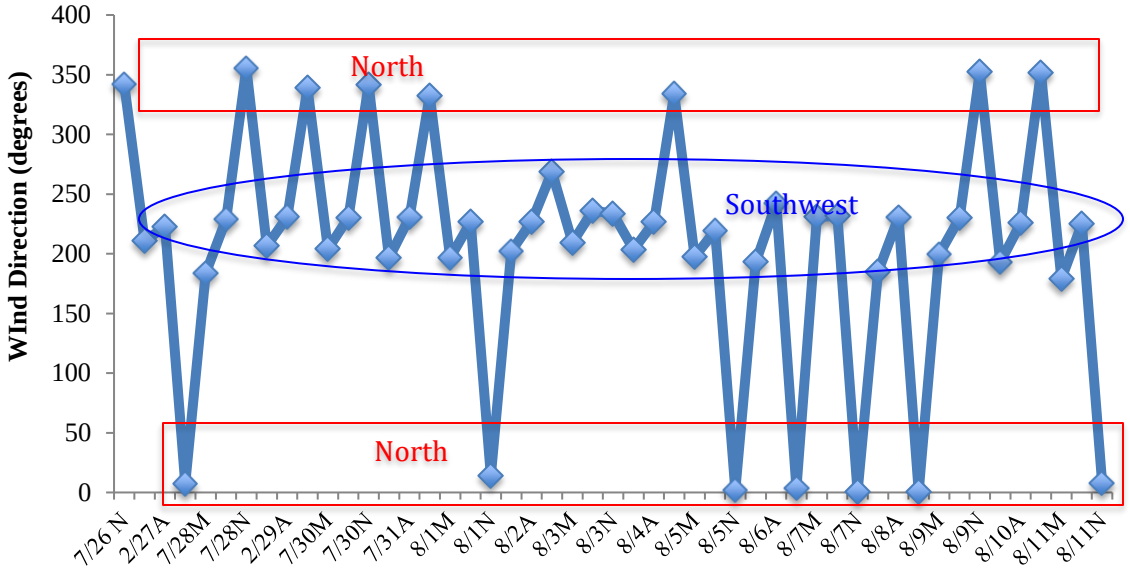

Fig. 3.4. Wind direction over the collection period in Claremont.

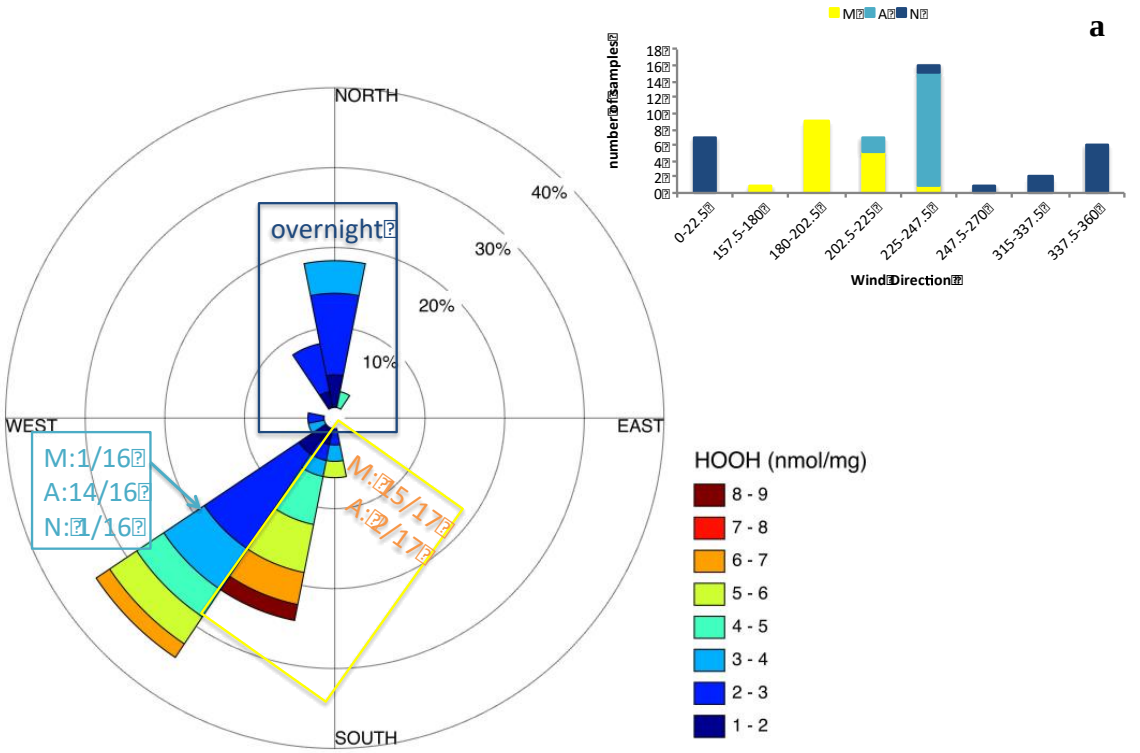

b

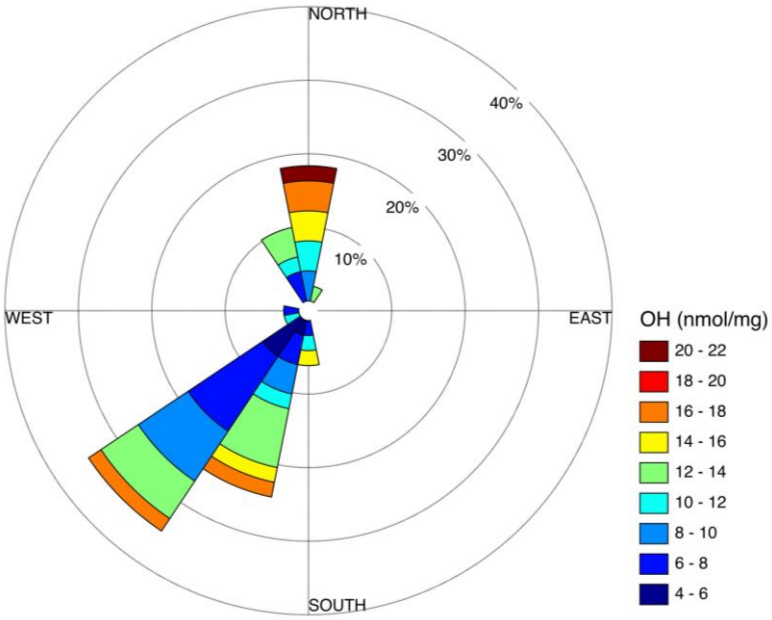
NORTH
40%
30%
20%
10%
WEST
EAST
SOUTH
OH (nmol/mg)
20 - 22
18 - 20
16 - 18
14 - 16
12 - 14
10 - 12
8 - 10
6 - 8
4 - 6

c

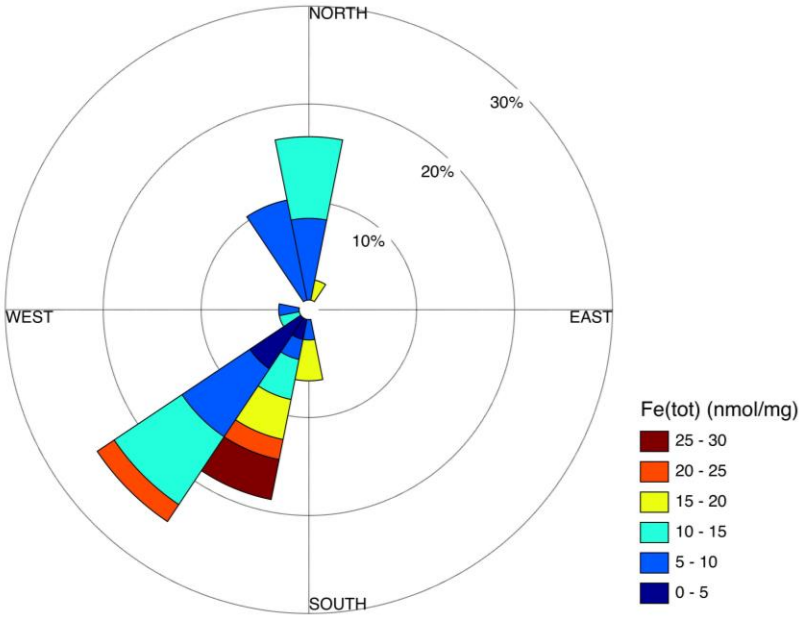
NORTH
30%
20%
10%
WEST
EAST
SOUTH
Fe(tot) (nmol/mg)
25 - 30
20 - 25
15 - 20
10 - 15
5 - 10
0 - 5

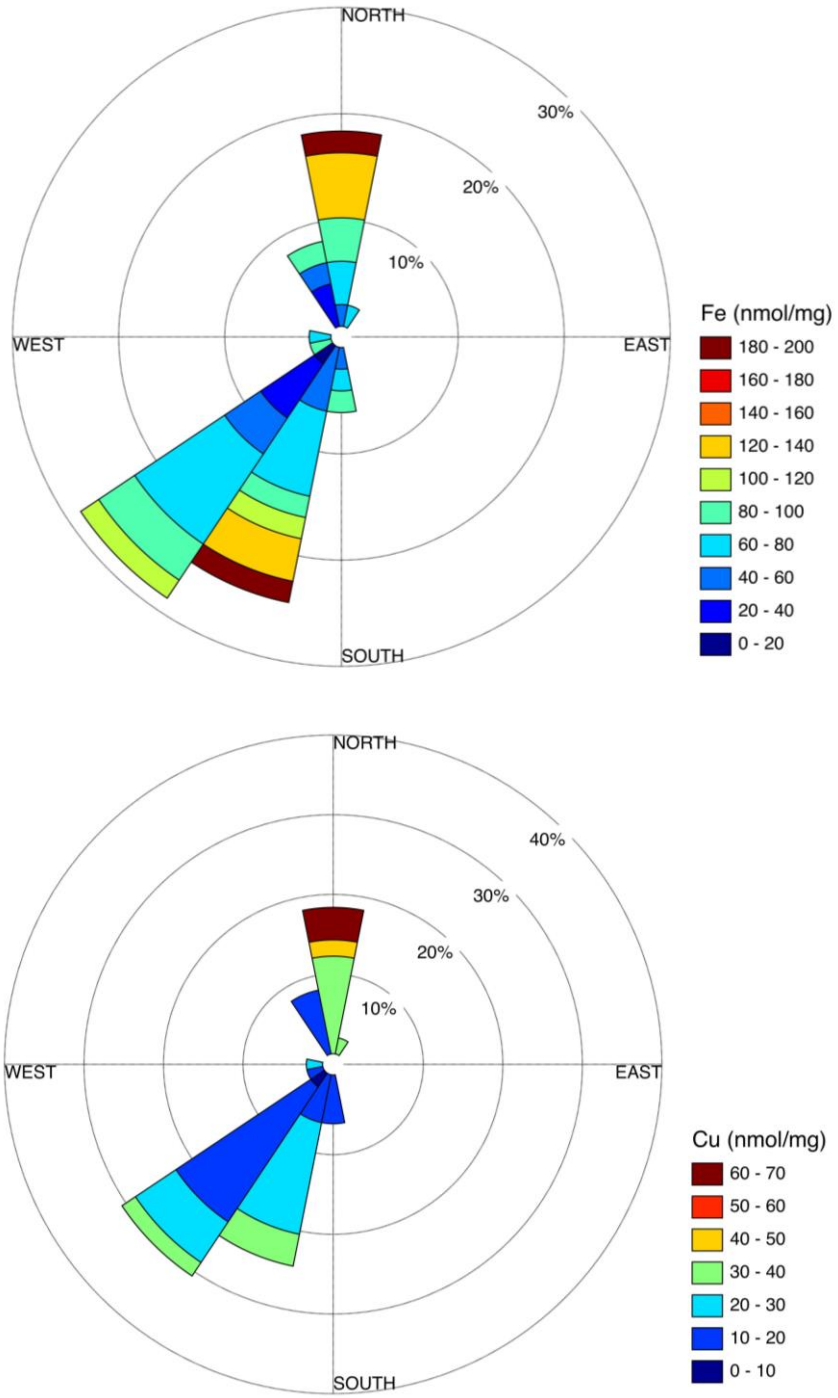

Fig. 3.5 Wind roses representing the ROS and soluble metal concentrations as a function of average wind direction. Percentage on the wind rose represents the amount of samples coming from that particular wind direction.

3.3.5 Back trajectory analysis

6 hour back trajectories were retrieved using the NOAA Hysplit Model (http://ready.arl.noaa.gov/HYSPLIT_traj.php). Based on the air mass elevation history, the samples were divided in two categories: 1. the air masses travelled along the surface during the entire 6 hours, and therefore presumably are dominated by PM that was recently emitted, and are more representative of fresh samples; and 2. samples with air masses partially descending from a higher elevation (above 200 meters), this consisting more aged samples. Aloft samples account for ~32% of the total number of samples. Mass, OH, H_2O_2, ferrozine iron have the same data set while the soluble ICP metals have a fewer data points. Fig. 3.6 shows that the samples with air masses coming from aloft results in somewhat higher concentrations of OH, H_2O_2, soluble Fe (both ICP and ferrozine), Cu, Mn and mass concentration than those travelled along surface during the sampling period. Higher metal solubility and OH formation were also observed in the more aged compared to of ship exhaust by Kuang et al (2017). While it is consistent with aging increasing metal solubility (there are several potential mechanisms), total metal concentrations would be required to test this hypothesis.

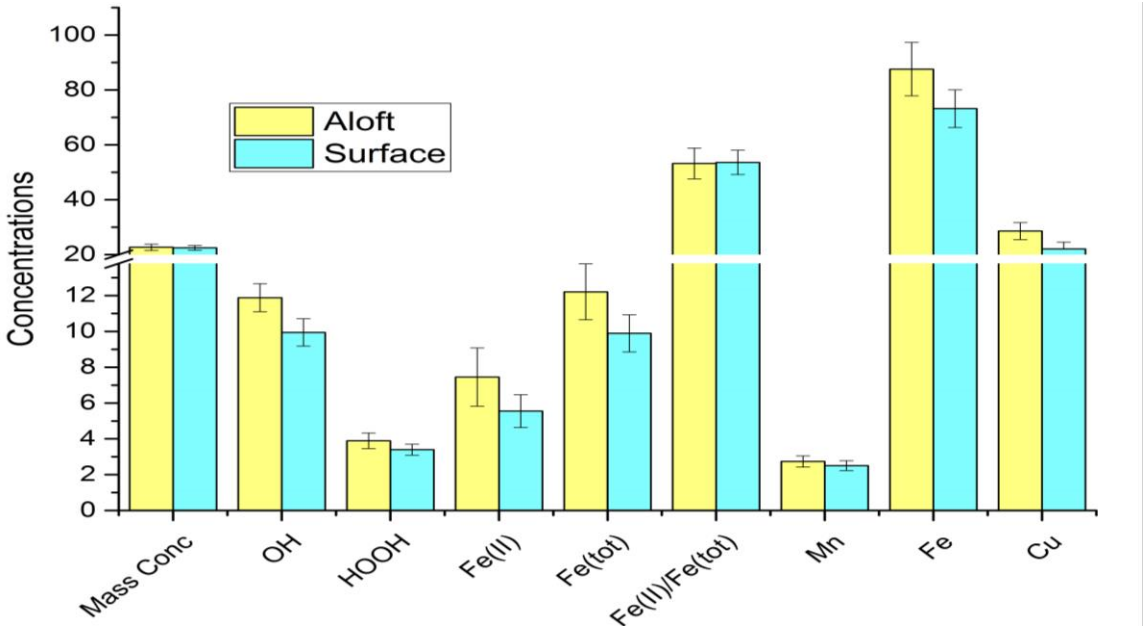

Fig. 3.6 Average concentrations of ROS and soluble metal concentrations for air masses arriving from aloft (yellow) and those travelled along the surface (light blue) Error bars represent standard errors.

3.3.6 Relationships between speciated iron, trace metals and mass

Significant correlations between aerosol mass and soluble metals are shown in Fig. 3.7; all statistics are shown in Tab. 3.4. Generally, mass correlations were only moderate ($r^2 < 0.36$), the strongest correlation is with Cu (Fig. 3.7, $r^2 = 0.46$). These data seem to show different trends for each time of day (Fig. 3.7a).

Fe and Cu were significantly well correlated with the other trace metals (at 95% confidence level), with the highest correlations between Fe and Mn, with correlation coefficient (r) of 0.91 (Tab. 3.3). The same correlations between metals are also reported by Zhou et al., (2014). These colinearities suggest that the trace metals may originate from the same sources. Using correlation coefficient and principle component analysis, Zhou et al., (2014) concluded Cu, Fe, Mn Zn and Pb originated from vehicular traffic emissions.

Tab. 3.3 Correlations between soluble trace metals. Correlation coefficients (r) are shown for the entire data set. Bold and red values indicate a p-value < 0.05.

	V	Cr	Mn	Fe	Ni	Cu	Zn	Se	Pb
V	1.00	0.26	0.24	**0.32**	0.18	**0.64**	0.13	**0.45**	**0.30**
Cr		1.00	**0.74**	**0.78**	**0.46**	**0.51**	0.29	0.20	0.22
Mn			1.00	**0.91**	0.09	**0.59**	**0.50**	0.12	**0.32**
Fe				1.00	0.07	**0.78**	**0.39**	**0.30**	**0.31**
Ni					1.00	0.05	0.08	-0.05	-0.06
Cu						1.00	0.26	**0.44**	**0.43**
Zn							1.00	0.10	0.39
Se								1.00	**0.37**
Pb									1.00

Tab. 3.4 Correlations between mass and non-mass corrected ROS concentration, and iron speciation, Claremont for 2 hour extractions. m is slope of the regression line. Orange, light blue and dark blue values represent morning, afternoon and nighttime correlations, respectively; and black values represent the entire data set.

		Mass (mg)		OH (nmol)	H_2O_2 (nmol)		Fe(II) (nmol)				Fe(tot) (nmol)	
OH (nmol	r^2	0.57										
	p	0										
	m	5.01										
H_2O_2 (nmol	r^2	0.19		0.16			0.5	0.52	0.3		0.57	0.5
	p	0.002		0.00			0	0.00	0.0		0	0.0
	m	0.69		1.63			0.2	0.19	0.1		0.19	0.1
Fe(III (nmol	r^2	0.41	0.39	0.36								
	p	0	0.04	0								
	m	2.24	5.02	1.12								
Fe(tot (nmol	r^2	0.23	0.41				0.6	0.87	0.5	0.51		
	p	0	0.03				0	0	0	0		
	m	3.02	6.73				0.9	1.03	2.1	0.56		
Fe(II) Fe(tot	r^2				0.13	0.3						
	p				0.02	0.0						
	m				0.64	0.7						

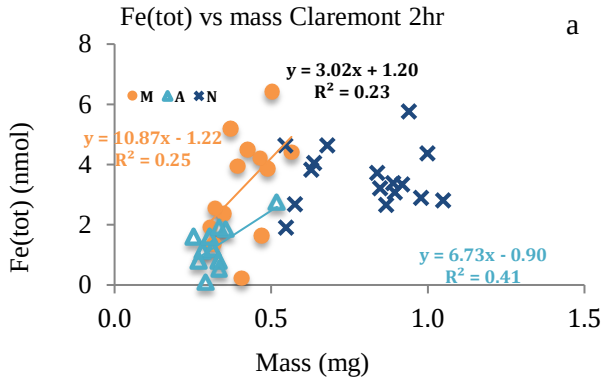

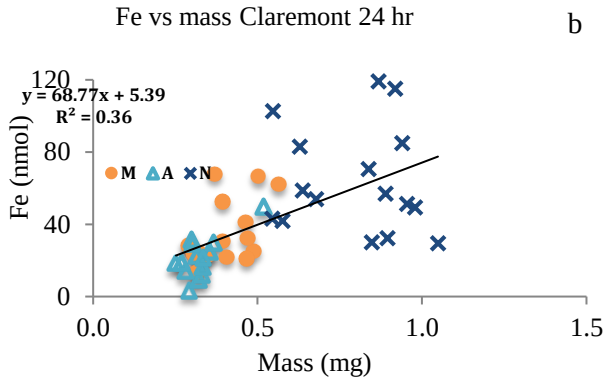

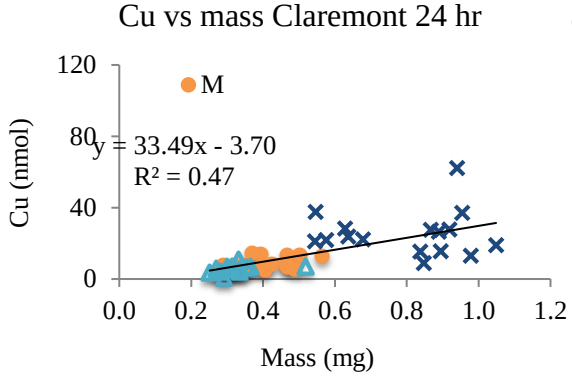

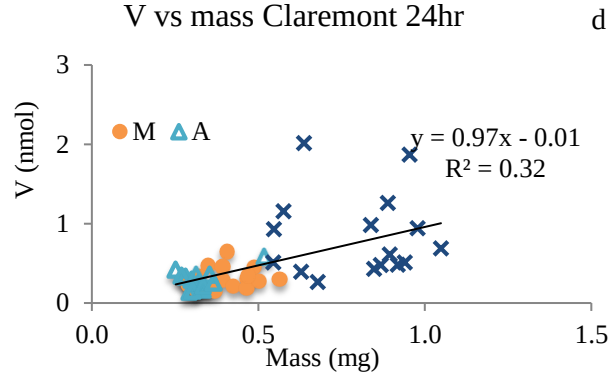

Fig. 3.7 Relationships betwee aerosol mass, speciated iron and trace metal concentrations in pH3.5 extraction solution at 2 hours, Claremont. Circles (M), triangles (A) and crossess (N) represent morning, afternoon and overnight samples, respectively.

3.3.6.1 Hydrogen peroxide

H_2O_2 concentrations were the highest in the morning samples for both 2 and 24 hours. They decreased slightly (23 and 25%) for morning and overnight samples at 24 hours, respectively, and more dramatically (~70%) for the afternoon samples, suggesting H_2O_2 reached a maximum well before 24 hrs, as observed in Wang et al., (2012), for H_2O_2 generation by fine PM collected at UCLA. In general, H_2O_2 formation by ambient fine aerosols measured in this study was much lower compared to most other measurements (Table 3.5). This is at least partly due to the storage of the filters (about 2 years) resulting in some loss of reactivity.

The H_2O_2 concentration is controlled by the balance of its production and destruction reactions (R1-R3), which can be impacted by average ligands substantially. This could potentially be attributed to the Fenton reaction (R3.1a), together with the observation that OH increased significantly at 24 hours for the afternoon samples (Fig. 3.1a). The differences in production of H_2O_2 at 2 hours and 24 hours are statistically insignificant for all samples except the afternoon samples (p=0.03).

Tab. 3.5 Comparison of H_2O_2 concentrations

Particle Type	Season	Extraction solution	nmol/mg	Reference
PM_4, Claremont, CA	Summer	pH3.5	3.6±0.2	This study
PM_4, Fresno, CA	Winter	pH3.5	3.1±0.3	This study
$PM_{2.5}$, Fresno		Phosphate buffer	20	Shen et al., 2011b
$PM_{2.5}$, I-110 Freeway			12.4±8.8	Arellanes et al., 2006
$PM_{2.5}$, UCLA		pH3.5 w/ 0.1mM EDTA	17.1±0.9	
$PM_{2.5}$, Riverside campus	Summer	pH3.5 w/ 0.1mM EDTA	27.9±0.20	Wang et al., 2012

CRCAES, Riverside	Summer		14.4±16.2	(Wang et al., 2012)
$PM_{2.5}$, UCLA			3.2±2.1	
α-pinene SOA		pH3.5 w/ 0.1mM EDTA	27.4±10.5	
β-pinene SOA			62.3±43.5	

3.3.6.2 Kinetics of H_2O_2

Concentration of H_2O_2 was measured every 30 minutes in the first 2 hours after extraction to assess the initial rate of H_2O_2 formation. The behavior of the kinetics of H_2O_2 formation was best described by a second order polynomial function, with 73% of the samples exhibited a concave downward behavior and 27% were convexing, examples are shown in Fig. 3.8a. The initial rate of H_2O_2 formation with the concave behavior was estimated by fitting the data to a second order polynomial function and taking the derivative at time = 0 min, and the average initial rate was found to be 3.7 ± 2.8 nM/min. This value is comparable to H_2O_2 formation by ambient fine particulate matter reported by Wang et al., (2012), with the average of 5.9 ± 2.8 nM/min.

Significant H_2O_2 has formed at 30 min, the initial point of our measurement. This implies that the formation of H_2O_2 was rather rapid before 30 mins, and our current initial rate value underestimates the actual rate of H_2O_2 formation. To address this information, additional measurement of the kinetics of H_2O_2 formation was performed (Fig. 3.8b); H_2O_2 was measured every minute for the 10 minutes, then every 5 minutes up to 60 minutes, and finally every 10 minutes to 2 hours. The initial rate estimated with the inclusion of the first 30 minute time points was significantly higher (~ 9 nM/min) compared to those with the first measurement taken at 30 mins.

H_2O_2 and OH formation begins with the reduction of oxygen to form superoxide anion and subsequently forming H_2O_2 and in the presence of metals, OH can be formed via Fenton and Fenton-like reactions. Since H_2O_2 serves as an intermediate species, it is likely that H_2O_2 is in steady state because H_2O_2 are formed and destroyed at significant rates. The observation that the rate of H_2O_2 formation is more rapid in the first 30 min than the later time points may suggest the H_2O_2 formation is more important initially then gradually being destroyed.

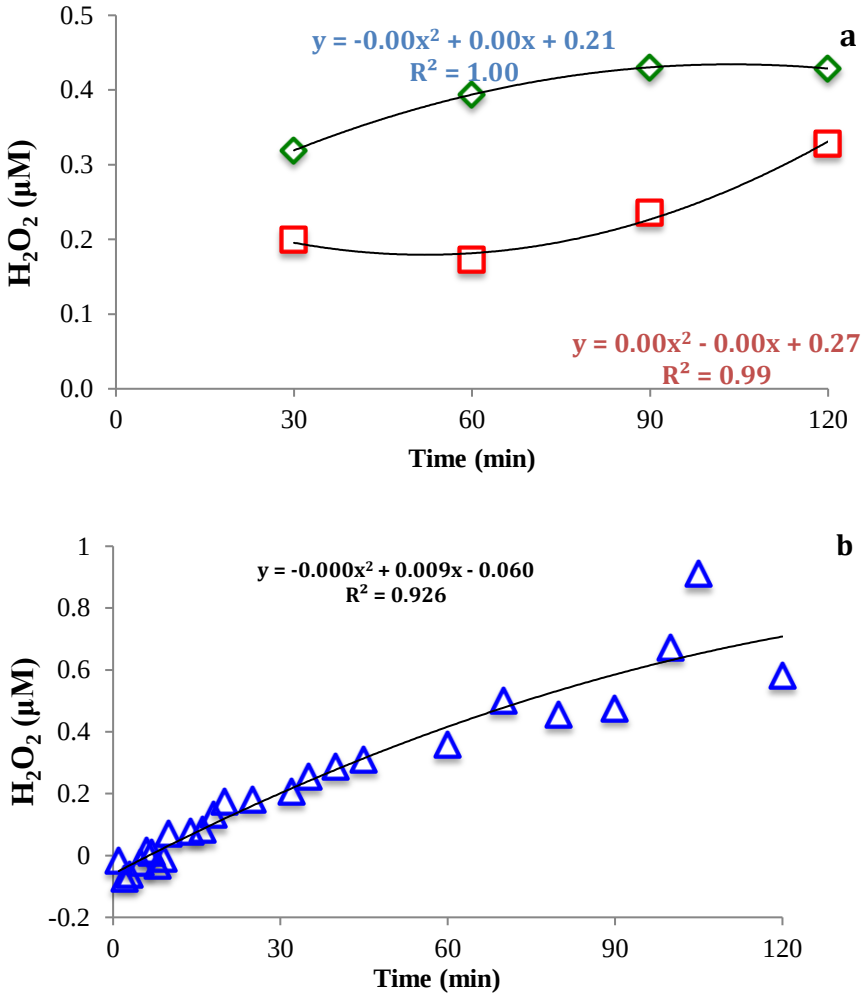

Fig. 3.8 Examples of kinetics of H_2O_2 formation by ambient fine PM in the first 2 hours: a) lower time resolution and b) higher time resolution.

3.3.6.3 Correlations between H_2O_2, mass and transition metals

H_2O_2 is weakly correlated with aerosol mass (r^2= 0.19, Fig. 3.9a). Of the ICP transition metals, H_2O_2 was most correlated with Mn (Fig. 3.9d), followed by Fe (Fig 3.9c), Pb and Cu (Figs. 3.9g and h). This relationship is strongest between H_2O_2 and total soluble Fe (r^2 = 0.57), slightly weaker relationships with $Fe(II)_{fzn}$ was observed (Fig 3.10g). There was no significant relationship between the oxidation state of the soluble Fe ($Fe(II)_{fzn}/Fe(tot)_{fzn}$) and H_2O_2 (Fig. 3.10h). Although speciated soluble Fe was measured on samples within hours of collection and H_2O_2 after samples had been frozen and stored, and it is not known how stable the oxidation state is under such conditions.

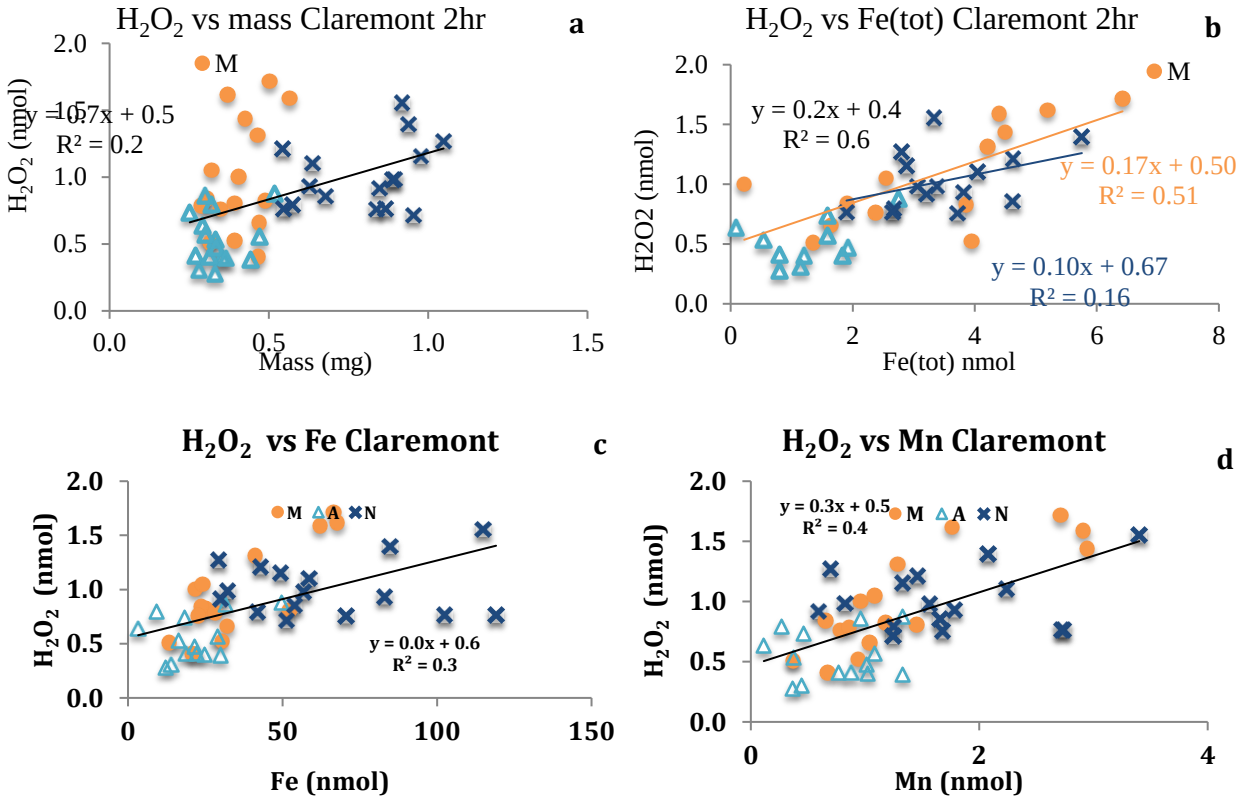

Fig. 3.9 Relationships betwee H_2O_2, aerosol mass, speciated iron and trace metal concentrations in pH3.5 extraction solution at 2 hours, Claremont. Circles (M), triangles (A) and crossess (N) represent morning, afternoon and overnight samples, respectively.

a

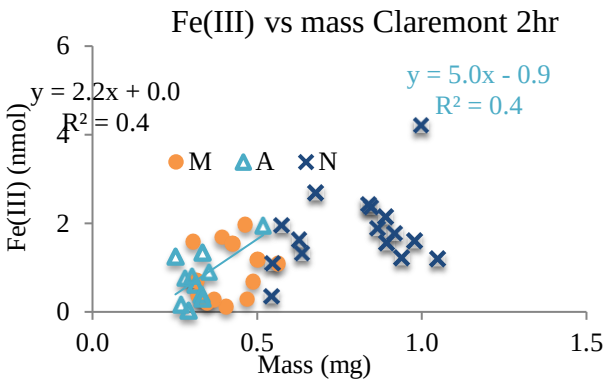
Fe(III) vs mass Claremont 2hr
y = 2.2x + 0.0
R² = 0.4
y = 5.0x - 0.9
R² = 0.4
M
A
N
Fe(III) (nmol)
Mass (mg)

b

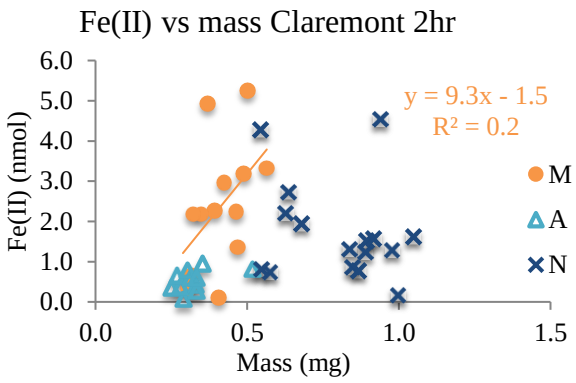
Fe(II) vs mass Claremont 2hr
y = 9.3x - 1.5
R² = 0.2
M
A
N
Fe(II) (nmol)
Mass (mg)

c

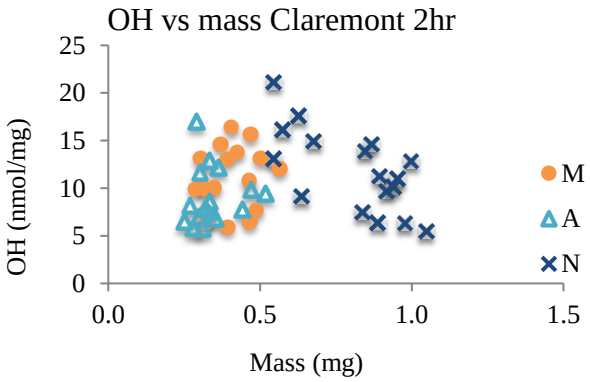
OH vs mass Claremont 2hr
M
A
N
OH (nmol/mg)
Mass (mg)

d

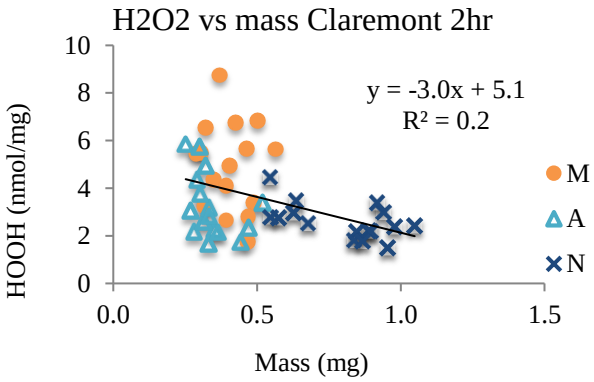
H2O2 vs mass Claremont 2hr
y = -3.0x + 5.1
R² = 0.2
M
A
N
HOOH (nmol/mg)
Mass (mg)

e

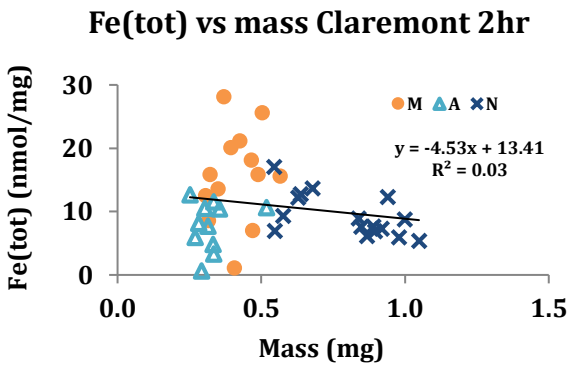
Fe(tot) vs mass Claremont 2hr
M
A
N
y = -4.53x + 13.41
R² = 0.03
Fe(tot) (nmol/mg)
Mass (mg)

f

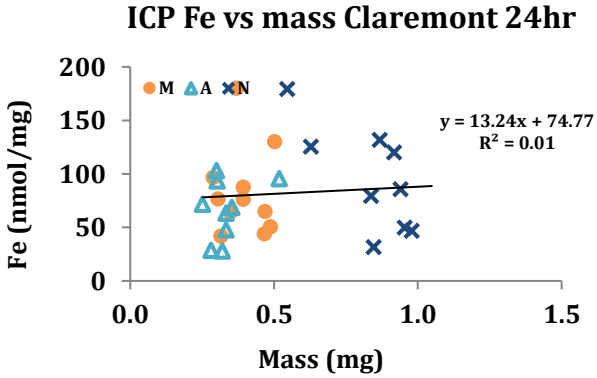
ICP Fe vs mass Claremont 24hr
M
A
N
y = 13.24x + 74.77
R² = 0.01
Fe (nmol/mg)
Mass (mg)

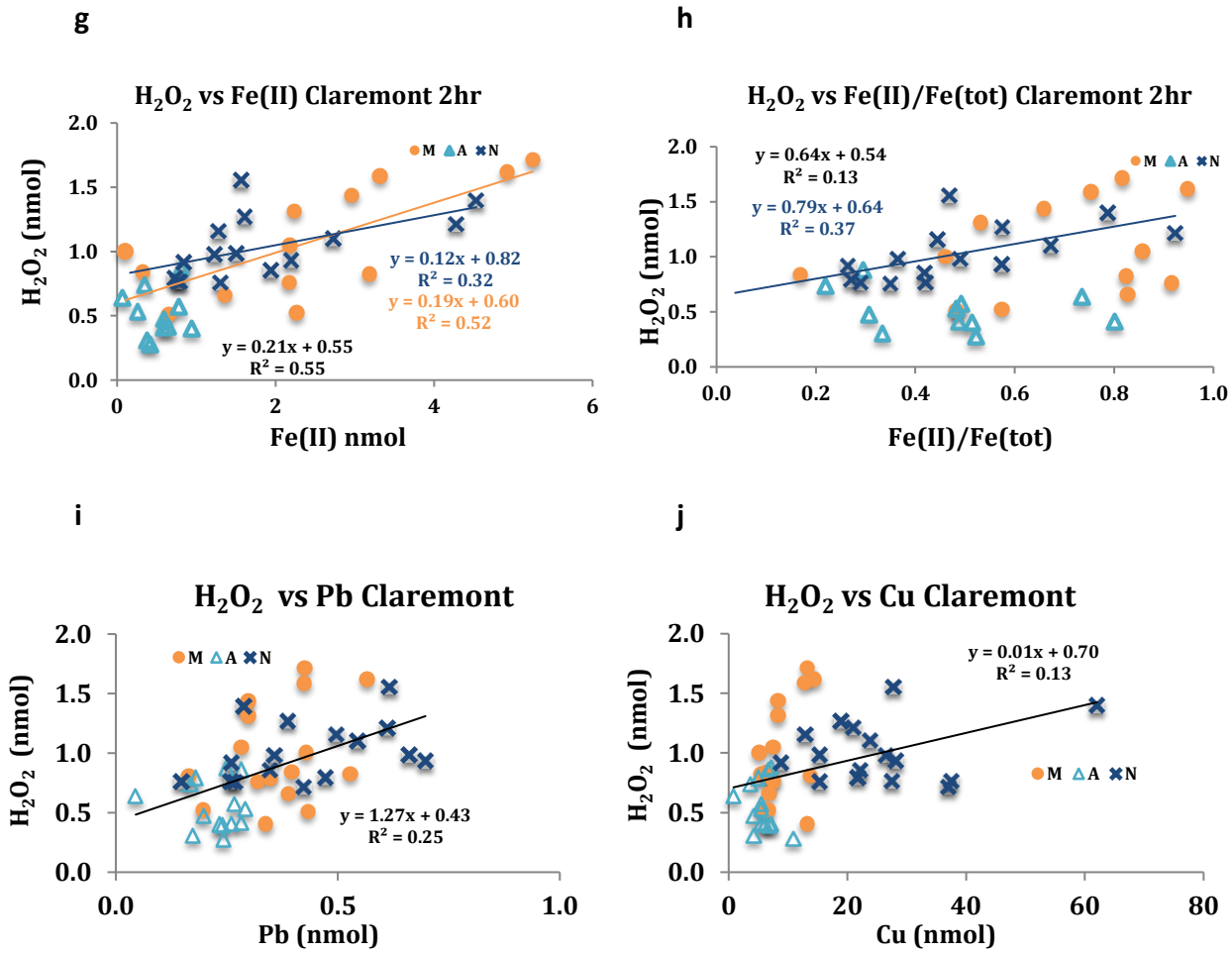

Fig. 3.10 Relationships betwee ROS, aerosol mass, speciated iron and trace metal concentrations in pH3.5 extraction solution at 2 hours, Claremont. Circles (M), triangles (A) and crossess (N) represent morning, afternoon and nighttime samples, respectively.

3.3.6.4 Hydroxyl radicals (OH)

OH production increased for both locations for all samples. The increase in OH concentration is more pronounced in the afternoon samples (over 200% increase) followed by morning and overnight samples (167 and 137% increase, respectively). The OH production at 2 and 24 hours are significantly different for all samples.

OH formation by ambient fine aerosols was comparable to other studies using extraction solutions without an electron donor (Tab. 3.6). Shen et al. (2011) showed that formation of H_2O_2

was much higher than OH for the same sample set. OH formation was negligible mass normalized in the absence of ascorbate. However, we observed higher OH formation compared to H_2O_2 in our study. Since we measured cumulative concentration of OH and steady state concentration of H_2O_2, it is difficult to make direct comparisons for these two measurements.

Tab. 3.6 Comparison of OH concentrations.

Particle Type	Season	Extraction solution	nmol/mg	Reference
$PM_{2.5}$, Claremont	Summer	pH3.5	15.9±5.9	This study
$PM_{2.5}$, Fresno	Winter	pH3.5	22.9±19.4	This study
$PM_{2.5}$, Fresno	Summer 06	Phosphate buffer	3.5±2.9	
$PM_{2.5}$, Fresno	Summer 08	Phosphate buffer	2.9±1.8	
$PM_{2.5}$, Fresno	Winter 07	Phosphate buffer	2.9±3.5	
$PM_{2.5}$, Fresno	Winter 09	Phosphate buffer	5.9±1.8	Shen et al., 2011a
$PM_{2.5}$, Westside	Summer 07	Phosphate buffer	2.9±4.1	
$PM_{2.5}$, Westside	Winter 08	Phosphate buffer	1.8±1.8	
$PM_{2.5}$, Davis		Phosphate buffer	21.1±15.6	
Carbon Black		+1mM H_2O_2	8.8±0.3	Jung et al., 2006
Flaming Soot			0.1±0.03	

3.3.6.5 Kinetics of OH

Similar to H_2O_2, the earliest OH measurement was taking at a rather long time point, at 20 mins, when significant amount of OH was already formed (e.g. Fig. 3.11). The rate of OH formation between 20 and 120 min was mostly linear, with an average of 1.9 ± 1.1 nM/min. However, later analysis with higher time resolution showed a substantial different behavior (Fig. 3.11), in which the OH formation rate exhibited a biphasic behavior. OH concentration increases abruptly from 1 s to 1 min, stays fairly constant up to 20 mins and then increases fairly slowly from 20 min to 2 hr. In most cases, > 60% of OH at 2 hours was formed at 20 mins, suggesting the chemical reactions forming OH happen almost instantaneously. This is

in good agreement with the observation that hydrogen peroxide concentration is negative in the first 10 mins or so (Fig. 3.8b), potentially due to the conversion of H_2O_2 to OH.

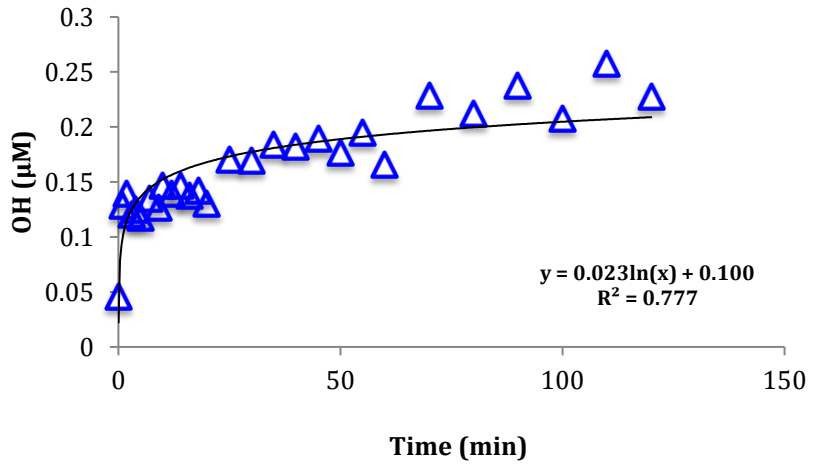

Fig. 3.11 Examples of kinetics of H_2O_2 formation by ambient fine PM in the first 2 hours: a) lower time resolution and b) higher time resolution.

3.3.6.6 Correlations between OH, mass and transition metals

Aerosol mass was a good predictor for OH formation (r^2 = 0.57). It is a much weaker predictor for H_2O_2 (r^2 = 0.19) and iron measured with the ferrozine assay (r^2 = 0.23) (Table 3.4). OH showed weaker correlations with speciated iron and Mn than H_2O_2 but stronger correlations with ICP Fe and Cu (Fig. 3-12). Of the transition metals, OH was most correlated with Cu, with an r^2 value (0.53); that's comparable with mass. The strong correlations between OH formation and Cu and Fe suggest that Fenton and Fenton-like reactions are the primary source of OH produced by ambient particles.

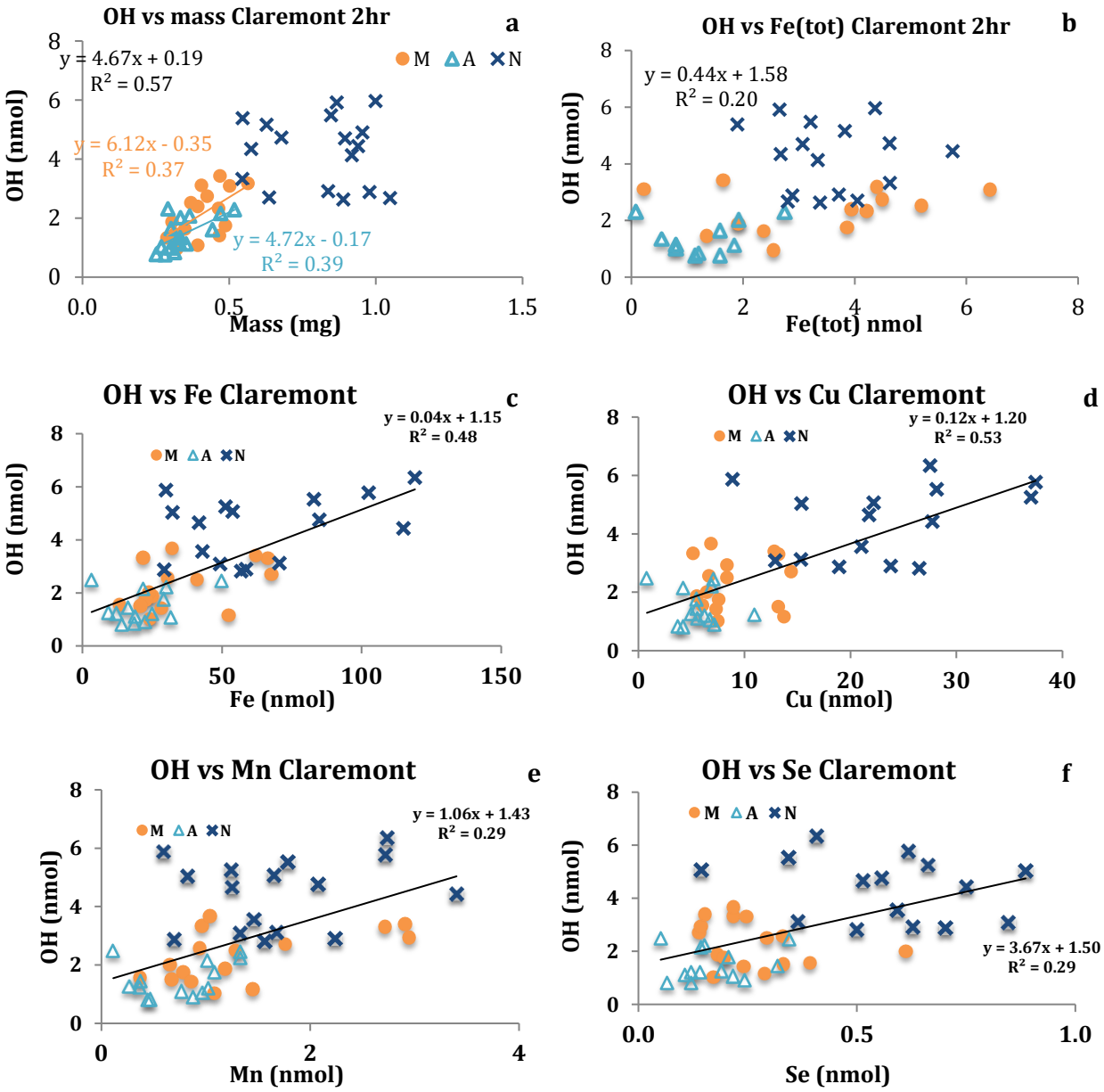

Fig. 3.12 Relationships between OH, aerosol mass, speciated iron and trace metal concentrations in pH3.5 extraction solution at 2 hours, Claremont. Circles (M), triangles (A) and crossess (N) represent morning, afternoon and overnight samples, respectively.

Multivariate regressions of OH and H_2O_2 formation and chemical components are shown in Fig. 3.13. Only regressions with variables with p-values less than 0.05 for all species are shown. OH and H_2O_2 regressions have adjusted r^2 of 0.54 and 0.63, respectively. The H_2O_2 value is slightly better than the realtionship for Fe. Equations derived from the multilinear regression

for OH and H_2O_2 are shown in Tab. 3.7. Fig. 3.14 shows the contribution of each component to ROS formation, Fe, wether measured by the ICP or the ferrozine method, has the highest contribution to ROS formation. Fe(II) and Mn were found to be the most significant contributors to H_2O_2 formation while Fe and Cu were more important in OH formation.

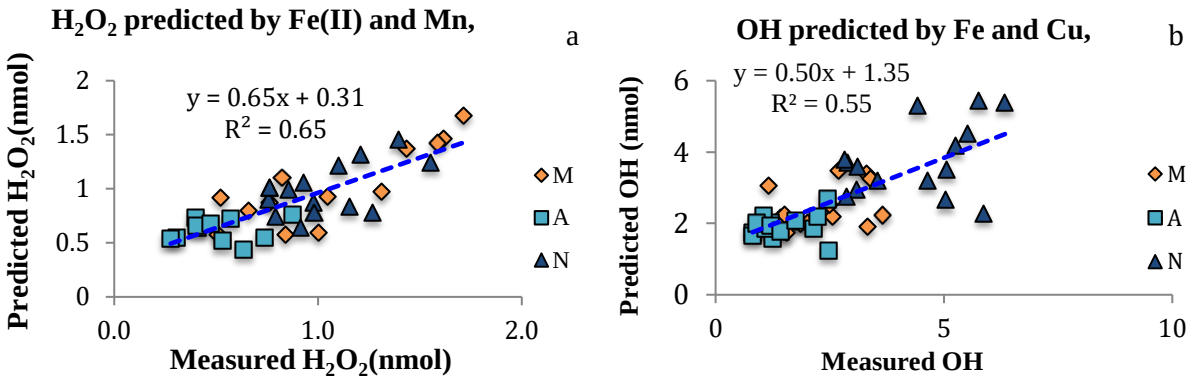

Fig. 3.13 Multivariate regressions for hydrogen peroxide and OH in Claremont.

Tab. 3.7 Equations derived from multivariate regression for H_2O_2 and OH.

	H_2O_2	OH
Claremont	0.4 + 0.2 * [Mn] + 0.15* [Fe(II)]	1.1 + 0.02 * [Fe] + 0.05 *[Cu]

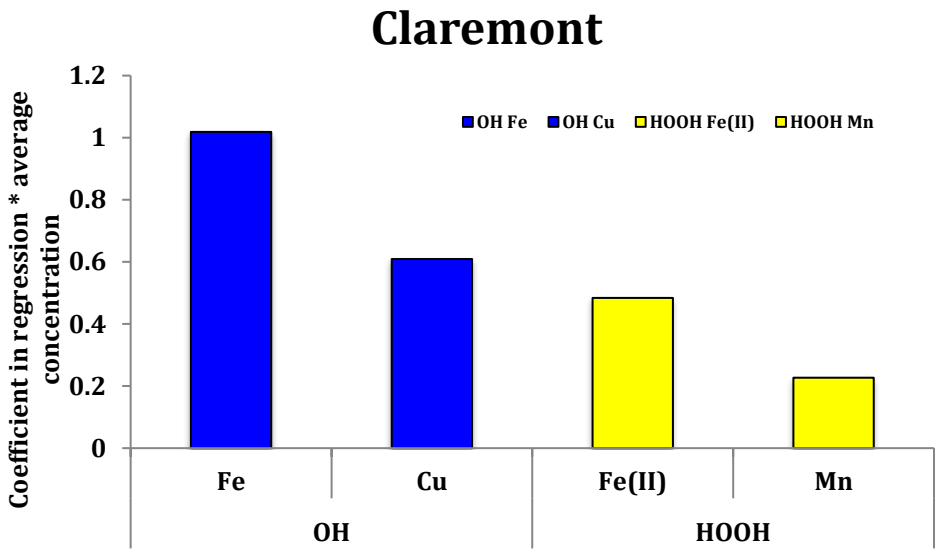

Fig. 3.14 Contribution of each chemical component (multivariate regression coefficient x average concentration of the component) to ROS formation.

3.4 Atmospheric Implication.

In this study, soluble transition metals, H_2O_2 and OH generation by summertime fine PM collected in Claremont, CA were measured simultaneously. Transition metal ions, particularly iron, are known to catalyze sulfur oxidation in cloud and rain droplets. Knowledge on the oxidation states of iron would shed light on its participation in producing reactive oxygen species. Further, the ability of particles to generate ROS in the dark suggests that in addition to nitrate radicals, a major oxidant in the atmosphere at night, H_2O_2 and OH may play an important role in oxidation of organic pollutants in the absence of photochemistry.

Reference

Alessandrini, F., I. Beck-Speier, D. Krappmann, I. Weichenmeier, S. Takenaka, E. Karg, B. Kloo, H. Schulz, T. Jakob, M. Mempel, H. Behrendt (2009). Role of Oxidative Stress in Ultrafine Particle-Induced Exacerbation of Allergic Lung Inflammation. Am J Respir Crit Care Med 179.10.1164/rccm.200807-1061OC.

Arellanes, C., S. E. Paulson, P. M. Fine, C. Sioutas (2006). Exceeding of Henry's law by hydrogen peroxide associated with urban aerosols. Env. Sci. Tech. 40:4859-4866,

Arellanes, C., S. E. Paulson, P. M. Fine, C. Sioutas (2006). Exceeding of Henry's Law by Hydrogen Peroxide Associated with Urban Aerosols. . Env. Sci. Tech.:DOI: 10.1021/es0513786.DOI: 10.1021/es0513786.

Asa-Awuku, A., R. H. Moore, A. Nenes, R. Bahreini, J. S. Holloway, C. A. Brock, A. M. Middlebrook, T. B. Ryerson, J. L. Jimenez, P. F. DeCarlo, A. Hecobian, R. J. Weber, R. Stickel, D. J. Tanner, L. G. Huey (2011). Airborne cloud condensation nuclei measurements during the 2006 Texas Air Quality Study. Journal Of Geophysical Research-Atmospheres 116.10.1029/2010jd014874.

Buxton, G. V., C. L. Greenstock, W. P. Helman, A. B. Ross (1988). Critical review of rate constants for reactions of hydrated electrons, hydrogen atoms and hydroxyl radicals (· OH/· O− in aqueous solution. Journal of Physical and Chemical Reference Data 17:513-886,

Chen, R. and J. J. Pignatello (1997). Role of quinone intermediates as electron shuttles in Fenton and photoassisted Fenton oxidations of aromatic compounds. Env. Sci. Tech. 31:2399-2406.

Chung, M. Y., R. A. Lazaro, D. Lim, J. Jackson, J. Lyon, D. Rendulic, A. S. Hasson (2006). Aerosol-borne quinones and reactive oxygen species generation by particulate matter extracts. Env. Sci. Tech. 40:4880-4886.10.1021/es0515957.

Deguillaume, L., M. Leriche, K. Desboeufs, G. Mailhot, C. George, N. Chaumerliac (2005). Transition metals in atmospheric liquid phases: Sources, reactivity, and sensitive parameters. Chem. Rev. 105:3388-3431, <Go to ISI>://000231916100008

Donahue, N. M., K. M. Henry, T. F. Mentel, A. Kiendler-Scharr, C. Spindler, B. Bohn, T. Brauers, H. P. Dorn, H. Fuchs, R. Tillmann (2012). Aging of biogenic secondary organic aerosol via gas-phase OH radical reactions. Proceedings of the National Academy of Sciences 109:13503-13508,

Duesterberg, C. K. and T. D. Waite (2007). Kinetic modeling of the oxidation of p-hydroxybenzoic acid by Fenton's reagent: implications of the role of quinones in the redox cycling of iron. Environmental science & technology 41:4103-4110,

Engelhart, G., A. Asa-Awuku, A. Nenes, S. Pandis (2008). CCN activity and droplet growth kinetics of fresh and aged monoterpene secondary organic aerosol. Atmospheric Chemistry and Physics 8:3937-3949,

Faust, B. C. and J. M. Allen (1993). AQUEOUS-PHASE PHOTOCHEMICAL FORMATION OF HYDROXYL RADICAL IN AUTHENTIC CLOUDWATERS AND FOGWATERS. Environmental science & technology 27:1221-1224.10.1021/es00043a024.

Gibbs, C. R. (1976). Characterization and application of ferrozine iron reagent as a ferrous iron indicator. Anal. Chem. 48:1197-1201,

Gonzalez, D. H., C. K. Cala, S. E. Paulson (Submitted). HULIS Enhancement of OH by Fe(II): Kinetics of Suwannee RIver Fulvic Acid-Fe(II) Complexes in the Presence of Lung Antioxidants. Env. Sci. Tech.,

Graedel, T., M. Mandich, C. Weschler (1986). Kinetic model studies of atmospheric droplet chemistry: 2. Homogeneous transition metal chemistry in raindrops. Journal of Geophysical Research: Atmospheres 91:5205-5221,

Hasheminassab, S., N. Daher, A. Saffari, D. Wang, B. Ostro, C. Sioutas (2014). Spatial and temporal variability of sources of ambient fine particulate matter (PM 2.5) in California. Atmospheric Chemistry and Physics 14:12085-12097,

Hasson, A. S. and S. E. Paulson (2003). An Investigation of the Relationship between Gas-phase and Aerosol-borne Hydroperoxides in Urban Air. J. Aerosol Sci. 34: 459-468,

Hu, S., A. Polidori, M. Arhami, M. Shafer, J. Schauer, A. Cho, C. Sioutas (2008). Redox activity and chemical speciation of size fractioned PM in the communities of the Los Angeles-Long Beach harbor. Atmospheric Chemistry and Physics 8:6439-6451,

Jung, H., B. Guo, C. Anastasio, I. M. Kennedy (2006). Quantitative measurements of the generation of hydroxyl radicals by soot particles in a surrogate lung fluid. Atmos. Environ. 40:1043-1052, <Go to ISI>://000235784800004

Kim, H., S. Liu, L.M. Russell, and S.E. Paulson, (2014). Real refractive indices and elemental composition of secondary organic aerosol generated from ozonolysis and photooxidation of limonene and α-pinene. . Aerosol Science and Technology. 48:498 - 507. .10.1080/02786826.2014.893278.

Kuang, X. M., J. A. Scott, G. O. da Rocha, R. Betha, D. J. Price, L. M. Russell, D. R. Cocker, S. E. Paulson (2017). Hydroxyl radical formation and soluble trace metal content in particulate matter from renewable diesel and ultra-low sulfur diesel in at-sea operations of a research vessel. Aerosol Sci. Tech.:1-12,

Majestic, B., J. Schauer, M. Shafer (2007). Application of synchrotron radiation for measurement of iron red-ox speciation in atmospherically processed aerosols. Atmospheric Chemistry and Physics 7:2475-2487,

Majestic, B. J., J. J. Schauer, M. M. Shafer, J. R. Turner, P. M. Fine, M. Singh, C. Sioutas (2006). Development of a wet-chemical method for the speciation of iron in atmospheric aerosols. Env. Sci. Tech. 40:2346-2351.10.1021/es052023p.

Manousakas, M., H. Papaefthymiou, K. Eleftheriadis, K. Katsanou (2014). Determination of water-soluble and insoluble elements in PM 2.5 by ICP-MS. Sci. Total Environ 493:694-700,

Oakes, M., N. Rastogi, B. J. Majestic, M. Shafer, J. J. Schauer, E. S. Edgerton, R. J. Weber (2010). Characterization of soluble iron in urban aerosols using near-real time data. Journal Of Geophysical Research-Atmospheres 115.10.1029/2009jd012532.

Oakes, M., R. J. Weber, B. Lai, A. Russell, E. D. Ingall (2012). Characterization of iron speciation in urban and rural single particles using XANES spectroscopy and micro X-ray fluorescence measurements: investigating the relationship between speciation and fractional iron solubility. Atmospheric Chemistry and Physics 12:745-756.10.5194/acp-12-745-2012.

Oakes, M., R. J. Weber, B. Lai, A. Russell, E. D. Ingall (2012). Characterization of iron speciation in urban and rural single particles using XANES spectroscopy and micro X-ray fluorescence measurements: investigating the relationship between speciation and fractional iron solubility. Atmos. Chem. Phys. 12:745-756.10.5194/acp-12-745-2012.

Pandis, S. N. and J. H. Seinfeld (1989). Sensitivity analysis of a chemical mechanism for aqueous‐phase atmospheric chemistry. Journal of Geophysical Research: Atmospheres 94:1105-1126,

Paulson, S. E., A. Hasson, C. Anastasio, Xiaobi M. Kuang, J. Adlin Scott, David H. Gonzalez-Martinez, Tiffany Charbouillot , Kennedy K-T Vu, James Baroi, Catalina Olea, Annabelle Lolinco and Kylie Markarian, Jessica G. Charrier, Alexander S. McFall, N. K. Richards-Henderson (2016). Probing the Intrinsic Ability of Particles to Generate Reactive Oxygen Species and the Effect of Physiologically Relevant Solutes. Calif. Air Resources Board Annu. Report, https://www.arb.ca.gov/research/apr/past/10-314-2.pdf

Saffari, A., N. Daher, C. Samara, D. Voutsa, A. Kouras, E. Manoli, O. Karagkiozidou, C. Vlachokostas, N. Moussiopoulos, M. M. Shafer (2013). Increased biomass burning due to the economic crisis in Greece and its adverse impact on wintertime air quality in Thessaloniki. Env. Sci. Tech. 47:13313-13320.

Sato, K., S. Nakao, C. H. Clark, L. Qi, D. R. Cocker Iii (2011). Secondary organic aerosol formation from the photooxidation of isoprene, 1, 3-butadiene, and 2, 3-dimethyl-1, 3-butadiene under high NO x conditions. Atmos. Chem. Phys. 11:7301-7317.

See, S. W., Y. H. Wang, R. Balasubramanian (2007). Contrasting reactive oxygen species and transition metal concentrations in combustion aerosols. Environ. Res, 103:317-324.

Shafer, M. M., D. A. Perkins, D. S. Antkiewicz, E. A. Stone, T. A. Quraishi, J. J. Schauer (2010). Reactive oxygen species activity and chemical speciation of size-fractionated atmospheric particulate matter from Lahore, Pakistan: an important role for transition metals. Journal of Environmental Monitoring 12:704-715.

Shang, Y., C. Chen, Y. Li, J. Zhao, T. Zhu (2012). Hydroxyl radical generation mechanism during the redox cycling process of 1, 4-naphthoquinone. Env. Sci. Tech. 46:2935-2942.

Shen, H., A. I. Barakat, C. Anastasio (2011). Generation of hydrogen peroxide from San Joaquin Valley particles in a cell-free solution. Atmospheric Chemistry and Physics 11:753-765.10.5194/acp-11-753-2011.

Shen, H. and C. Anastasio (2012). A comparison of hydroxyl radical and hydrogen peroxide generation in ambient particle extracts and laboratory metal solutions. Atmos. Environ. 46:665-668.http://dx.doi.org/10.1016/j.atmosenv.2011.10.006.

Shilling, J. E., S. M. King, M. Mochida, S. T. Martin (2007). Mass spectral evidence that small changes in composition caused by oxidative aging processes alter aerosol CCN properties. J. Phys. Chem. A 111:3358-3368.10.1021/jp068822r.

Shrivastava, M. K., T. E. Lane, N. M. Donahue, S. N. Pandis, A. L. Robinson (2008). Effects of gas particle partitioning and aging of primary emissions on urban and regional organic aerosol concentrations. J. Geophys. Res., [Atmos.] 113.

Stookey, L. L. (1970). FERROZINE - A NEW SPECTROPHOTOMETRIC REAGENT FOR IRON. Anal. Chem. 42:779.

Suda, S. R., M. D. Petters, G. K. Yeh, C. Strollo, A. Matsunaga, A. Faulhaber, P. J. Ziemann, A. J. Prenni, C. M. Carrico, R. C. Sullivan, S. M. Kreidenweis (2014). Influence of Functional Groups on Organic Aerosol Cloud Condensation Nucleus Activity. Environmental Science & Technology 48:10182-10190.10.1021/es502147y.

Upadhyay, N., B. J. Majestic, P. Herckes (2011). Solubility and speciation of atmospheric iron in buffer systems simulating cloud conditions. Atmospheric Environment 45:1858-1866.

Valavanidis, A., K. Fiotakis, E. Bakeas, T. Vlahogianni (2005). Electron paramagnetic resonance study of the generation of reactive oxygen species catalysed by transition metals and quinoid redox cycling by inhalable ambient particulate matter. Redox Report 10:37-51.

Vidrio, E., H. Jung, C. Anastasio (2008). Generation of hydroxyl radicals from dissolved transition metals in surrogate lung fluid solutions. Atmospheric Environment 42:4369-4379.

Wang, Y., C. Arellanes, D. Curtis, S. E. Paulson (2010). Probing the Source of Hydrogen Peroxide Generation by Coarse Mode Aerosols in Southern California. Env. Sci. Tech. 44:4070-4075.10.1021/es100593k.

Wang, Y., C. Arellanes, S. E. Paulson (2012). Hydrogen peroxide associated with ambient fine-mode, diesel, and biodiesel aerosol particles in Southern California. Aerosol Sci.Technol. 46:394-402.

Xia, T., P. Korge, J. N. Weiss, N. Li, M. I. Venkatesen, C. Sioutas, A. Nel (2004). Quinones and aromatic chemical compounds in particulate matter induce mitochondrial dysfunction: implications for ultrafine particle toxicity. Environ. Health Perspect.:1347-1358.

Yamamoto, M., A. Nishida, K. Otsuka, T. Komai, M. Fukushima (2010). Evaluation of the binding of iron (II) to humic substances derived from a compost sample by a colorimetric method using ferrozine. Bioresource technology 101:4456-4460.

Zhang, Y., J. J. Schauer, M. M. Shafer, M. P. Hannigan, S. J. Dutton (2008). Source apportionment of in vitro reactive oxygen species bioassay activity from atmospheric particulate matter. Env. Sci. Tech. 42:7502-7509.

4. Assessing contribution of particulate matter components to formation of hydroxyl radical and hydrogen peroxide by aerosols under atmospherically relative conditions

4.1 Introduction

Reactive Oxygen Species include hydroxyl radical (OH), superoxide anion ($O_2^{\cdot -}$), hydrogen peroxide (H_2O_2), hydroperoxyl radicals (HO_2), organic peroxyl radicals (RO_2) and organic peroxides. ROS are important oxidants in natural water systems, including aerosols, clouds and surface waters. OH is the most reactive, able to react with a variety of organic compounds at diffusion-controlled rates (Buxton et al., 1988), and modifies aerosol composition by contributing significantly to secondary organic aerosol formation (SOA) (Baker et al., 2005; Tan et al., 2012), and the degradation of organic contaminants (Neyens and Baeyens 2003; Pignatello et al., 2006).

A number of studies have suggested transition metals are capable of producing ROS (Charrier et al., 2014; Charrier and Anastasio 2015; See et al., 2007; Shafer et al., 2010; Wang et al., 2012). While the reactions that govern the concentrations of ROS are not well understood, a few important reaction categories that will likely to contribute are as follows (Deguillaume et al., 2005). The reactions are illustrated with iron, however many can also be mediated by other transition metals, including Cu and Mn.

Formation of superoxide:

$$Fe(II)/Cu(I) + O_2 \rightarrow Fe(III)/Cu(II) + O_2^{\cdot -} \quad \text{(R4.1)}$$

Conversion of $O_2^{\cdot -}$ to H_2O_2 has several pathways:

$$Fe(II) + O_2^{\cdot -} + 2H^+ \rightarrow Fe(III) + H_2O_2 \quad \text{(R4.2)}$$

$$O_2^{\cdot -} + H^+ \rightarrow HO_2 \quad \text{(R4.3)}$$

$HO_2 + HO_2 \rightarrow H_2O_2 + O_2$ (R4.4)

$O_2^{\cdot -} + 2H^+ \rightarrow H_2O_2$ (R4.5)

$2\ O_2^{\cdot -} + 2H_2O \rightarrow H_2O_2 + 2OH^- + O_2$ (R4.6)

and the Fenton reaction:

$Fe(II) + H_2O_2 \rightarrow Fe(III) + OH + OH^-$ (R4.7)

Quinones also undergo redox cycling, especially in the presence of transition metals, to form ROS (Li and Trush 1993), where QH_2, $Q^{\cdot -}$ and Q are the hydroquinone, the semiquinone radical and the quinone, respectively.

$QH_2 + Cu(II) \rightarrow Q^{\cdot -} + Cu(I) + 2H^+$ (R4.8)

$Q^{\cdot -} + O_2 \rightarrow Q + O_2^{\cdot -}$ (R4.9)

$O_2^{\cdot -} + 2H^+ + Cu(I) \rightarrow H_2O_2 + Cu(II)$ (R4.10)

These reactions are often depends strongly on the pH of the solutions. For example, superoxide will form hydrogen peroxide spontaneously at low pHs. In the absence of an external sources of H_2O_2, OH formation relies on the initial production of $O_2^{\cdot -}$ and H_2O_2. The presence of redox active. quinones, can facilitate the rate of formation of $O_2^{\cdot -}$ from the reduction of oxygen by metals (i.e. R4.8-9; Li and Trush (1993)). It was also shown that quinones are able to produce ROS in the absence of metals (Chung et al., 2006; Shang et al., 2012). Humic Like Substances (HULIS) can substantially enhance ROS formation by complexing metals and increasing the rates of R1 and R6 (Gonzalez et al., 2017; Voelker and Sulzberger 1996) and the potential to reduce Fe(III) to Fe(II) by humic substances (Nevin and Lovley 2002; Voelker et al., 1997).

HULIS is a substantial component of atmospheric aerosols so named due to its similarity to terrestrial and aquatic humic and fulvic acid (Havers et al., 1998). These substances share, many functional groups including phenolic, hydroxyl, carboxylic, aliphatic chains, aromatic

rings and polysaccharides (Decesari et al., 2001; Duarte et al., 2005; Krivácsy et al., 2001); either as aggregates of smaller molecules or macromolecules (Piccolo and Conte 2000). HULIS can be directly emitted from biomass burning or formed in to the atmosphere via secondary organic aerosol formation (Lin et al., 2012), although the composition and properties of HULIS from these sources can be very different. To avoid confusion, we use biomass burning aerosol (BBA) for soluble HULIS associated with biomass burning, and photochemical SOA eponymously.

Here we quantify the intrinsic ability of particulate matter to produce hydrogen peroxide and OH in aqueous extracts at pH3.5 and the dependence of these properties on transition metals, quinones and BBA. Samples were collected in a field campaign that was carried out in Fresno, CA. Fresno is a mid-sized city located in a broad valley in Central California. Winter PM concentrations average > 30 $\mu g/m^3$ (ARB), and the site has a substantial contribution from biomass burning/wood smoke, particularly during the night (Parworth et al., 2017).

4.2 Methods

4.2.1 Sample Collection and Extraction

Sample collection, materials and measurement methods are provided in detail in Kuang et al., (2017) and are described only briefly here. Fine PM was collected on 47mm Teflon filters (PALL, 2μm pore size acid-washed) using 5 cyclone inlets in parallel. Samples were collected three times a day: 7am – 1pm (morning), 1-6pm (afternoon) and 6 pm -7am (overnight) from Jan. 16- Feb. 7, 2013. Field blanks were collected in the same manner, except that filters were in the holders only briefly and the pump was on for only 30 s. Biomass burning aerosol samples were collected in January-February in Fresno in 2013, on Teflon coated glass filters (8" x 10", 0.45μm), using a Hi-Volume $PM_{2.5}$ sampler (TE-6070 Tisch Environmental) operating at 1.13 m^3

min^{-1}. Shortly after collection, the filters were weighed using a microbalance (1μg precision, ME 5, Satorius) in a temperature (22-24°C) and humidity (40-45%) controlled dark room. Filters are analyzed for iron speciation and OH formation (on site, usually within an hour of collection) and trace metal concentration, BBA estimation and H_2O_2 formation were analyzed on stored frozen filters. All containers used here were rigorously cleaned prior to each experiment (Kuang et al., 2017).

Filters were cut in half using a ceramic blade and extracted in water at pH3.5 adjusted using 0.1 N sulfuric acid. Triflruoethanol was added to filters prior to extraction to increase PM solubility, and all extraction solutions were 4 mL except speciated iron (Fe_{fzn}). All experiments were performed in the dark. Quantification of OH, H_2O_2 and iron speciation was performed at 2 and 24 hours after the beginning of the extraction.

4.2.2 Iron Speciation

Soluble Fe(II) and Fe(tot) concentrations were quantified using ferrozine.(Stookey 1970) Ferrozine forms a magenta complex with $Fe(II)_{fzn}$ and can be detected by UV-Vis spectroscopy at λ = 562nm. This assay was performed using a Liquid Waveguide Capillary Cell (LWCC, 1 meter, World Precision Instruments) and a UV-Vis spectrometer. Total soluble iron ($Fe(tot)_{fzn}$) was quantified by adding hydroxylamine hydrochloride, a strong reducing agent that converts $Fe(III)_{fzn}$ to $Fe(II)_{fzn}$. Calibration was performed daily and the LWCC was cleaned rigorously prior to each experiment.

4.2.3 Hydrogen Peroxide

H_2O_2 was analyzed using a High Performance Liquid Chromatography (HPLC)(Arellanes et al., 2006). The eluent was water adjusted with 0.1 N sulfuric acid to pH3.5 and with 0.1 mM ethylenediaminetetraacetic acid (EDTA) added. H_2O_2 elutes from the guard column at about 0.5

min, and is then mixed with the fluorescence reagents containing Horseradish peroxidase and para-hydroxyphenyl acetic acid (POHPAA). The peroxidase enzyme catalyzes the reaction between H_2O_2 and POHPAA, forming a fluorescent dimer, which is detected at the excitation/emission wavelengths of 300/420 nm. Calibrations were performed weekly or when the HPLC conditions were changed.

4.2.4 Hydroxyl Radical

OH was quantified with the probe terephthalate (Kuang et al., Submitted; Matthews 1980). Terephthalate reacts with OH to form a fluorescent product, 2-hydroxyterephthalic acid (hTA). hTA was detected at excitation/emission wavelengths of 320/420 nm using a stand-alone fluorometer (Lumina, Thermo Scientific). A calibration curve was performed daily using standards ranging from 5×10^{-8} to 8×10^{-7} M of hTA.

4.2.5 Soluble Trace Metals

Aliquots of extraction solution used for H_2O_2 analysis were filtered through 0.2 μm polypropylene syringe filters then acidified using 2% (by weight) Nitric acid and stored in 15 mL Falcon tubes. Trace elements and metals (Mg, Al, V, Vr ,Mn, Fe, Co, Cu, Zn, Se, Cd, La and Pb) were analyzed Triple Quadruple ICP-MS (Agilent).

4.2.6 Estimation of Biomass Burning Aerosol

Quantification of the contribution of biomass burning aerosols (BBA) on Teflon filters was accomplished using optical absorption using a dual wavelength transmissometer (OT21, Magee Scientific Corporation). We used an absorption cross section of 9.6 m^2 g^{-1} to calculate BBA concentrations. A mass loading correction method developed by Jimenez et al. (2007) was

applied to samples with higher mass loading; see also Paulson et al., (2016) for a more complete discussion.

4.2.7 Back Trajectory Analysis and Wind Directions

Six-hr back trajectories of air masses were calculated using a Hybrid Single Particle Lagrangian Integrated Trajectory (HYSPLIT) model developed by NOAA (NOAA 2017). Wind direction data were obtained from the Air Resource Board monitoring site at Clovis on N Villa ave, from Jan 13 to Feb 7, 2013. The hourly data for each sampling period were averaged.

4.3 Results and discussion

4.3.1 General Features: mass, ROS, speciated iron and trace metal concentrations in PM extracts

Fresno exhibited higher average mass concentrations (33 ± 15 μg/m^3) compared to Claremont (23 ± 5 μg/m^3), even though there were three rain events during the Fresno field campaign (Fig. 4.1) and did not vary significantly with time of day (Fig. 4.2a). H_2O_2 and Fe_{fzn} concentrations were highest in the morning samples, as was observed in Claremont, but the overnight samples produced the most OH (Figs. 4.2a and b). $Fe(II)_{fzn}$ accounted for more than half of the $Fe(tot)_{fzn}$ in all samples and at both 2 and 24 hrs. (Fig. 4.2c)

Biomass burning aerosol (BBA) has been widely observed in Fresno during winter (Ge et al., 2012; Parworth et al., 2017; Young et al., 2016), attributed primarily to residential wood burning (Gorin et al., 2006). BBA on the filters had several distinctive features: observable yellow color in solution, strong fluorescence, with some sample to sample variability in 3-D scans; and strong absorption at 370 and 880nm, wavelengths used to quantify black and brown carbon. Slopes of BBA vs. mass were 0.23 ± 0.08, 0.11 ± 0.06 + 0.12 ± 0.1 for overnight, morning and afternoon, including much higher BBA in the overnight samples (Fig. 2.2d). A

simple calculation of percent BBA places morning and overnight samples as very similar (0.27 and 0.31, respectively), but this is due to some low mass morning samples with high contribution from BBA, thus the relatively higher intercepts. As discussed below, BBA has an important effect on complexation with iron and formation of ROS.

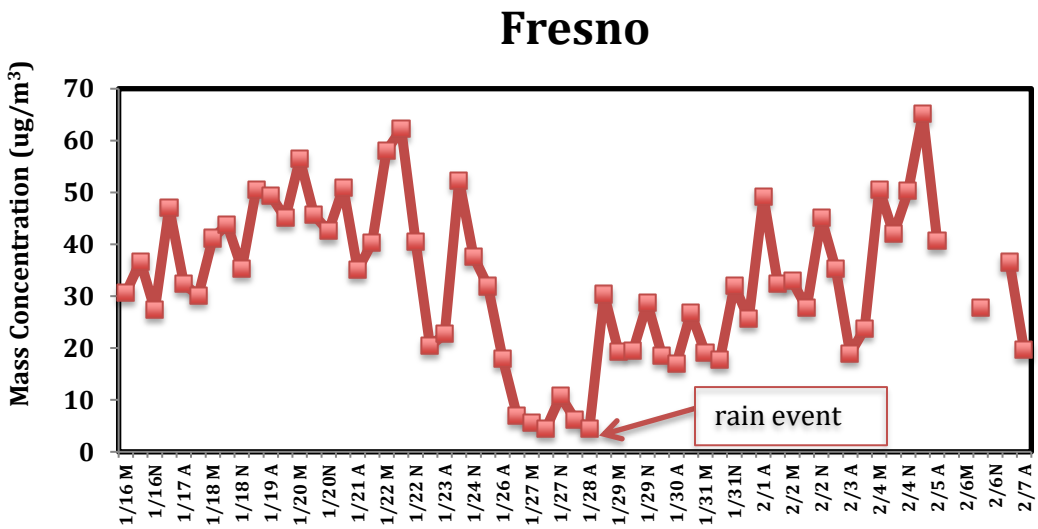

Fig. 4.1. Mass concentration during the Fresno campaign, Jan 16-Feb 7, 2013.

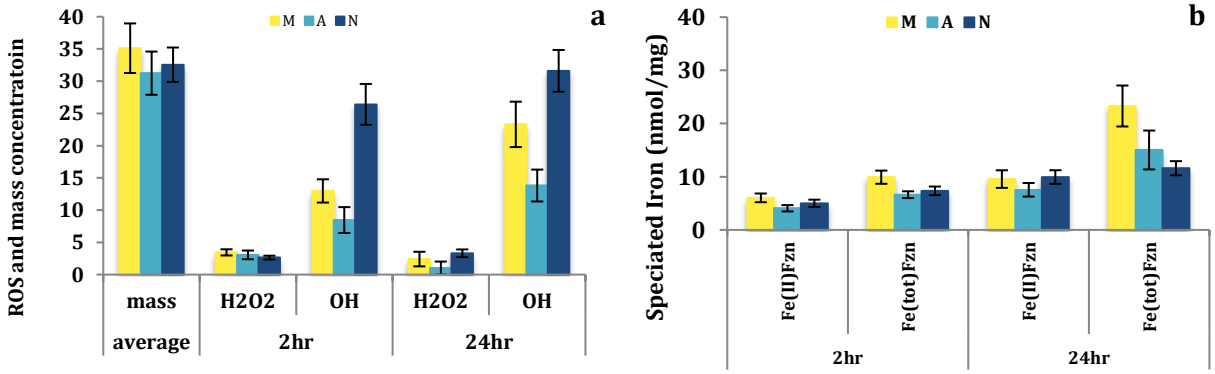

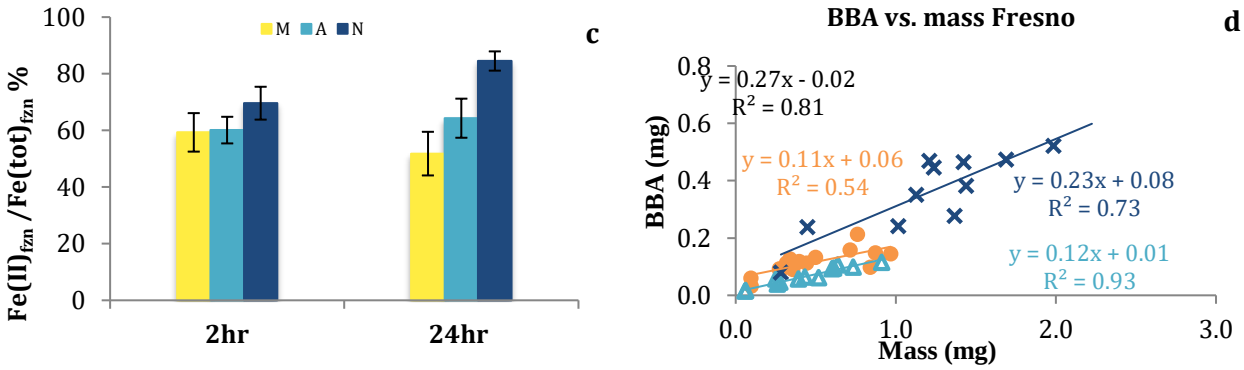

Fig. 4.2 Mass concentration (μg/m^3), concentrations of ROS and speciated iron (nmol/mg) and $Fe(II)_{fzn}$ to $Fe(tot)_{fzn}$ ratios at 2 and 24 hours in Fresno. Yellow, light blue and dark blue bars represent morning (M), afternoon (A) and overnight (N) samples, respectively. Standard errors are shown.

4.3.2 Speciated Iron

$Fe(II)_{fzn}$ and $Fe(tot)_{fzn}$ (Fig 4.2b) was highest in the morning and was similar for afternoon and overnight samples. $Fe(II)_{fzn}$ values increased by 59, 85 and 99% at 24 hr for M, A and N samples. $Fe(tot)_{fzn}$ concentrations increased substantially for morning (135%) and afternoon (126%) but by a much smaller amount for the overnight samples (58%) (Tab. 4.1). $Fe(II)_{fzn}/Fe(tot)_{fzn}$ ratios were highest in the overnight samples and nearly identical for morning and afternoon samples. These ratios decreased at 24 hrs for the morning but increased slightly for afternoon and overnight samples, although none of the differences were significant for all samples ($p>0.05$). The interpretation of this behavior is difficult as two or three processes are taking place simultaneously: aqueous oxidation/or reduction of $Fe(II)_{fzn}$ to $Fe(III)_{fzn}$, dissolution of $Fe(II)_{fzn}$ and $Fe(III)_{fzn}$ and release (or uptake) of Fe(II)/Fe(III) by BBA. Some studies have shown that BBA is able to reduce $Fe(III)_{fzn}$ to $Fe(II)_{fzn}$ (Moonshine et al., 2008), resulting in higher concentration of $Fe(II)_{fzn}$ at 24 hours. Due to many competing processes, we have not attempted to measure this process in our BBA-containing samples. However, we have tested

Suwannee River Fulvic Acid (a standard material that has had native Fe removed). Under many conditions in cloud, pH3.5 have formed no evidence for reduction of Fe(III) to Fe(II) by this material.

On average, ferrozine iron concentrations were higher in the Claremont samples than the Fresno samples (Fig. 4.3), however, we observed slightly higher $Fe(II)_{fzn}/Fe(tot)_{fzn}$ (0.62) in the Fresno winter samples than the Claremont summer samples (0.53, at 2 h). Claremont samples were collected during summer and at a site expected to receive significantly oxidized aerosols while Fresno winter samples are expected to have much lower level of oxidation. Oakes et al. (2012) found significant higher $Fe(II)_{fzn}/Fe(tot)_{fzn}$ for winter samples compared to summer samples for series of same-site comparisons. Consistent with this notion, however, the differences are remarkably small, suggesting overall oxidation state of soluble species in particles is not a strong determinant of the iron oxidation state.

Tab. 4.1 Percent change of ROS and speciated iron concentration at 24 hours compared to those at 2 hours.

	HOOH	OH	Fe(II)	Fe(tot)	Fe(II)/Fe(tot)
M	-30	80	59	135	-13
A	-67	63	85	127	7
N	26	20	99	58	21

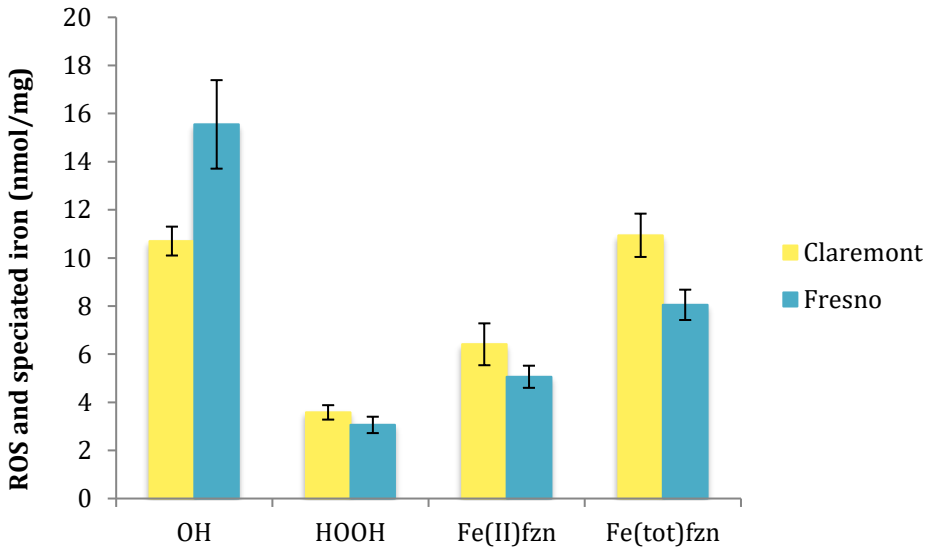

Fig. 4.3 Comparison of average aerosol mass-normalized ROS and ferrozine iron concentrations in Claremont and Fresno, CA.

4.3.3 Soluble Trace Metals

Fig. 4.4 shows the mass-normalized concentration of soluble trace metals measured by ICP-MS on samples extracted for 24 h (sufficient samples were not available for 2 h samples). Similar to the Claremont samples, the most abundant trace metals was Fe (70 ± 5 nmol/mg of aerosol), followed by Zn and Cu (39 ± 7 and 17 ± 2 nmol/mg, respectively), the rest of the trace metals were generally lower than 3 nmol/mg. Most samples were most abundant in the morning samples but Cr had the highest concentration in the afternoon. Correlations between metals are shown in Tab. 4.2.

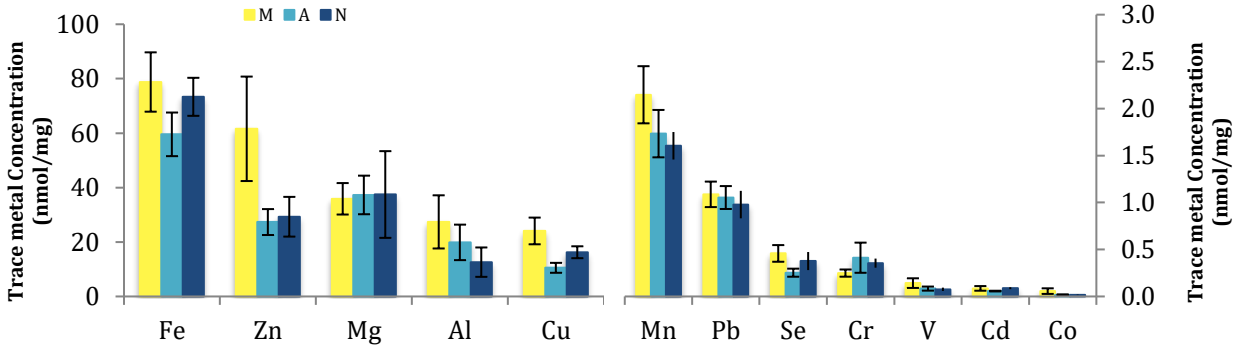

Fig. 4.4 Concentration of metals analyzed by ICP-MS at 24 hours in Fresno; yellow, light blue and dark blue bars represent morning (M), afternoon (A) and overnight (N) samples, respectively. Standard errors are shown.

Tab. 4.2 Correlations between soluble trace metals. Correlation coefficients (r) are shown for the entire data set. Bold and red values indicate a p-value < 0.05

	V	Cr	Mn	Fe	Ni	Cu	Zn	Se	Pb
V	1	**0.26**	0.11	0.07	0.12	-0.03	0.08	**0.68**	0.22
Cr		1	**0.72**	**0.73**	0.23	**0.52**	**0.30**	**0.33**	**0.79**
Mn			1	**0.91**	-0.04	**0.79**	0.27	**0.31**	**0.63**
Fe				1	-0.02	**0.84**	**0.28**	**0.29**	**0.57**
Ni					1	-0.11	0.09	**0.32**	0.16
Cu						1	0.20	0.06	**0.45**
Zn							1	0.01	**0.29**
Se								1	**0.46**
Pb									1

Mass normalized Fe, Zn, Cr and Ni were all very similar in the Claremont and Fresno samples. Cu, Mn, V, Se, and Pb were higher in Claremont ($P < 0.05$). Cu is only slightly higher (29%), Mn is higher by 44%, Pb by 31%, Se by about a factor of 2 and V by a factor of 10.

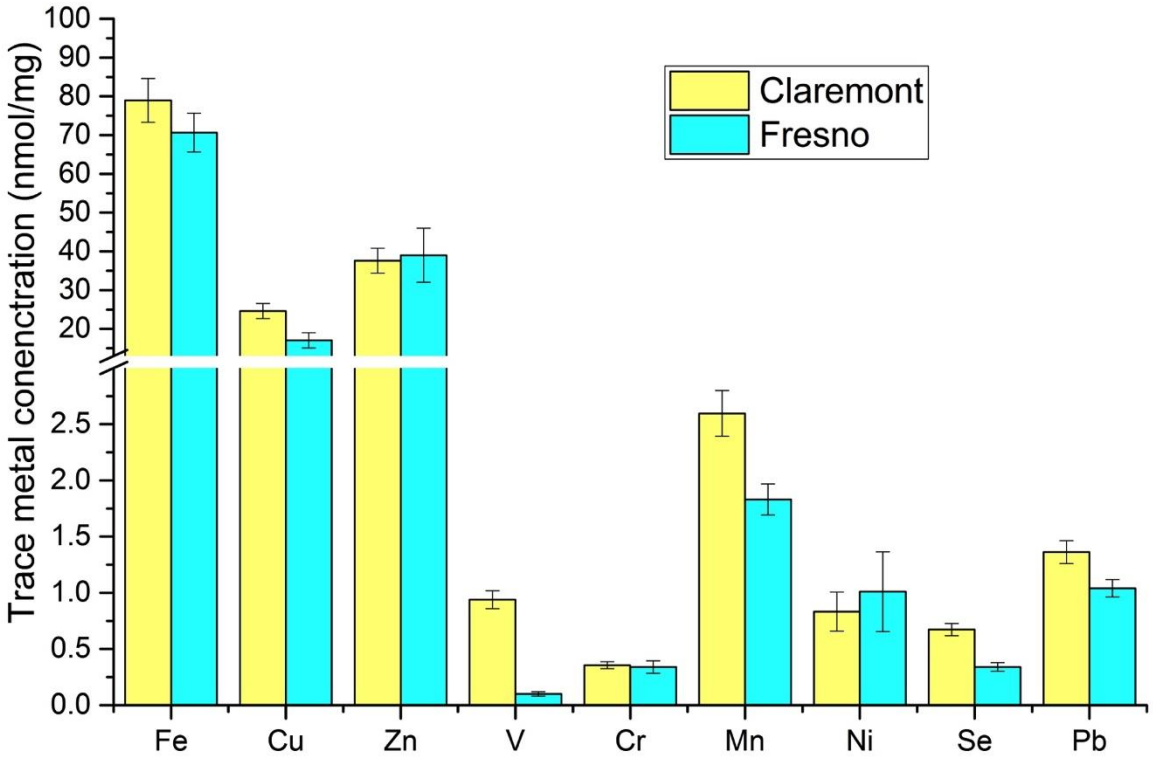

Fig. 4.5 Comparison of average soluble trace metals/Se in Claremont and Fresno, CA.

4.3.4 Concentration wind direction roses

To show relationships between area of origin and chemical composition, we show wind direction-concentration roses in Fig. 4.6. The plots show the frequencies of particular combinations of concentration and wind direction; the wind roses are divided into 10 equal slices (36 degrees per slice). The bar graph inserts show the number of samples (M, A and N) associated with each slice and the patterns in the bar graph indicate the sample type with the highest concentration in the particular slice.

Morning winds were variable. Majority of the afternoon samples came from N/NW and with a few samples from the SE/SW. The overnight samples were predominantly from N/NE. Average ROS, transition metals and BBA content are shown as a function of wind direction

(Figs. 4.6a-f). The highest and the lowest average H_2O_2 were associated with the air samples coming form the SW and W, respectively. Average H_2O_2 in samples from other directions was fairly uniform. Fig 4.6b shows the single highest OH concentration was observed in the sample from the NW from a nighttime sample (1/27 N) and the highest average concentation was obseved in the E (72-108˚). ICP Fe and Cu concentrations were relatively lower in the air masses came from W and NNW (Figs 5d-e), $Fe(tot)_{fzn}$ is the lowest in the air masses came from the NNW but fairly similar in the other directions (Fig 4.6c). $Fe(tot)_{fzn}$ and ICP Fe plots do not have much overlap, consistent with different sources ICP Fe and Cu are similar, with the highest concnetration arriving from the East and NW.

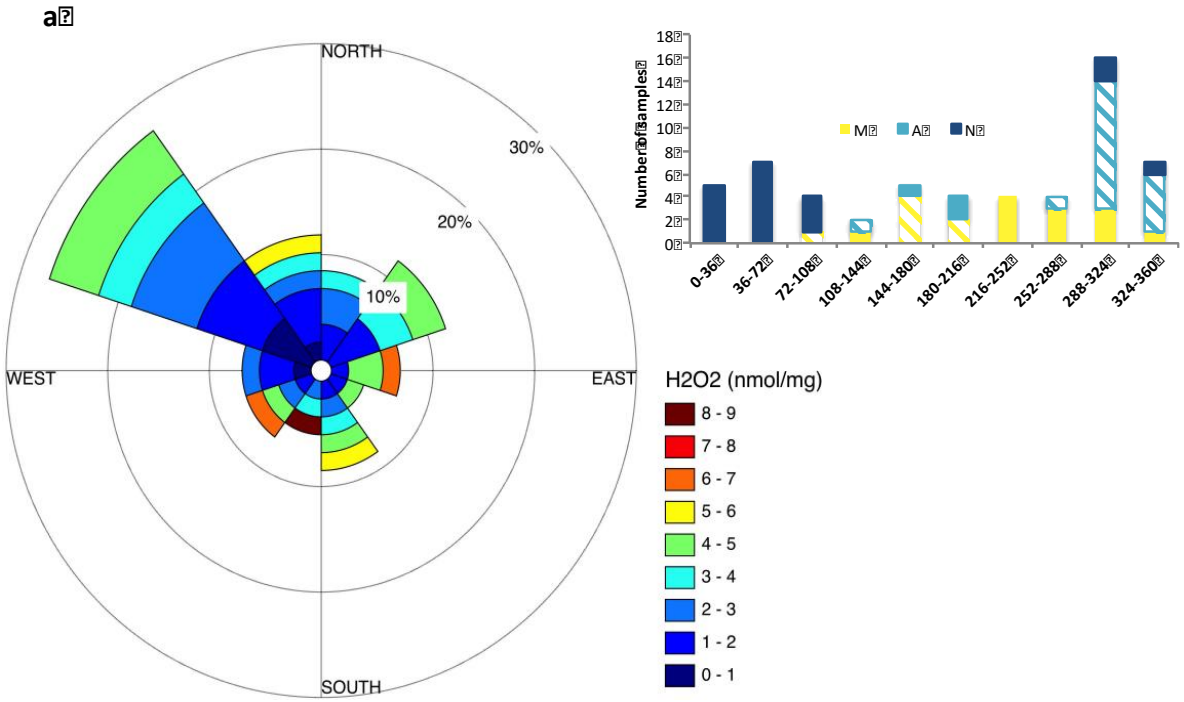

b

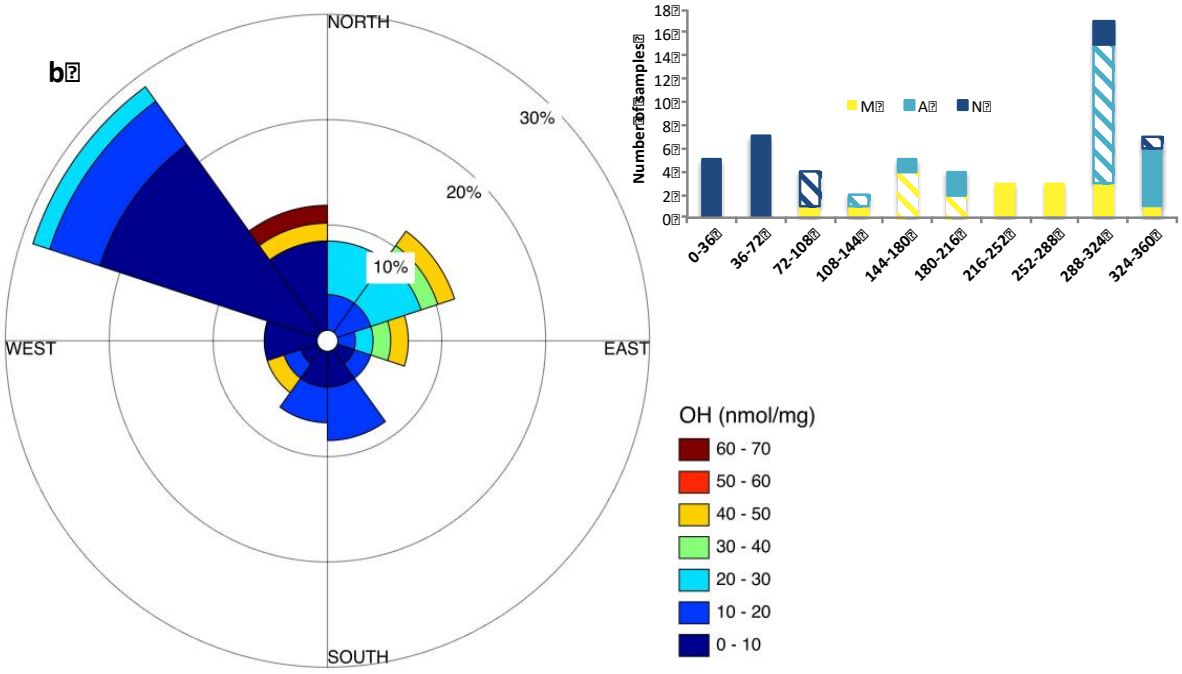
NORTH
30%
20%
10%
WEST
EAST
SOUTH
OH (nmol/mg)
60 - 70
50 - 60
40 - 50
30 - 40
20 - 30
10 - 20
0 - 10
Number of samples
M
A
N
0-36
36-72
72-108
108-144
144-180
180-216
216-252
252-288
288-324
324-360

c

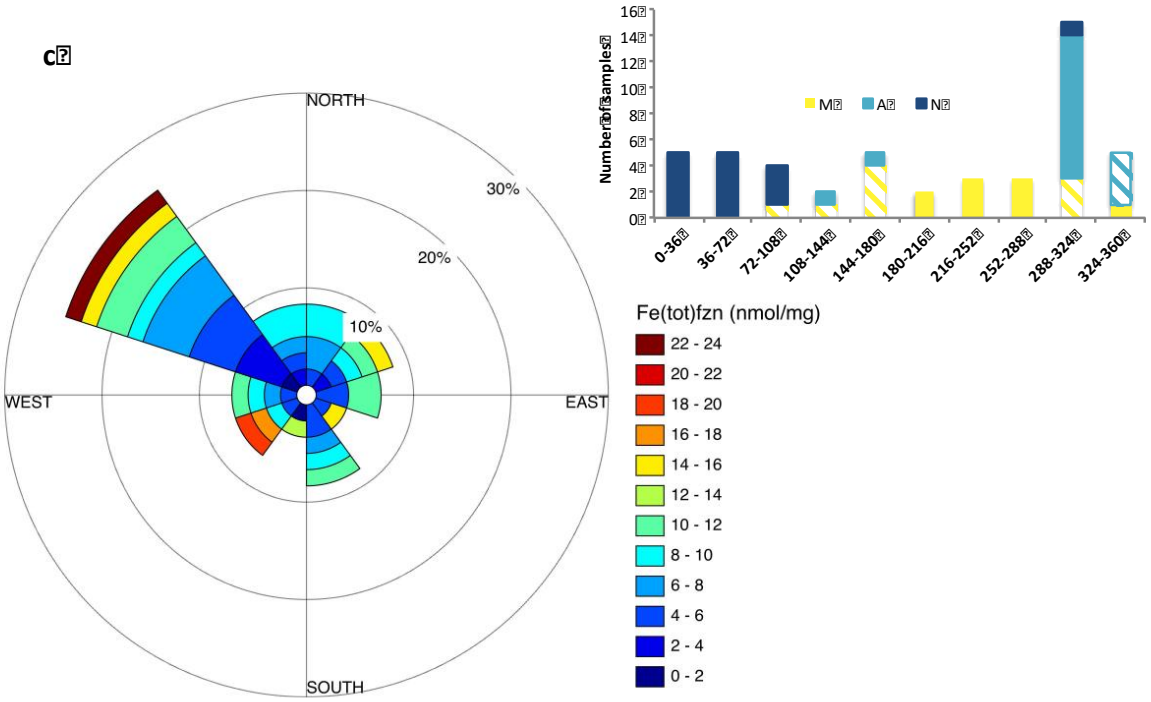
NORTH
30%
20%
10%
WEST
EAST
SOUTH
Fe(tot)fzn (nmol/mg)
22 - 24
20 - 22
18 - 20
16 - 18
14 - 16
12 - 14
10 - 12
8 - 10
6 - 8
4 - 6
2 - 4
0 - 2
Number of samples
M
A
N
0-36
36-72
72-108
108-144
144-180
180-216
216-252
252-288
288-324
324-360

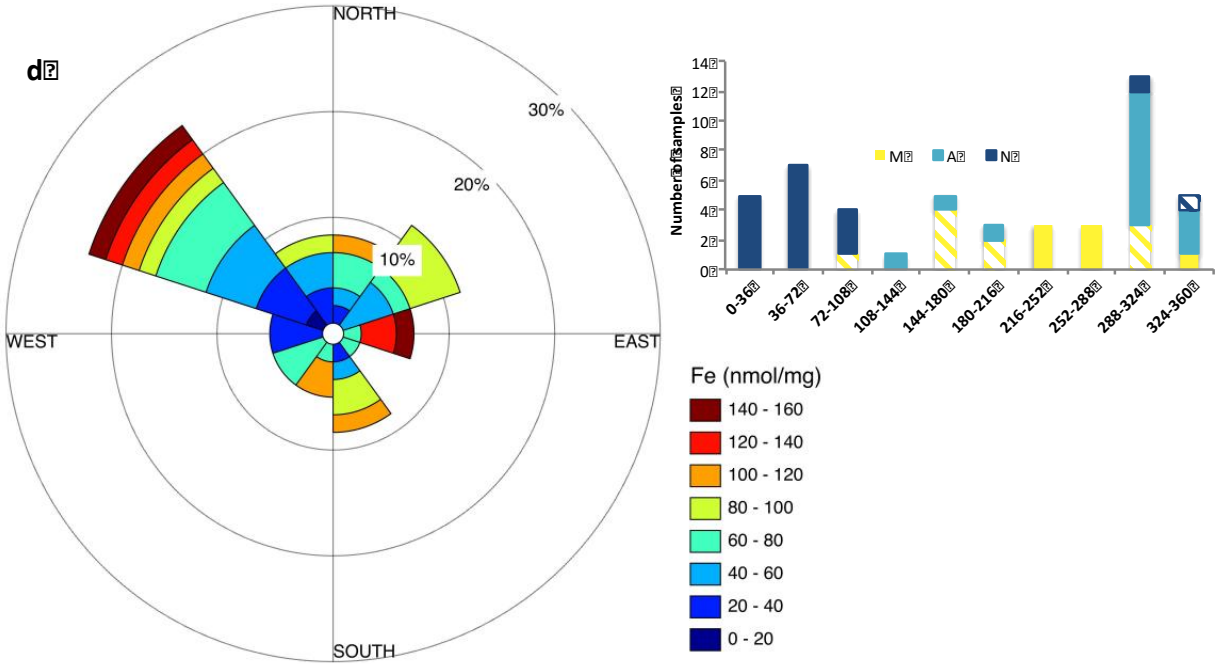
d
NORTH
30%
20%
10%
WEST
EAST
SOUTH
Number of samples
M
A
N
0-36
36-72
72-108
108-144
144-180
180-216
216-252
252-288
288-324
324-360
Fe (nmol/mg)
140 - 160
120 - 140
100 - 120
80 - 100
60 - 80
40 - 60
20 - 40
0 - 20

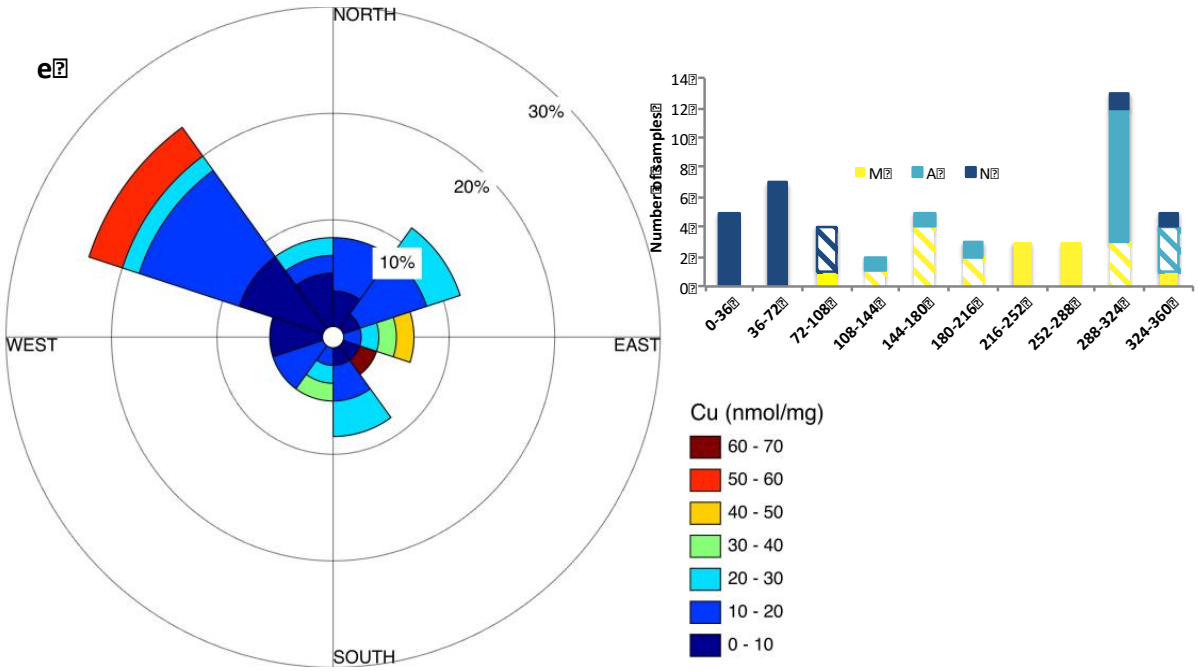
e
NORTH
30%
20%
10%
WEST
EAST
SOUTH
Number of samples
M
A
N
0-36
36-72
72-108
108-144
144-180
180-216
216-252
252-288
288-324
324-360
Cu (nmol/mg)
60 - 70
50 - 60
40 - 50
30 - 40
20 - 30
10 - 20
0 - 10

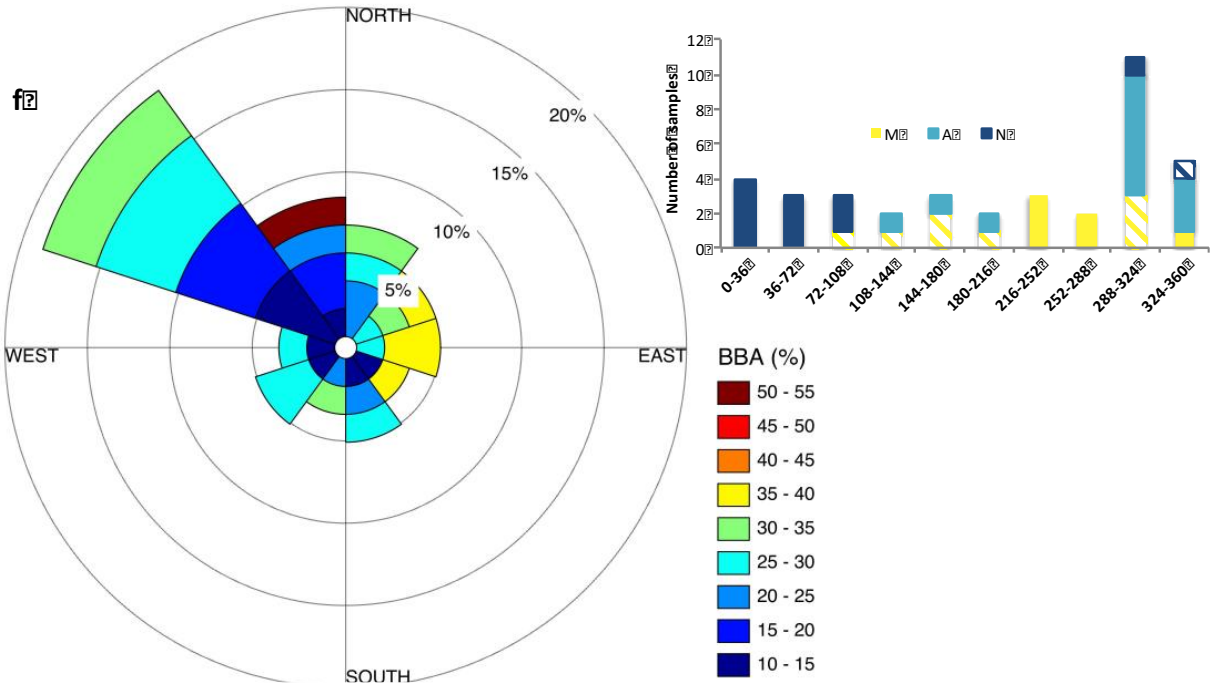

Fig. 4.6 Wind roses representing the ROS and soluble metal concentrations as a function of average wind direction in Fresno. Percentage on the wind rose indicates the amount of samples coming from that particular wind direction; colors indicate concentrations.

4.3.5 Relationships between speciated iron, trace metals and mass

Fig. 4.7 shows the relationships between iron and copper and mass. Generally the M, A and N samples have different relationships with mass. BBA is also strongly correlated with mass, it is the strongest correlation with mass among all other metrics measured but with markedly different slopes for M, A and N (Fig. 4.2d). $Fe(tot)_{fzn}$, ICP Fe and Cu are strongly correlated with aerosol mass (Fig. 4.7a-d; with $P<0.05$. Several soluble transition metals, especially copper, have relative lower concentrations in the afternoon samples than the morning and overnight samples (Figs 4.7a, c-d). $Fe(tot)_{fzn}$ is moderately correlated with mass at both 2 h and 24 h with the two outliers removed.

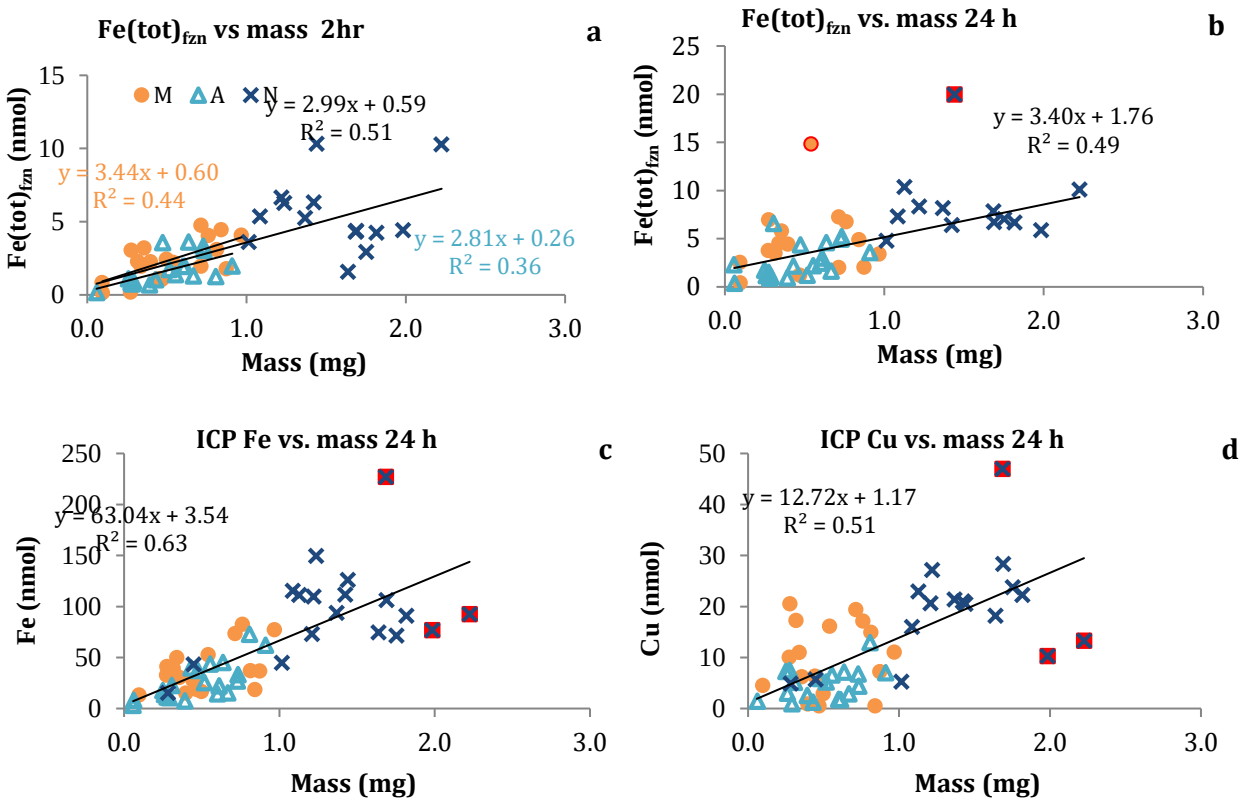

Fig. 4.7 Relationships between aerosol mass, speciated iron and trace metal concentrations in pH3.5 extraction solution, Fresno. Circles (M), triangles (A) and crosses (N) represent morning, afternoon and overnight samples, respectively. Black trend lines show the overall correlations. Outliers are highlighted in red and not inlcuded in the overall regression.

4.3.5.1 Hydrogen Peroxide.

The steady-state concentration of H_2O_2 was highest in the morning, which is comparable to the afternoon but higher than the overnight samples (Fig. 1a). H_2O_2 concentrations at 24 h were not significantly different from 2 h at $p < 0.05$ level. However, concentrations decreased for the morning and afternoon samples but increased for the overnight samples (Tab. 4.1), potentially due to the BBA in the overnight samples.

Relationships between H_2O_2, speciated iron, trace metals and BBA. H_2O_2 is weakly correlated with mass ($r^2 = 0.33$, Fig. 4.8i) but strongly correlated with $Fe(II)_{fzn}$ ($r^2 = 0.65$), Fe ($r^2 = 0.75$), Mn ($r^2 = 0.58$), BBA ($r^2 = 0.64$, Figs. 4.8a-e) at 2 hours. These correlations were also

strong at 24 hours of extraction with slightly lower r^2 values (Fig. 4.9). Copper was more correlated with the 24 H_2O_2 concentrations, with r^2 of 0.52 at 24 hr vs. 0.46 at 2 hr. Consistent with the Claremont samples, ferrozine iron is a good predictor for H_2O_2 concentration. The relationships between redox active metals (Fe, Cu and Mn) and H_2O_2 are more significant in the Fresno samples ($r^2 > 0.5$, $p < 0.05$) than those relationships in the Claremont samples. Furthermore, redox active metals such as Fe and Cu are strongly correlated with BBA (Figs. 4.8f-h). Of these metals, BBA is the most correlated with ICP Fe. Gonzalez et a;. (2017) show that fulvic acid, a complex organic with similar functional groups as BBA, can enhance both Fe(II) mediated superoxide formation (R4.1, usually the rate limiting step in the formation of H_2O_2) and its destruction via the Fenton reaction (R4.7). These experiments were however carried out at pH 7.4, when the carboxylate groups may have different chelation abilities than at pH3.5. Laboratory studies of Fe(II) and fulvic acid at pH3.5 do not show the same behavior.

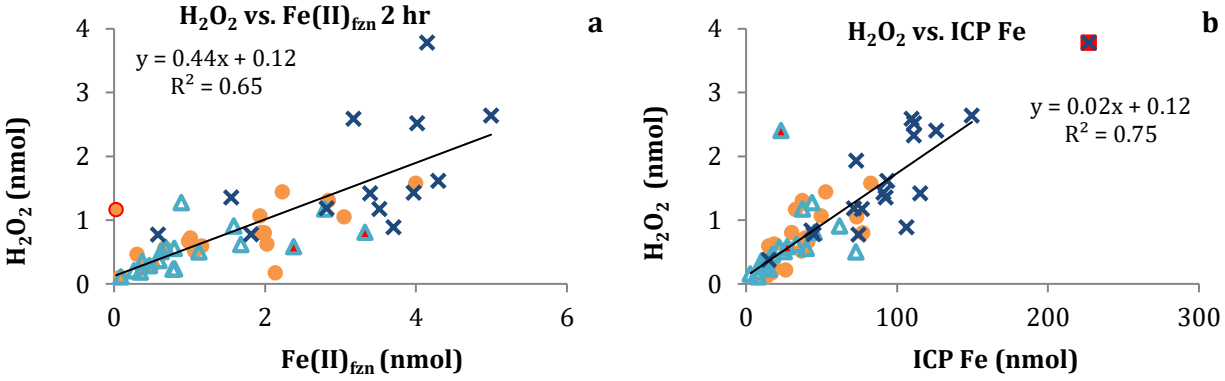

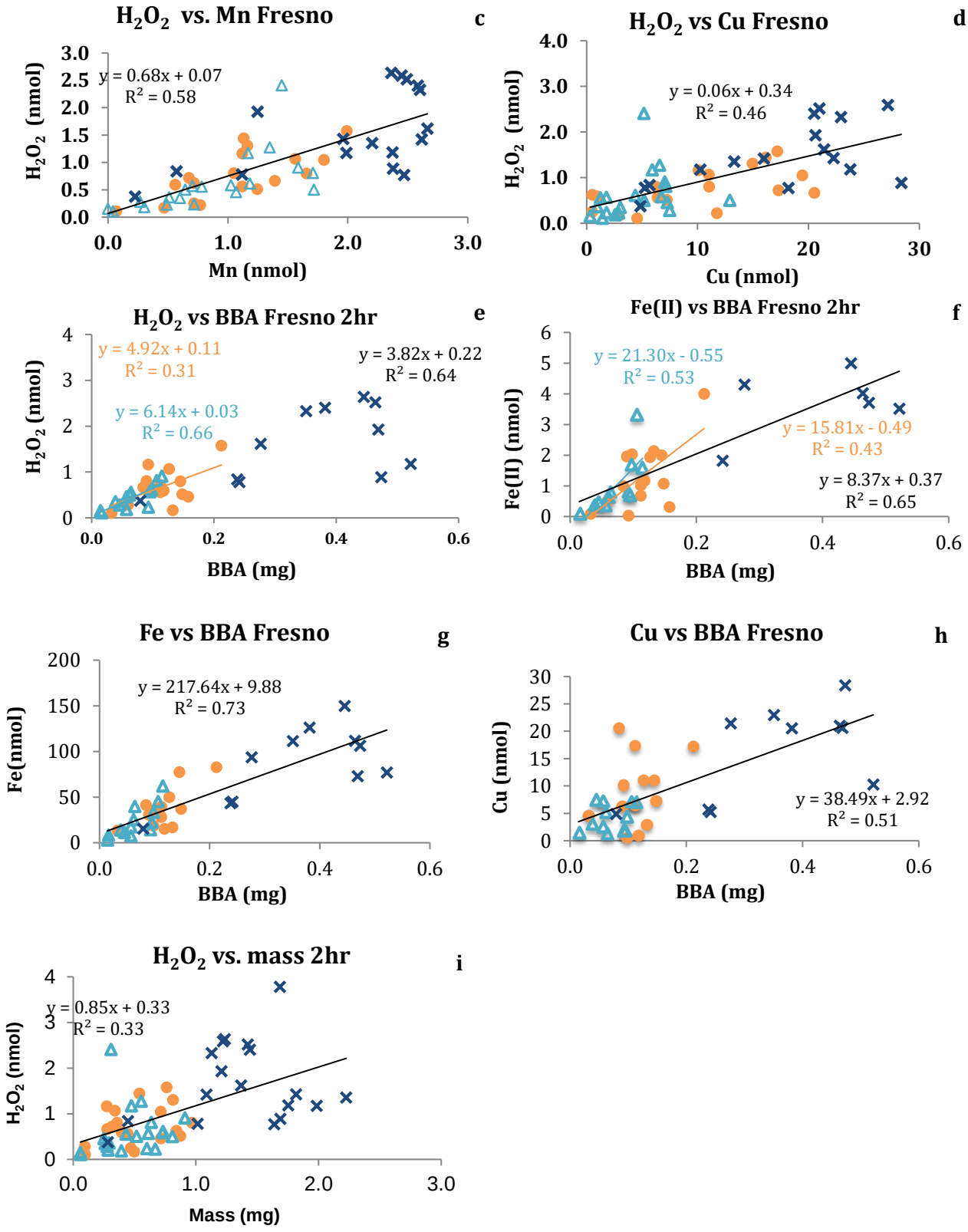

Fig. 4.8 Relationships between aerosol mass, speciated iron, trace metal concentrations, BBA and H_2O_2 in pH3.5 at 2 hours, Fresno. Circles (M), triangles (A) and crossess (N) represent

morning, afternoon and overnight samples, respectively. Black trend lines show the overall correlations. Outliers are highlighted in red and not inlcuded in the overall regression.

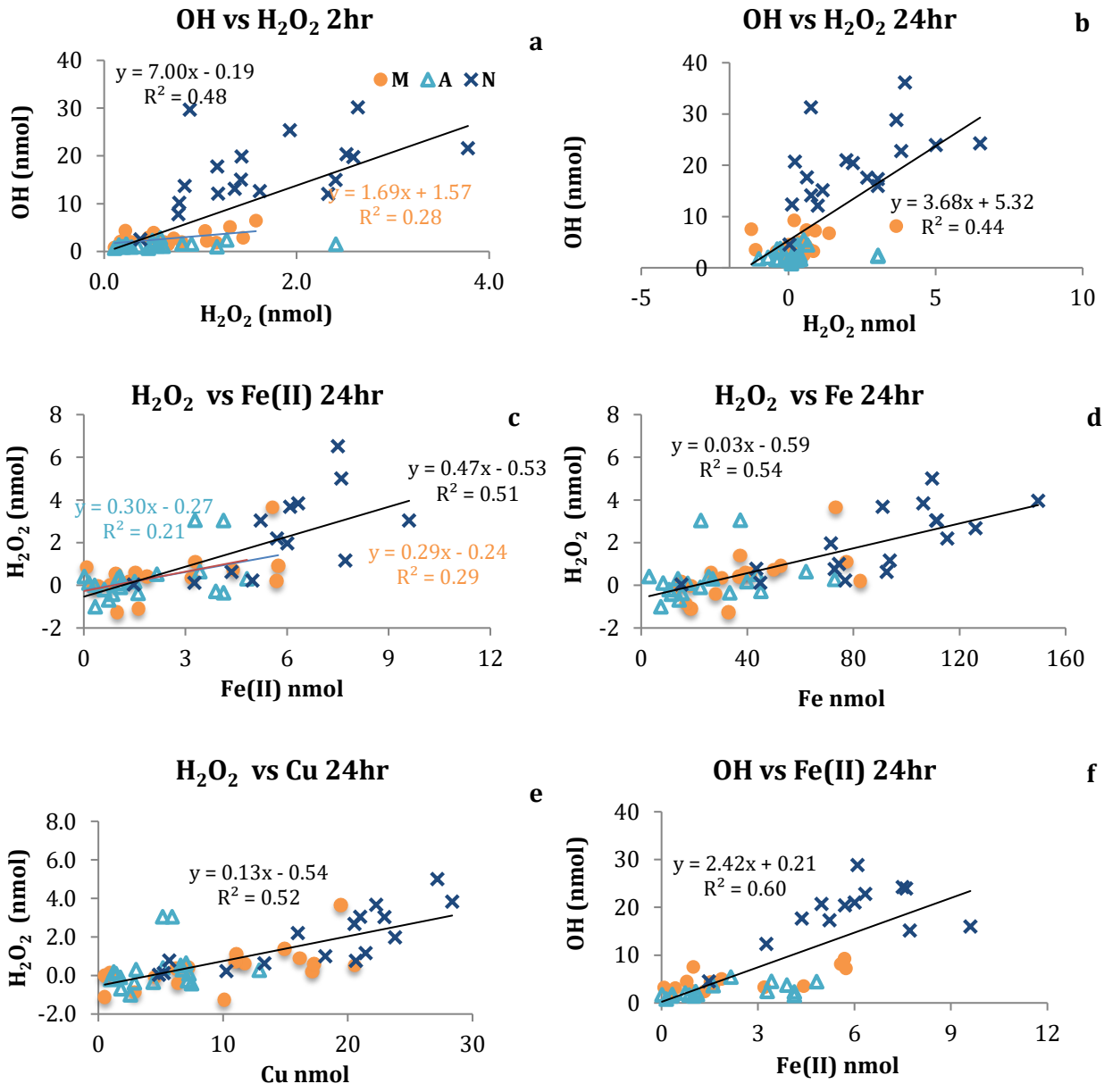

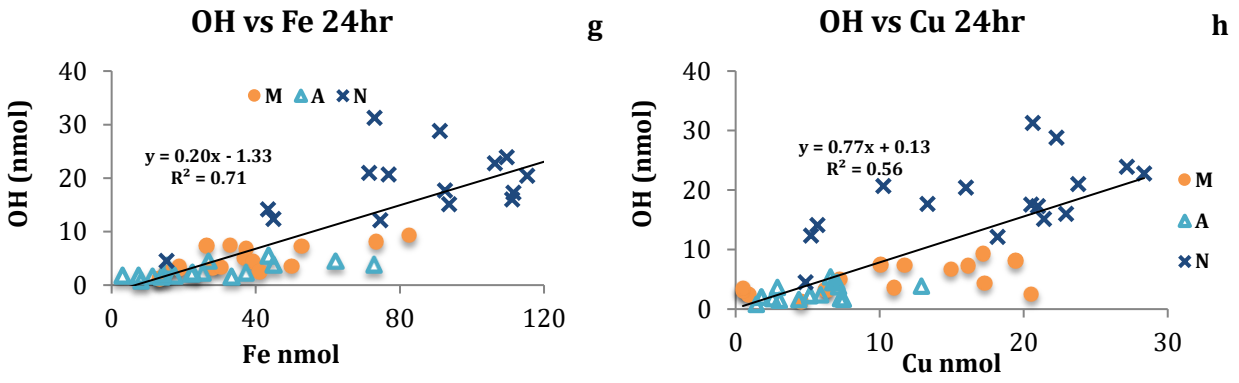

Fig. 4.9 Correlations between ROS and soluble trace metals at 24 hours. Circle (M), triangle (A) and crosses (N) represent morning, afternoon and overnight samples, respectively.

4.3.5.2 Hydroxyl radicals.

A significant diurnal trend was observed for OH formation; was much higher in the overnight samples. (Fig 4.2a). Although OH production increased for all samples at 24 hours, the increase was substantially lower at night (~20%) than the morning and afternoon samples (up to 80%). The increase in OH concentration after 24 hours was more pronounced in the Claremont samples (up to 200% increase) (Kuang et al. 2017).

Relationships between OH, speciated iron, trace metals and BBA. The ROS behavior of the Fresno samples, as well as soluble iron, was strongly dominated by the presence of BBA (Fig. 4.8-9). OH formation is tightly correlated with BBA but with slightly different slopes for morning and overnight samples (Fig. 4.9a). Afternoon samples are slightly less correlated. OH has reasonably strong correlations with Fe(II) (Fig. 4.9c), ICP Fe (Fig. 4.9d) and weaker correlations with mass, Mn and Cu (Figs. 4.9b, e and f), increasing from afternoon, morning to overnight. Clearly BBA is the dominant controlling factor in OH formation. The strongest correlation in the entire data set, r^2=0.88, is between OH formation and BBA. H_2O_2, Fe(II) and Fe(tot) were also strongly correlated with BBA (r^2= 0.64, 0.58 and 0.58, respectively, Fig. 4.10).

As a precursor of OH, H_2O_2 was correlated with OH at both 2 and 24 h (Figs. 4.9a and b), however, these relationships were much weaker in the Claremont samples.

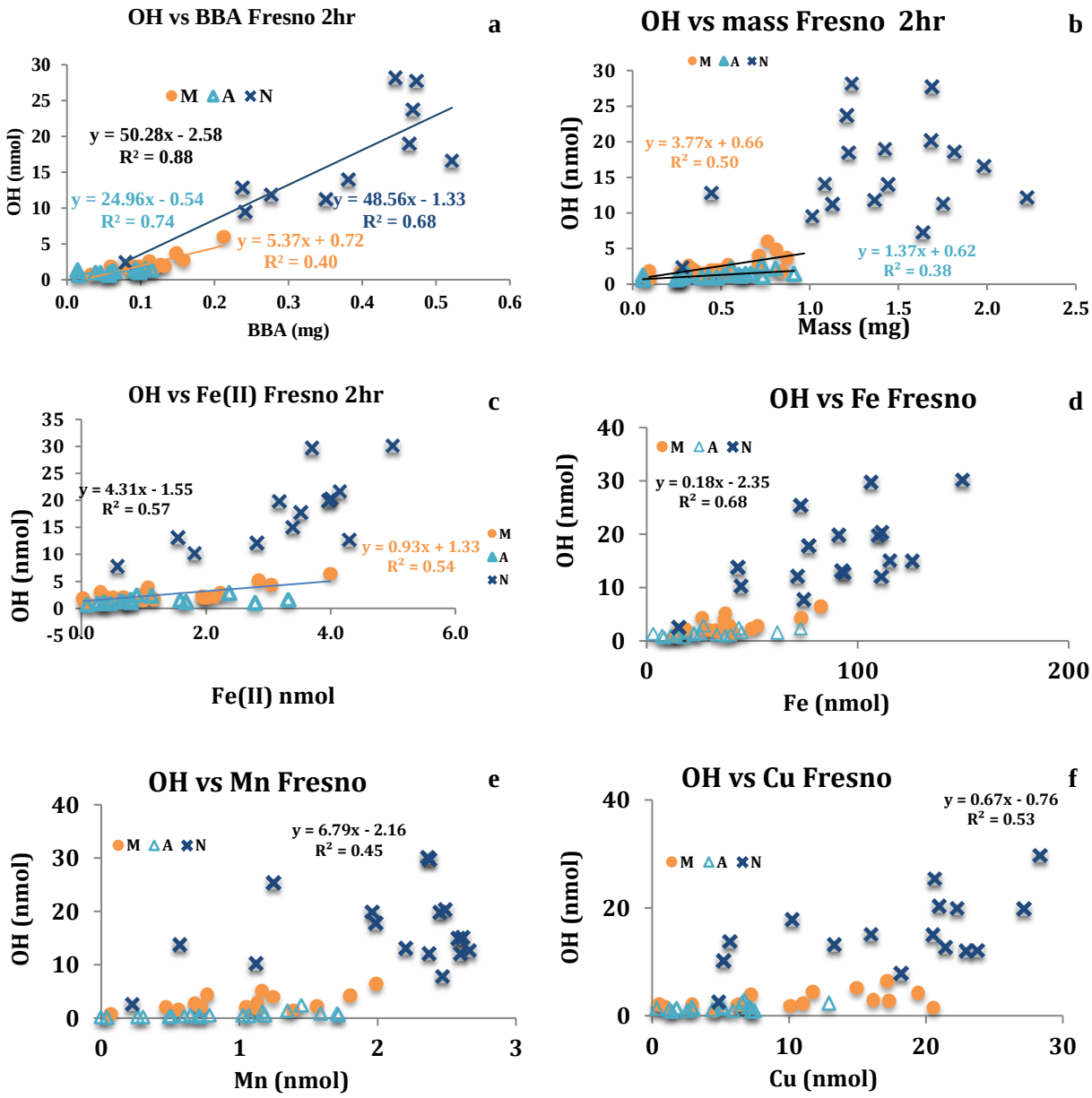

Fig. 4.10 Relationships betwee aerosol mass, speciated iron, trace metal concentrations, BBA and OH in pH3.5 extraction solution, Fresno. Circle (M), triangle (A) and crosses (N) represent morning, afternoon and overnight samples, respectively.

4.3.6 Kinetics of H_2O_2 and OH.

Steady-state H_2O_2 concentrations were measured at 0.5, 1, 1.5 and 2 h after extraction. As observed in the Claremont samples, the kinetics of H_2O_2 was best fitted with a second order polynomial function, majority of the samples (67%) followed the concave upward trend and 33% of the samples were concaving downward; examples of these behaviors are shown in Fig. 4.11a.

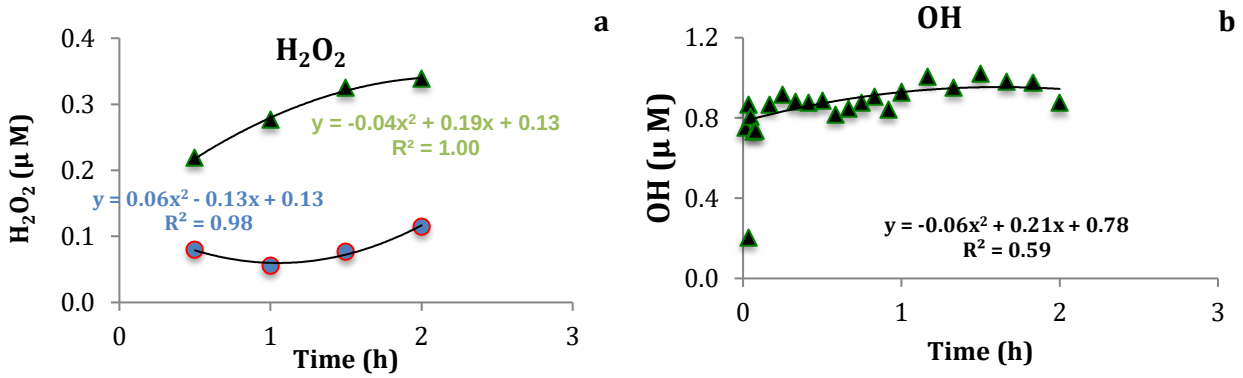

Fig. 4.11 Kinetics of (a) H_2O_2 every 30 mins in the first 2 hours and (b) OH every 1 min in the first 5 mins then every 5 mins in the first hour and every 10 mins up to 2 hours.

4.3.7 Multivariate regression.

Multivariate regressions for which all species have $p < 0.05$ are summarized in ab. 4.3 and Fig. 4.12. The BBA data set is rather small and thus expanded by extrapolating BBA concentration from its correlation with mass, which has an r^2 value of 0.8. The regressions with extrapolated BBA values resulted in lowered the r^2 of the overall regressions; this difference is likely due to the increased sample size. In the Fresno samples, combinations of redox active metals and BBA can explain vast majortiy of variance in ROS production. Higher r^2 values were observed between the predicted ROS formation from the combination of different variables and the measured concentration than those single variable correlations. BBA was the best single predictor for OH formation and the regressions with BBA and metals can better predict OH

concentrations than those with metals only (Tab 4.3a), As discussed, BBA played an important role in ROS formations, i.e. can increase the rate constants of reactions involving superoxide and hydrogen peroxide formation from Fe(II). This was also evident in the Fresno samples in which OH production was 2 and 3 times higher at night than in the morning and afternoon, respectively. Fig. 4.13 shows the relative contribution of each variable to the ROS formation. For OH formation, the relative contribution from Fe and BBA are fairly similar (Fig 4.13a) while Fe being the most significant contributor to H_2O_2 concentrations (Fig 4.13b).

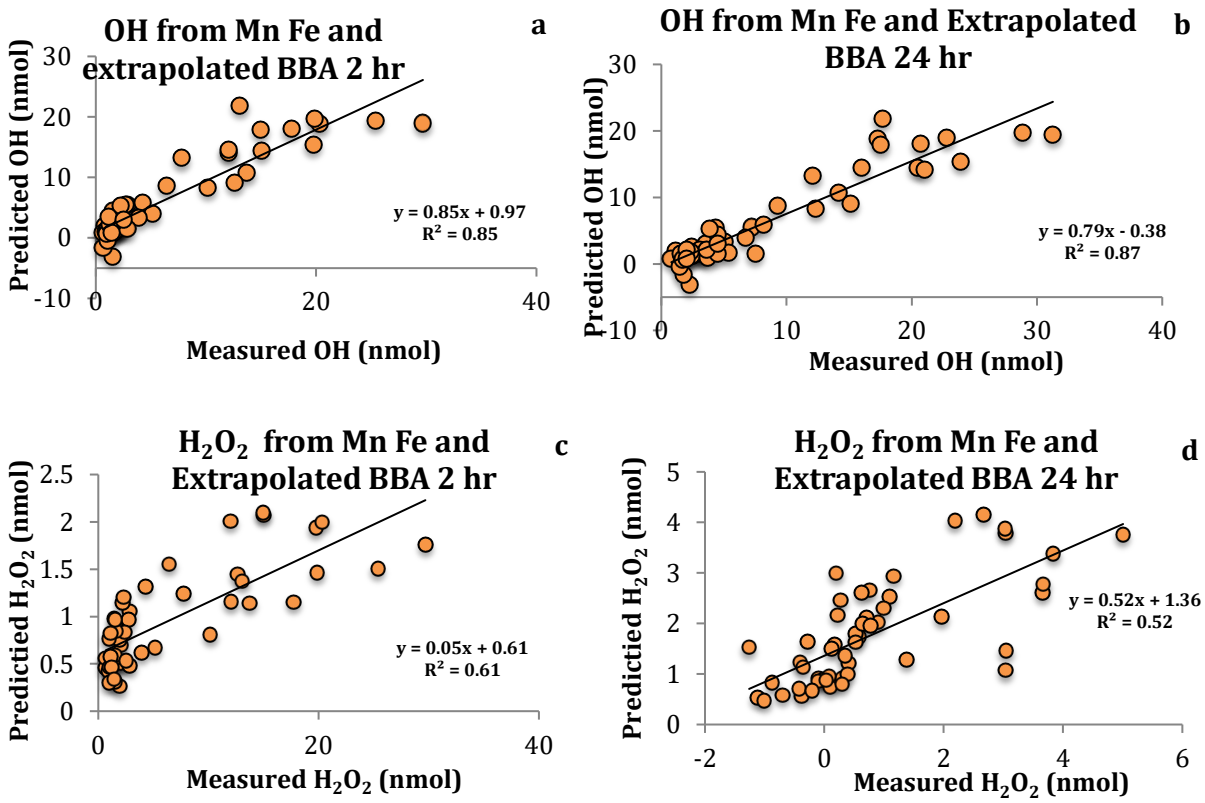

Fig. 4.12 Relationships between measured ROS and predicted ROS from significant variables.

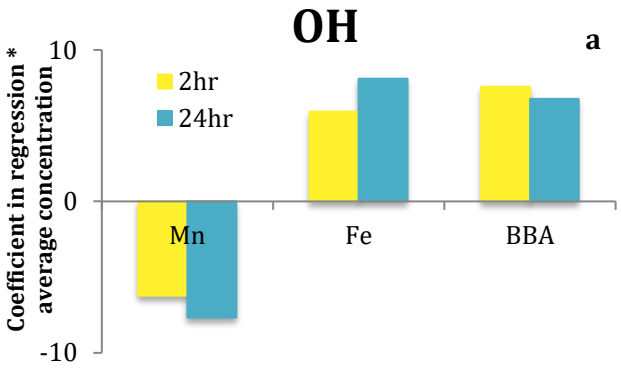
OH
a
Coefficient in regression * average concentration
10
0
-10
2hr
24hr
Mn
Fe
BBA

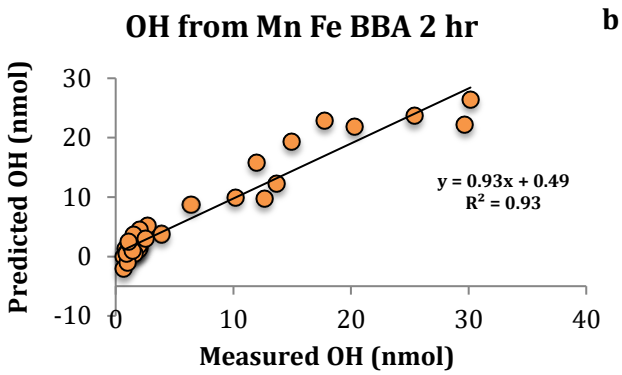
OH from Mn Fe BBA 2 hr
b
Predicted OH (nmol)
30
20
10
0
-10
0
10
20
30
40
y = 0.93x + 0.49
R² = 0.93
Measured OH (nmol)

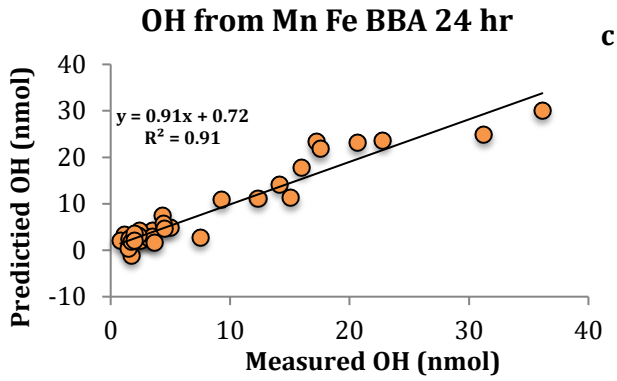
OH from Mn Fe BBA 24 hr
c
Predicted OH (nmol)
40
30
20
10
0
-10
0
10
20
30
40
y = 0.91x + 0.72
R² = 0.91
Measured OH (nmol)

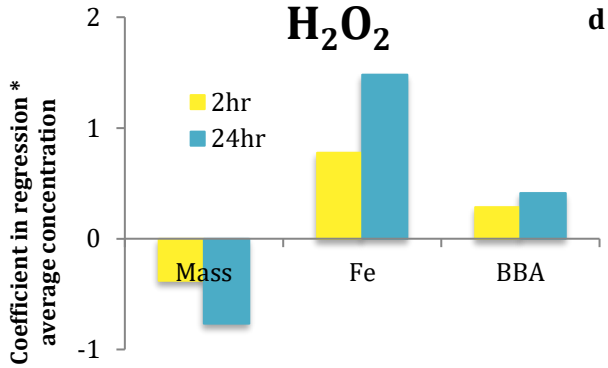
H2O2
d
Coefficient in regression * average concentration
2
1
0
-1
2hr
24hr
Mass
Fe
BBA

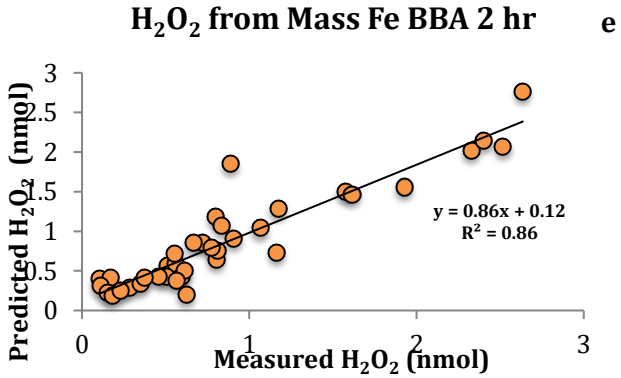
H2O2 from Mass Fe BBA 2 hr
e
Predicted H2O2 (nmol)
3
2.5
2
1.5
1
0.5
0
0
1
2
3
y = 0.86x + 0.12
R² = 0.86
Measured H2O2 (nmol)

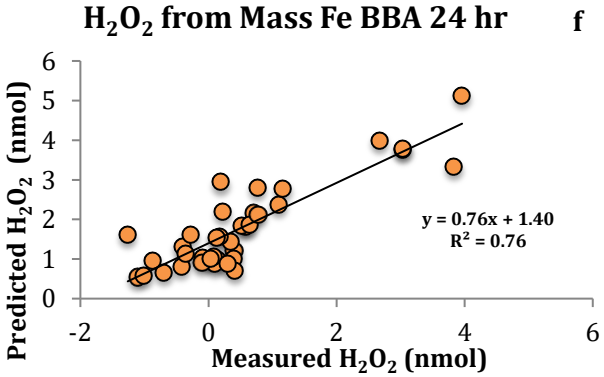
H2O2 from Mass Fe BBA 24 hr
f
Predicted H2O2 (nmol)
6
5
4
3
2
1
0
-2
0
2
4
6
y = 0.76x + 1.40
R² = 0.76
Measured H2O2 (nmol)

Fig. 4.13 Contribution of each variable to OH (a) and H_2O_2 (b) in the Fresno samples.

Tab. 4.3 Multivariate linear regressions for H_2O_2 and OH at 2 and 24 hr.
Tab. 4.3a. Equations derived from multivariate regression for H_2O_2 and OH.

	p-value							
OH 2hr	**Mass**	**Mn**	**Fe**	**Cu**	**BBA**	**Intercept**	**Adjusted r2**	**n**
OH =- 1.80 + 9.31 * mass - 8.88 * Mn + 0.27 * Fe	2E-4	1E-4	5E-7			0.14	0.828	35
OH =- 1.58 - 5.15 * Mn + 0.13 * Fe + 47.80 * BBA		6E-4	1E-3		1E-9	0.06	0.919	35
OH =- 1.85 - 3.00 * Mn + 0.25 * Cu + 53.21 * BBA		1E-3		3E-3	0	0.01	0.928	34
OH 24 hr								
OH =- 0.40 - 2.64 * Mn + 0.21 * Cu + 52.58 * BBA		7E-3		0.021	0	0.58	0.919	32
OH = 0.11 - 6.34 * Mn + 0.17 * Fe + 42.76 * BBA		3E-4	3E-4		4E-7	0.9	0.906	33
HOOH 2 hr								
HOOH = 0.12 - 0.24 * mass + 0.07 * Mn + 0.02 * Fe	0.19	0.66	1E-5			0.24	0.82	36
HOOH = 0.17- 0.55 * mass + 0.02 * Fe + 1.81 * BBA	0.02		4E-8		0.03	0.04	0.848	37
HOOH 24hr								
HOOH =- 0.67 - 0.417 * mass - 0.53 * Mn + 0.04 * Fe	0.288	0.14	9E-7			3E-3	0.765	36
HOOH =- 0.64- 1.12 * mass + 0.03 * Fe + 2.59 * BBA	0.04		2E-6		0.18	2E-3	0.741	37

Tab.4.3b. Equations derived from multivariate regression for H_2O_2 and OH including extrapolated BBA values.

	P-value							
OH 2hr	**Mass**	**Mn**	**Fe**	**Cu**	**BBA**	**Intercept**	**Adjusted r2**	**n**
OH =- 0.86 - 5.34 * Mn + 0.13* Fe + 0.17* Cu + 32.33 * BBA		5E-4	2E-3	0.08	3E-9	0.31	0.844	50
OH =- 0.56 - 2.56 * mass - 4.67 * Mn + 0.12 * Fe + 0.14 * Cu + 39.88 * BBA	0.33	5E-3	4E-3	0.19	5E-5	0.54	0.844	50
OH =- 0.80 - 5.10 * Mn + 0.15 * Fe + 32.92 * BBA		1E-3	1E-4		3E-9	0.36	0.837	50
OH =- 1.27 - 2.09 * Mn + 0.30 * Cu + 37.87 * BBA		0.06		0.004	5E-11	0.17	0.812	50
OH 24 hr								
OH =- 0.38 - 1.97 * Mn + 0.32 * Cu + 41.97 * BBA		0.07		0.001	9E-13	0.67	0.864	48
OH = 0.20 - 4.37 * Mn + 0.14 * Fe + 37.94 * BBA		5E-3	6E-04		1E-10	0.82	0.869	48
HOOH 2 hr								
HOOH= 0.1842 - 0.3441 * mass + 0.3554 * Mn + 0.0115 * Fe	0.07	0.09	2E-2			0.17	.589	52
HOOH= 0.25- 0.91 * mass + 0.48* Mn + 0.01 * Fe - 0.0012 * Cu + 2.25 * BBA	0.01	0.03	2E-1	0.93	0.06	0.05	0.605	52
HOOH= 0.34- 0.64 * mass + 0.02 * Fe + 1.55 * BBA	0.05		1E-6		0.16	0.01	0.581	52
HOOH 24hr								
HOOH =- 0.49 - 0.91 * mass + 0.03 * Fe + 1.55 * BBA	0.24		1.E-5		0.56	0.09	0.49	52
24 HOOH =- 0.63 - 0.61 * mass + 0.32 * Mn + 0.03 * Fe	0.18	0.52	1E-2			0.03	0.491	52

4.4 Atmospheric Implication

In this study we quantified ROS generation by ambient PM relevant to the processes taking place in cloud and rainwaters in the dark. The PM concentrations in extraction solutions are higher than those found in atmospheric water but more resemble those in aerosol water. Our results indicated that ROS generation are greatly enhanced in the presence of BBA. Several other studies have shown that BBA can promote Fenton and Fenton-like reactions by enhancing the

redox cycles of metals; this would likely influence the chemistry in atmospheric waters and potentially enhance organic pollutant degradation. Further studies on BBA quantification and the understanding of the mechanism of BBA promoted Fenton reaction are required to incorporate these processes in cloud water chemistry models.

References

Arellanes, C., S. E. Paulson, P. M. Fine, C. Sioutas (2006). Exceeding of Henry's law by hydrogen peroxide associated with urban aerosols. Env. Sci. Tech. 40:4859-4866.

Baker, J., J. Arey, R. Atkinson (2005). Formation and reaction of hydroxycarbonyls from the reaction of OH radicals with 1, 3-butadiene and isoprene. Env. Sci. Tech. 39:4091-4099.

Buxton, G. V., C. L. Greenstock, W. P. Helman, A. B. Ross (1988). Critical review of rate constants for reactions of hydrated electrons, hydrogen atoms and hydroxyl radicals (· OH/· O− in aqueous solution. J. Phys. Chem. Reference Data 17:513-886.

Charrier, J. G., A. S. McFall, N. K. Richards-Henderson, C. Anastasio (2014). Hydrogen Peroxide Formation in a Surrogate Lung Fluid by Transition Metals and Quinones Present in Particulate Matter. Env. Sci. Tech. 48:7010-7017.

Charrier, J. G. and C. Anastasio (2015). Rates of Hydroxyl Radical Production from Transition Metals and Quinones in a Surrogate Lung Fluid. Env. Sci. Tech. 49:9317-9325.

Chung, M. Y., R. A. Lazaro, D. Lim, J. Jackson, J. Lyon, D. Rendulic, A. S. Hasson (2006). Aerosol-borne quinones and reactive oxygen species generation by particulate matter extracts. Env. Sci. Tech. 40:4880-4886.10.1021/es0515957.

Decesari, S., M. C. Facchini, E. Matta, F. Lettini, M. Mircea, S. Fuzzi, E. Tagliavini, J. P. Putaud (2001). Chemical features and seasonal variation of fine aerosol water-soluble organic compounds in the Po Valley, Italy. Atmos. Environ. 35:3691-3699.

Deguillaume, L., M. Leriche, K. Desboeufs, G. Mailhot, C. George, N. Chaumerliac (2005). Transition metals in atmospheric liquid phases: Sources, reactivity, and sensitive parameters. Chem. Rev. 105:3388-3431.

Duarte, R. M., C. A. Pio, A. C. Duarte (2005). Spectroscopic study of the water-soluble organic matter isolated from atmospheric aerosols collected under different atmospheric conditions. Analytica Chimica Acta 530:7-14.

Ge, X., Q. Zhang, Y. Sun, C. R. Ruehl, A. Setyan (2012). Effect of aqueous-phase processing on aerosol chemistry and size distributions in Fresno, California, during wintertime. Environmental Chemistry 9:221-235.

Gonzalez, D. H., C. K. Cala, S. E. Paulson (Submitted). HULIS Enhancement of OH by Fe(II): Kinetics of Suwannee RIver Fulvic Acid-Fe(II) Complexes in the Presence of Lung Antioxidants. Env. Sci. Tech.

Gorin, C. A., J. L. Collett Jr, P. Herckes (2006). Wood smoke contribution to winter aerosol in Fresno, CA. Journal of the Air & Waste Management Association 56:1584-1590.

Havers, N., P. Burba, J. Lambert, D. Klockow (1998). Spectroscopic characterization of humic-like substances in airborne particulate matter. Journal of Atmospheric Chemistry 29:45-54.

Krivácsy, Z., A. Gelencsér, G. Kiss, E. Mészáros, Á. Molnár, A. Hoffer, T. Mészáros, Z. Sárvári, D. Temesi, B. Varga (2001). Study on the chemical character of water soluble organic compounds in fine atmospheric aerosol at the Jungfraujoch. J. Atmos. Chem. 39:235-259.

Kuang, X. M., J. A. Scott, G. O. da Rocha, R. Betha, D. J. Price, L. M. Russell, D. R. Cocker, S. E. Paulson (2017). Hydroxyl radical formation and soluble trace metal content in particulate matter from renewable diesel and ultra-low sulfur diesel in at-sea operations of a research vessel. Aerosol Sci. Tech.:1-12.

Kuang, X. M., D. H. Gonzales, d. l. R. G., J. A. Scott, C. K. Cala, P. S.E. (Submitted). The Terephthalate Probe for Hydroxyl Radicals: Yield of 2-Hydroxy Terephthalic acid, Transition Metal Interference and Separation from Complex Organics in Environmental Samples.

Li, Y. and M. A. Trush (1993). DNA damage resulting from the oxidation of hydroquinone by copper: role for a Cu (II)/Cu (I) redox cycle and reactive oxygen generation. Carcinogenesis 14:1303-1311.

Li, Y. B. and M. A. Trush (1993). Oxidation of Hydroquinone by Copper: Chemical Mechanism and Biological Effects. Arch. Biochem. Biophys. 300:346-355.

Lin, P., A. G. Rincon, M. Kalberer, J. Z. Yu (2012). Elemental Composition of HULIS in the Pearl River Delta Region, China: Results Inferred from Positive and Negative Electrospray High Resolution Mass Spectrometric Data. Env. Sci. Tech. 46:7454-7462.

Matthews, R. W. (1980). The Radiation Chemistry Of The Terephthalate Dosimeter. Radiation Research 83:27-41.10.2307/3575256.

Moonshine, M., Y. Rudich, S. Katsman, E. Graber (2008). Atmospheric HULIS enhance pollutant degradation by promoting the dark Fenton reaction. Geophys. Res. Lett. 35.

Nevin, K. P. and D. R. Lovley (2002). Mechanisms for Fe (III) oxide reduction in sedimentary environments. Geomicrobiol. J. 19:141-159.

Neyens, E. and J. Baeyens (2003). A review of classic Fenton's peroxidation as an advanced oxidation technique. Journal of Hazardous materials 98:33-50.

NOAA (2017). Air Resources Laboratory.

Parworth, C. L., D. E. Young, H. Kim, X. Zhang, C. D. Cappa, S. Collier, Q. Zhang (2017). Wintertime water- soluble aerosol composition and particle water content in Fresno, California. J. Geophys. Res., Atmos.

Piccolo, A. and P. Conte (2000). Molecular size of humic substances. Supramolecular associations versus macromolecular polymers. Adv. Environ. Res 3:508-521.

Pignatello, J. J., E. Oliveros, A. MacKay (2006). Advanced oxidation processes for organic contaminant destruction based on the Fenton reaction and related chemistry. Critical reviews in environmental science and technology 36:1-84.

See, S. W., Y. H. Wang, R. Balasubramanian (2007). Contrasting reactive oxygen species and transition metal concentrations in combustion aerosols. Environ. Res, 103:317-324.

Shafer, M. M., D. A. Perkins, D. S. Antkiewicz, E. A. Stone, T. A. Quraishi, J. J. Schauer (2010). Reactive oxygen species activity and chemical speciation of size-fractionated atmospheric particulate matter from Lahore, Pakistan: an important role for transition metals. Journal of Environmental Monitoring 12:704-715.

Shang, Y., C. Chen, Y. Li, J. Zhao, T. Zhu (2012). Hydroxyl radical generation mechanism during the redox cycling process of 1, 4-naphthoquinone. Env. Sci. Tech. 46:2935-2942.

Stookey, L. L. (1970). FERROZINE - A new Spectrophotometric reagent for iron. Anal. Chem. 42:779.

Tan, Y., Y. B. Lim, K. Altieri, S. Seitzinger, B. J. Turpin (2012). Mechanisms leading to oligomers and SOA through aqueous photooxidation: insights from OH radical oxidation of acetic acid and methylglyoxal. Atmospheric Chemistry and Physics 12:801-813.

Voelker, B. M. and B. Sulzberger (1996). Effects of Fulvic Acid on Fe(II) Oxidation by Hydrogen Peroxide. Env. Sci. Tech. 30:1106-1114.

Voelker, B. M., F. M. M. Morel, B. Sulzberger (1997). Iron Redox Cycling in Surface Waters: Effects of Humic Substances and Light. Env. Sci. Tech. 31:1004-1011.

Wang, Y., C. Arellanes, S. E. Paulson (2012). Hydrogen Peroxide Associated with Ambient Fine Mode, Diesel and Biodiesel Aerosol Particles in Southern California. Aerosol Sci. Tech. 46:394–402.

Young, D. E., H. Kim, C. Parworth, S. Zhou, X. Zhang, C. D. Cappa, R. Seco, S. Kim, Q. Zhang (2016). Influences of emission sources and meteorology on aerosol chemistry in a polluted urban environment: results from DISCOVER-AQ California. Atmos. Chem. Phys. 16:5427-5451.

5. Hydroxyl Radical Formation and Trace Metal Content in Particulate Matter from Renewable Diesel and Ultra Low Sulfur Diesel in At-Sea Operations of a Research Vessel

5.1 Introduction

In order to reduce carbon emissions and their effects on global warming and ocean acidification, conversion of marine vessels to fuels derived from renewable (plant-based) sources could be a reasonable alternative to fossil fuel based diesels, such as ultra-low sulfur diesel or ULSD. Hydrotreating of vegetable oil has been shown to produce a renewable biodiesel (hydrogenation-derived renewable diesel or HDRD; also referred to as hydrogenated vegetable oil or HVO) that is more compatible with many existing diesel engines than other untreated biofuels (Aatola et al., 2008; Bugarski et al., 2015; 2016; Heikkilä et al., 2012; Kim et al., 2014; Prokopowicz et al., 2015; Westphal et al., 2013). However, there is little information on whether using HDRD instead of ULSD in marine vessels would improve or exacerbate health effects in and near port areas. Clearly both HDRD and ULSD are improvements over the heavy fuel oil (HFO) currently in wide use in ocean transport. While currently they comprise a small fraction of fuel used for ocean transport, ULSD and similar cleaner fuels are currently required inside the 200 mile zone around the coastal United States, in major shipping lanes and ports throughout Europe, and in other areas, HFO is scheduled for global phase-out in 2020 (ICCT 2014). Shipping-related particle emissions have been estimated to be responsible for nearly 60,000 deaths annually (Corbett et al., 2007). Although the mechanisms for most of these deaths is unknown, inhaled PM is thought to induce oxidative stress via biochemical reactions mediated by reactive oxygen species (ROS) (Baulig et al., 2003; Dellinger et al., 2001), and oxidative

stress is believed to underlie a number of diseases related to particulate matter inhalation (Diaz et al., 2013; Li et al., 2003). ROS are a class of reactive oxygen-bearing compounds that include the hydroxyl radical (OH), hydrogen peroxide (H_2O_2) and superoxide (O_2^-) and related species.

A handful of studies have examined the ability of diesel PM to produce ROS and pro-inflammatory responses in both cellular and a-cellular assays (Baulig et al., 2003; Cheung et al., 2009; Verma et al., 2010; Wang et al., 2012). Baulig et al. (2003) showed that the pro-inflammatory response of bronchial epithelial cells was induced by PAH-related compounds associated with the diesel exhaust particles. The response was further shown to be reduced by the addition of antioxidants, suggesting that the response to the PM is due to the presence of species in the particles that produce ROS. Verma et al. (2010) assessed the contribution of water-soluble transition metals present in diesel exhaust to the formation of reactive oxygen species (ROS), using a macrophage-based in vitro assay to determine the ROS activity of collected particles. Results indicated that soluble metals, especially Fe but also Cr, Co and Mn accounted for a significant fraction of the ROS activity. Cheung et al. (2009) used the dithiothreitol assay to examine ROS production from biodiesel and conventional diesel particles, and found relationships with organic carbon, including both water soluble and water-insoluble fractions. The biodiesel particles had significantly more ROS formation activity than the diesel particles. Wang et al. (2012) found that diesel and biodiesel particles from a diesel generator produced similar H_2O_2 formation, in both cases at much higher levels than urban ambient particles. H_2O_2 is one of the precursors to OH formation, however it is measured in steady state, rather than cumulatively as is OH, thus the H_2O_2 is more sensitive to species that can destroy it, such as free iron.

Several studies have reported that HDRD combustion results in lower PAH emissions than diesel fuel (Heikkilä et al., 2012; Jalava et al., 2012; Westphal et al., 2013). Westphal et al. (2013) further accessed the potential toxicity of diesel, hydrotreated vegetable oil and other biodiesel fuels using *Salmonella Typhimurium* strains, which are particularly sensitive to mutagens in organic extracts of diesel exhaust particles. Results showed that the mutagenicity of the HDRD emissions was the lowest compared to all other fuels tested. Furthermore, Jalava et al., (2012) collected PM from a EURO IV automobile engine powered by different fuel and performed inflammation, cytotoxicity and cell apoptosis analyses and ROS production using an intracellular dichlorofluorescein (DCFH) assay. In most cases, HDRD showed lower toxic potencies than conventional diesel fuel. While studies on HFO particulate emissions are few, in a recent and thorough study using lung epithelial cells and other analyses, Oeder et al., (2015) found that HFO particulate emissions had higher metal and organic content but lower black carbon content in comparison to conventional diesel emissions. Consistent with the relationships between ROS production, inflammation and transition metals, Oeder et al. (2015) also found that HFO particles had much higher inflammatory responses than conventional diesel emissions.

ROS, and particularly the hydroxyl radical investigated here, can also mediate particle aging processes in ambient aerosols and cloud drops. Aerosol aging plays an important role in modifying aerosol chemical composition (Donahue et al., 2012; Sato et al., 2011; Shrivastava et al., 2008; Shrivastava et al., 2008), hygroscopicity (Buchholz et al., 2009; Zhang et al., 2008), cloud condensation nuclei activity (Engelhart et al., 2008; Shilling et al., 2007; Wang et al., 2010) and optical properties (Reid et al., 1999). While much of the aerosol aging is likely mediated by heterogeneous reactions of OH radicals from the gas phase, the contribution of

reactions within the particles is not well understood. Similar ROS-mediated oxidation chemistry in cloud water may underlie some secondary organic aerosol (SOA) formation associated with cloud processing (Larsen et al., 2001; Zhang et al., 2010), some of this is photochemical, but the (dark) ROS chemistry probed here may be particularly important when photochemical processes shut down (Graedel et al., 1986). While ROS formation under physiological and environmental conditions are related, because of the differences in pH and concentrations of solutes, they are not necessarily well correlated.

Currently there are a number of assays available to measure ROS as a general class, as well as assays for specific ROS. General acellular assays include dichlorofluorescein (King and Weber 2013), dithiothreitol (Fang et al., 2014) or antioxidant consumption (Godri et al., 2011). Each has a different and largely uncharacterized response to H_2O_2, OH, and O_2^- etc. There are several assays for specific ROS assays such as OH (this work, (Charrier and Anastasio 2011; DiStefano et al., 2009) and H_2O_2 (Arellanes et al., 2006; Shen et al., 2011). Differences in the assays and their sensitivities to specific ROS likely explain at least some of the differences in conclusions about which particulate matter components are responsible for ROS. A series of studies by Charrier, Anastasio and co-workers have provided many insights into the behavior of a series of contributors to ROS by quantifying differences in responses to individual and pairs of transition metals and quinones to several individual antioxidants (Charrier and Anastasio 2011; 2012; Charrier et al., 2014), but there is more work to be done to develop an understanding of ambient aerosol behavior. Still uncertain are the roles of other variables including particularly organic/brown carbon but also pH, other solutes and black carbon, as well as the concentrations of the reactants.

Here we probe OH formation, which has been shown to be mediated by transition metals, with contribution from quinones (Charrier and Anastasio 2011; DiStefano et al., 2009). Other aerosol components are expected to influence OH formation by altering the activity of transition metals (Gonzalez et al., 2017), or other unknown mechanisms. We measure OH production and trace metal content of particle samples collected both from the engine stack and by intercepting the ship plume alternately on HDRD and ULSD fuels in 2014 and 2015. Samples were extracted either in simulated lung fluid (SLF) containing three antioxidants present in lung lining fluid: ascorbate, glutathione and uric acid (Charrier and Anastasio 2011; Kelly et al., 1995), with citrate added to mimic transition metal chelating ability of proteins in lung fluid (Godri et al., 2011; Lund and Aust 1992; Smith and Aust 1997) or in water adjusted to pH3.5 to probe in-situ reactivity of the PM in marine air. Samples were analyzed for OH formation activity, water-soluble elements, PM and black carbon mass concentrations normalized to both particle mass and kg fuel burned. The measurements provide an evaluation of the changes in reactivity and soluble transition metals, under both physiological and environmental conditions, associated with switching fuels, and a measure of their reactivity compared to urban and mixed marine particulate matter.

Simultaneous measurements of particle and gas mass emission and chemical composition and concentrations are reported in two companion papers (Betha et al., 2016; Price et al., 2016). Betha et al. (2016) showed that emission factors for CO and NO_x were higher for ULSD than HDRD, and EFs decreased with increasing engine speed. Different trends were observed for black carbon and particle number, with higher number and mass emission factors for HDRD. The organic composition of particle-phase ship emissions from both fuels consisted of two types

of hydrogen-like organic aerosol, one containing more saturated alkane fragments (diesel type) and the other more mono-unsaturated fragments (cooking type). The latter was more abundant in PM from HDRD. The ULSD aerosol emissions also contained significant oxidized organic material, while HDRD emission did not, although this result is based on a small number of samples of ULSD-derived PM. The aged plumes consisted of a larger contribution from sulfate (a major component of the marine background), and contributions from oxygenated and in some cases diesel-type hydrocarbon organic aerosol. Cooking type aerosol was completely reduced or absent in HDRD aged plumes (Price et al., 2016).

5.2 Methods

During two dedicated sampling cruises in 2014 (29 September to 3 October) and 2015 (4 to 7 September and 26 to 28 September), the fuel tanks of the R/V *Robert Gordon Sproul* were filled with Ultra Low Sulfur Diesel (ULSD) and Hydrogenation-Derived Renewable Diesel (HDRD), which were used alternately in the existing diesel engines. Properties of the HDRD and ULSD fuels used in this study are shown in Tab. 5.1. Since the ship was not equipped with an engine dynamometer, sampling was conducted at four engine speeds (1600 rpm, 1300 rpm, 1000 rpm, 700 rpm). Nonetheless, emissions at any engine speed did vary with sea state and other conditions (Betha et al., 2016). Simultaneous measurements of gas and particle emissions are described in companion papers (Betha et al., 2016; Price et al., 2016).

Tab. 5.1 Properties of HDRD and ULSD in this study as well as other biodiesels. (Betha et al., 2016; Betha et al., 2016)

	HDRD[a]	**ULSD[b]**	**Biodiesel[c]**
Cetane Number	75.2	>41[b,f]	41.7 - 63.6
Density@15 C (kg/m^3)	780.4	<876 [b]	864 - 894
Sulphur (mg/kg)[d]	<1	< 1	
Flash Point (^{0}C)	69 C	>52 C[b]	
Ash Content (wt%)	<0.001	<0.01[b]	

Water Content (mg/kg)	67	0.05[b]	
Sedimentation (mg/kg)	1.5		
Oxidation Stability (g/m^3)	4		
Total Acid Number (mgKOH/g)	0.002		0.01-10.1
Viscosity @40 C (mm^2/s)	3.048	1.9 – 4.1[b]	3.99 - 5.82
Final Boiling Point (^{0}C)	306.6		
Cloud Point (^{0}C)	-19		
Electrical Conductivity @21 ^{0}C (pS/m)	169	>50[b]	
Aromatics (Vol %)	<1		
FAME Content (Vol %)[d]	< 0.5	< 0.5	
Carbon (wt%)[d]	84.69 - 85.02	84.59 - 86.22	75.15-76.25
Nitrogen (wt%)[d]	0.0001 – 0.0016	0.0002-0025	
Oxygen (wt%) [e]	0 – 0.16	0.12 – 0.16	11.04 - 11.82
Hydrogen (wt%) [d]	14.82 – 15.35	13.62 – 15.26	12.59 - 13.62

[a]From the certificate of analysis of the fuel batch bought from Neste Oil. Neste Oil manufactures HDRD from Animal Fats, Used Cooking oil and Technical Corn oil (https://www.neste.com/fi/en/companies/products/renewable-products/neste-renewable-diesel-0; https://en.wikipedia.org/wiki/NEXBTL)
[b]ULSD specifications from US OIL & Refining Co. (http://www.usor.com/files/pdf/5/ULSDspec.pdf)
[c] Fuel properties of 28 different biodiesels produced through transesterification (Graboski et al., 2003)
[d] Fuel analysis results conducted by Southwest Research Institute
[e] Estimated as 100 – (C-H-N-S)
[f] Cetane Index

5.2.1 Particle Collection

All samples subjected to ROS and related analyses were collected on pre-weighed, acid cleaned 47mm Teflon filters (0.2µm pore size, Pall Corp; Paulson et al. 2016). Prior to collection of each sample, the collection flow rate was checked using a digital mass flow meter (TSI). After collection, the filters were transported and stored in individual Teflon petri dishes sealed with Teflon tape and stored in a freezer at or below 0°C for later analysis. The mass of samples collected was determined gravimetrically by weighing the filters before and after sample collection using a micro balance (1 μg precision, ME 5, Sartorius) in a temperature (22-24º C)

and humidity (40-45%) controlled room, equipped with a sodium lamp to avoid interactions with light.

For the 2014 cruise, fresh emissions were collected directly from the ship stack using a Venturi probe (Nigam 2007) followed by a $PM_{2.5}$ cyclone operating at 16.05 LPM, for 15-20 minutes for each. A separate sampling van located on the aft deck equipped with a $PM_{2.5}$ cyclone (URG-2000-30ENB) operating at 92 LPM was used to collect 2015 samples as well as the 2014 mixed samples. Fresh emissions were collected as the vessel was moving so the travel time from the stack to the van inlet (a distance of approximately 20 m) was less than 30 s. These samples were much more diluted and cooled compared to the stack samples, and collection times were about 60 min. Additional samples were collected from re-intercepting the aged ship plume, and overnight samples captured a mixture of ship emissions and marine background aerosols. Both of these types of samples are classified as "mixed" in the following sections primarily because there are too few to treat them separately.

To create full field blanks, able to detect contamination from any where along the sample train, blanks were collected in the same manner as the samples, by loading blank filters into the filter holders for 30 s. Very minimal to no detectable material was collected on the blank filters.

5.2.2 Analyses

5.2.2.1 Materials

Trifluoroethanol (TFE), sodium citrate tribasic dihydrate (Cit), L-ascorbic acid (Asc), uric acid sodium salt (UA), and L-glutathione reduced (Yan et al.,), Chelex-100 sodium form (50-100 dry mesh) and 0.1 N sulfuric acid were purchased from Sigma Aldrich. Sodium

phosphate dibasic and potassium phosphate monobasic were purchased from Acros Organics. Nitric acid (70% trace metal grade) was purchased from Fisher. All materials were used as received.

5.2.2.2 Extraction solutions

Simulated Lung Fluid (SLF) was prepared by adding four antioxidants (Cit, Asc, UA, and GSH) at 100 μM UA and GSH, 300 μM Cit and 200 μM Asc, to phosphate buffer at pH 7.2-7.4. Phosphate buffer contained 114 mM of NaCl, 7.8 mM of sodium phosphate dibasic and 2.2 mM of potassium phosphate monobasic, and was chelex-treated to remove trace metals prior adding the antioxidants. The antioxidants were freshly prepared in phosphate buffer for each experiment.

pH 3.5 solution was prepared by acidifying 18 MΩ deionized (DI) water using 0.1N sulfuric acid. The pH meter was calibrated prior to each use.

5.2.2.3 Trace metal cleaning and particle extraction

A rigorous cleaning process was followed for all glass and Teflon containers. After each use, each vessel was washed with warm water and soap, and then rinsed in deionized (18 MΩ-cm DI) water (3x), ethanol (3x), and finally DI water (3x). The vessels were then soaked in 1 M nitric acid bath overnight, rinsed with DI water and air dried. Nitric acid baths were replaced after being used twice and kept covered to avoid dust deposition. All analytical solutions were prepared with 18 MΩ-cm DI water that had been passed through a chelex column to remove trace metals.

Filters were cut in half using a cleaned ceramic blade. Half filters were extracted in 6 mL SLF or pH3.5 solution in Teflon petri dishes with gentle agitation. To increase particle solubility,

the filters were wetted first with 50 μ L of trifluoroethanol.

5.2.2.4 Hydroxyl radical quantification

OH formation by PM was monitored by adding excess (10mM) sodium terephthalate (TA) to extraction solutions and allowing it to react for two hours. 2-hydroxyterephthalic acid (HTA), a strongly fluorescent product, is produced from the OH reaction with TA with 33% yield at pH 7.2 and 31% at pH 3.5 (Matthews 1980). HTA is detected at excitation/emission wavelength ($\lambda_{ex}/\lambda_{em}$) of 320/420 nm using a fluorometer (Lumina, Thermo Scientific), resulting in a detection limit of about 10^{-10} M. The microcuvettes were cleaned with water and ethanol and dried between each sample measurement. Calibrations were performed daily. To verify the PM did not interfere with our assay, extracts of PM and fuel samples were scanned and observed to have no native fluorescence over any wavelengths of interest.

Many ROS assays have unequal sensitivities to different sources and types of ROS. In some cases, the probe interacts directly with one or more of the metals, potentially changing its redox activity, as in the case for benzoate and Mn (Charrier and Anastasio, 2011). We have carefully examined the terephthalate assay for iron and copper; its response to iron is in excellent agreement with well-known Fenton and related chemistry for iron (Gonzalez et al., 2017), and we additionally verified that the interactions between copper observed at high concentrations and terephthalic acid (Cardarelli et al., 1979) do not take place at the lower concentrations observed here (Kuang et al., in preparation).

5.2.2.5 Water Soluble Metals

Due to limited numbers of samples, soluble element analysis was only performed on samples extracted in SLF. Aliquots from extraction solutions after 2 hours were filtered through 0.2 um polypropylene syringe filters (VRW International) and then acidified to 2% (by weight) with HNO_3, and stored in 15 ml Falcon conical centrifuge tubes. An Agilent 8800 Triple Quadrupole ICP-MS was used to measure the following elements and transition metals in the MS/MS mode: Mg, S, K, Ca, V, Cr, Mn, Fe, Co, Ni, Cu, Zn, Se, Cd, La, Pb. Calibration curves were made from a 10 ppm 33 multi-element standard (SCP Science) using ^{89}Y as an internal standard (Inorganic Ventures MSY-100PPM) to correct for matrix effects. Five replicate measurements were averaged for each individual sample. All reported metals were well above their detection limits. The average variation between replicate measurements of the same sample was 1.3%, and it never exceeded 5% for any individual sample.

Fuel samples were collected from the tank truck as the fuel was pumped into the research vessel. A micro-emulsion technique following the ICP manufacturer's protocol was used to dissolve crude oil into a water matrix. 1% of crude oil was mixed with 1% of the surfactant TRITON-X100 (Electrophoresis Grade, International Biotechnologies Inc.) and sonicated for 60 minutes, and then analyzed for metals following the above procedures.

5.2.2.6 Black carbon quantification

Black carbon was quantified using an OT21 duel wavelength optical transmissometer (Magee Scientific Corporation). A quartz diffuser backing (Pallflex Fiberfilm) was placed under each 47mm Teflon filter to provide an even distribution of light to the detector. Absorption at

880 nm is proportional to the concentration of black carbon (Hansen et al., 1984) expressed by the following equation:

$$[BC] = \frac{bATN}{\sigma(\lambda)} \quad (5.1)$$

Where b_{ATN} is the attenuation coefficient and $\sigma(\lambda)_{ATN}$ (m^2/g) is the specific attenuation cross section. The EPA empirically determined $\sigma(\lambda)_{ATN}$ value of 16.6 m^2g^{-1}, suggested by the manufacturer for engine derived BC, was used for this calculation.

5.3 Results

5.3.1 OH formation in SLF.

The number of samples analyzed for each fuel and year, together with the numbers of samples analyzed for soluble elements is summarized in Tab. 5.2. Fig. 5.1a shows the averages, medians and standard errors (1σ) for OH production in SLF, normalized to aerosol mass, by year and fuel. Most of the sample sets included one or two samples with much higher activity than the others, resulting in a high degree of sample variability, thus medians may be a better metric than averages.

OH production normalized to kilograms of fuel burned is shown in Fig. 5.1b. Values are shown only for 2015, as in 2014 stack sample CO_2 measurements were not available due to instrument problems (Betha et al., 2016). Consistent with the observation that PM mass emissions were higher for HDRD than ULSD (Betha et al., 2106), once normalized to fuel burned, the differences between 2015 ULSD and HDRD OH generation activity is larger than the PM-mass normalized data.

For both fuels, the 2015 samples had higher activity than the 2014 samples. The averages of the HDRD samples were higher than the ULSD samples for both years (Fig. 5.1a, Tab. 3), and medians were higher for 2014 but almost identical for 2015. Differences were significant ($p < 0.05$) for 2014 averages and medians on a PM mass basis (Fig. 5.1a), and 2015 averages on a per kg fuel basis (Fig. 5.1b). OH production from PM in mixed/aged ship samples was much higher than the fresh samples, and all samples in this study were significantly lower than average OH formation for Los Angeles urban air samples analyzed with the same techniques (Paulson et al., 2016). Relationships with chemical composition of the particle are presented below.

OH production separated by fuel, by engine speed and by year

Fig. 5.2 shows OH production in SLF separated by fuel, year and engine speed. While most engine condition and fuels were tightly clustered, frequently a single sample from a set was higher by a factor of 3 or more than the comparison samples. As a result, when separated by engine speed, none of the conditions are different at the 95% confidence level. For HDRD, OH generation increased at lower engine speed, while for ULSD there was a slight decrease as engine speed was lowered.

Fig. 5.2a shows the average values in SLF by engine speed for both years combined, and Fig 5.2b shows each year separately. Fig. 5.2c shows values for samples extracted in pH3.5. For S1a, 2014 and 2015 data were combined after adjusting the 2014 values by multiplying them by $\bar{x}_{2015}/\bar{x}_{2014}$ for each engine speed and fuel to place values on the same scale. For HDRD, OH generation increases at lower engine speed, while for ULSD there is a slight decrease. When grouped by engine speed, none of the conditions are different at the 95% confidence level. Figures S1b and S1c show the average OH production by engine speed for both fuels in both

years. Without adjusting OH concentration at the same scale, OH production in SLF is substantially higher in 2015 at all engine speeds (Fig. 5.2b). Such difference is not as large for OH production in pH3.5 solutions, a result that may be a result of small sample numbers; e.g. there are one or two samples at each engine speed (Fig. 5.2c).

Tab. 5.2 Number of samples analyzed for ULSD and HDRD in 2014 and 2015 cruises. Numbers in parentheses indicate the number of metal samples analyzed and bolded values indicate average aerosol mass in mg.

2014 Cruise		1600 rpm	1300 rpm	1000 rpm	700 rpm	Total
ULSD	SLF	4 (2) **0.69**	3 (1) **0.26**	1 **0.18**	2 (1) **0.25**	10 **0.42**
	pH3.5	2 **0.82**	2 **0.24**	1 **0.18**	2 **0.25**	7 **0.40**
HDRD	SLF	2 (1) **1.00**	2 (1) **0.32**	2 (2) **0.10**	2 (1) **0.15**	8 **0.39**
	pH3.5	1 **1.63**	1 **0.40**		1 **0.18**	3 **0.74**
Mixed	SLF	3 (2) ULSD **0.51**	5 (2) HDRD **0.61**			8 **0.57**
	pH3.5	2 **0.18**				1
2015 Cruise		**1600 rpm**	**1300 rpm**	**1000 rpm**	**700 rpm**	**Total**
ULSD	SLF	2 (1) **0.09**	2 (1) **0.11**	2 (1) **0.11**	3 (2) **0.09**	9 **0.10**
	pH3.5	1 **0.04**	1 **0.03**	1 **0.04**	1 **0.06**	4 **0.04**
HDRD	SLF	6 (5) **0.05**	6 (5) **0.06**	7 (6) **0.10**	7 (6) **0.09**	26 **0.08**
	pH3.5	1 **0.03**	1 **0.05**	1 **0.08**	1 **0.12**	4 **0.07**
Mixed	SLF	3 (3) ULSD **0.03**	11(9) HDRD **0.07**			14
	pH3.5	1 **0.09**				

Tab. 5.3 Summary of mass normalized average and standard errors for all metrics. BC and BrC concentrations were not reported for the 2015 data sets due to low aerosol mass on the filters.

2014 Cruis	Mass (mg)	OH (SLF)	OH (pH3.5)	BC	Mg	Ca	S	Zn	Ni	V	Cr	Mn	Fe	Cu	Se	Co	Ag	Cd	Pb
		(ng/µg)								(pg/µg)									
ULSD	0.42 ±0.09	0.09 ±0.03	0.03 ±0.005	225 ±50	4.0 ±1.2	21 ±7	156 ±40	8.6 ±2.5	0.06 ±0.01	40.2 ±33	20 ± 8	16 ±3	190 ±50	570 ±270	16 ±3	1.5 ±0.5	0.24 ±0.1	0.6 ±0.4	9 ±3
HDRD	0.39 ±0.2	0.14 ±0.03	0.02 ±0.002	190 ±40	4.1 ±0.6	25 ±5	290 ±50	27 ±10	0.12 ±0.02	7.2 ±2.0	35 ±12	21 ±6	150 ±30	181 ±45	44 15	3.5 ±0.8	0.15 ±0.1	0.12 ±0.07	11 ±6
Mixed	0.57 ±0.18	0.47 ±0.15	0.12 ±0.04	142 ±20	3.1 ±1.0	6.7 ±1.5	145 ±40	3.6 ±0.7	0.055 ±0.02	40.5 ±27.1	12.8 ±6.5	16 ±9	180 ±100	600 ±310	12 ±4	1.5 ±0.4	2.9 ±1.1	0.85 ±0.15	18 ±8
2015 Cruis	**Mass (mg)**	**OH (SLF)**	**OH (pH3.5)**	**BC**	**Mg**	**Ca**	**S**	**Zn**	**Ni**	**V**	**Cr**	**Mn**	**Fe**	**Cu**	**Se**	**Co**	**Ag**	**Cd**	**Pb**
		(ng/µg)								(pg/µg)									
ULSD	0.10 ±0.02	0.35 ±0.06	0.01 ±0.002		6.6 ±0.9	18 ±5	14 ±13	9 ±2	0.06 ±0.02	2.7 ±1	14 ±6	18 ±3	160 ±50	380 ±120	22 ±9	2.2 ±0.7	0.47 ±0.3	0.6 ±0.2	6 ±3
HDRD	0.13 ±0.03	0.42 ±0.07	0.05 ±0.001		15 ±1.7	60 ±17	492 ±190	60 ±30	0.12 ±0.02	48 ±15	40 ±8	65 ±10	276 ±61	2016 ±360	29 ±5	7.4 ±3	4.8 ±3.5	3.3 ±1.3	45 ±10
Mixed	0.07 ±0.01	0.50 ±0.05	0.02		23 ±3	52 ±18	94 ±46	46 ±30	0.08 ±0.02	29 ±5	37 ±6	79 ±20	530 ±140	1070 ±165	56 ±13	5.0 ±1	15 ±9	2.6 ±1.3	14 ±4

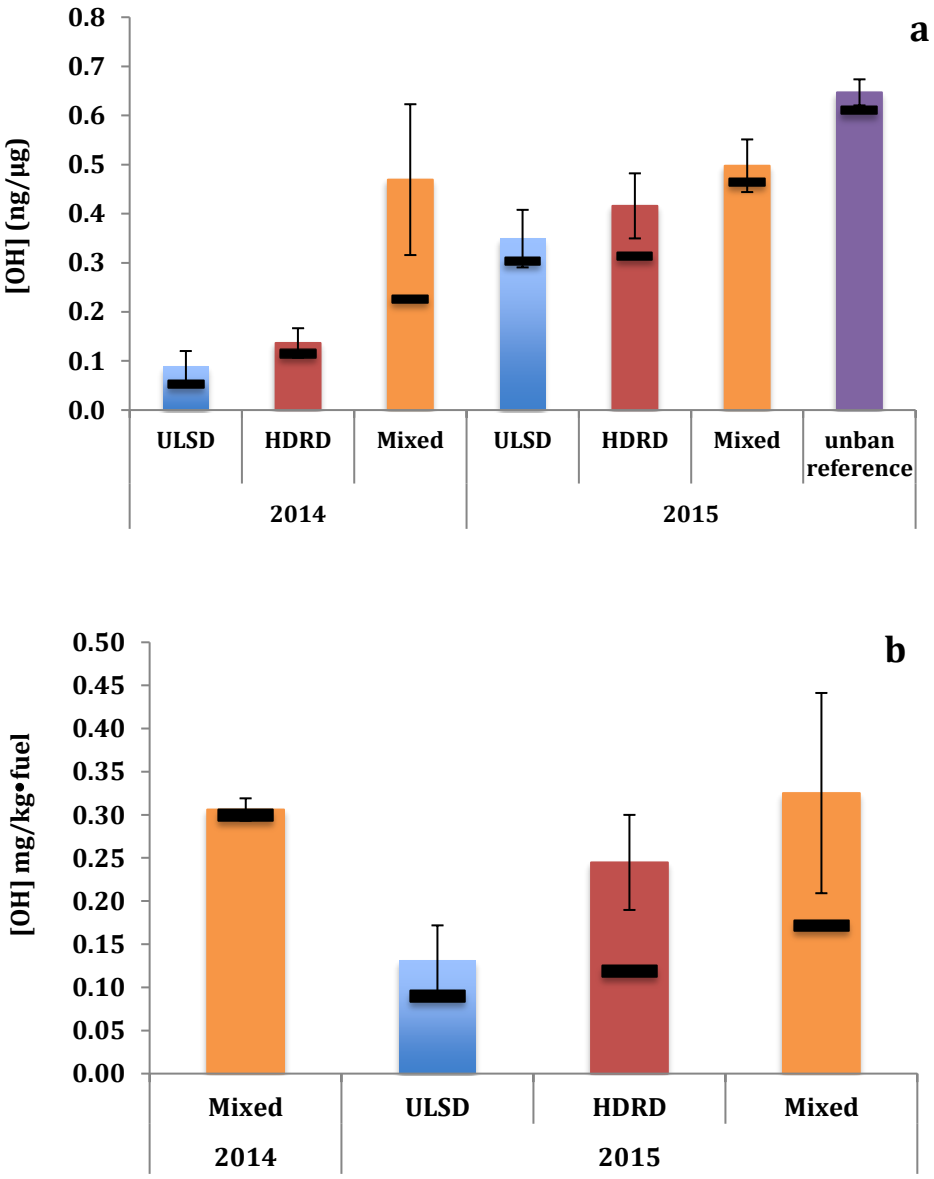

Fig. 5.1 a) Average (color bar), median (black horizontal bar) and standard errors (vertical error bars) of OH (ng/µg PM) production by year and fuel (1a) and Average and standard error of OH (mg/kg fuel) in b) ULSD and HDRD are the samples from engine cycle tests, with all of the engine speed combined.

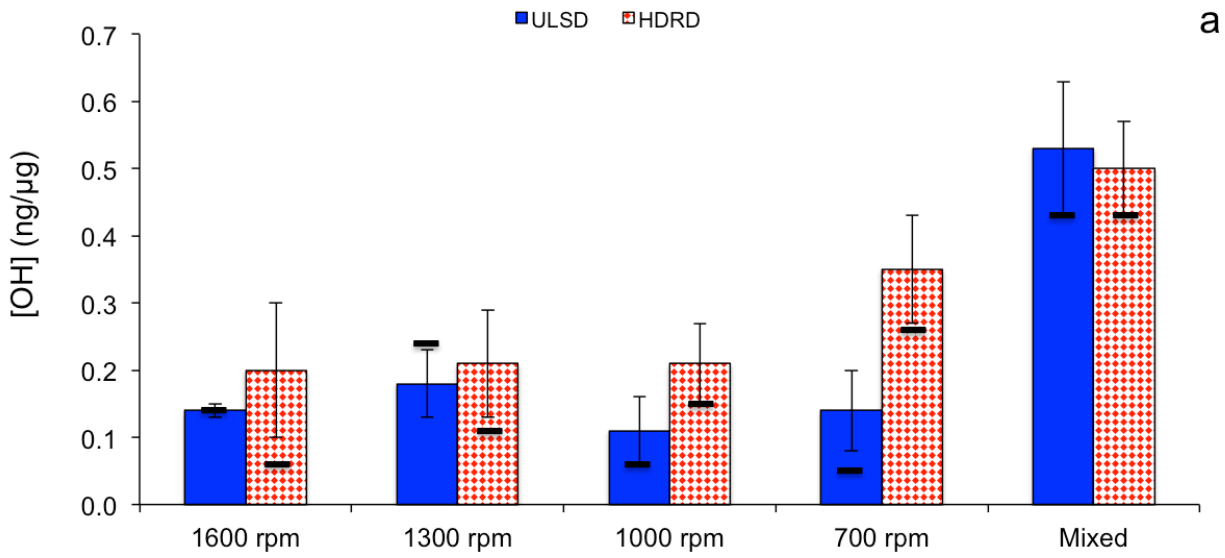
a
ULSD
HDRD
[OH] (ng/µg)
0.7
0.6
0.5
0.4
0.3
0.2
0.1
0.0
1600 rpm
1300 rpm
1000 rpm
700 rpm
Mixed

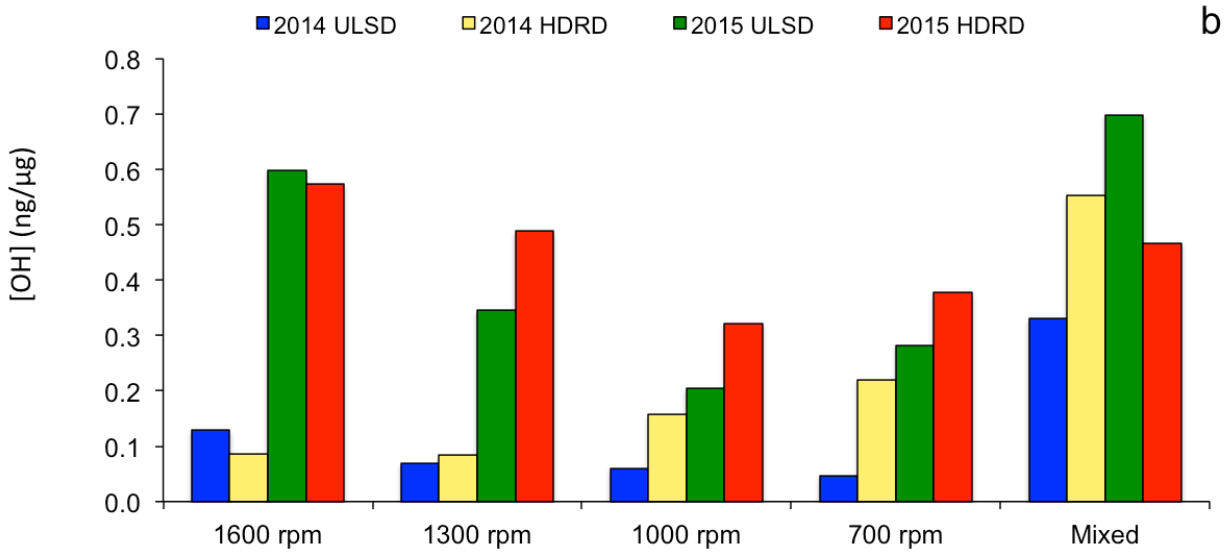
b
2014 ULSD
2014 HDRD
2015 ULSD
2015 HDRD
[OH] (ng/µg)
0.8
0.7
0.6
0.5
0.4
0.3
0.2
0.1
0.0
1600 rpm
1300 rpm
1000 rpm
700 rpm
Mixed

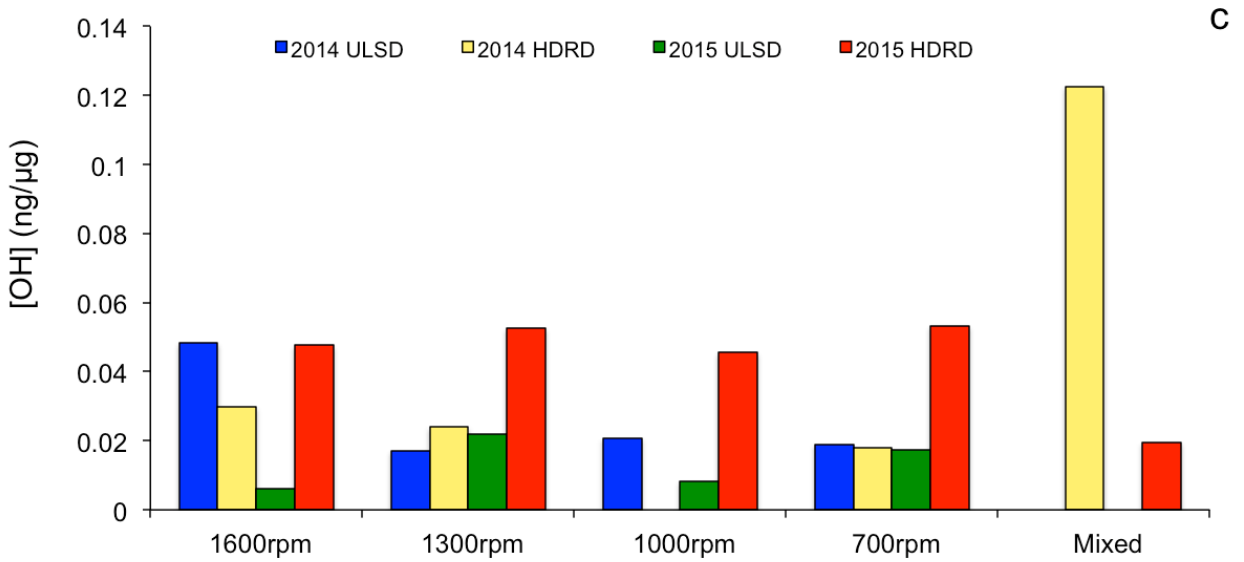

Fig. 5.2 Average and standard error of OH production in SLF by fuel and engine speed. 2014 and 2015 values were combined after adjusting for the average difference between 2014 and 2015, black bars represent median values (1a), average and standard error of OH production in SLF (1b) and pH3.5 (1c) divided by year and engine speed.

5.3.2 Relationship between OH formation and PM mass

For combined 2014 and 2015 data, OH formation by particles was not correlated to mass. However, for the ULSD, HDRD and mixed subsets of the 2014 data, OH formation was strongly correlated with mass (Fig. 5.3). The 2015 data (which had much lower masses) still showed little or no correlation with mass when separated by sample type (Fig. 5.3). 2014 fuel-specific slopes were 1.4, 2.7 and 5.5, for ULSD, HDRD and mixed samples respectively (adjusted r^2 of 0.34 to 0.96, Fig. 5.3). Similar trends were observed for OH activity vs. absorbance at 880 nm (a proxy for black carbon) for the 2014 samples (Fig. 5.4), measured on the filters by transmissometer; 2015 filters had too little absorbance for accurate measurement of BC. The clearly differentiated behavior of different sets of samples indicates that components (such as transition metals) other

than total mass, BC and/or associated organics are driving factors in OH production, consistent with results presented below.

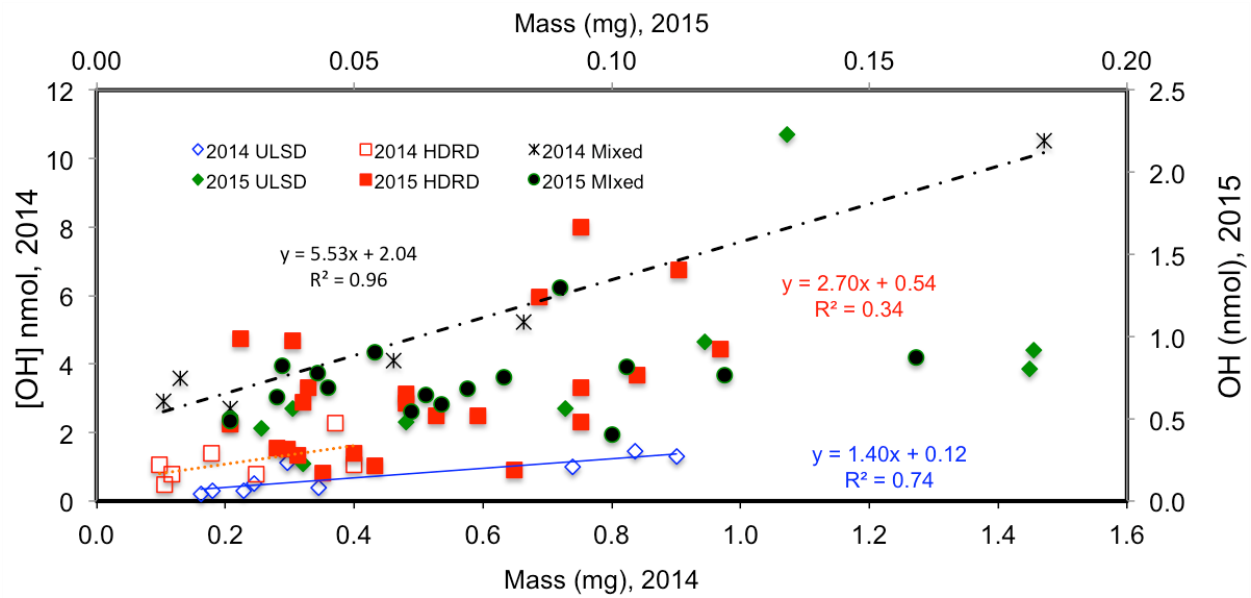

Fig. 5.3 Correlations between OH production (nmol) and mass (mg) for ULSD, HDRD and mixed samples in 2014 and 2015 cruises. The secondary x-axis and y-axis represent ULSD and mixed samples in 2015, which has much lower PM mass and non-mass normalized OH production.

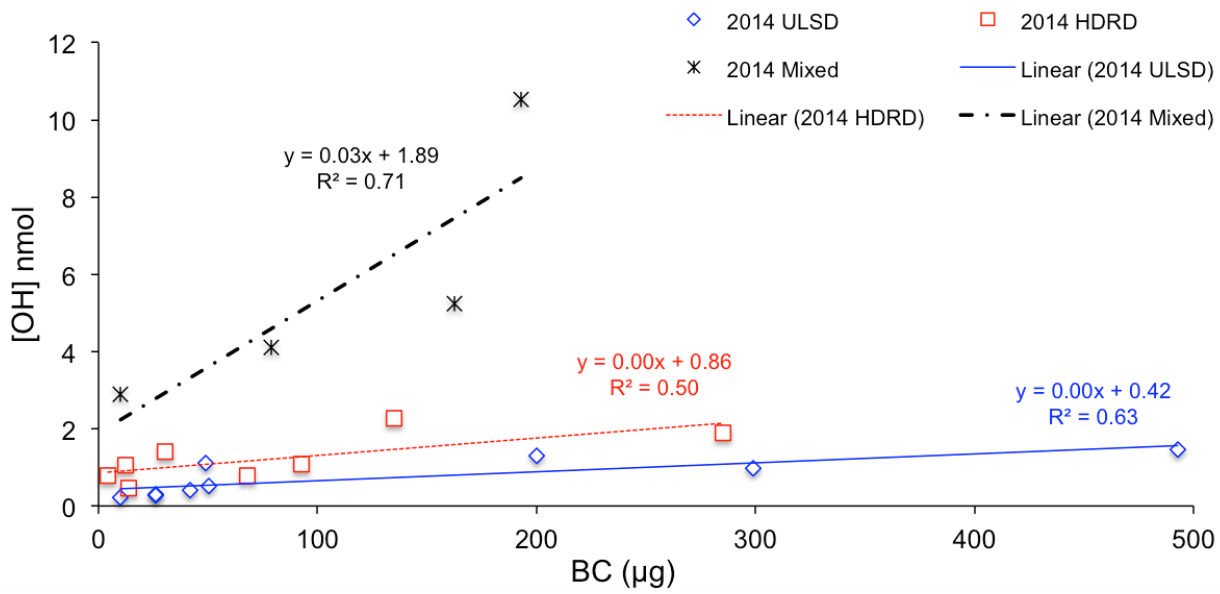

Fig. 5.4 Correlation between OH production (nmol) and black carbon (μg) measured with an Aethalometer (Magee Scientific) at 880nm. Average and standard error of BC is reported in Table S1 and it accounts for 33% of total aerosol mass.

5.3.3 Water soluble trace metals

Median concentrations and standard errors for transition metals, sulfur and selenium in the ship samples extracted in SLF are shown in Fig. 5.5a. 68 % of SLF-extracted samples were analyzed for trace metals, thus corresponding OH production for this subset of samples, with slightly different values from Fig. 5.1a, is also shown in Figure 5.5a. The metal concentrations for a Los Angeles urban data set, analyzed with the same methods (Paulson et al., 2016) are also included for reference, as well as metal concentrations for fresh diesel PM collected from a school bus and extracted in water by Verma et al. (2010).

All of the soluble PM metal concentrations in the ship samples were in the same range as the urban and bus emission PM concentrations (Fig. 5.5a). Compared to the urban concentrations, ship PM had similar V, similar or slightly higher Ni, Cr and Se, and lower Mn and Fe. Cu and Pb were lower in the ship PM except in the case of 2015 HDRD, which had markedly higher Cu and Pb than the other ship samples. Concentrations of V, Cr and Mn in the ULSD ship emissions were similar to those observed by Verma et al. (2010) for conventional diesel emissions while Cu, Fe and Pb were much lower. For all ship samples except 2015 ULSD, sulfur was much higher than the bus emissions. The 2014 stack samples generally had lower soluble metal concentrations than the 2015 samples. While the reasons for this are not clear, it may be related to the lack of even minimal atmospheric processing of the particles in the stack samples, differences in OM content (unfortunately the OM content wasn't measured in the 2014

stack samples due to an instrument issue). It could also possibly stem from an artifact from the stack dilution system, such as size dependent sampling losses in the Venturi inlet.

Few other reports of soluble transition metals in related samples are available. Jalava et al. (2012) reported trace metal concentrations, in PM from a heavy duty Euro IV engine on a chassis dynamometer burning HDRD and ULSD (En590) extracted in aqueous 0.08N HNO_3. Compared to our 2015 HDRD values, they observed lower Cu, V, Ni and Pb (4-23% of our values), and Cr at 124%, Mn at 54% and Fe at 232% (not shown in Fig. 5.5 for clarity). For reference, the Jalava et al. (2012) ULSD trace metal concentrations were 55-243% of the values reported by Verma et al. (2010) except V and Pb, which were 21, and 6% respectively. Jalava et al. (2012) found slightly lower intercellular ROS activity for HDRD in comparison to ULSD PM, consistent with the slightly lower transition metals in the HDRD compared to the ULSD PM.

Figure 5.5b shows the 2015 mass of soluble metals per kg of fuel, as well as the mass of metals per kg of fuel for three of the fuels used in this study, 2014 and 2015 ULSD and 2015 HDRD. Generally, the trace metal PM concentrations shown in Fig. 5.5b (Cr, Cu, Fe, Mn, Pb, Se and V) are in reasonably good agreement with the corresponding fuel values, averaging 146 and 242% for ULSD and HDRD, respectively. V is much higher in the PM for both fuels, Mn and Cu are somewhat higher in the PM, and Fe is much lower, Ni and Pb are lower in PM than the fuels, while Cr for both fuels and Se in ULSD are similar (Fig. 5.5b and Tab. 5.4), although none of the differences are significant given the variability in the measurements. If V is excluded, the PM from ULSD and HDRD average 79 and 131% of the fuel values. Overall however, given the scatter in the data, too much should not be made of the differences. There are several potential

sources of differences between fuel and PM metal concentrations, including engine wear (Agarwal et al., 2003), lubricating oil, and deposition within the engine (Wang et al., 2003). We were not able to measure metals in the lube oil as part of the study. Metals in lube oil have been reported to be dominated by non-redox active oil additives such as Ca, Zn and P (Agarwal et al., 2010) and to account for < 1% of the resulting total PM mass (Storey et al., 2015). The lower concentrations of Fe in the fuel and PM may be due to losses of Fe in the engine, but they may also be explained by a significant portion of the Fe in the PM being in an insoluble form. Fe forms many complexes and tends to be less soluble especially at higher pHs than many other transition metals (Deguillaume et al., 2005).

In comparison to fresher PM, trace element concentrations in plume chase and nighttime samples (labeled "mixed," Fig. 5.5) were higher for 2015 V, Mn, Fe, Se and Cu and in 2014 for Cu; other elements were similar except 2014 Fe, which was lower. OH formation in the mixed samples was higher than the corresponding fresh samples, consistent with the higher concentrations of soluble redox active metals, and suggesting metal solubility increases rapidly as aerosols are aged. Evidence for increasing ROS production as fresh combustion aerosols are aged, although not necessarily directly linked to metal solubility, has also been provided by McWhinney et al. (2012), Li et al. (2009) and Rattanavaraha et al., (2011).

We were unfortunately not able to collect pure marine background filter samples, however online measurements indicated very low PM mass concentrations in the marine boundary layer, less than about 0.5 $\mu g/m^3$ (Price et al., 2016), compared to average mass concentrations in the mixed samples above 15 $\mu g/m^3$. Metals in marine aerosols have been reported in a few instances (Baker et al., 2013; Chance et al., 2015) but these studies did not

report aerosol mass, and extracted in organic solvent, so it is difficult to compare with these measurements.

For the whole dataset, some soluble elements were fairly strongly correlated with one another (Tab. 5.5), including Cr and Co (R^2 = 0.57), Mn and Fe (R^2 = 0.47), Mn and Cu (R^2 = 0.61), and Cu and Pb (R^2 = 0.50). Additionally, Mn, Fe, Cu and Pb were all cross-correlated with one another at the $p < 0.05$ level. Divided by fuel, there are a handful of strong correlations, but no consistent patterns for ULSD or HDRD between the two years (not shown). S and V are commonly used as tracers of ships burning high sulfur fuels such as bunker fuel (Arhami et al., 2009; BluewaterNetwork 2000; Lin et al., 2005). The much cleaner ULSD and HDRD used here did not consistently produce high S and produced little V emissions. Further, the ratio of V/Ni was less than one, similar to on-road diesel engine exhaust (Lin et al. 2005) rather than above 1.5, the expected value for heavy oil marine fuels (Arhami et al. 2009).

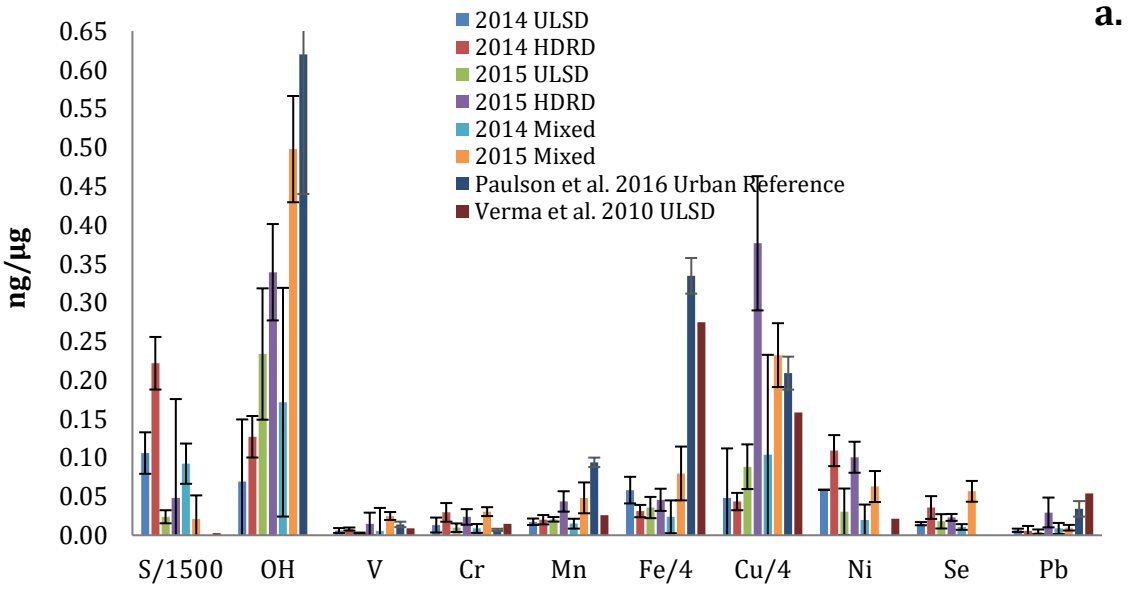

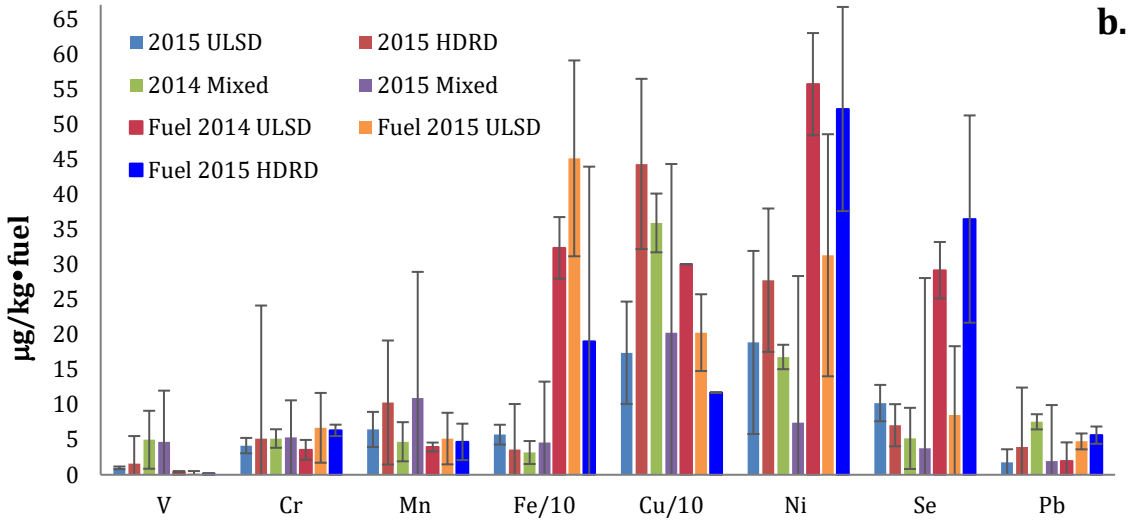

Fig. 5.5 a) ICP-MS/MS concentrations of water-soluble transition metals in the exhaust PM (in ng metal or element/µg PM), S and Se in the ship samples, an urban data set (Paulson et al., 2016) and in diesel engine exhaust (Verma et al. 2010). All samples were extracted in SLF solution (see text) except Verma et al. (2010), who used water. Note that there are somewhat fewer samples with metal analysis than OH (Table 1), thus the average OH generation for the corresponding sample set is included here. b) Concentrations of water-soluble transition metals in the ship exhaust (**µ**g metal per kg of fuel burned) and in the fuels (**µ**g metal per kg of fuel).

Tab. 5.4 Ratios of median contribution of water-soluble metals in PM extracts to water-soluble metals in fuels.

2015	ULSD	HDRD
V	576%	907%
Cr	62%	82%
Mn	125%	219%
Fe	13%	19%
Cu	86%	377%
Se	120%	19%
Pb	37%	70%

Tab. 5.5 Cross correlations between elements (r^2 values), mass normalized in ng/ μ g. Significant correlations ($p < 0.05$) are in bold; red values indicate a group of metals that all have significant correlations with one another. n indicates the number of samples.

All Fuels, R^2	S	V	Cr	Mn	Fe	Cu	Se	Pb	Co	Ni	n
S	1	0.04	0.01	0.05	0.04	0.10	0.002	0.005	0.001	**0.30**	44
V		1	0.04	**0.07**	0.01	**0.11**	**0.07**	0.06	0.007	**0.16**	57
Cr			1	0.2	**0.10**	**0.11**	**0.10**	0.02	**0.570**	**0.18**	57
Mn				1	**0.47**	**0.61**	**0.22**	**0.29**	**0.070**	**0.47**	58
Fe					1	**0.11**	**0.16**	**0.15**	0.010	**0.17**	56
Cu						1	0.09	**0.50**	0.020	**0.49**	57
Se							1	0.04	0.010	0.12	51
Pb								1	0.010	**0.14**	55
Co									1	0.04	58
Ni										1	57

5.3.4 Relationships between OH generation and transition metals

Overall, OH has reasonably strong single variable correlations with transition metals, after controlling for mass (Tab. 5.6); mass normalization is necessary for this data set because the 2014 ship stack samples had much higher masses than the 2015 van samples (Tab. 5.2). The correlations were strongest for Mn (R^2 = 0.52) followed by Co, Cu, and V all (R^2 = 0.37 – 0.41), and significant ($P < 0.05$) for Fe and Se, as well as Pb, Ni and Mg. Mn, Cu, Fe and V have all been shown to produce OH in SLF in other studies (Charrier and Anastasio 2011; DiStefano et al., 2009; Gonzalez et al., 2017; Paulson et al., 2016); cobalt and the other elements are not expected to be redox active under our conditions (Tab. 5.6). The correlation analyses are confounded by significant co-linearities, as well as large differences in other components in the particles, including BC and organic material (Fig. 5.7 and (Price et al., 2016).

Multivariate analysis of all of the data resulted in the correlation shown in Fig. 5.6; the only combination for which the independent variables were all significant (at $p < 0.05$; here $p < 10^{-3}$ for both Mn and V) includes only Mn and V. Co-linearity tends to reduce the apparent

significance of other variables, thus this result should not be interpreted as ruling out a role for other trace metals. Based on the single variable correlations combined with results from other studies (Charrier and Anastasio 2011; DiStefano et al., 2009; Gonzalez et al., 2017; Paulson et al., 2016) and many others, it is likely that iron and copper also contribute to OH formation here.

Tab. 5.6 Correlations between OH and metals mass normalized in ng/ μ g. Bolded values indicate the significant correlations with p values < 0.05. Italic values indicate that outliers (one for Fe, two each for Ca and Co) were removed. Outliers are defined as the values at least 3 times higher than the next highest value.

	Ca	Mg	S	V	Cr	Mn	Fe	Cu	Se	Pb	Co	Ag	Ni
N	57	59	44	57	57	58	56	57	51	55	58	45	58
R^2	***0.12***	**0.25**	0.03	**0.37**	**0.40**	**0.52**	***0.23***	**0.40**	**0.23**	**0.32**	***0.41***	0.08	**0.28**
Slope	0.002	0.01	-	2.93	5.75	3.42	0.37	0.13	4.98	2.16	44.3	-	1.95

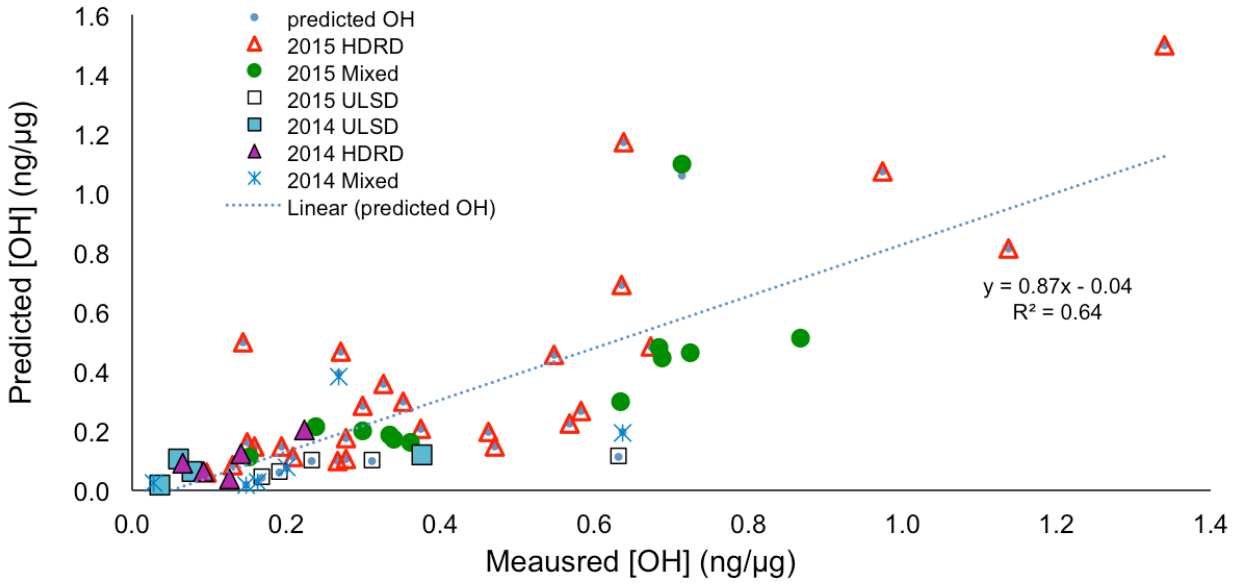

Fig. 5.6 Measured vs. predicted OH (ng/µg) based on the expression 1.84 [V] + 4.23 [Mn] (ng/µg).

5.3.5 Relationships between OH and other chemical components

Fig. 5.7 shows overall chemical composition of the particles using all data that was available for all of the samples. 'Metals' is dominated by Ca, followed by Mg and Zn (Table 5.3), none of which are included in Fig., 5.5, as these are not expected to be redox active. While soluble trace metal concentrations (Figs. 5.5 and 5.7) are able to explain a reasonable amount of the observed variability in OH formation among sample types, the data imply other components are also important. By sample type, OH production generally increases with increasing redox active transition metals; e.g., the sum of Mn, Cu, Fe and V (Fig. 5.5a). However, close examination of the data in Fig. 5.6 shows differences in slopes between sample types; the ULSD slopes are both lower than other data, especially for 2015. These differences may be related to the marked differences in BC content (Fig. 5.7) and in the composition of the organic fraction. In both years, HDRD samples had a smaller fraction of BC in comparison to the ULSD samples. The organic material in the ULSD and HDRD PM was also different; the ULSD particles contained more diesel-type hydrocarbon-like organic aerosol (HOA), while HDRD had more cooking-type HOA (Price et al., 2016). Mixed samples (aged in Price et al. 2016) were more depleted in cooking-type HOA. Organic interactions with metals have been shown repeatedly to be capable of enhancing transition metal solubility (Paris and Desboeufs 2013; Sun and Pignatello 1992; Weng et al., 2002), and differences in organics may be responsible for the higher concentrations of soluble metals and higher OH production in the HDRD and mixed samples, although lower BC could also play a role. The only organic characteristics for which we had sufficient data to perform a regression, the O/C and H/C ratio, were not correlated with OH formation. However, the strong correlations of OH with the several of the metals, may mask more moderate

relationships with other characteristics. The sample set (and subsets) for which we have complete data for OH, elements, O/C and H/C, and BC are unfortunately not sufficiently overlapping to perform a multivariate analysis that includes transition metals together with any of the carbon-based variables, thus further testing of this hypothesis is not possible with this data set.

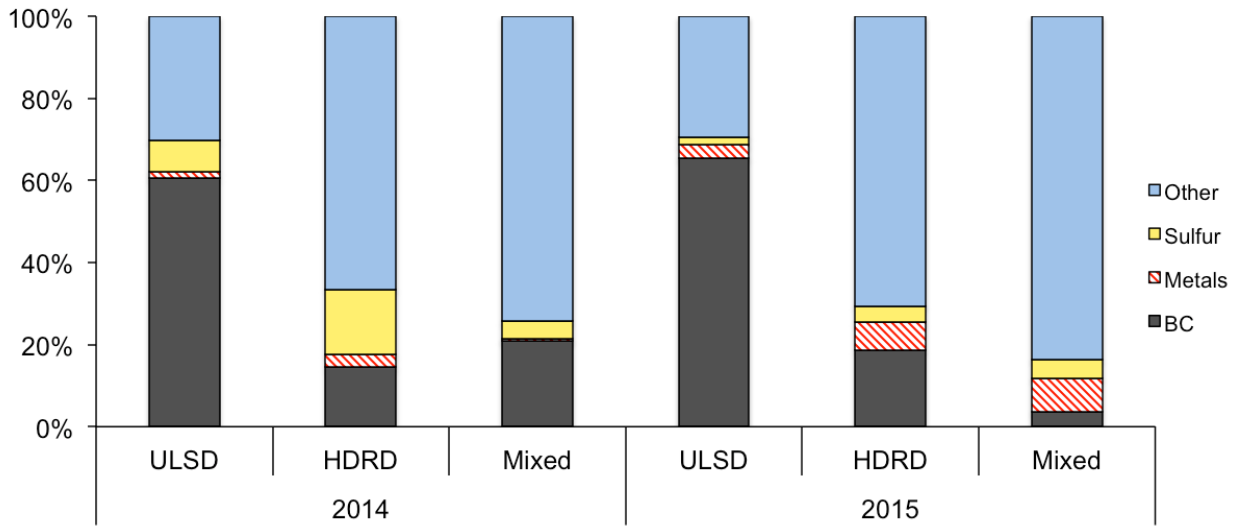

Fig. 5.7 Median chemical composition of different sample types. Total "Metals" includes 13 metals and Se, but was dominated by Mg, Ca, and Zn (Table S2). BC mass concentrations in all 2014 samples were measured with an Aethalometer (Paulson et al. 2016) and BC mass concentrations in 2015 samples were measured with an SP2 (Betha et al. 2016).

5.3.6 pH 3.5: OH production under atmospherically relevant conditions

OH production by ULSD and HDRD PM emissions was also measured by extracting particles in water at pH 3.5, to mimic acidic aerosol liquid water and nascent cloud water particles (Fig. 5.8). In all cases, activity of the fresh emission samples and the plume chasing samples was substantially smaller than the urban reference data by a factor of 8 ± 4. Similar to SLF extraction, the most active samples were the 2015 HDRD emissions, however in contrast to SLF the pH 3.5 2014 HDRD had slightly lower activity than the ULSD.

OH production averaged 4 ± 2 times lower in pH3.5 compared to SLF extraction solution. The differences between OH production in SLF and pH3.5 solutions are likely largely driven by two factors: the pH dependence of metal solubility, and the availability of antioxidants to chelate metals and/or act as electron donors. Metals such as manganese and copper are already fairly soluble at high pH, while iron solubility increases dramatically between pH 7.2 and 3.5 (Deguillaume et al., 2005). Charrier and Anastasio (2011) showed that in a simplified solutions, one of the antioxidants, ascorbate, can enhance OH formation by more than two orders of magnitude for some metals (particularly Fe, Cu and V). This enhancement was strongly moderated by glutathione and citrate in the solution for Cu and V, but further enhanced for iron. Benzoate, the OH probe used in that study interacts with manganese, so the effect of SLF solutes is not well understood for Mn. These aerosols also contain substantial amounts of black and organic carbon, and this material is also expected to influence OH formation in ways that are pH dependent. For example, the chelation activity of carboxylic acid groups present in complex organic molecules is pH dependent (Tan 2014).

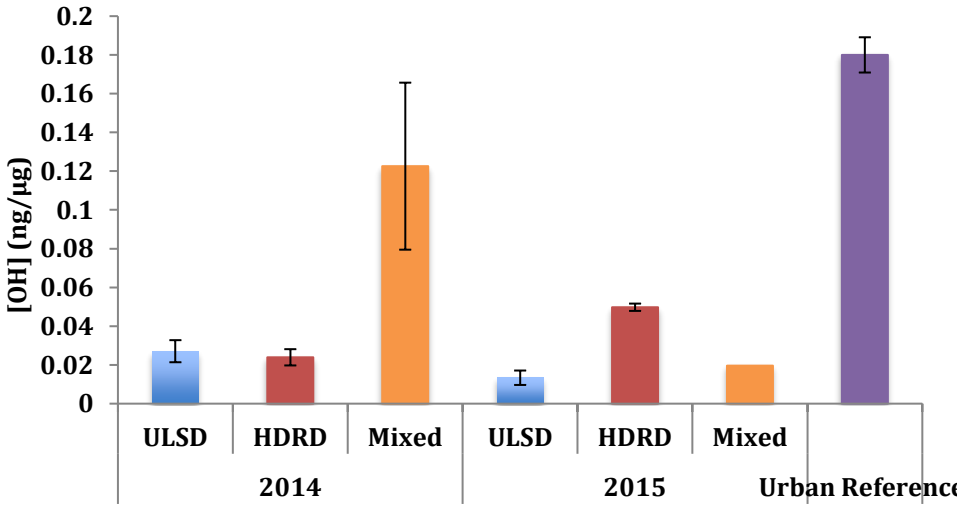

Fig. 5.8 Average and standard error of OH production divided by fuel and year in pH3.5. The 2015 mixed bar contains only one data point, and 2014 contains two.

5.3.7 Comparisons of OH production by different types of particles in SLF

Under the same experimental conditions, OH formation by PM from fresh engine emissions was comparatively lower than the urban PM collected in Claremont and Beijing, but OH from HDRD PM was comparable to those samples collected in Fresh, though slightly lower. The summer PM samples collected in Claremont and Beijing generated substantially more OH. These differences are likely arising from the differences in chemical composition in these samples, particularly due to the presence of the amount of redox active metals, e.g, the sum of Fe, Cu and Mn. As shown in Fig. 5.10, metals typically accounts for ~ 1% of the total aerosol mass. The most abundant metal in most cases is Fe, followed by Zn and Cu. When analyzed together, Figs 5.9 and 5.10 shows that OH concentration increases with the increasing amount of Fe in the samples, implying OH formation is strongly driven by iron chemistry.

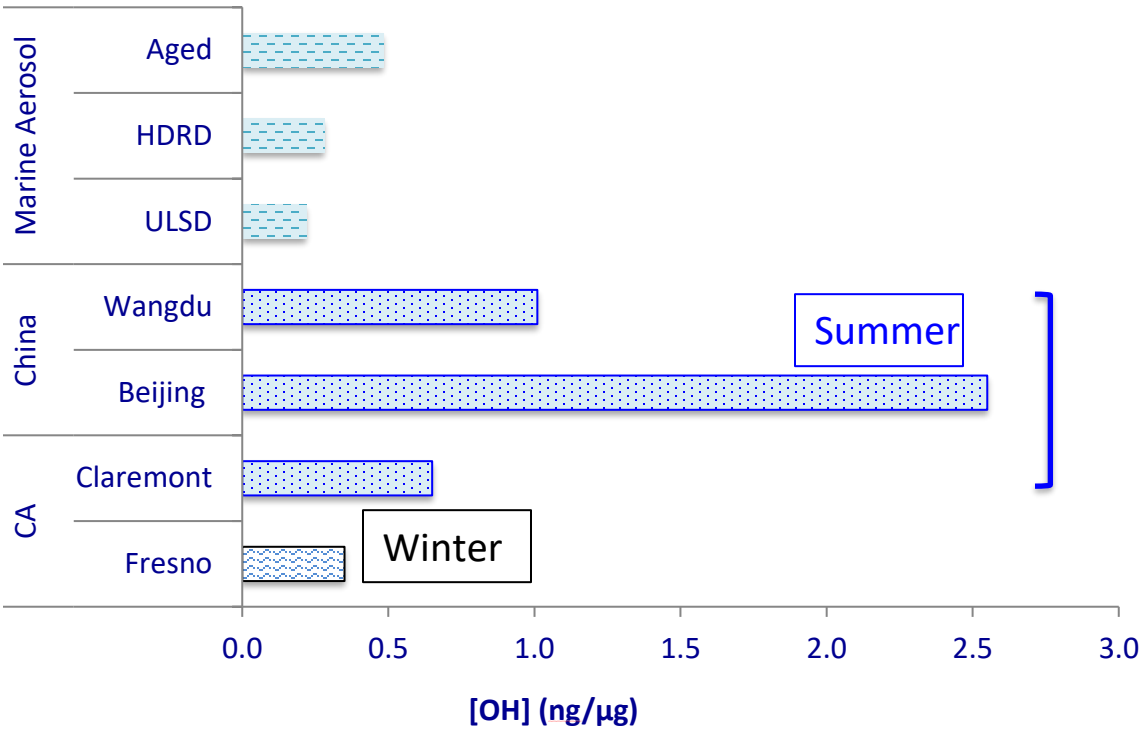

Fig. 5.9 OH production by different particle types in SLF. Claremont, Fresno and Beijing are urban ambient samples; marine aerosols are samples collected from PM of engine emissions operating of ULSD and HDRD.

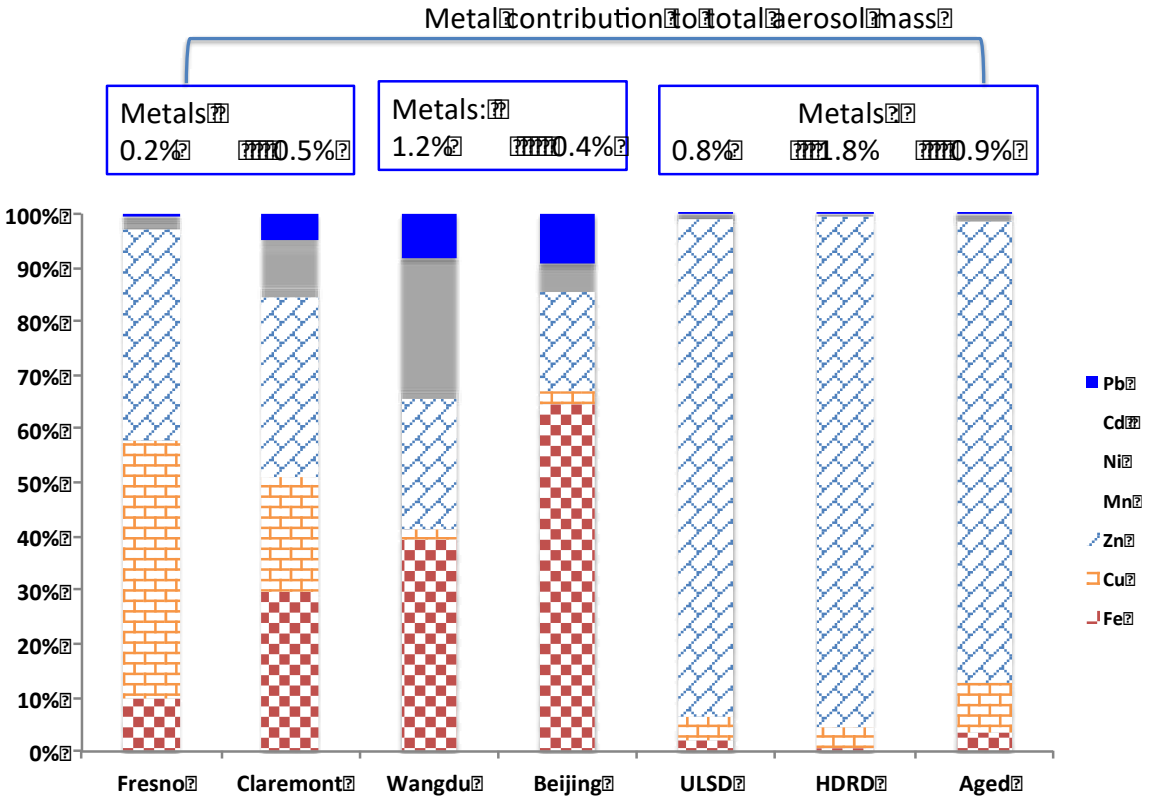

Fig. 5.10 Composition of soluble transition metals in PM collected from Fresno, Claremont, Beijing and marine environment.

5.4 Discussion and Conclusions

The results indicate a large fraction of OH generation is controlled by soluble redox-active transition metals, and are further consistent with the notion that metal solubility increases rapidly as freshly emitted particles are released into the marine boundary layer, which in turn increases OH formation. Concentrations of trace metals in the PM emissions appear to be largely due to trace metals in the fuels. OH formation and soluble metals were as high or higher in HDRD compared to ULSD emissions.

Simultaneous measurements of particle chemical composition and concentrations show that the mass and number of particles also increases in HDRD compared to ULSD engine emissions (Betha et al., 2016). Taken together, these measurements indicate that switching fuels may result in particles that are as or more harmful to human health. However, due to the variability of the results between samples and engine conditions, these results should be verified with additional sampling under a variety of sea and ship conditions.

References

Aatola, H., M. Larmi, T. Sarjovaara, S. Mikkonen (2008). Hydrotreated vegetable oil (HVO) as a renewable diesel fuel: trade-off between NOx, particulate emission, and fuel consumption of a heavy duty engine. SAE paper:2500.

Agarwal, A. K., J. Bijwe, L. Das (2003). Effect of biodiesel utilization of wear of vital parts in compression ignition engine. Journal of Engineering for Gas Turbines and Power 125:604-611.

Agarwal, A. K., T. Gupta, A. Kothari (2010). Toxic potential evaluation of particulate matter emitted from a constant speed compression ignition engine: a comparison between straight vegetable oil and mineral diesel. Aerosol Science And Technology 44:724-733.

Arellanes, C., S. E. Paulson, P. M. Fine, C. Sioutas (2006). Exceeding of Henry's Law by Hydrogen Peroxide Associated with Urban Aerosols. Envir. Sci. Tech. DOI: 10.1021/es0513786.

Arhami, M., M. Sillanpää, S. Hu, M. R. Olson, J. J. Schauer, C. Sioutas (2009). Size-segregated inorganic and organic components of PM in the communities of the Los Angeles Harbor. Aerosol Science And Technology 43:145-160.

Baker, A., C. Adams, T. Bell, T. Jickells, L. Ganzeveld (2013). Estimation of atmospheric nutrient inputs to the Atlantic Ocean from 50n from 50om 50 from 50uts t‐scale field sampling: Iron and other dust‐associated elements. Global Biogeochemical Cycles 27:755-767.

Baulig, A., M. Garlatti, V. Bonvallot, A. Marchand, R. Barouki, F. Marano, A. Baeza-Squiban (2003). Involvement of reactive oxygen species in the metabolic pathways triggered by diesel exhaust particles in human airway epithelial cells. American Journal of Physiology-Lung Cellular and Molecular Physiology 285:L671-L679.

Betha, R., K. J. Sanchez, J. Liu, D. J. Price, M. A. Lamjiri, C.-L. Chen, X. M. Kuang, G. O. da Rocha, S. E. Paulson, J. W. Miller, D. R. Cocker, L. M. Russell (2016). Lower NOx but Higher Particle and Black Carbon Emissions from Renewable Diesel compared to Ultra Low Sulfur Diesel in At-Sea Operations of a Research Vessel. Aerosol Science And Technology:00-00.10.1080/02786826.2016.1238034.

BluewaterNetwork (2000). A stacked deck: Air pollution from large ships. San Francisco , https://georgiastrait.org/wp-content/uploads/2015/03/StackedDeck.pdf.

Buchholz, A., T. F. Mentel, R. Tillmann, E. Schlosser, K. Mildenberger, T. Clauss, S. Henning, A. Kiselev, F. Stratmann (2009). Photochemical aging of secondary organic aerosols: effects on hygroscopic growth and CCN activation, in EGU General Assembly Conference Abstracts, 11:8288.

Bugarski, A. D., J. A. Hummer, S. Vanderslice (2016). Effects of hydrotreated vegetable oil on emissions of aerosols and gases from light-duty and medium-duty older technology engines. Journal of occupational and environmental hygiene 13:293-302.

Cardarelli, E., G. D'Ascenzo, A. Magri, A. Pupella (1979). Complexes of Cobalt (II), Nickel (II) and Copper (II) with the benzenedicarboxylic acids. Thermal properties. Thermochimica Acta 33:267-273.

Chance, R., T. D. Jickells, A. R. Baker (2015). Atmospheric trace metal concentrations, solubility and deposition fluxes in remote marine air over the south-east Atlantic. Marine Chemistry 177:45-56.

Charrier, J. G. and C. Anastasio (2011). Impacts of antioxidants on hydroxyl radical production from individual and mixed transition metals in a surrogate lung fluid. Atmospheric Environment 45:7555-7562. 10.1016/j.atmosenv.2010.12.021.

Charrier, J. G. and C. Anastasio (2012). On dithiothreitol (DTT) as a measure of oxidative potential for ambient particles: evidence for the importance of soluble transition metals. Atmospheric chemistry and physics (Print) 12:11317-11350.10.5194/acpd-12-11317-2012.

Charrier, J. G., A. S. McFall, N. K. Richards-Henderson, C. Anastasio (2014). Hydrogen Peroxide Formation in a Surrogate Lung Fluid by Transition Metals and Quinones Present in Particulate Matter. Environmental science & technology 48:7010-7017.10.1021/es501011w.

Cheung, K. L., A. Polidori, L. Ntziachristos, T. Tzamkiozis, Z. Samaras, F. R. Cassee, M. Gerlofs, C. Sioutas (2009). Chemical characteristics and oxidative potential of particulate matter emissions from gasoline, diesel, and biodiesel cars. Environmental science & technology 43:6334-6340.

Corbett, J. J., J. J. Winebrake, E. H. Green, P. Kasibhatla, V. Eyring, A. Lauer (2007). Mortality from ship emissions: a global assessment. Environmental science & technology 41:8512-8518.

Deguillaume, L., M. Leriche, K. Desboeufs, G. Mailhot, C. George, N. Chaumerliac (2005). Transition metals in atmospheric liquid phases: Sources, reactivity, and sensitive parameters. Chemical Reviews 105:3388-3431, <Go to ISI>://000231916100008.

Dellinger, B., W. A. Pryor, R. Cueto, G. L. Squadrito, V. Hegde, W. A. Deutsch (2001). Role of free radicals in the toxicity of airborne fine particulate matter. Chem. Res. Toxicol. 14:1371-1377.

Diaz, E. A., Y. Chung, D. P. Lamoureux, V. Papapostolou, J. Lawrence, M. S. Long, V. Mazzaro, H. Buonfiglio, R. Sato, P. Koutrakis, J. J. Godleski (2013). Effects of fresh and aged traffic-related particles on breathing pattern, cellular responses, and oxidative stress. Air Quality Atmosphere and Health 6:431-444.10.1007/s11869-012-0179-2.

DiStefano, E., A. Eiguren-Fernandez, R. J. Delfino, C. Sioutas, J. R. Froines, A. K. Cho (2009). Determination of metal-based hydroxyl radical generating capacity of ambient and diesel exhaust particles. Inhalation Toxicology 21:731-738.

Donahue, N. M., K. M. Henry, T. F. Mentel, A. Kiendler-Scharr, C. Spindler, B. Bohn, T. Brauers, H. P. Dorn, H. Fuchs, R. Tillmann (2012). Aging of biogenic secondary organic aerosol

via gas-phase OH radical reactions. Proceedings of the National Academy of Sciences 109:13503-13508.

Engelhart, G., A. Asa-Awuku, A. Nenes, S. Pandis (2008). CCN activity and droplet growth kinetics of fresh and aged monoterpene secondary organic aerosol. Atmospheric Chemistry and Physics 8:3937-3949.

Fang, T., V. Verma, H. Guo, L. E. King, E. S. Edgerton, R. J. Weber (2014). A semi-automated system for quantifying the oxidative potential of ambient particles in aqueous extracts using the dithiothreitol (DTT) assay: results from the Southeastern Center for Air Pollution and Epidemiology (SCAPE). Atmospheric Measurement Techniques Discussions 7:7245-7279.

Godri, K. J., R. M. Harrison, T. Evans, T. Baker, C. Dunster, I. S. Mudway, F. J. Kelly (2011). Increased oxidative burden associated with traffic component of ambient particulate matter at roadside and urban background schools sites in London. PLoS One 6:e21961. 10.1371/journal.pone.0021961.

Gonzalez, D. H., C. K. Cala, S. E. Paulson (submitted). HULIS Enhancement of OH by Fe(II): Kinetics of Suwannee RIver Fulvic Acid-Fe(II) Complexes in the Presence of Lung Antioxidants. Environmental science & technology.

Graedel, T., M. Mandich, C. Weschler (1986). Kinetic model studies of atmospheric droplet chemistry: 2. Homogeneous transition metal chemistry in raindrops. Journal of Geophysical Research: Atmospheres 91:5205-5221.

Hansen, A., H. Rosen, T. Novakov (1984). The aethalometer—an instrument for the real-time measurement of optical absorption by aerosol particles. Science of the Total Environment 36:191-196.

Heikkilä, J., M. Happonen, T. Murtonen, K. Lehto, T. Sarjovaara, M. Larmi, J. Keskinen, A. Virtanen (2012). Study of Miller timing on exhaust emissions of a hydrotreated vegetable oil (HVO)-fueled diesel engine. Journal of the Air & Waste Management Association 62:1305-1312.

ICCT, T. I. C. O. C. T. (2014). The end of the era of heavy fuel oil in maritime shipping. http://www.theicct.org/blogs/staff/end-era-heavy-fuel-oil-maritime-shipping.

Jalava, P. I., P. Aakko-Saksa, T. Murtonen, M. S. Happo, A. Markkanen, P. Yli-Pirilä, P. Hakulinen, R. Hillamo, J. Mäki-Paakkanen, R. O. Salonen (2012). Toxicological properties of emission particles from heavy duty engines powered by conventional and bio-based diesel fuels and compressed natural gas. Particle and Fibre Toxicology 9:1.

Kelly, F., M. Cotgrove, I. Mudway (1995). Respiratory tract lining fluid antioxidants: the first line of defence against gaseous pollutants. Central European journal of public health 4:11-14.

Kim, D., S. Kim, S. Oh, S.-Y. No (2014). Engine performance and emission characteristics of hydrotreated vegetable oil in light duty diesel engines. Fuel 125:36-43.

King, L. E. and R. J. Weber (2013). Development and testing of an online method to measure ambient fine particulate reactive oxygen species (ROS) based on the 2 ',7 '-dichlorofluorescin (DCFH) assay. Atmospheric Measurement Techniques 6:1647-1658.10.5194/amt-6-1647-2013.

Larsen, B. R., D. Di Bella, M. Glasius, R. Winterhalter, N. R. Jensen, J. Hjorth (2001). Gas-phase OH oxidation of monoterpenes: Gaseous and particulate products. Journal of Atmospheric Chemistry 38:231-276.

Li, N., M. Hao, R. F. Phalen, W. C. Hinds, A. E. Nel (2003). Particulate air pollutants and asthma: A paradigm for the role of oxidative stress in PM-induced adverse health effects. Clinic. Immunol. 109:250-265.

Lin, C.-C., S.-J. Chen, K.-L. Huang, W.-I. Hwang, G.-P. Chang-Chien, W.-Y. Lin (2005). Characteristics of metals in nano/ultrafine/fine/coarse particles collected beside a heavily trafficked road. Environmental science & technology 39:8113-8122.

Lund, L. G. and A. E. Aust (1992). Iron mobilization from crocidolite asbestos greatly enhances crocidolite-dependent formation of DNA single-strand breaks in øX174 RFI DNA. Carcinogenesis 13:637-642.

Matthews, R. W. (1980). THE RADIATION-CHEMISTRY OF THE TEREPHTHALATE DOSIMETER. Radiation Research 83:27-41.10.2307/3575256.

Nigam, A. (2007). Emissions assessment of selected diesel sources at ports: Baseline conditions and benefits through use of control technologies, http://search.proquest.com/docview/304877450?accountid=14512.

Oeder, S., T. Kanashova, O. Sippula, S. C. Sapcariu, T. Streibel, J. M. Arteaga-Salas, J. Passig, M. Dilger, H.-R. Paur, C. Schlager (2015). Particulate matter from both heavy fuel oil and diesel fuel shipping emissions show strong biological effects on human lung cells at realistic and comparable in vitro exposure conditions. PLoS One 10:e0126536.

Paris, R. and K. Desboeufs (2013). Effect of atmospheric organic complexation on iron-bearing dust solubility. Atmospheric Chemistry and Physics 13:4895-4905.

Paulson, S. E., A. Hasson, C. Anastasio, Xiaobi M. Kuang, J. Adlin Scott, David H. Gonzalez-Martinez, Tiffany Charbouillot , Kennedy K-T Vu, James Baroi, Catalina Olea, Annabelle

Lolinco and Kylie Markarian, Jessica G. Charrier, Alexander S. McFall, N. K. Richards-Henderson (2016). Probing the Intrinsic Ability of Particles to Generate Reactive Oxygen Species and the Effect of Physiologically Relevant Solutes. California Air Resources Board annual report, https://www.arb.ca.gov/research/apr/past/10-314-2.pdf.

Price, D. J., C.-L. Chen, M. A. Lamjiri, R. Betha, K. Sanchez, J. Liu, A. K. Y. Lee, D. R. Cocker, L. M. Russell (2016). More unsaturated, cooking-type hydrocarbon-like organic aerosol particle emissions from renewable diesel compared to ultra low sulfur diesel in at-sea operations of a research vessel. Aerosol Science And Technology:00-00.10.1080/02786826.2016.1238033.

Prokopowicz, A., M. Zaciera, A. Sobczak, P. Bielaczyc, J. Woodburn (2015). The Effects of Neat Biodiesel and Biodiesel and HVO Blends in Diesel Fuel on Exhaust Emissions from a Light Duty Vehicle with a Diesel Engine. Environmental science & technology 49:7473-7482.

Rattanavaraha, W., E. Rosen, H. Zhang, Q. Li, K. Pantong, R. M. Kamens (2011). The reactive oxidant potential of different types of aged atmospheric particles: An outdoor chamber study. Atmospheric Environment 45:3848-3855.

Reid, J. S., T. F. Eck, S. A. Christopher, P. V. Hobbs, B. Holben (1999). Use of the Ångstrom exponent to estimate the variability of optical and physical properties of aging smoke particles in Brazil. Journal of Geophysical Research: Atmospheres 104:27473-27489.

Sato, K., S. Nakao, C. H. Clark, L. Qi, D. R. Cocker Iii (2011). Secondary organic aerosol formation from the photooxidation of isoprene, 1, 3-butadiene, and 2, 3-dimethyl-1, 3-butadiene under high NO x conditions. Atmospheric Chemistry and Physics 11:7301-7317.

Shen, H., A. I. Barakat, C. Anastasio (2011). Generation of hydrogen peroxide from San Joaquin Valley particles in a cell-free solution. Atmospheric Chemistry and Physics 11:753-765.10.5194/acp-11-753-2011.

Shilling, J. E., S. M. King, M. Mochida, S. T. Martin (2007). Mass spectral evidence that small changes in composition caused by oxidative aging processes alter aerosol CCN properties. Journal of Physical Chemistry A 111:3358-3368.10.1021/jp068822r.

Shrivastava, M. K., T. E. Lane, N. M. Donahue, S. N. Pandis, A. L. Robinson (2008). Effects of gas particle partitioning and aging of primary emissions on urban and regional organic aerosol concentrations. Journal of Geophysical Research: Atmospheres 113:n/a-n/a.10.1029/2007JD009735.

Smith, K. R. and A. E. Aust (1997). Mobilization of iron from urban particulates leads to generation of reactive oxygen species in vitro and induction of ferritin synthesis in human lung epithelial cells. Chemical Research in Toxicology 10:828-834.

Storey, J., S. Curran, A. Dempsey, S. Lewis, N. R. Walker, R. Reitz, C. Wright (2015). The contribution of lubricant to the formation of particulate matter with reactivity controlled compression ignition in light-duty diesel engines. Emission Control Science and Technology 1:64-79.

Sun, Y. and J. J. Pignatello (1992). Chemical treatment of pesticide wastes. Evaluation of iron (III) chelates for catalytic hydrogen peroxide oxidation of 2, 4-D at circumneutral pH. Journal of Agricultural and Food Chemistry 40:322-327.

Tan, K. H. (2014). Humic matter in soil and the environment: principles and controversies. CRC Press.

Verma, V., M. M. Shafer, J. J. Schauer, C. Sioutas (2010). Contribution of transition metals in the reactive oxygen species activity of PM emissions from retrofitted heavy-duty vehicles. Atmospheric Environment 44:5165-5173.

Wang, Y., A. Chung, S. E. Paulson (2010). The effect of metal salts on quantification of elemental and organic carbon in diesel exhaust particles using thermal-optical evolved gas analysis. Atmospheric Chemistry and Physics 10:11447-11457.10.5194/acp-10-11447-2010.

Wang, Y., C. Arellanes, S. E. Paulson (2012). Hydrogen Peroxide Associated with Ambient Fine Mode, Diesel and Biodiesel Aerosol Particles in Southern California. Aerosol Sci. Tech. 46:394–402.

Wang, Y.-F., K.-L. Huang, C.-T. Li, H.-H. Mi, J.-H. Luo, P.-J. Tsai (2003). Emissions of fuel metals content from a diesel vehicle engine. Atmospheric Environment 37:4637-4643.

Weng, L., E. J. Temminghoff, S. Lofts, E. Tipping, W. H. Van Riemsdijk (2002). Complexation with dissolved organic matter and solubility control of heavy metals in a sandy soil. Environmental science & technology 36:4804-4810.

Westphal, G. t. A., J. r. Krahl, A. Munack, N. Rosenkranz, O. Schröder, J. Schaak, C. Pabst, T. Brüning, J. r. Bünger (2013). Combustion of hydrotreated vegetable oil and jatropha methyl ester in a heavy duty engine: emissions and bacterial mutagenicity. Environmental science & technology 47:6038-6046.

Zhang, X., Z. Chen, Y. Zhao (2010). Laboratory simulation for the aqueous OH-oxidation of methyl vinyl ketone and methacrolein: significance to the in-cloud SOA production. Atmospheric Chemistry and Physics 10:9551-9561.

Zhang, Y., J. J. Schauer, M. M. Shafer, M. P. Hannigan, S. J. Dutton (2008). Source apportionment of in vitro reactive oxygen species bioassay activity from atmospheric particulate matter. Environmental science & technology 42:7502-7509.

6. Quantification of ROS from individual and mixture of redox active components.

6.1 Introduction

ROS formation by ambient particles is likely resulting from the reactivity of individual redox active species as well as their interactions. As described in Chapter 1, a major source of OH in the absence of light is its production through the Fenton reaction. Other reduced transition metals, including Cu(I), Ni(II) and Co(II) can also produce OH through Fenton-like reactions (Leonard et al., 1998; Torreilles and Guérin 1990; Urbañski and Beresewicz 2000). In addition to metals, redox active quinones such as phenanthraquinone, 1,2-Naphthoquine and 1,4-Naphthoquinone, have shown to play important roles in ROS production (Chung et al., 2006; Valavanidis et al., 2005). Chung et al., (2006) showed that the rate of H_2O_2 formation in large excess of DTT (as an election donor) was linearly dependent on the concentration of quinone concentrations and it is 1-2 orders of magnitude higher than H_2O_2 formation by fine PM.

Very limited studies have quantified ROS formation from individual redox active species or in combination. In pH7.4 phosphate solutions containing added electron donors, Charrier and Anastasio (2011) showed that OH formed by Cu and Fe together was 10-70% higher than the sum of the individual metals. Under similar laboratory conditions, Charrier and coworkers (Charrier et al., 2014; Charrier and Anastasio 2015) also measured the rate of formation of H_2O_2 and OH from transition metals and quinones. The results indicated the major source of H_2O_2 is copper (96%) and sum of three quinones (4%): 1,2-naphthoquinone, 1,4-naphthoquinone and phenanthraquinone (Charrier et al., 2014). In contrast to H_2O_2, copper and iron have similar contribution to OH formation when added alone, while the contribution from

quinones were similar in both formation of H_2O_2 and OH. Rates of OH formation from synergisms of Cu/Fe and quinones were 20-130% higher than the sum of individual redox active compounds (Charrier and Anastasio 2015). When present together with metals, hydroquinones and semi-quinone radicals are able to reduce Fe^{3+} to Fe^{2+} and can act as electron transfer catalysts (Chen and Pignatello 1997; Duesterberg and Waite 2007), potentially enhancing ROS formation. In this work, the ability of metals and quinones to produce H_2O_2 and OH in pH3.5 solutions is explored to further understand the underlying ROS mechanism under atmospheric conditions. Both single metals or quinones and binary or more complex mixtures of metals and or quinones at concentrations relevant to ambient particles are tested. For each species difference concentrations were tested at concentrations typical of a range from dilute clouds to reasonably dry aerosols. The role of electron donors that may be present in PM (such as phenol and oxalate) is tested by adding them to the single-component system. Results form single component systems are referred to as the "ROS generation curves"; that is, the dependence of H_2O_2 or OH formed on the concentration of metals/quinones. Ideally, by combining these ROS generation curves with concentrations of metals and quinones measured in the PM extracts, we can calculate the corresponding H_2O_2/OH generation from the metal/quinone components of the PM. Comparing the calculated results to the total ROS formed will allow us to estimate the contribution from each metal/quinone to H_2O_2/OH generation. Results from the multiple-component systems will be used to examine the effect of interactions between these redox active species and their significance in producing ROS.

While several related studies suggested humic-like substances (HULIS) from various sources can produce ROS, including cigarette smoke and ambient particles, the process is poorly

understood. To our knowledge, no direct quantification of H_2O_2 and OH formation from HULIS has been reported. Standard HULIS compounds are not commercially available, however, fulvic and humic acids are commonly used as surrogates in the investigations of properties of HULIS. Therefore, to construct a more complete picture of the ability of redox active species to produce ROS, fulvic and humic acids are included in the ROS generation curves.

6.2 Methods

The redox active species used in this study include copper(II) sulfate, iron(II) sulfate, manganese, 1,4-Naphthoquinone, 9,10-Phenanthraquinone, hydroquinone, 1,2-dihydroxynaphthalene were purchased from Sigma Aldrich and used as received. Table 6.1 shows species tested along with the ambient concentration ranges, and concentrations used in the experiments described. All experiments are carried out at pH 3.5 solutions (water adjusted to pH3.5 with sulfuric acid). Detailed methods of H_2O_2 and OH quantification are described in Chapter 2. In all experiments, the blanks in the OH and H_2O_2 assays are pH 3.5 solutions and 10 mM terephthalate.

6.2.1 Individual Redox-Active Species

Simultaneous measurement of OH and H_2O_2 production from redox active species (Fe(II), Cu(II), phenanthraquinone and 1,4-Naphthoquinone) as a function of their concentrations were performed. Stock solutions (10^{-4} M) of Fe(II) and Cu(II) are freshly prepared in pH3.5 prior to each experiment. Stock quinone and hydroquinone solutions (10^{-4}M) are prepared in acetonitrile and are stored in the freezer.

Kinetic measurements of ROS formation were performed by taking aliquots of solutions at 0, 30, 60, 90 and 120 mins. Some kinetic measurements were taken at 15, 40, 60, 90 and 120

mins. Detailed description of the measurement methods are found in Chapters 2-5. Concentration curves were constructed by reporting the OH and H_2O_2 formation at 2 hours as a function of the concentration of the tested species.

6.2.2 Mixtures of Redox-Active Species

Simultaneous measurement of OH and H_2O_2 production from combination of transition metals, transition metals + quinones and transition metals + fulvic acid are investigated. Different ratios and concentrations (Tab. 6.2) for each combination were also tested.

6.2.3 Fenton and Fenton-like reactions

Destruction of H_2O_2 and production of OH were monitored in the classic Fenton reaction (H_2O_2 + Fe(II) → OH + OH^- + Fe(III)) and Fenton-like reactions, i.e. H_2O_2 + Cu(I)/Mn(II). The effect of ligands-Fe interaction on destruction of H_2O_2 and production of OH were tested by adding 5 μg/mL of FA together with Fe(II) in the presence of H_2O_2. Measurements were taken at 0, 30, 60, 90 and 120 mins.

Tab. 6.1 Median ambient concentration of concentration of each species and the concentration range used in "ROS concentration curves"

	H_2O_2 concentration curves		
Sp	**Range of ambient concentration[b] (ng/m^3)**	**Range of ambient concentration[c] (μM)**	**Ranges of Concentration Tested (μM)**
Cu	0.6-361	0.06-34	0.1-250
Fe	5-123	0.6-13	0.1-250
Mn	0.4-63	0.04-7	0.1-10
1,4	0.11	0.004	0.1-250
HQ			0.1-5
HN			0.1-5
PQ	0.31	0.009	0.01-1
FA	11.8[c]	0.07[d]	5-50[d]

a. 1,2-NQN: 1,2-naphthoquinone; 1,4-NQN: 1,4-naphthoquinone; PQN: Phenanthraquinone, HQN: hydroquinone, HNQN: 1,2-dihydroxynapthlene

b. Estimated based on the average air sampled during the field campaigns ($24m^3$) and the solution volume used in these analyses (4mL)

c. HULIS mass concentration in ambient $PM_{2.5}$ sample determined by Lin et al. 2010.

d. FA/HA concentration in μg/mL.

Tab. 6.2 Concentrations (in μM unless otherwise noted) of redox active species used in the ROS formation experiments as individual species or in combinations. OH and H_2O_2 formations kinetic analysis were measured in all experiments. Mn(II) and Cu(I) alone did not produce ROS thus are not included in the table under individual species.

Concentrations	**Fe(II)**	**Cu(II)**	**1,4-NQN**	**PQN**	**HQN**	**HNQN**	**Metal Mixture**
Individual species							
	0.1-250	0.1-250	0.1-250	0.1-250	0.1-10	0.1-10	1-50 ppb
Mixtures of redox active species							
Fe(II)			10 μM Fe(II) + 10, 50,100 and 250 μM 1,NQN	10 μM Fe(II) + 10, 50,100 and 250 μM PQN			
Cu(II)			10 μM Cu(II) + 10, 50,100 and 250 μM 1,4-NQN	10 μM Cu(II) + 10, 50,100 and 250 μM PQN			
Cu(I)					500nM HQN + 0.1, 0.5, 1 and 10 μM Cu(I)	500nM HNQN + 0.1, 0.5, 1 and 10 μM Cu(I)	
1,4NQN	10 μM 1,4 NQN + 10, 50, 100 and 250 μM Fe(II)	10 μM 1,4 NQN+ 10, 50, 100 and 250 μM Cu(II)					
PQN	10 μM PQN + 10, 50,100 and 250 μM Fe(II)	10 μM PQN+ 10, 50,100 and 250 μM Cu(II)					
HQN							500nM HQN+ 1, 10, 50,250 and 500 ppb metal mixtures
HNQN							500nM HNQN+ 1, 10, 50,250 and 500 ppb metal mixtures
FA	1 μM H_2O_2 + 5 μg/mL FA + 1 μM Fe(II)						
H_2O_2	1 μM H_2O_2 + 5 μg/mL FA + 0.5, 1,5 10 μM Fe(II)	1 μM H_2O_2 + 5 μg/mL FA + 0.5, 1,5 10 μM Fe(II)					1 μM H_2O_2 +1, 10, 50,100 and 250 ppb metal mixtures

6.3 Results

6.3.1 Formation of H_2O_2 and OH by individual redox active species

Figure 6.1 shows the formation of H_2O_2 as a function of time at different concentrations of metals and quinones (Tab. 6.2). All OH and H_2O_2 are blank corrected. For all the species tested, statistically significant amounts of H_2O_2, defined as statistically significant concentrations are > three times the standard deviation of the blank, (here, 0.15 μM), were only formed at high concentrations of redox active solutes; > 10 μM for both Fe (II) and Cu(II) and >> 20 μM for quinones. H_2O_2 from Fe(II) formed more rapidly than we are able to measure (within 1 minute) (Fig. 6.1a). After the initial production, no additional formation was observed for the next 2 hours. Fe(II) produced substantially more H_2O_2 than Cu(II) at the same concentrations. Cu(II) (Fig 6b) also produces an initial burst of H_2O_2 but unlike Fe(II), H_2O_2 production slowly increases with time over the next 2 h. Both phenanthraquinone (PQN) and 1,4-Naphthoquinone (1,4-NQN) produced H_2O_2 at the highest concentration tested (250 μM). The relative capability of each redox active species, in decreasing order, to produce H_2O_2 at 250 μM was: Fe(II)>1,4-NQN>PQN>Cu(II).

Of the redox active species tested, PQN did not produce OH, and Cu(II) produced only very minimal OH (data not shown). At equal concentrations, 1,4-NQN produced the most OH, followed by Fe(II). By comparing Fig 6.1a and 6.1 e, H_2O_2 produced from Fe(II) was not efficiently converted OH. For example, about 14 μM of H_2O_2 was produced from 250 μM of Fe(II) but only 0.3 μM OH was formed.

Both hydroquinone and 1,2-dihydroxynaphthalene showed greater ability to produce OH than Fe(II), Cu(II), Cu(I), PQN and 1,4-NQN, 1,2-dihydroxynaphthalene also formed H_2O_2

(Figs. 6.1e, Figs 6.2c-d).

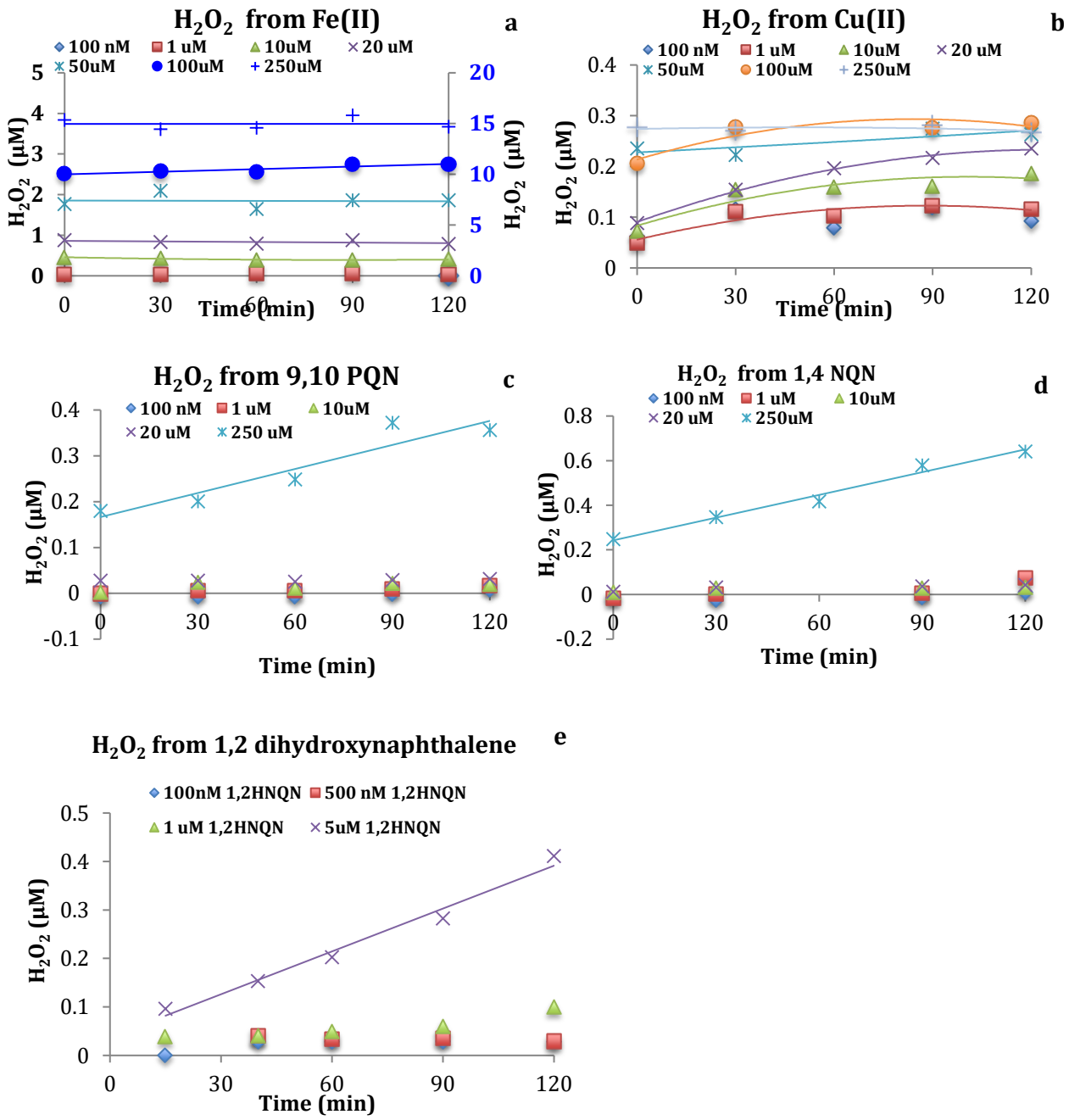

Fig. 6.1 Formation of H_2O_2 from a) Fe(II), with 100 and 250 µM Fe(II) plotted on the secondary y-axis, b) Cu(II), c) 9,10-PQN, d) 1,4-NQN and e) 1,2-dihydroxynaphthalene at different concentrations ranging from 0.1-250 µM.

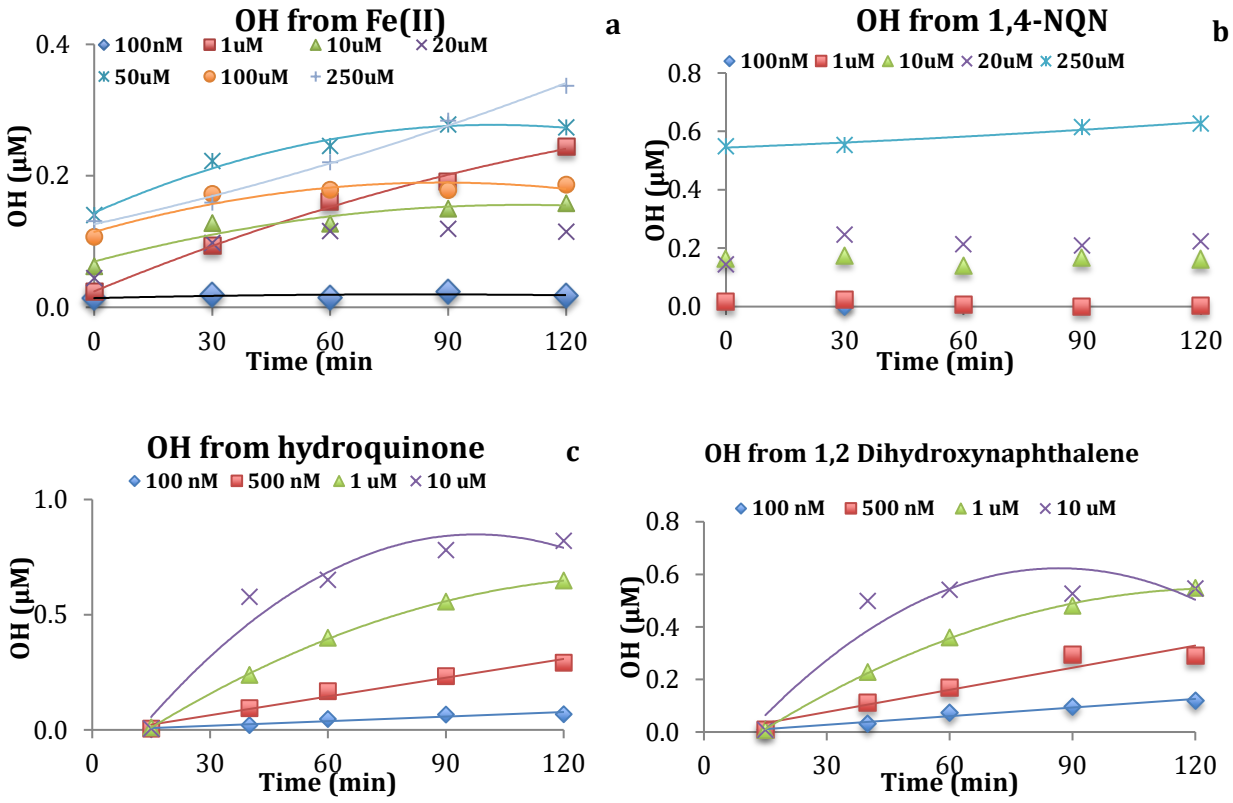

Fig. 6.2 Formation of OH from a) Fe(II), b) 1,4-NQN, c) hydroquinone and d) 1,2-dihydroxynaphthalene at different concentrations ranging from 0.1-250 µM.

6.3.2 ROS generation curves

Due to the minimal production of OH from the individual redox active species, there was not enough data to construct an OH generation. Similarly, H_2O_2 generation curve can be produced from Fe(II) and Cu(II) but not quinones, as shown in Fig 6.3a. These curves were applied to the metal concentrations measured in Fresno and Claremont to predict ROS formation from metals measured in the field (Figs 6.3b-c) using the equations shown in Fig. 6.3a. The correlations between predicted H_2O_2 concentration from Fe(II) and Cu(II) and measured H_2O_2 in the field samples are fairly strong, with $r^2 > 0.4$ (Figs 63.b-c). Fe tends to over predict H_2O_2

formation while Cu greatly underestimated it. Because these are simple single component systems, they cannot mimic interactions between metals and other organic ligands in ambient PM that can alter the H_2O_2 formation chemistry significantly, such as by enhancing the Fenton reaction, thus destroying more H_2O_2.

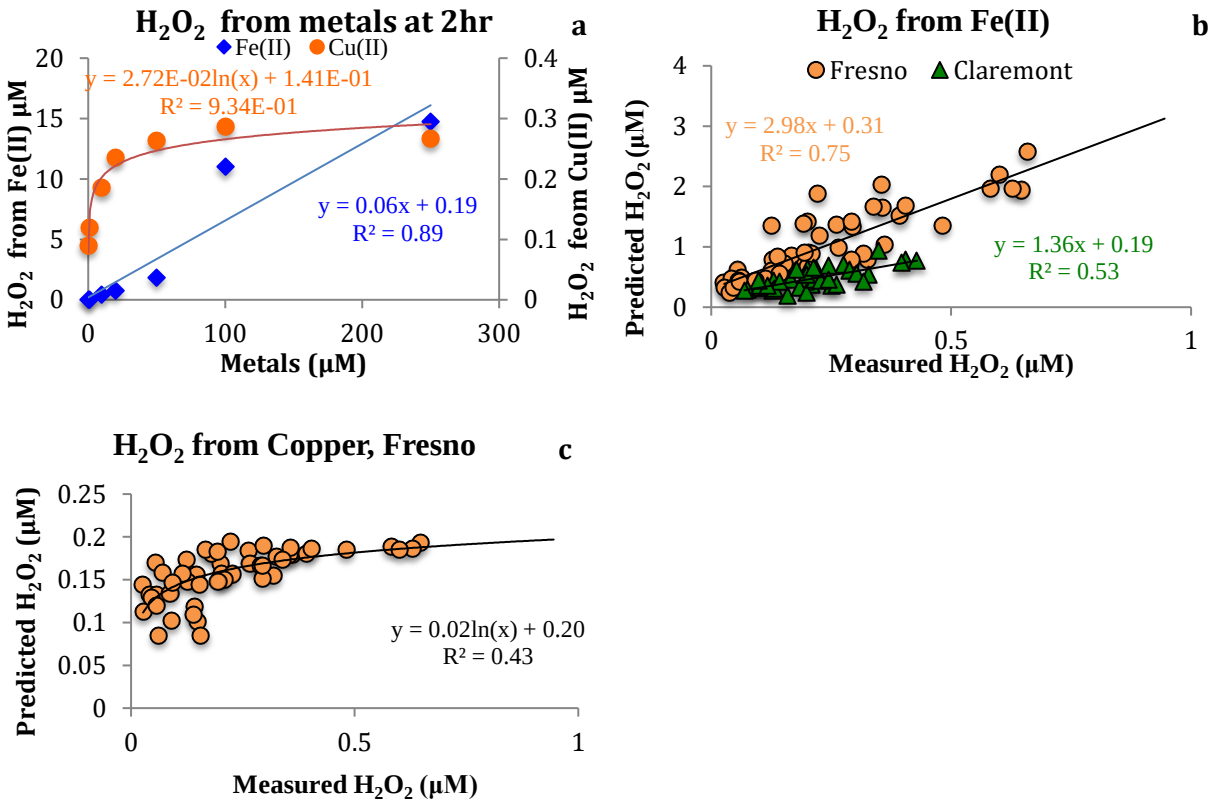

Fig. 6.3 a) H_2O_2 generation curves from Fe(II) and Cu(II); b) Predicted H_2O_2 formation from Fe(II) vs. measured H_2O_2 in Claremont and Fresno and c) Predicted H_2O_2 formation from Cu(II) vs. measured H_2O_2 in Fresno.

6.3.3 Mixtures of Metals and Quinones

Fig. 6.4 shows H_2O_2 production from the metal/quinone mixtures with different metal/quinone ratios, concentrations of these species are presented in Tab. 6.2. Addition of quinone did not enhance H_2O_2 production from Fe with excess Fe in the mixture (Figs 6.4a and

c). H_2O_2 formation from Fe(II) and Cu(II) are presented in open symbols to aid observing the effect of the addition of quinones to metals (solid symbols for mixture of quinones and metals). When PQN is added in excess, 5 and 10 times more PQN) than Fe(II), H_2O_2 production from Fe(II) is slightly enhanced: 10 µM Fe(II) produces about 0.4 µM H_2O_2 (Fig 6.1a) and the addition of 50 and 100 µM PQN to 10 µM produced up to 0.66 µM H_2O_2 at 2 h; but when added at large excess (25 times higher), H_2O_2 destruction dominated (Fig 6.4b). The behavior is different in the Fe(II) + 1,4NQN system with the same concentrations: when 1,4NQN is present at higher concentrations compared to Fe(II), H_2O_2 was formed instantly when Fe(II) and 1,4NQN were mixed but slowly destroyed over time (Fig 6.4d). Similarly, when Cu(II) is added in excess, addition of quinone did not or only slightly enhanced H_2O_2 production (Figs 6.3e and g). Comparatively greater enhancement of H_2O_2 production from Cu(II) was observed when quinones were added in excess.

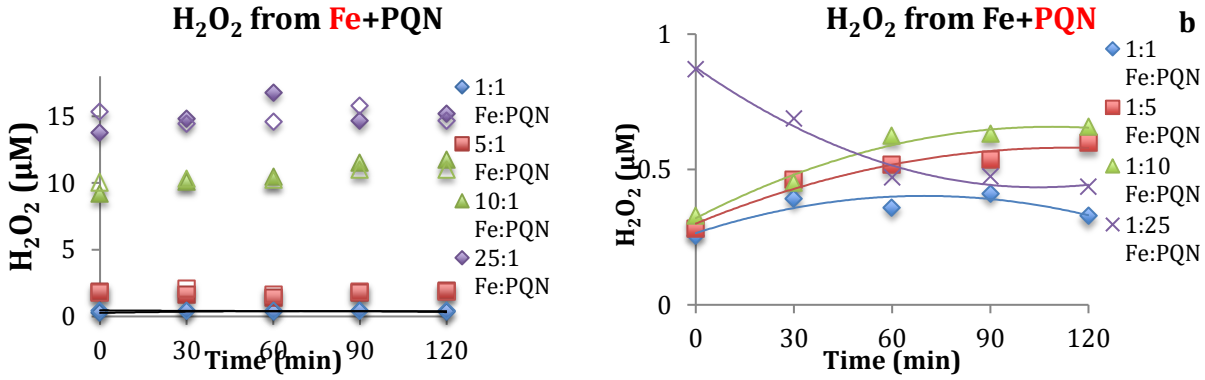

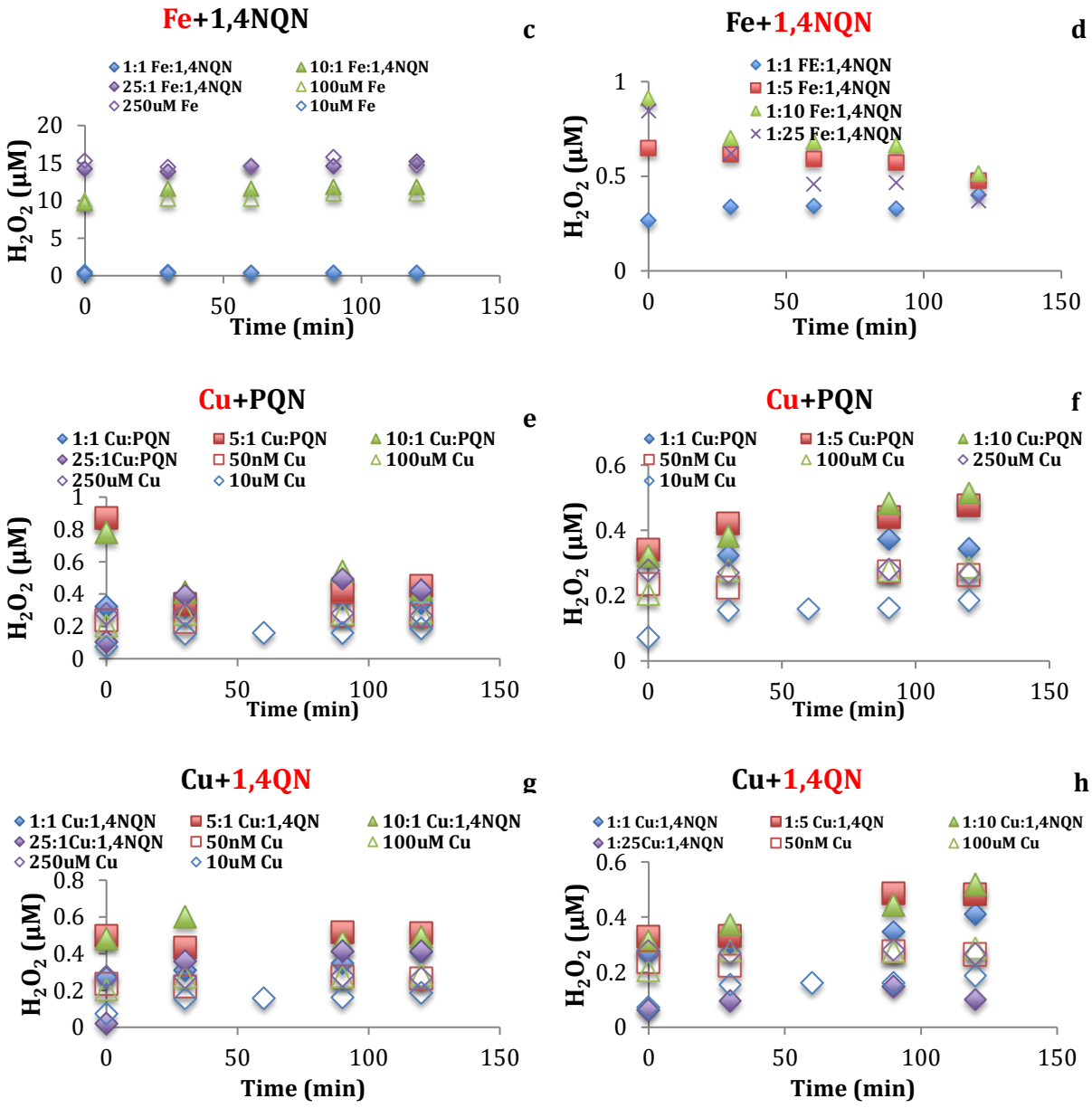

Fig. 6.4 H_2O_2 formation from the metal + quinone mixtures in different ratios. In all plots, the x-axis is analysis time in minutes and the y-axis is H_2O_2 formation in µM.

Addition of PQN to either Fe(II) or Cu(II) did not result in significnat enhancement of OH formation, in some cases, supressed OH formation from iron (Fig 6.5a). Mixtures of 1,4-NQN and metals enhanced OH formation from metals in all cases except the highest

concentration added (250 μM). 1,4-NQN appears to be more active in OH production from metals, OH formed from the mixture was significantly higher than the individual redox active species.

Fig. 6.6 shows the H_2O_2 and OH formation from the mixture of 1 μM Cu(II) and various concentrations of Fe(II). The stacked bars represent ROS formed from Cu(II) (orange) and Fe(II) (light green) and the blue bars indicate the ROS formation from the mixture of the metals. At lower metal concentrations, the mixture of the metals produced less H_2O_2 and OH than the production from the sum of the individual metal (Figs. 6.6 a and b). At higher metal concentrations, H_2O_2 concentrations are lower in the mixture than the sum of individual metals (except at larger excess of Cu(II), Fig. 6.6c) but substantially more OH (up to 7 times) than the sum of individual metals. The increase is more significant when Cu(II) is in greater excess or at the same concentration as Fe(II) (Fig. 6.6d).

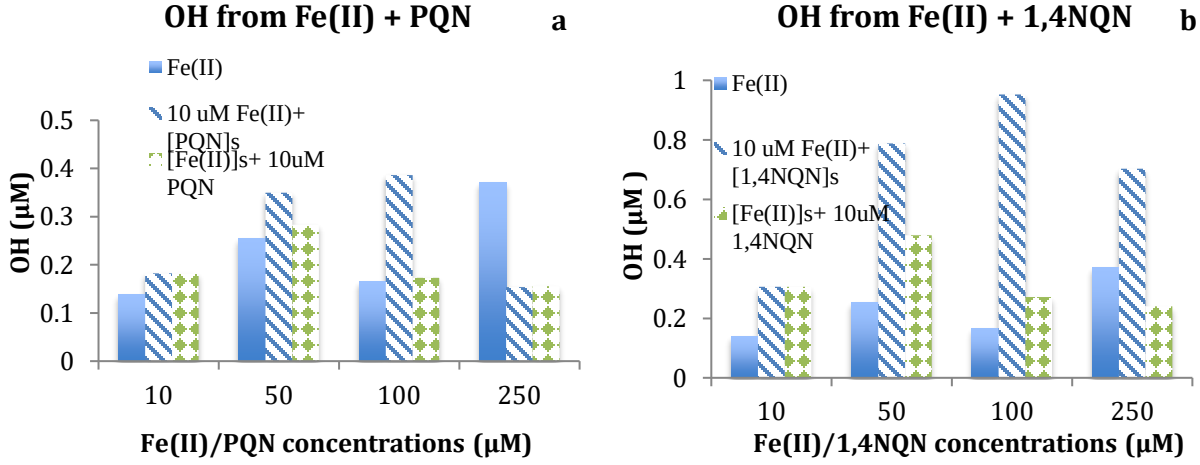

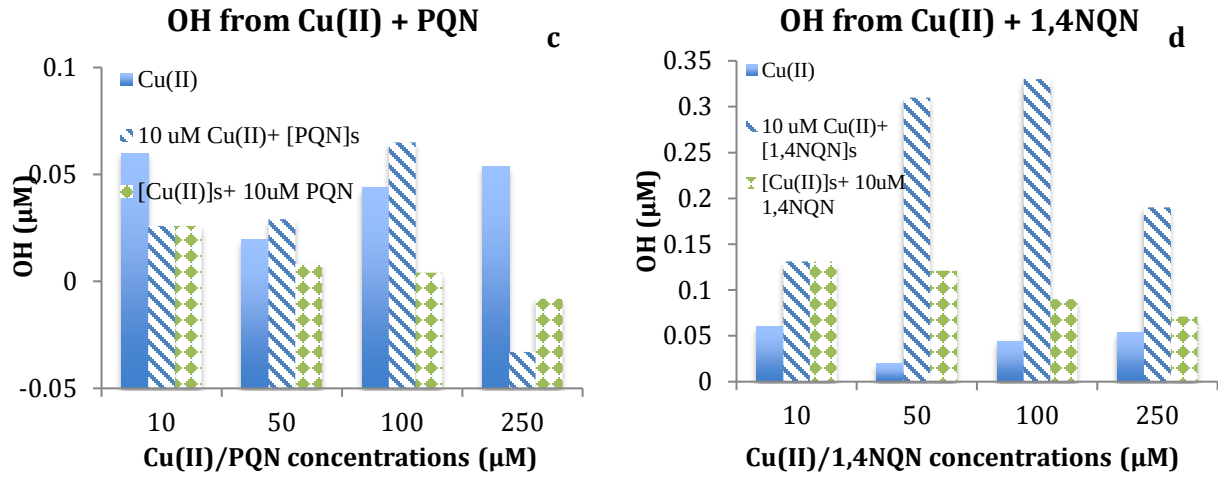

Fig. 6.5 OH formation from metal/quinones mixture.

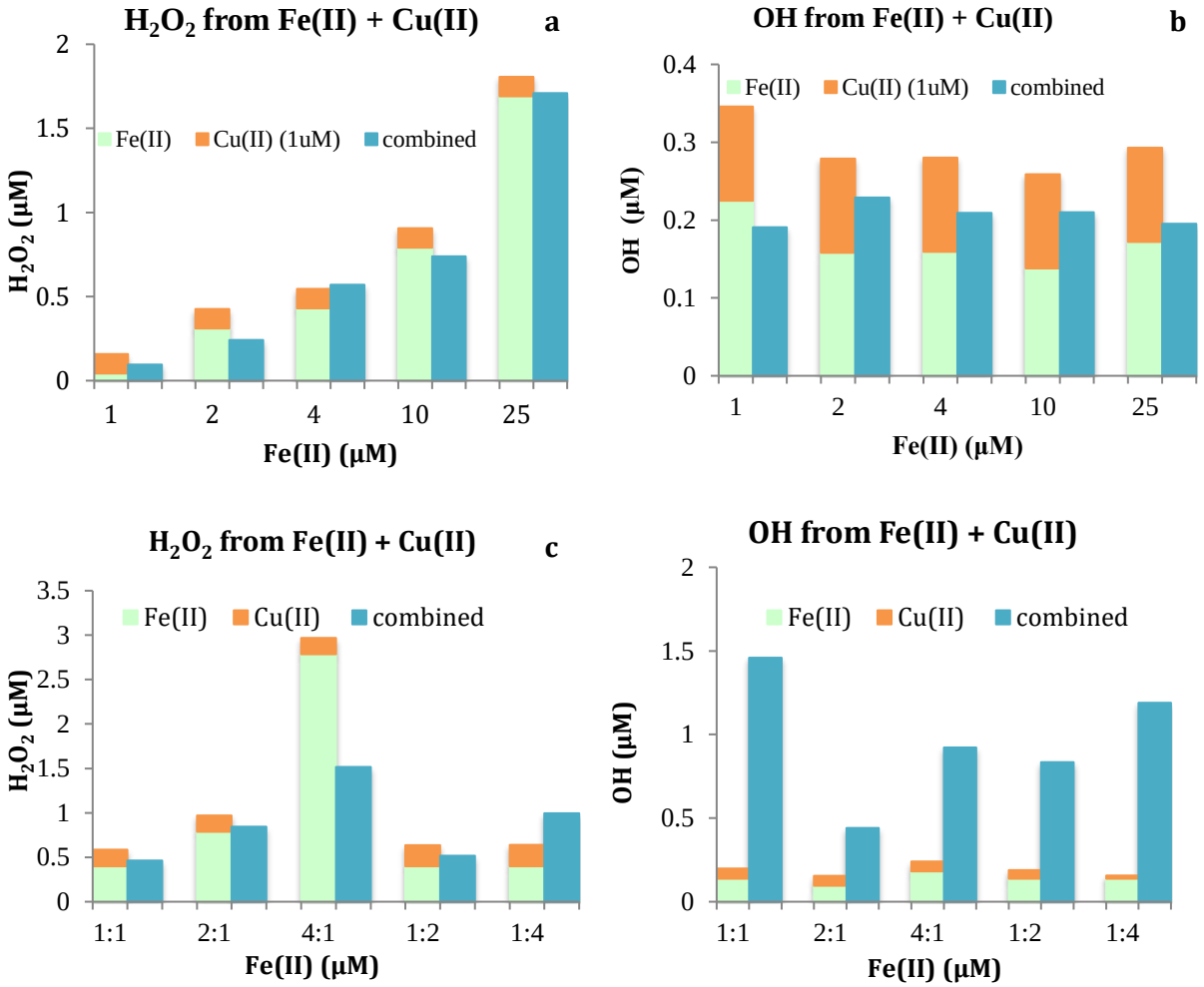

Fig. 6.6 H_2O_2 and OH formation from Fe(II) in the presence of Cu(II). a) and b) consisting 1 μM Cu(II) and 1-25 μM Fe(II). c) and d) ROS formation as a fuction of Fe(II)/Cu(II) ratios, with '1' indicating 10 μM of metal.

6.3.4 Fenton and Fenton-like reactions

Fenton and Fenton-like reactions are explored to better understand the balance between H_2O_2 and OH. In these experiments, destruction of 1 μM H_2O_2 in the presence of Fe(II) and Cu(II) at 0.5, 1, 5, and 10 μM are monitored over a period of 40 minutes for or 2 hours. At equal concentrations, Fe(II) destroys H_2O_2 at a much faster rate than Fenton-like reactions involving Cu(II), resulting in higher OH formation from the Fenton reaction. Closer examination of the Fenton reactions reveal that OH formation depends on Fe(II)/H_2O_2 ratios, reaching a maximum when this ratio is 10. At lower concentrations of Fe(II), 0.5 and 1 μM of Fe(II) did not effectively destroy 1 μM H_2O_2. The rate of H_2O_2 destruction doubled when the Fe(II) concentrations increased to 5 and 10 μM (Fig. 6.6a and Tab. 6.3). As a result, the rate of OH formation increased significantly at higher Fe(II) concentrations.

Fig. 6.6e shows OH formation from a mixture of 33 metals, including Fe, Cu, Mn, V, Zn, Pb, Ni, Co etc.; with or without 1 μM H_2O_2 added. OH formation of 10 μM Fe(II) (equivalent to 143 ppb Fe(II)) with 1 μM H_2O_2 was shown for comparison purposes. In the absence of 1 μM H_2O_2, only trace amount of OH was formed (~0.2 μM) from the mixture of metals; however, OH formation increased significantly (> 10 times higher) when 1 μM H_2O_2 was added to the metal mixture, and significantly higher than OH formed from 10 μM Fe(II) with 1 μM H_2O_2. This result indicates that the interaction between metals play an important role in OH formation, however, such interactions are still not well understood.

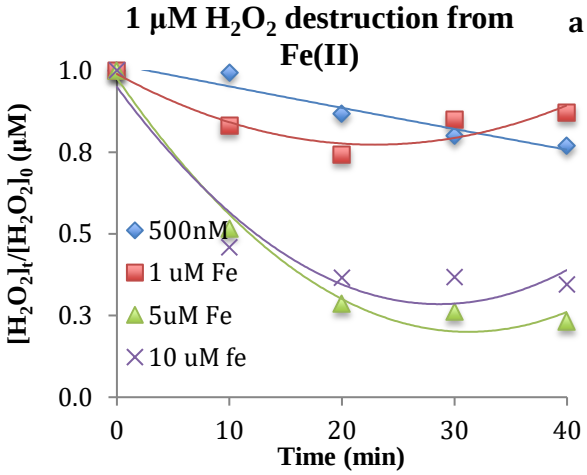
1 µM H2O2 destruction from Fe(II)
a
[H2O2]t/[H2O2]0 (µM)
1.0
0.8
0.5
0.3
0.0
500nM
1 uM Fe
5uM Fe
10 uM fe
0
10
20
30
40
Time (min)

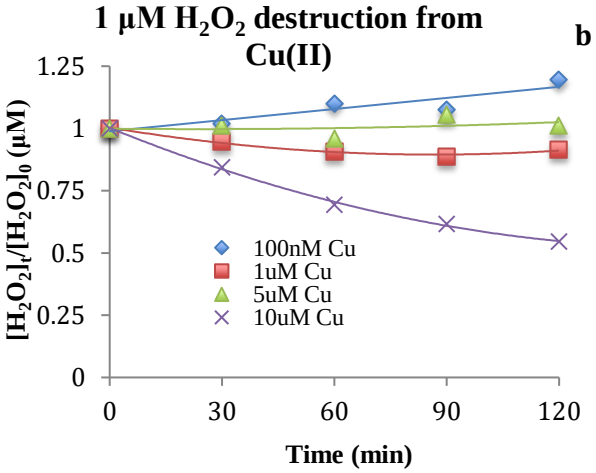
1 µM H2O2 destruction from Cu(II)
b
[H2O2]t/[H2O2]0 (µM)
1.25
1
0.75
0.5
0.25
0
100nM Cu
1uM Cu
5uM Cu
10uM Cu
0
30
60
90
120
Time (min)

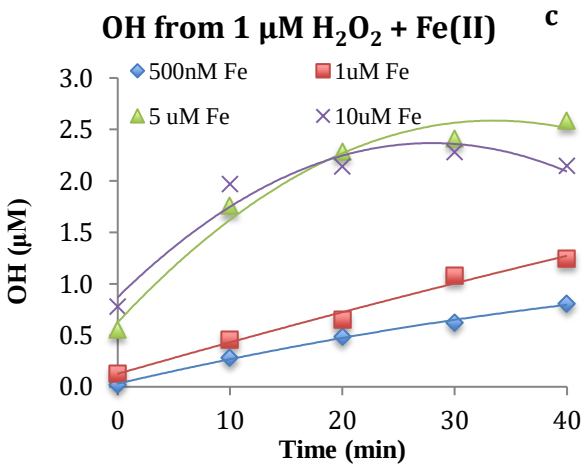
OH from 1 µM H2O2 + Fe(II)
c
OH (µM)
3.0
2.5
2.0
1.5
1.0
0.5
0.0
500nM Fe
1uM Fe
5 uM Fe
10uM Fe
0
10
20
30
40
Time (min)

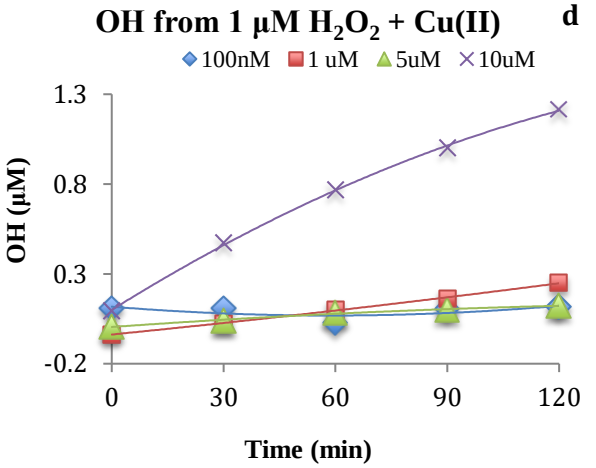
OH from 1 µM H2O2 + Cu(II)
d
OH (µM)
1.3
0.8
0.3
-0.2
100nM
1 uM
5uM
10uM
0
30
60
90
120
Time (min)

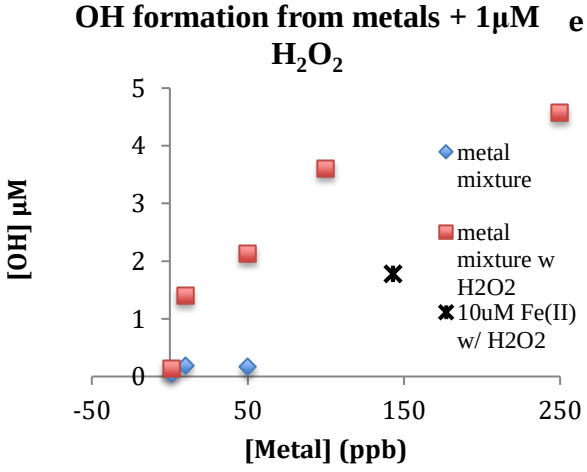
OH formation from metals + 1µM H2O2
e
[OH] µM
5
4
3
2
1
0
metal mixture
metal mixture w H2O2
10uM Fe(II) w/ H2O2
-50
50
150
250
[Metal] (ppb)

Fig. 6.7 H_2O_2 destruction and OH formation in Fenton and Fenton-like reactions.

Tab. 6.3 Equations derived from the kinetics analysis of destruction and OH formation

Fe(II)	**500 nM**	**1 µM**	**5 µM**	**10 µM**
H_2O_2 destruction	$y = 0.000x^2 - 0.007x + 1.02$ $R^2 = 0.94$	$y = 0.000x^2 - 0.02x + 0.99$ $R^2 = 0.86$	$y = 0.001x^2 - 0.05x + 0.98$ $R^2 = 0.98$	$y = 0.001x^2 - 0.046x + 0.95$ $R^2 = 0.93$
OH formation	$y = -0.00x^2 + 0.03x + 0.03$ $R^2 = 1.00$	$y = -0.00x^2 + 0.03x + 0.13$ $R^2 = 0.98$	$y = -0.00x^2 + 0.12x + 0.63$ $R^2 = 0.98$	$y = -0.00x^2 + 0.11x + 0.87$ $R^2 = 0.95$
Cu(II)	**500 nM**	**1 µM**	**5 µM**	**10 µM**
H_2O_2 destruction	$y = 0.0015x + 0.99$ $R^2 = 0.83$	$y = 0.000x^2 - 0.003x + 1.0$ $R^2 = 0.98$	$y = 0.000x^2 - 0.000x + 0.99$ $R^2 = 0.11$	$y = 0.00x^2 - 0.01x + 1.00$ $R^2 = 1.00$
OH formation	$y = 0.00x^2 - 0.002x + 0.12$ $R^2 = 0.43$	$y = 0.000x^2 + 0.002x - 0.038$ $R^2 = 0.99$	$y = -0.000x^2 + 0.001x + 0.004$ $R^2 = 0.99$	$y = -0.000x^2 + 0.013x + 0.1$ $R^2 = 0.99$

6.4 Conclusion

We have quantified H_2O_2 and OH concentrations from redox active species, including redox active metals such as Fe(II), Cu(II), Cu(I) and Mn(II) and quinones. Cu(I) and Mn(II) did not produce H_2O_2 and OH at all concentrations tested (0.5-10 µM) when added alone. Fe(II) and Cu(II) were able to produce significant amount of H_2O_2 at higher concentrations (> 10 µM of metals). Fe(II) was more active in ROS production compared to Cu(II) regarding both H_2O_2 and OH formation. The hydroquinones exhibited higher ROS activity than quinones. This could be attributed to the electron donor nature of the hydroquinones. In the absence of reducing agents,

quinones were converted to the hydroquinones less effectively, thus less effectively producing ROS.

When added together, 1,4-naphtoquinone increased both H_2O_2 and OH formation from Fe(II) and Cu(II). H_2O_2 and OH formation mixtures of Fe(II) and Cu(II) were generally higher than those produced by individual metals but less than the sum of those metals. However, a more complicated metal mixture revealed that OH formation in the presence of H_2O_2 was greatly enhanced. This shows the interaction between metals plays an important role in OH formation; however, the underlying mechanism is not well understood.

References

Charrier, J. G. and C. Anastasio (2011). Impacts of antioxidants on hydroxyl radical production from individual and mixed transition metals in a surrogate lung fluid. Atmos. Environ. 45:7555-7562.10.1016/j.atmosenv.2010.12.021.

Charrier, J. G., A. S. McFall, N. K. Richards-Henderson, C. Anastasio (2014). Hydrogen Peroxide Formation in a Surrogate Lung Fluid by Transition Metals and Quinones Present in Particulate Matter. Env. Sci. Tech. 48:7010-7017.10.1021/es501011w.

Charrier, J. G. and C. Anastasio (2015). Rates of Hydroxyl Radical Production from Transition Metals and Quinones in a Surrogate Lung Fluid. Env. Sci. Tech. 49:9317-9325.

Chen, R. and J. J. Pignatello (1997). Role of quinone intermediates as electron shuttles in Fenton and photoassisted Fenton oxidations of aromatic compounds. Env. Sci. Tech. 31:2399-2406,

Chung, M. Y., R. A. Lazaro, D. Lim, J. Jackson, J. Lyon, D. Rendulic, A. S. Hasson (2006). Aerosol-borne quinones and reactive oxygen species generation by particulate matter extracts. Env. Sci. Tech. 40:4880-4886.10.1021/es0515957.

Duesterberg, C. K. and T. D. Waite (2007). Kinetic modeling of the oxidation of p-hydroxybenzoic acid by Fenton's reagent: implications of the role of quinones in the redox cycling of iron. Env. Sci. Tech. 41:4103-4110,

Leonard, S., P. M. Gannett, Y. Rojanasakul, D. Schwegler-Berry, V. Castranova, V. Vallyathan, X. Shi (1998). Cobalt-mediated generation of reactive oxygen species and its possible mechanism. J. Inorg. Biochem. 70:239-244,

Torreilles, J. and M.-C. Guérin (1990). Nickel (II) as a temporary catalyst for hydroxyl radical generation. FEBS Letters 272:58-60.

Urbañski, N. K. and A. Beresewicz (2000). Generation of OH initiated by interaction of Fe 2+ and Cu+ with dioxygen; comparison with the Fenton chemistry. Acta Biochim Pol. 47:951-962.

Valavanidis, A., K. Fiotakis, E. Bakeas, T. Vlahogianni (2005). Electron paramagnetic resonance study of the generation of reactive oxygen species catalysed by transition metals and quinoid redox cycling by inhalable ambient particulate matter. Redox Report 10:37-51

7. Conclusion

Reactive Oxygen Species (ROS) plays an important role in the oxidation of aerosols, thus can modify the chemical composition, optical properties and hygroscopicity of aerosols. Excessive ROS formation by particulate matter in the body has thought to be the initial step of oxidative stress, leading to numerous adverse health impacts such as respiratory and cardiovascular diseases, pulmonary inflammation and mortality. Determining the causative agents in PM responsible for ROS formations by PM under atmospherically and physiologically relevant conditions will enable us to better understand the underlying mechanism of ROS formation and the interplay between H_2O_2 and OH.

Quantification of ROS formation by PM requires suitable assays to accurately measure H_2O_2 and OH. Quantification of H_2O_2 is performed using the HPLC-fluorescence technique with para-hydroxyphenyl acetic acid and horseradish peroxidase as fluorescent reagents. This assay has been extensively used by several studies, including those have previously reported by our group (Chung et al., 2006; Hasson et al., 2001a; Hasson and Paulson 2003; Shen and Anastasio 2011). A direct measurement of OH radicals in aqueous solution is rather difficult due to its high reactivity and short lifetime. Several chemical probes, including benzene, benzoate and terephthalate (Charbouillot et al., 2011; Faust and Allen 1993; Jung et al., 2006; Matthews 1980) have been used to trap OH radicals and the hydroxylated products can be detected via fluorescence or UV-Vis detection. Terephthalate is a particularly sensitive probe for hydroxyl radical (OH), with a detection limit as low as 2 nM. However, there is uncertainty in OH quantification using this method and the potential for interference from fluorescent compounds and/or some transition metals. Terephthalate reacts with OH to form a fluorescent product, 2-

hydroxylterephthalic acid (hTA). However, there is disagreement in the literature on the yield of the fluorescent product (Y_{hTA}), which introduces a large uncertainty in the quantification of OH. Additionally, the highest sensitivities (~ 2 nM) and ease of use are available if the assay can be performed without separating hTA from the sample. For many applications this approach works well, but it can be subject to interference from fluorescent compounds in the sample. Some complex organics, including fulvic and humic acids and biomass burning aerosol, fluoresce and/or absorb in the hTA measurement region. Samples containing significant amounts of humic substances or similar compounds (> about 10 mg/L) may interfere particularly at higher pH, when organics are partly or completely unprotonated. Finally, TA and similar organic probes are known to complex Cu(II) at high concentrations, thus if this reaction is important at lower concentrations, Cu(II) could reduce apparent hTA formation, and reduce activity of Cu(II) in target samples. Using a pH 3.5 dark ferrous Fenton system to generate OH radicals, we find that Y_{hTA} = 31.5 ± 7%. This is about double the recent literature value measured, but in line with earlier measurements. Additionally, we present a method to separate hTA from complex fluorescent organics, including fulvic and humic acids and soluble organics in biomass burning, using small, reasonably inexpensive Hydrophilic-Lipophilic Balance (HLB) cartridges. Finally, we find that interactions between Cu(II) and hTA are small enough to be ignored at Cu(II) concentrations below ~50 μM.

A field campaign was carried out at Claremont, CA in summer and resulting samples collected on Teflon filters were extracted in an atmospherically relevant solution (water at pH3.5), and analyzed for particle mass, H_2O_2 and OH generation, soluble trace metals and speciated soluble iron. The average mass normalized concentrations of ferrozine iron and H_2O_2

were the highest in the morning samples, as observed for a few other soluble ICP metals such as Zn, Mn, Ni and Pb. OH did not show a strong diurnal variation, but higher concentrations were observed in the morning and overnight samples. Generally, the afternoon samples have lower trace metal contents and lower ROS activity than the morning and overtime samples. Fe was the most abundant trace metal, followed by Zn and copper. Soluble speciated iron was about 50% Fe(II) and 50% Fe(III). H_2O_2 was relatively poorly correlated with aerosol mass, but strongly correlated with soluble ICP iron and manganese. OH on the other hand shows good correlations with mass, Fe and Cu but did not correlate with speciated iron. A numbers of studies reported trace metals played an important role in ROS formation; however, different sets of metals were found to be responsible for the observed ROS activity. Shafer et al., (2010) identified the ROS-active metals as Fe, Mn, Co and Ni. See et al., (2007) found a similar set of metals (Mn, Cd, Co, Cu, Fe and Ni) that are responsible for ROS formation by wood smoke, gas cooking and traffic influenced aerosols. ROS formation was quantified using dichlorofluorescein assay in these two studies. The dichlorofluorescein assay responds to a wide variety of ROS, including but not limited to H_2O_2, OH, organic peroxides and peroxynitrite anion ($ONOO^-$) (Cohn et al., 2008; Rota et al., 1999). Since this assay is not specific to H_2O_2 and OH, it makes it more difficult to interpret the role of metals. In a more specific assay to measure H_2O_2, Wang et al., (2010) showed that H_2O_2 generated by coarse particles collected in Riverside, CA, a city with heave photochemical smog influence, was strongly correlated with Fe, Cu and Zn. Similarly, our results show that Fe, Cu and Mn are the most important trace metals in ROS formation. Specifically, H_2O_2 was most correlated with ferrozine iron, followed by ICP Fe and Cu while Cu was the best single metal predictor for OH, followed by Fe and Mn. Finally, more processed

aerosols contained more soluble trace metals and produced more H_2O_2 and OH than freshly emitted aerosol.

Another field campaign was carried out in wintertime in Fresno, CA. These samples were extracted in pH 3.5 aqueous solutions to analyze for H_2O_2 and OH formation, iron speciation, and soluble trace metal concentrations. Biomass burning aerosol (BBA) and mass were measured on the filters. Of the trace metals measured, iron was the most abundant followed by zinc and copper. Iron speciation results indicated that iron in the Fresno samples were predominantly in its reduced form (Fe(II)). Samples that contained significant amount of BBA produced substantially higher OH. A multivariate linear regression showed that a combination of mass, iron and BBA explained majority of variability in H_2O_2 concentrations (> 80%) while manganese, iron and BBA were the significant contributors to OH formation, with $r^2 > 0.9$.

Mass was generally better correlated with ROS and trace metals than those observed in the Claremont samples. The same subset of metals (Fe, Cu and Mn) were found to be important for ROS formation, as identified in the Claremont samples, however, the relative importance was different. OH was most correlated with biomass burning aerosols (BBA, $r^2 = 0.88$), followed by Fe and Cu. BBA was also correlated with H_2O_2 ($r^2 = 0.64$) but the strongest correlation was with ICP Fe ($r^2 = 0.75$) and ferrozine Fe(II) ($r^2 = 0.65$). BBA also increased the correlation between H_2O_2 and ICP Fe from $r^2 = 0.75$ to 0.89. The interaction between BBA and Fe(II) greatly increase ROS by enhancing the rate constant of superoxide formation from Fe(II) and oxygen as well as the rate constant of the Fenton reaction (Gonzalez et al., 2017).

We also assess the impacts of switching marine vessels from conventional diesel to renewable fuel on the ability of particles to generate hydroxyl radical when extracted in a

simulated lung lining fluid or in water at pH 3.5, for samples of engine emissions from a research vessel when operating on Ultra Low Sulfur Diesel (ULSD) and Hydrogenation-Derived Renewable Diesel (HDRD). Samples were collected during dedicated cruises in 2014 and 2015, including aged samples collected by re-intercepting the ship plume. After normalizing to particle mass, particles generated from HDRD combustion had slightly to significantly (5-50%) higher OH generation activity than those from ULSD, a difference that was statistically significant for some permutations of year/fuel/engine speed. Soluble trace metal concentrations were similar to the fuel metal concentrations, and compared to urban Los Angeles samples lower in soluble iron and manganese, but similar for most other trace metals. Because PM mass emissions were higher for HDRD, normalizing to fuel increased this difference. Freshly emitted PM had lower activity than the "plume chase" samples, and samples collected on the ship had lower activity than the urban reference. The differences in OH production correlated reasonably well with redox-active transition metals, most strongly with soluble manganese, with roles for vanadium and likely copper and iron. The results also suggest that atmospheric processing of fresh combustion particles rapidly increases metal solubility, which in turn increases OH production.

As shown in both the ship and urban samples, ROS production in SLF was generally higher than that in pH 3.5, particularly for H_2O_2. Fig 7.1 shows OH and H_2O_2 production in pH3.5 and SLF for PM collected in Claremont and Fresno. H_2O_2 formation was about 6 and 40 times higher in SLF than pH 3.5 for the Claremont and Fresno samples, respectively. Since transition metal solubility are much lower at higher pHs (Deguillaume et al., 2005) and H_2O_2 generation are highest in the pH range 3.5-5.5 (Wang et al., 2012), the higher H_2O_2 concentration in SLF may attribute to the presence of an electron donor, ascorbate, in SLF solution, which can

enhance redox cycling of metals, thus producing more ROS than pH 3.5. Furthermore, BBA are more soluble at higher pH's, thus more BBA are expected to be dissolved in SLF (pH 7.4) than pH 3.5 solutions. The higher H_2O_2 production was associated with higher mass loading of BBA (mainly the overnight samples).

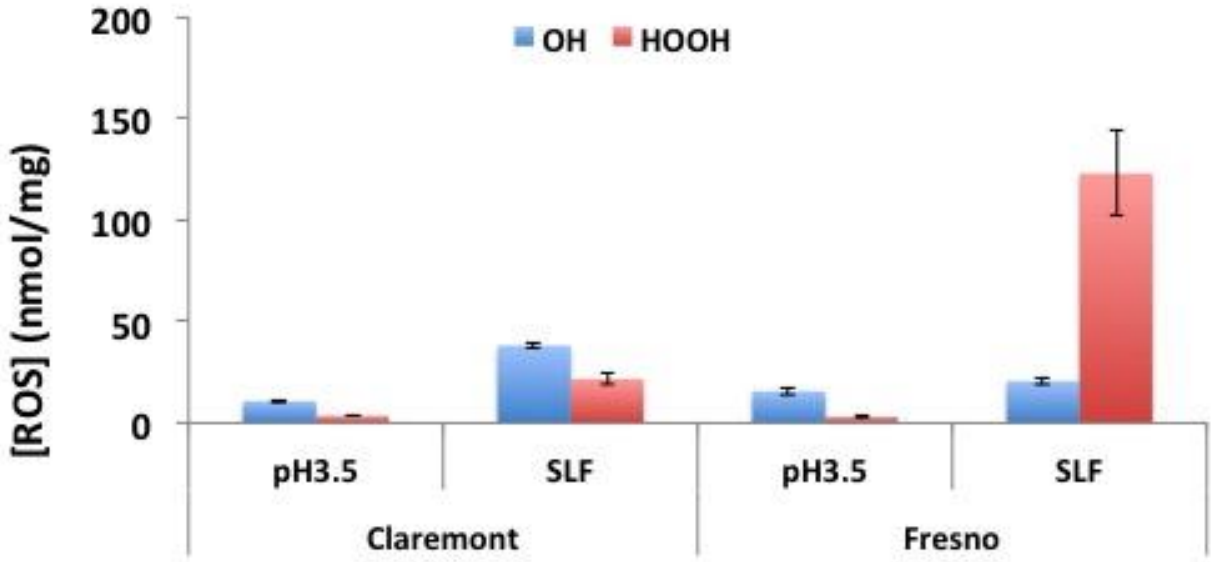

Fig. 7.1 H_2O_2 and OH formation in pH3.5 and SLF, for both Claremont and Fresno samples. Error bars indicate standard errors.

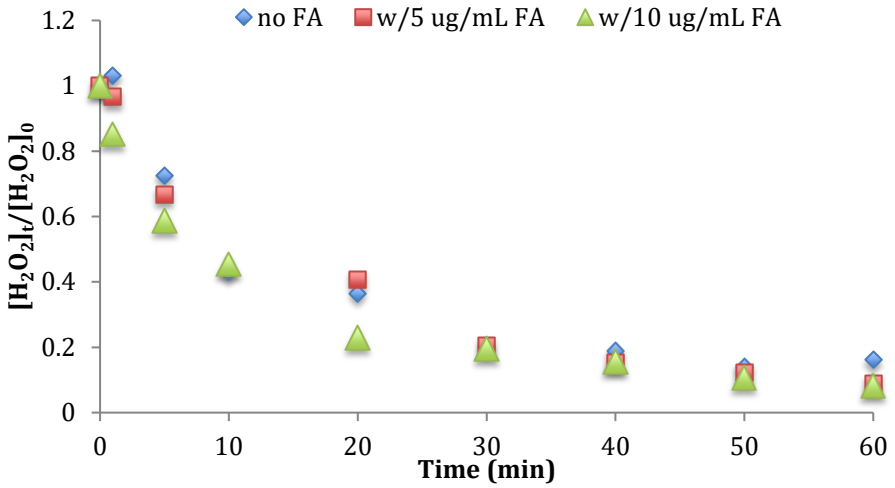

Fig. 7.2 Destruction of H_2O_2 ($[H_2O_2]_0$ 5 μM) by Fe(II) ($[Fe(II)]_0$ = 5 μM) with 0, 5 and 10μg/mL of FA in pH3.5.

Our field and experimental results have shown that HULIS, as BBA in field samples and FA as a surrogate, can increase H_2O_2 destruction by Fe(II) (Fig. 7.2) and enhance OH formation (Gonzalez et al., 2017). Our results also indicate BBA was strongly correlated with several transition metals, including Fe, Cu, Mn and Pb. While a handful of studies investigated the interaction between BBA and Fe, very little data have looked at its relations with other metals. Further investigation in the role of humic like substances in metal solubility will provide a better understanding of how they interacts with transition metals, which may change their reactivity and their ability to produce ROS. The composition of HULIS depends on the sources and the degree of oxidation in the atmosphere; further understanding of HULIS formed from secondary reactions will gain insight into the processes occurring in the atmosphere. Secondary organic aerosol (SOA) formation can be simulated in chambers. The SOA system is a great tool to study single and simple mixed particles. It is intermediate to between laboratory bulk solutions and

ambient aerosols, in terms of both complexity and representativeness. SOA formation in highly controlled chamber experiments involving biomass-burning derived VOCs such as m-Cresol (Iinuma et al., 2010) and guaiacol (Lauraguais et al., 2014; Ofner et al., 2011; Yee et al., 2013) can be used to study the fate of compounds emitted from biomass burning and the role of the oxidation products on ROS formation.

Reference

Hasson, A. S., G. E. Orzechowska, S. E. Paulson (2001a). Production of stabilized Criegee intermediates and peroxides in the gas phase ozonolysis of alkenes: 1. Ethene, trans-2-butene, and 2,3-dimethyl-2-butene. J. Geophys. Res. 106:34,131-134,142.

Chung, M. Y., R. A. Lazaro, D. Lim, J. Jackson, J. Lyon, D. Rendulic, A. S. Hasson (2006). Aerosol-borne quinones and reactive oxygen species generation by particulate matter extracts. Env. Sci. Tech. 40:4880-4886.

Shen, H. and C. Anastasio (2011). Formation of hydroxyl radical from San Joaquin Valley particles extracted in a cell-free surrogate lung fluid. Atmospheric Chemistry and Physics 11:9671-9682.

Hasson, A. S. and S. E. Paulson (2003). An Investigation of the Relationship between Gas-phase and Aerosol-borne Hydroperoxides in Urban Air. J. Aerosol Sci. 34: 459-468.

Jung, H., B. Guo, C. Anastasio, I. M. Kennedy (2006). Quantitative measurements of the generation of hydroxyl radicals by soot particles in a surrogate lung fluid. Atmos. Environ. 40:1043-1052.

Matthews, R. W. (1980). The Radiation Chemistry Of The Terephthalate Dosimeter. Radiation Research 83:27-41.

Faust, B. C. and J. M. Allen (1993). Aqueous-phase photochemical formation of hydroxyl radical in authentic cloudwaters and fogwaters. Env. Sci. Tech. 27:1221-1224.

Charbouillot, T., M. Brigante, G. Mailhot, P. R. Maddigapu, C. Minero, D. Vione (2011). Performance and selectivity of the terephthalic acid probe for (OH)-O-center dot as a function of temperature, pH and composition of atmospherically relevant aqueous media. Journal of Photochemistry and Photobiology a-Chemistry 222:70-76.

Armstrong, W. A., R. A. Facey, D. W. Grant, W. G. Humphreys (1963). A tissue-equivalent chemical dosimeter sensitive to 1 rad. Can. J. Chem. 41:1575-1577.

Son, Y., V. Mishin, W. Welsh, S.-E. Lu, J. D. Laskin, H. Kipen, Q. Meng (2015). A Novel High-Throughput Approach to Measure Hydroxyl Radicals Induced by Airborne Particulate Matter. Int. J. Environ. Res. Pub. Health 12:13678-13695.

Charrier, J. G. and C. Anastasio (2011). Impacts of antioxidants on hydroxyl radical production from individual and mixed transition metals in a surrogate lung fluid. Atmospheric Environment 45:7555-7562.

Shafer, M. M., D. A. Perkins, D. S. Antkiewicz, E. A. Stone, T. A. Quraishi, J. J. Schauer (2010). Reactive oxygen species activity and chemical speciation of size-fractionated atmospheric particulate matter from Lahore, Pakistan: an important role for transition metals. J. Environ. Monit. 12:704-715.

See, S. W., Y. H. Wang, R. Balasubramanian (2007). Contrasting reactive oxygen species and transition metal concentrations in combustion aerosols. Environ. Res, 103:317-324.

Cohn, C. A., S. R. Simon, M. A. Schoonen (2008). Comparison of fluorescence-based techniques for the quantification of particle-induced hydroxyl radicals. Particle and Fibre Toxicol. 5:1-9.

Rota, C., C. F. Chignell, R. P. Mason (1999). Evidence for free radical formation during the oxidation of 2'-7'-dichlorofluorescin to the fluorescent dye 2'-7'-dichlorofluorescein by horseradish peroxidase: possible implications for oxidative stress measurements. Free Radical Bio. Med. 27

Wang, Y., C. Arellanes, D. B. Curtis, S. E. Paulson (2010). Probing the Source of Hydrogen Peroxide Associated with Coarse Mode Aerosol Particles in Southern California. Environmental Science & Technology 44:4070-4075.

Gonzalez, D. H., C. K. Cala, S. E. Paulson (2017). HULIS Enhancement of OH by Fe(II): Kinetics of Suwannee RIver Fulvic Acid-Fe(II) Complexes in the Presence of Lung Antioxidants. Env. Sci. Tech.

Deguillaume, L., M. Leriche, K. Desboeufs, G. Mailhot, C. George, N. Chaumerliac (2005). Transition metals in atmospheric liquid phases: Sources, reactivity, and sensitive parameters. Chem. Rev. 105:3388-3431.

Wang, Y., C. Arellanes, S. E. Paulson (2012). Hydrogen peroxide associated with ambient fine-mode, diesel, and biodiesel aerosol particles in Southern California. Aerosol Sci.Technol. 46:394-402.

Iinuma, Y., O. Böge, R. Gräfe, H. Herrmann (2010). Methyl-nitrocatechols: atmospheric tracer compounds for biomass burning secondary organic aerosols. Enviro. Sci. Tech. 44:8453-8459.

Lauraguais, A., C. Coeur-Tourneur, A. Cassez, K. Deboudt, M. Fourmentin, M. Choël (2014). Atmospheric reactivity of hydroxyl radicals with guaiacol (2-methoxyphenol), a biomass burning emitted compound: Secondary organic aerosol formation and gas-phase oxidation products. Atmos. Environ. 86:155-163.

Ofner, J., H.-U. Krüger, H. Grothe, P. Schmitt-Kopplin, K. Whitmore, C. Zetzsch (2011). Physico-chemical characterization of SOA derived from catechol and guaiacol–a model substance for the aromatic fraction of atmospheric HULIS. Atmos. Chem. Phys. 11:1-15.

Yee, L., K. Kautzman, C. Loza, K. Schilling, M. Coggon, P. Chhabra, M. Chan, A. Chan, S. Hersey, J. Crounse (2013). Secondary organic aerosol formation from biomass burning intermediates: phenol and methoxyphenols. Atmos. Chem. Phys. 13:8019-8043.